

# Hydrodynamics of orbital shaken bioreactors

THÈSE N° 5759 (2013)

PRÉSENTÉE LE 30 AOÛT 2013

À LA FACULTÉ DES SCIENCES ET TECHNIQUES DE L'INGÉNIEUR  
LABORATOIRE DE MACHINES HYDRAULIQUES  
PROGRAMME DOCTORAL EN MÉCANIQUE

ÉCOLE POLYTECHNIQUE FÉDÉRALE DE LAUSANNE

POUR L'OBTENTION DU GRADE DE DOCTEUR ÈS SCIENCES

PAR

**Martino RECLARI**

acceptée sur proposition du jury:

Prof. M. Parlange, président du jury  
Dr M. Farhat, directeur de thèse  
Prof. A. Aroussi, rapporteur  
Prof. F. Gallaire, rapporteur  
Prof. F. Sotiropoulos, rapporteur  
Prof. F. M. Wurm, rapporteur



ÉCOLE POLYTECHNIQUE  
FÉDÉRALE DE LAUSANNE

Suisse  
2013



A man who carries a cat by the tail  
learns something he can learn in no other way.

— Mark Twain





# Acknowledgements

Apart from the candidate's efforts, the success of a Ph.D. research depends also on those who supported, encouraged and guided him. Although a document as thick as the present thesis would be necessary to acknowledge them appropriately, I attempt here to express my gratitude in a somehow shorter way.

First of all I would like to express my most sincere thanks to my thesis director, Dr. Mohamed Farhat, who encouraged, guided and sided with me even in my most unorthodox choices, never limiting my freedom of action. I am glad he almost tricked me into doing a Ph.D.! Moreover, the present work would not have existed without Prof. Florian Wurm, who kindled our interest in the hydrodynamics of orbital shaken liquids. I would also like to acknowledge the other members of the Sinergia team: Stephanie Tissot, Samuel Quinodoz, Dominique Monteil, Prof. Alfio Quarteroni and the Swiss National Science Foundation who supported the work. Furthermore, I would like to thank the head of LMH, Prof. François Avellan, for the opportunity he offered me to work in his laboratory, and for several interesting conversations on wave dynamics. I would like to express the deepest gratitude to the members of the thesis jury: Prof. Parlange, Prof. Aroussi, Prof. Gallaire and Prof. Wurm for providing me with various, interesting inputs. I received many other advices from “Danio” Obreschkow and Nicolas Dorsaz with whom I had fruitful conversations during their stay at LMH; from Dr. Ducruet and Dr. Bach (HES of Changin, oh what an inestimable experience in wine and oenology!), and from George Crittin for the electronic parts. My thanks go also to the LMH mechanics, for their efficiency and precision of execution: Luis, Maxime, Raymond, Victor, David, Jean-Daniel, Mattias, Simon and Christian. I would like also to acknowledge Paul, Gwenaël and Samuel for their contribution to the researches.

During a Ph.D. research we do not face tough work only: we meet also excellent colleagues and friends. I have to thank the big family of the LMH: our secretary Isabelle; those who have already finished as Philippe A., Sébastien (many thanks for the kite!) and Cécile, Nicolas R., Amir, Ali, Francisco, Martin, Stefan, Vlad, Bob, Marc, Philippe K. and Pierre; and those who are currently working on their thesis: Arthur, Arturo, Christian L., Christian V., Ebrahim, Julien, Simon P. and Keita. I wish you all the best for your thesis! Many thanks also to Steven, for his long lasting friendship, to Pacot (the best telemarketing teacher in the world) and Andres for everything – hold fast men, it is almost over!

A very special thank goes to Matthieu, for his help in several experiences and discussions, for his good humour and for sharing good music with me!

## Acknowledgements

---

I would also like to acknowledge Pascal, who contributed to diversify my researches by enlisting me in several projects. In this respect, I also thank Bernard, Gautier, Sébastien, Philippe B. and all the other people involved with the Rivage project for the friendly collaboration.

Thanks go to Maître Altanov, Joël, Luca, Gauvain, Carole, Nicolas, the people from the small (but full of fighting spirit) fencing group of the University. I also thank Lt. Col. Bonfio, Lt. Col. Paganini, Cap. Barlocchi and Cap. Galli who made it possible to conciliate my studies with the army duty.

As one can notice, most of the thanks are for encouragement. Indeed, while we handle the hard work, we need sometimes a pat on the back or a couple of kind words. In this respect, I would like to thank my family: Wania, Luigi, Fabrizio, Lina, Giorgia and Francesco, who constantly encouraged me during this long and not easy journey. Last but certainly not least, I wish to deeply thank my girlfriend Martina, for her relentless help in finding all my English errors, and especially for her kindness and her love. Thank you from my heart for your unfailing support.

*May 16, 2013*

Martino Reclari

# Abstract

Be it to aerate a glass of wine before tasting, to accelerate a chemical reaction or to cultivate cells in suspension, the “swirling” (or orbital shaking) of a container ensures good mixing and gas exchange in a simple and intuitive way. Despite being used in such a large variety of applications, the flow generated in a container subject to orbital shaking is far from being understood, and presents a richness of patterns and behaviours which has not yet been reported. While orbital shaken cell cultures are very efficient and productive at small scale, their increase in scale is hampered by several issues, some of which are thought to have their origin in the motion of the liquid medium. The present research remedies to this situation, charting the evolution of the wave behaviour with the operating parameters, highlighting the importance of the wave regimes and assessing their mixing efficiency. We present here a mathematical solution, based on the potential hypothesis and on techniques used in sloshing dynamics, predicting the shape of the free surface and the liquid motion. The validity and the limits of this model were assessed by comparison with a very large number of free surface measurement, obtained using a specifically developed automated acquisition system, and with non intrusive velocity measurements of several shaking configurations. A large variety of wave patterns (i.e. free surface shapes) were identified, ranging from single and multiple crested waves to breaking waves and waves having a shape constantly changing as they rotate. Our research revealed the importance of free surface natural modes and their sub-harmonics in the behaviour of the waves. From the results of the potential model and the measurements, we identified four dimensionless groups ensuring hydrodynamic similarity of the flow between different scales. Moreover, we were able to identify the most efficient waves in terms of mixing, and to suggest optimal ranges of the operating parameters to enhance the mixing and oxygenation of the cell cultures.

**Keywords:** free surface flow, waves, sloshing, orbital shaking, bioreactors



## Résumé

Que ce soit pour aérer un verre de vin, pour accélérer une réaction chimique ou pour cultiver des cellules en suspension, l'agitation orbital d'un récipient garantit, d'une façon simple et intuitive, de bonnes performances en terme de mélange et d'échange de gaz. Alors qu'il est utilisé dans une vaste gamme d'applications, l'écoulement dans un récipient en agitation orbitale n'est pas encore compris, et présente une richesse de formes et de régimes jusqu'à maintenant inconnues. Dans le cas des cultures cellulaires plusieurs phénomènes, générés par le mouvement du liquide, empêchent l'optimisation des cultures de grande taille. Le but de cette recherche est d'acquérir une compréhension de la physique du mouvement du liquide suffisante pour garantir une optimisation rigoureuse de des écoulement. Nous présentons ici un modèle mathématique, fondé sur l'hypothèse d'écoulement potentiel et inspiré des techniques utilisées dans l'étude du ballotement liquide, qui permet de prédire la forme de la surface et les champs de vitesse du liquide. La validité du modèle et ses limites sont identifiés par comparaison avec une grande quantité de mesures expérimentales de la hauteur de la surface libre, obtenues avec un installation expérimentale spécifiquement développée, et ainsi qu'avec des mesures de champs de vitesse. Une grande quantité de formes de vagues a été identifiée : des vagues avec une ou plusieurs crêtes et jusqu'aux déferlantes de même que des vagues ayant une déformation pendant qu'elles tournent. En utilisant les résultats du modèle et des expériences nous avons identifié quatre paramètres adimensionnels, garantissant la similarité hydrodynamique de l'écoulement à différentes échelles. Nous avons aussi identifié les vagues ayant les meilleures performances en termes de mélange, et nous pouvons proposer des plages de fonctionnement garantissant le meilleur mélange et la meilleure oxygénation.

**Mots clés :** écoulement à surface libre, vagues, ballotement, agitation orbitale, bioréacteurs



# Contents

<b>Acknowledgements</b>	<b>v</b>
<b>Abstract (English/Français)</b>	<b>vii</b>
<b>Contents</b>	<b>xii</b>
<b>List of figures</b>	<b>xv</b>
<b>Nomenclature</b>	<b>xvii</b>
<b>1 Introduction</b>	<b>1</b>
1.1 Orbital shaking . . . . .	1
1.2 Framework of the project . . . . .	5
1.3 The case study . . . . .	5
<b>2 Analytical approach</b>	<b>7</b>
2.1 General governing equations . . . . .	7
2.2 Gravity waves dynamics . . . . .	8
2.3 Sloshing dynamics . . . . .	14
2.3.1 Dimensionless formulation . . . . .	25
2.3.2 Weakly non-linear solution . . . . .	26
2.4 Considerations . . . . .	37
<b>3 Experimental setup</b>	<b>39</b>
3.1 The orbital shaker . . . . .	39
3.2 Free surface visualization and measurement . . . . .	41
3.2.1 Wall liquid elevation measurement . . . . .	41
3.2.2 Automated measurements . . . . .	44
3.2.3 Free surface measurements operating conditions . . . . .	45
3.2.4 Instantaneous visualization of the free surface height at the entire wall . . . . .	47
3.3 Velocity fields measurements . . . . .	48
3.3.1 Laser Doppler Velocimetry . . . . .	48
3.3.2 Particle Image Velocimetry . . . . .	49
3.3.3 Proper Orthogonal Decomposition . . . . .	51
3.3.4 Operating conditions of the measurements . . . . .	53

## Contents

---

3.4	Mixing measurement . . . . .	54
<b>4</b>	<b>Dynamics of waves induced by orbital shaking</b>	<b>57</b>
4.1	Observations . . . . .	57
4.1.1	The periodicity of the waves . . . . .	62
4.1.2	Wave classification . . . . .	63
4.2	Synchronous waves motion . . . . .	64
4.2.1	Non-breaking waves . . . . .	64
4.2.1.1	Single crest waves . . . . .	65
4.2.1.2	Multiple crested waves . . . . .	70
4.2.2	Toward breaking waves . . . . .	76
4.2.2.1	Breaking of single crested waves . . . . .	78
4.2.2.2	Breaking of multiple crested waves . . . . .	80
4.2.3	After the breaking of the waves . . . . .	83
4.3	Non-synchronous waves . . . . .	88
4.3.1	Continuously changing waves . . . . .	88
4.3.2	Liquid motion . . . . .	89
<b>5</b>	<b>Application to orbital shaken bioreactors</b>	<b>93</b>
5.1	Scale-up . . . . .	93
5.1.1	Dimensionless parameters . . . . .	94
5.1.2	Parameters validation . . . . .	95
5.1.3	Influence of the Reynolds number . . . . .	97
5.2	Mixing . . . . .	99
5.2.1	Average flow mixing . . . . .	100
5.2.2	Turbulent mixing . . . . .	103
5.2.3	Mixing in non-synchronous waves . . . . .	104
5.3	Optimal wave pattern . . . . .	106
5.3.1	Prediction of the wave pattern and flow regimes . . . . .	106
5.3.2	Engineering considerations . . . . .	108
5.3.3	The best shaking configuration . . . . .	111
<b>6</b>	<b>Conclusions</b>	<b>113</b>
<b>7</b>	<b>Perspectives</b>	<b>115</b>
	<b>Appendices</b>	<b>117</b>
A	Surface from diffraction reconstruction . . . . .	117
B	Bessel's functions . . . . .	119
B.1	The Fourier-Bessel Series . . . . .	120
C	Three-dimensional drift calculations . . . . .	122
D	Combination of time coefficients of first order solution . . . . .	125
	<b>Bibliography</b>	<b>129</b>



# List of Figures

1.1	Uses and applications of the orbital shaking. . . . .	1
1.2	Wine glasses improving the aeration during swirling. . . . .	2
1.3	Orbital shaker in biological applications. . . . .	3
1.4	Stirred tanks vs. orbital shaker . . . . .	4
1.5	The case study . . . . .	5
2.1	Bi-dimensional linear waves velocity fields and trajectories. . . . .	12
2.2	Stokes drift in linear waves. . . . .	14
2.3	Dimensions of the container and references frames used in the potential sloshing model . . . . .	15
2.4	Natural modes of the free surface . . . . .	18
2.5	Examples of potential free surface shapes . . . . .	20
2.6	Potential free surface elevation from lateral point of view. . . . .	21
2.7	Velocity fields from the solution of the potential theory . . . . .	22
2.8	Potential predicted trajectories followed by particles during orbital shaking. . .	23
2.9	Stokes drift in orbital shaken containers . . . . .	24
2.10	Example of free surface elevation according to the weakly non-linear solution .	37
3.1	Kuhner ES-X orbital shaker . . . . .	40
3.2	Modifications of the orbital shaker . . . . .	40
3.3	Free surface visualization and measurement at the wall . . . . .	41
3.4	Optical relations during free surface measurement . . . . .	42
3.5	Automated free surface displacement measurement . . . . .	44
3.6	List of shaking configurations whose wave displacements at the wall $\delta(\theta, t)$ has been measured . . . . .	46
3.7	Setup of time resolved imaging of the waves. . . . .	47
3.8	Laser Doppler Velocimetry (LDV) setup . . . . .	48
3.9	Particle Image Velocimetry (PIV) setup . . . . .	49
3.10	Limitations of the PIV measurement regions . . . . .	51
3.11	Laser induced fluorescence for mixing measurements setup . . . . .	54
4.1	Detected wave patterns . . . . .	57
4.2	Evolution of a wave with increasing $\Omega$ . . . . .	58
4.3	Lateral visualization of waves shapes with increasing $\Omega$ . . . . .	60

## List of Figures

---

4.4	Evolution of the waves with changing $d_s$ and $H_0$ . . . . .	61
4.5	Phase averaging of synchronous (and non-synchronous) wave height. . . . .	62
4.6	Summary of the wave pattern categories . . . . .	63
4.7	Wave amplitudes at low shaking frequency . . . . .	65
4.8	LDV measurements of three dimensional velocity fields in potential regime of the flow. . . . .	66
4.9	Trajectories of liquid particles of single crested waves, both from measurements of the velocity fields and from potential solution. . . . .	67
4.10	Averaged flow velocities $\bar{v}_i(r, z)$ of single crested waves . . . . .	68
4.11	Position of particles after various revolutions of single crested waves . . . . .	69
4.12	Amplitude spectra of multiple crested waves. . . . .	70
4.13	Example of decomposition of multiple crested waves . . . . .	71
4.14	Amplitude of sub-harmonics waves as a function of the shaking frequency . . .	72
4.15	Amplitudes spectra of multiple crests waves at $\omega_{11}/3$ and $\omega_{21}/4$ . . . . .	73
4.16	Phase shift of sub-harmonic waves as a function of the shaking frequency . . .	73
4.17	Sub-harmonic waves at $\Omega$ around $\omega_{21}/2$ compared to the non-linear model predictions. . . . .	74
4.18	Trajectories followed by groups of particles in a double crested wave . . . . .	75
4.19	Amplitude of the waves with $\Omega$ between $\omega_{21}/2$ and $\omega_{11}$ , at $\tilde{d}_s=0.1$ . . . . .	76
4.20	Breaking waves at the transition . . . . .	77
4.21	Single crest waves close to the breaking . . . . .	79
4.22	Tangential velocity at the breaking of single crested wave . . . . .	79
4.23	Velocity measurements of double crested wave at breaking inception . . . . .	81
4.24	Trajectories followed by groups of particles at the transition to the breaking. . .	82
4.25	Influence of the scale on transitions phenomena at the breaking . . . . .	83
4.26	Breaking waves after the transition to the breaking . . . . .	84
4.27	LDV measurements of three dimensional velocity fields in rotary regime of the flow. . . . .	85
4.28	Averaged tangential velocity from PIV measurements for various shaking frequencies . . . . .	85
4.29	Trajectories of liquid particles in rotating regime, from PIV measurements of the velocity fields at three shaking frequencies . . . . .	86
4.30	Evolution of free surface amplitude of a wave with $\tilde{d}_s=0.01$ . . . . .	87
4.31	Example of non-synchronous waves . . . . .	88
4.32	Free surface behaviour of non-synchronous waves . . . . .	90
4.33	POD analyses of non synchronous waves . . . . .	91
4.34	Trajectories of particles in non-synchronous waves . . . . .	92
5.1	RMS difference of wave height at various shaking configurations . . . . .	96
5.2	Comparison of LDV velocity measurements obtained at different scales . . . . .	96
5.3	Influence of the $Re$ number . . . . .	97
5.4	Phase shift of the principal plane of inertia . . . . .	98

5.5	Dye dispersion from the free surface into the liquid bulk . . . . .	100
5.6	Average dispersion of particles at various shaking frequencies . . . . .	101
5.7	Vertical distance between the particles in average flow mixing . . . . .	102
5.8	Dispersion of particles due to velocity fluctuations . . . . .	103
5.9	Dispersion of particles in non-synchronous waves . . . . .	105
5.10	Mixing times measured by LIF for synchronous and non-synchronous waves .	105
5.11	Evolution of the potential velocities with the depth . . . . .	108
5.12	Estimated shaking frequencies and moments of inertia of a 1000 litres culture at the breaking inception . . . . .	110
5.13	Estimated centripetal force of a 1000l culture at the breaking inception . . . . .	111
A.1	Surface by diffraction . . . . .	118
B.1	Bessel functions of the first and second kind. . . . .	119



# Nomenclature

## Latin

$\tilde{A}$	Amplitude of the wave at the wall	[m]
$a_{mn}(t)$	First time dependent coefficient of the free surface solution of the potential problem, corresponding to the $m^{th}$ mode in the radial direction and to the $n^{th}$ mode in the tangential direction, see Eq.2.65	[m]
$a_i(t)$	Time dependent coefficient of the expansion of the velocity fluctuations, $i^{th}$ mode, in the POD analyses, see Eq. 3.5	[-]
$c_p$	Phase velocity, or propagation celerity, of the wave	[m/s]
$b_{mn}(t)$	Second time dependent coefficient of the free surface solution of the potential problem, see $a_{mn}$	[m]
$D$	Internal diameter of the container	[m]
$d_s$	Diameter of the shaking circular trajectory	[m]
$\mathbf{e}_x, \mathbf{e}_y, \mathbf{e}_z$	Basis vectors of Cartesian coordinates systems	[-]
$\mathbf{e}_r, \mathbf{e}_\theta, \mathbf{e}_z$	Basis vectors of cylindrical coordinates systems	[-]
$F_c$	Centripetal force	[N]
$g$	Apparent gravitational acceleration	[m/s <sup>2</sup> ]
$H_0$	Liquid elevation in the container at rest	[m]
$I_m$	Moment of inertia	[kg m <sup>2</sup> ]
$J_m$	Bessel's function of the first kind, $m^{th}$ order	[-]
$\mathbf{k}$	Wave numbers vector, with magnitude $  \mathbf{k}   = k$	[1/m]
$p$	Pressure	[N/m <sup>2</sup> ]
$p_a$	Atmospheric pressure	[N/m <sup>2</sup> ]
$\mathbf{q}(\mathbf{x}, t)$	Velocity vector issued from the potential model, in Eulerian description, with components:	[m/s]
$(q_x, q_y, q_z)$	Components of the velocity issued from the potential model, Eulerian description, in Cartesian coordinates system	[m/s]

## Nomenclature

---

$(q_r, q_\theta, q_z)$	Components of the velocity issued from the potential model, Eulerian description, in cylindrical coordinates system	[m/s]
$\mathbf{q_L}(\mathbf{x}_0, t)$	Velocity vector issued from the potential model, in Lagrangian description, may be used in Cartesian or cylindrical coordinates system	[m/s]
$\mathbf{v}(\mathbf{x}, t)$	Velocity vector issued from experimental measurements, with components:	[m/s]
$(v_x, v_y, v_z)$	Measured components of the velocity, in Cartesian coordinates system	[m/s]
$(v_r, v_\theta, v_z)$	Measured components of the velocity, in cylindrical coordinates system	[m/s]
$\mathbf{x}(t)$	Vector position of a fluid particle, with components:	
$(x, y, z)$	Cartesian coordinates of a fluid particle	[m]
$(r, \theta, z)$	Cylindrical coordinates of a fluid particle at	[m,rad,m]
$\mathbf{x}_0$	Vector position of a fluid particle at $t=0$ , with components:	
$(x_0, y_0, z_0)$	Cartesian coordinates of a fluid particle at $t=0$	[m]
$(r_0, \theta_0, z_0)$	Cylindrical coordinates of a fluid particle at $t=0$	[m,rad,m]

## Greek

$\alpha_{mn}(t)$	First time dependent coefficient of the velocity potential solution of the potential problem, corresponding to the $(m, n)$ mode, see Eq.2.46	[m <sup>2</sup> /s]
$\alpha$	Position of the container on its shaking trajectory	[rad]
$\beta_{mn}(t)$	Second time dependent coefficient of the velocity potential solution of the potential problem, see $\alpha_{mn}$	[m <sup>2</sup> /s]
$\Delta I_{RMS}$	Root mean squared difference of the light intensity between two images, used in mixing measurements	[-]
$\overline{  \Delta_z  }$	Average vertical distance between a group of liquid particles	[m]
$\delta$	Liquid height measured at the wall	[m]
$\varepsilon_{mn}$	$n^{th}$ root of the derivative of the Bessel's function of the first kind, $m^{th}$ order.	[-]
$\epsilon$	Expansion parameter in perturbation series	[-]
$\lambda$	Wavelength	[m]
$\mu$	Dynamic viscosity	[Pa s]
$\nu$	Kinematic viscosity	[m <sup>2</sup> /s]

$\xi$	Elevation of the free surface predicted by the potential model	[m]
$\rho$	Density	[kg/m <sup>3</sup> ]
$\tau$	Shear stress	[N/m <sup>2</sup> ]
$\Phi$	Velocity potential of the container and liquid motion	[m <sup>2</sup> /s]
$\Phi_0$	Velocity potential of the container motion	[m <sup>2</sup> /s]
$\tilde{\Phi}$	Velocity potential of the liquid motion	[m <sup>2</sup> /s]
$\phi_i$	$i^{th}$ POD mode	[m]
$\Omega$	Shaking frequency. Note that it may sometimes be expressed in revolutions per minute.	[1/s]
$\omega_{mn}$	Natural frequency corresponding to the mode $(m, n)$ .	[1/s]

### Dimensionless

$\tilde{A}_\delta = \frac{A_\delta}{D}$	Measured dimensionless amplitude of the wave at the wall
$\tilde{A}_\xi = \frac{A_\xi}{D}$	Potentially predicted dimensionless amplitude of the wave at the wall
$\tilde{A}_b = \frac{A_b}{D}$	Dimensionless amplitude of the wave at the breaking
$\tilde{d}_s = \frac{d_s}{D}$	Dimensionless shaking diameter
$\tilde{H}_0 = \frac{H_0}{D}$	Dimensionless unperturbed liquid height
$Fr = \sqrt{\frac{d_s \Omega^2}{g}}$	Froude number
$Re = \frac{d_s^2 \Omega}{\nu}$	Reynolds number
$\tilde{\delta} = \frac{\delta}{D}$	Measured dimensionless liquid height at the container wall
$\tilde{\mathbf{v}} = \frac{\mathbf{v}}{d_s \Omega}$	Measured dimensionless velocity
$\tilde{\mathbf{q}} = \frac{\mathbf{q}}{d_s \Omega}$	Potentially predicted dimensionless velocity
$\tilde{\xi} = \frac{\xi}{D}$	Potentially predicted dimensionless free surface elevation

### Acronims

LDV	Laser Doppler Velocimetry, see Sec. 3.3.1
PIV	Particle Image Velocimetry, see Sec. 3.3.2
POD	Proper Orthogonal Decomposition, see Sec. 3.3.3





# 1 Introduction

## 1.1 Orbital shaking

The “orbital shaking” is the motion of a container, maintaining a fixed orientation with respect to an inertial frame of reference, on a circular trajectory at a constant angular velocity. Underneath this technical, rather cryptic definition, lies the simple and elegant gesture of “swirling” a glass of wine to release its bouquet, and other countless everyday-life applications. The same movement has been used in biological, chemical and food industries for its mixing and gas exchange characteristics, as well as for its ease and low cost of implementation. Despite this large use, the flow generated in a container subjected to orbital shaking is far from being understood, and presents a richness of patterns and behaviours which has not yet been reported.

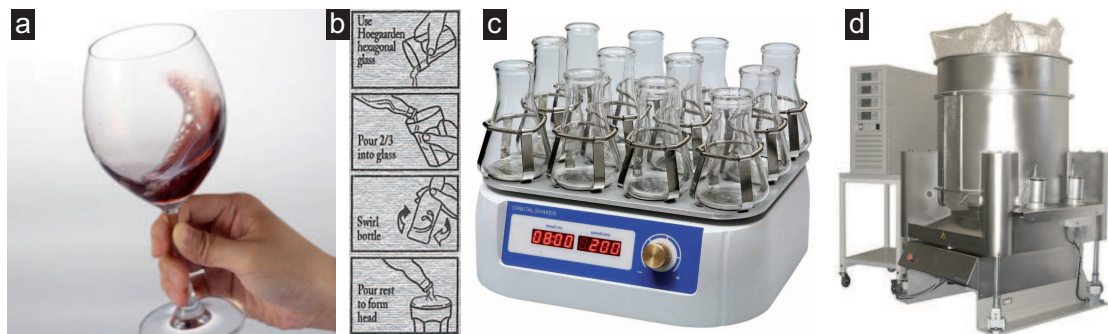


**Figure 1.1** | Example of uses of orbital shaking: **a:** wine swirling, **b:** the instructions on the label of a weizen beer suggest to swirl the bottle to mix the residuals of yeasts and to increase the foam formation, **c:** orbital shaking used for chemical reactions or analyses; **d:** large (200L) bio-reactor for cell cultures produced by Kuhner AG.

In oenology the orbital shaking is usually called “swirling” and it is employed during wine tasting, especially for visual and olfactory analyses [52]. Visually, a gentle swirling could be used to estimate the wine viscosity [96] and to create “wine tears”, which provide a visual representation of the amount of alcohol in the wine [37, 52]. More considerable is the con-

tribution of orbital shaking to olfactory assessment: it is usual to swirl the wine between a first “sniffing”, where the more volatile aromas are detected, and a second one where the wine releases more substantial aromas thanks to increased agitation and aeration. Therefore, although no scientific publication has appeared on the subject, wine experts agree that the swirling motion promotes the release of aromas of the wine [1, 96, 27]. Another beneficial effect of the swirling is the dissolution of distasteful odors (“off-odors”), e.g. sulphur dioxide in young and fresh wines [27].

The shape of the glass seems to influence the perception of wine flavours [49], both for its alleged influence on the stratification and segregation of evaporated aromas and for its effect on the motion of the swirled wine. Hence it is not surprising that a large amount of shapes aiming at increasing the volatilization of aromas has been produced. Some examples are given in Fig. 1.2. However, wine tasting is a delicate matter, where tradition mixes with marketing, and where it is often unclear if the introduction of a new glass shape is dictated by experience, researches or mere economical interest.



**Figure 1.2** | Wine glasses, some of which have been designed to increase the evaporation of aroma: **a:** INAO glass, international reference as testing glass. **b:** Peugeot “Impitoyable Le Tester” has an indent (where the thumb is inserted) which creates an obstacle to the wine travelling at the wall, supposedly breaking the molecules of wine. **c:** Peugeot “Impitoyable No1” designed for aeration and stratification of the aromas. **d:** Riedel Red Wine Swirl, supposedly increasing aeration in swirling. **e:** patent US 2006/0249518 A1 also with an indent.

Several other applications require enhancement of gas exchange between a liquid and a gaseous phase, as well as mixing. It is likely that engineers concerned with the design of early mixing devices were inspired by the motion of the glass of wine to create the first orbital shaker for chemical applications. Orbital shaking experienced anyway an incredible diffusion, and it is nowadays used in laboratories all over the world especially to mix and aerate chemical reactions, bacterial cultures [75, 38] and more recently cellular cultures [115]. The vessels typically range from small microtiter plates [32, 31] to Erlenmeyer flasks of a working volume of less than one litre, as depicted in Fig. 1.3.

Although animal cells cultivation proved to be feasible already a century ago [45], it was only

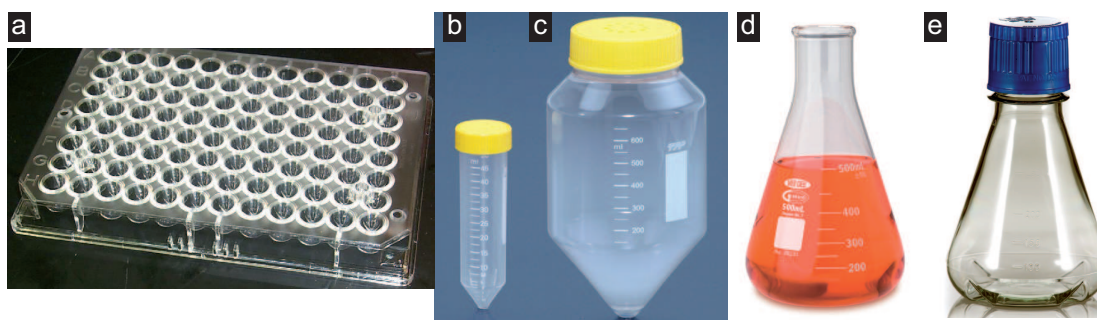


**Figure 1.3** | Examples of containers used with orbital shakers: **a:** microtiter plates used for screening. **b:** TubeSpin are small volume (35ml) cylindrical containers designed for use in centrifuges, could be fitted with vented caps as bioreactor for screening purposes, while **c:** maxi tube spin are similar but have increased capacity (600ml). **d:** Erlenmeyer flask are quite well characterized for use with orbital shaker. **e:** modifications have been tried on Erlenmeyer flasks to increase the mixing efficiency, such as the introduction of baffles.

with the introduction of molecular cloning [28] and DNA delivery [103] that its full potential in the production of proteins could be exploited [42]. Today 60 to 70 % of pharmaceutical recombinant proteins (e.g. antibodies) are produced by mammalian cells and the worldwide demand is still increasing [58]. Cells are cultivated in suspensions of liquid medium, where they multiply (increasing the size of the culture) and produce the required protein. The main issue of suspension cultures is the need to provide oxygen to the cells and evacuate the carbon dioxide without creating harming conditions.

Traditionally, orbital agitation is used for sub-litre scale cell cultures [61] and for screening of cell lines [30]. As the culture grows, it is transferred to stirred tanks, a technology adapted from bacteria cultivations [42]. Stirred tanks maintain the cells in suspension by reason of a convective flow imposed to the liquid by an impeller [81], while gas is injected from bottom-located spargers (Fig. 1.4a). In this way,  $O_2$  is exchanged at the bubbles interface, while  $CO_2$  is evacuated at the free surface. However, animal cells proved to be less resistant than bacteria: it was found that bursting of gas bubble at the free surface may damage them [44] and that strong agitation may generate excessive shear stresses, likewise harmful to the cells [59, 82]. These reasons kindled interest in the use of large scale orbital shaken devices up to several hundred litres [68, 78, 30].

In orbital shaking the suspension is maintained by the wave-like flow generated by the motion of the vessel, while the gas exchange from and to the liquid phase is ensured at the free surface (Fig. 1.4b). They present several advantages with respect to stirred tanks, namely smaller hydrodynamic stresses [22, 99], smaller mixing times [107] and require less control [21, 109]. Moreover, cultures in orbital shaken reactors are usually grown in disposable bags, reducing contamination risks and the need of components (e.g. the impeller) sterilization.

Thus, a large number of the researches that have been carried out aimed at ensuring the feasibility of this daring size increase. Studies have been performed on the gas exchange [21, 79, 74]

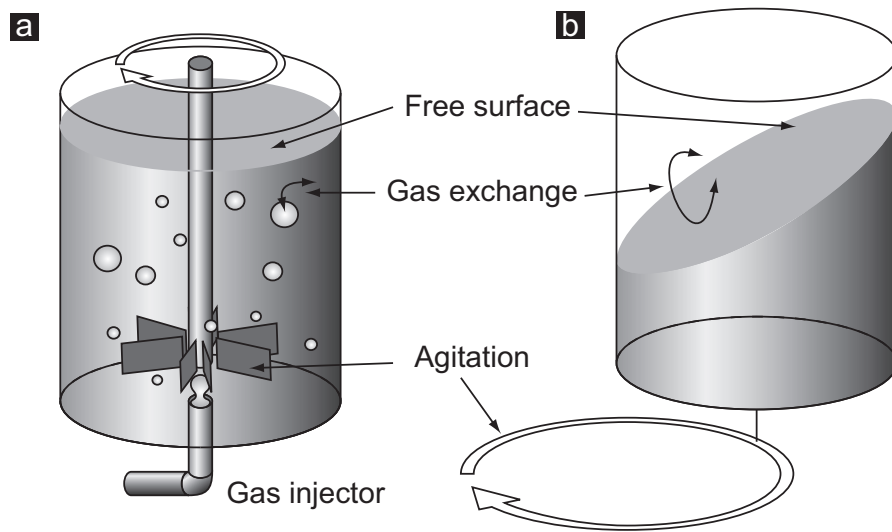


**Figure 1.4 | a:** stirred tank in operation: gas and chemicals are injected at the bottom, the agitation is ensured by the propeller, which also breaks the largest bubbles. Gas exchange occurs at the interface of the bubbles. **b:** orbitally shaken bioreactor: the motion is imposed at the whole vessel, and transmitted to the liquid by the walls, the gas exchange occurs at the free surface.

and mixing [77, 104, 108]. Global quantities such as the volumetric power consumption [22], the gas transfer capacity [119, 39] and the mixing time [77, 104, 108] have been investigated focusing on their effect on cell cultivations. In some cases, correlations have been proposed in order to quantify the variation of those quantities with the culture scale. Although measurements of the velocity fields have been performed in Erlenmeyer flasks [110] and cylindrical containers [112], no significant effort has been so far dedicated to the hydrodynamics of the liquid which carries the cells, and to its influence on the scaling of the cultures.

On the other hand, the physic of free surface liquid in shaken containers has been extensively studied, especially from the analytical point of view of potential (inviscid) flows [50]. Most of the early work, at the beginning of the space exploration age, focused on sloshing of spacecraft propellant in cylindrical or rectangular tanks [16, 70, 69, 4, 3]. More recently, the main problem investigated is the transport of liquids in naval carriers [66]. Moreover, analytical solutions have been found for several tank geometries: conical [13], rectangular [18] and, since the main aim is usually to reduce the sloshing amplitude and the forces it generates, compartmented tanks [17] or motion of liquids partially covered with elastics or rigid floating covers [14, 15] have also been investigated. Besides the analytical solutions, several numerical simulations have been also performed (e.g. [25]), to address various issues such as the collision of liquid carriers [117]. Surprisingly, researches never considered the use of sloshing for mixing purposes so far.

A lack of knowledge concerning the flow (mixing, velocity field, hydrodynamic stresses) within a container subject to orbital agitation, as well as a link between the physics of the flow and the cells cultures, is therefore flagrant, and the present thesis is intended as a remedy to it.

## 1.2 Framework of the project

The present study arises from the collaboration between three EPFL laboratories, in the frame of SNSF-Sinergia projects: the Cellular Biotechnology Laboratory (LBTC), the Chair of Modelling and Scientific Computing (CMCS) and the Laboratory for Hydraulic Machines (LMH). The LBTC provides the knowledge in cellular suspension cultures, and characterizes the key factors of the cultures, such as the mixing time, the gas transfer, the power consumption and the cells viability and productivity [107]. The main contribution of the CMCS is to produce a numerical simulation of the free surface flow, as well as a model taking into account the cell growth [89]. The LMH, and therefore the present thesis, studied the physics of the flow within an orbital shaken bioreactor through analytical and experimental investigation.

## 1.3 The case study

This work focuses on the hydrodynamics of orbitally shaken circular cylinders with upright walls. The parameters characterising each shaking configuration are the inner diameter of the container  $D$ , the diameter of the circular shaking trajectory  $d_s$ , the height of the liquid at the rest  $H_0$  and the shaking frequency  $\Omega$  (Fig. 1.5a). The angular location of the container along its trajectory is defined as  $\alpha \in [0, 2\pi[$ , thus  $\alpha = \Omega t$ . A coordinates system is associated with

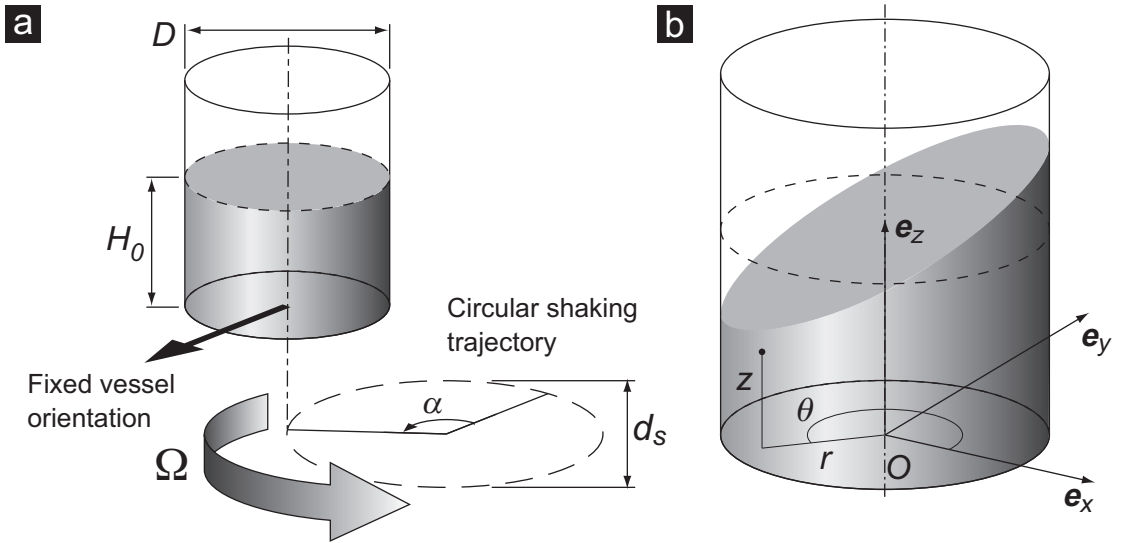


**Figure 1.5 | a:** definition of the operating parameters of the shaking. **b:** coordinates system associated with the vessel.

the container, with its origin  $O$  at the vessel bottom, and the direction  $\mathbf{e}_z$  collinear with the revolution axis of the container. Any position within the container is identified as  $\mathbf{x} = (x, y, z)$  in Cartesian coordinates or as  $\mathbf{x} = (r, \theta, z)$  in cylindrical coordinates (Fig. 1.5b).

In the following, we will first describe the historical development leading to an analytical solution for surface waves, and present the use and adaptation of existing models to the

## **Chapter 1. Introduction**

---

problem of orbital shaking (Chap. 2). Then, in Chap. 3 the experimental methods used throughout this work are detailed. Chapter 4 presents the dynamics of the wave, comparing the experimental results to the analytical model. Finally, in Chap. 5 the application to the specific field of cell cultures is highlighted.

## 2 Analytical approach

The motion of free surface flows within shaken containers may be described analytically when a series of hypothesis are made: namely that the liquid is inviscid and incompressible and the flow is irrotational. Flows respecting those conditions are usually known as potential flows [93], and their governing equations are presented in Sec. 2.1. For the benefit of readers unfamiliar with wave motion, we present first the traditional solutions for gravity waves (Sec. 2.2). Their dynamics has been studied by Laplace, Newton and Lagrange among others, and was formally published for linear waves by Airy [29]. Important advances, especially the extension of the theory to non-linear waves, was proposed shortly after by Stokes [100]. The method was further extended with the introduction of moving container at the beginning of space travel age [50]. Using those techniques, in the third section of this chapter we present the equations of motion of liquid within orbital shaken containers.

### 2.1 General governing equations

The motion of fluids in a Cartesian frame of reference is appropriately described by the equations of conservation of mass:

$$\frac{\partial \rho}{\partial t} + \nabla \cdot (\rho \mathbf{q}) = 0 \quad (2.1)$$

and the conservation of momentum [64]:

$$\rho \left( \frac{\partial \mathbf{q}}{\partial t} + (\mathbf{q} \cdot \nabla) \mathbf{q} \right) = -\nabla p - \nabla \mathbb{T} - \mathbf{f}. \quad (2.2)$$

where  $\mathbf{q}$  is the velocity vector,  $\rho$  is the density of the fluid,  $p$  is the pressure,  $\mathbb{T}$  is the deviatoric stress tensor [93], and  $\mathbf{f}$  is the resultant of volume forces on the liquid. In a Cartesian coordinates system, defined by a reference frame  $O(\mathbf{e}_x, \mathbf{e}_y, \mathbf{e}_z)$ , the velocity is  $\mathbf{q}(x, y, z, t)$  with components  $\mathbf{q} = q_i = (q_x, q_y, q_z)$  in the directions  $\mathbf{e}_x$ ,  $\mathbf{e}_y$  and  $\mathbf{e}_z$ , and the operator

$\nabla = (\partial/\partial x, \partial/\partial y, \partial/\partial z)$ . Equation 2.2 could be rewritten as:

$$\rho \left( \frac{\partial \mathbf{q}}{\partial t} - \mathbf{q} \times (\nabla \times \mathbf{q}) + \frac{1}{2} \nabla (q_i^2) \right) = -\frac{1}{\rho} \nabla p - \nabla \mathbb{T} - \mathbf{f}. \quad (2.3)$$

The only body force considered here is the one induced by the gravitational apparent acceleration: we have therefore  $\mathbf{f} = \nabla(gz)$ , where  $g$  is the apparent gravitational acceleration.

In case of potential flow, various hypotheses are then introduced: the flow is incompressible ( $\rho$  is constant in space and time, but may have different values for different fluids, e.g. water and air), irrotational ( $\nabla \times \mathbf{q} = 0$ ) and inviscid, the last hypothesis leading to  $\nabla \mathbb{T} = 0$ . Moreover, if the motion is irrotational, a velocity potential  $\Phi$  exists whose gradient defines the velocity field:  $\mathbf{q} = \nabla \Phi$ . Under these conditions Eq. 2.1 and 2.3 could be rewritten respectively as:

$$\nabla^2 \Phi = 0 \quad (2.4)$$

$$\nabla \frac{\partial \Phi}{\partial t} + \frac{1}{2} \nabla (q_i^2) = -\frac{\nabla p}{\rho} - \nabla (gz) \quad (2.5)$$

Equation 2.4 is the Laplace's equation, while integration of Eq. 2.5 lead to the unstationary Bernoulli equation:

$$\frac{\partial \Phi}{\partial t} + \frac{1}{2} (q_i^2) + \frac{p}{\rho} + (gz) = C(t) \quad (2.6)$$

where  $C(t)$  is any arbitrary function of time. Boundary conditions are introduced to solve Eqs. 2.4 and 2.6. A typical condition is the non penetration of liquid at solid walls: the liquid velocity at the wall in the direction  $\mathbf{n}$  normal to the wall must be equal to the velocity of the wall  $\dot{\mathbf{X}}$  in the same direction:

$$\mathbf{q} \cdot \mathbf{n} = \dot{\mathbf{X}} \cdot \mathbf{n}. \quad (2.7)$$

In the usual case where the wall is stationary and its normal vector is collinear to one of the direction of the frame of reference Eq. 2.7 becomes:

$$q_n = \frac{\partial \Phi}{\partial n} = 0 \quad (2.8)$$

where  $n$  is  $x$ ,  $y$  or  $z$  in case  $\mathbf{n}=(1,0,0)$ ,  $(0,1,0)$  or  $(0,0,1)$  respectively.

## 2.2 Gravity waves dynamics

A solution is searched for Eq. 2.4, for a flow having a solid wall as lower boundary and a free surface as upper boundary. The elevation of the free surface is defined as  $z = \xi(x, y, t)$  while the solid wall is located at  $z = -H_0$ . More details about the following developments are found in the books of Lamb [64] and of Phillips [86].



The velocity of the particles at the free surface is the velocity of the free surface itself. This condition is called the kinematic condition of the free surface and reads:

$$w_\xi = \frac{D\xi}{Dt} = \frac{\partial \xi}{\partial t} + \mathbf{q} \cdot \nabla \xi \quad \text{or} \quad \left( \frac{\partial \Phi}{\partial z} \right)_\xi = \frac{\partial \xi}{\partial t} + \frac{\partial \Phi}{\partial x} \frac{\partial \xi}{\partial x} + \frac{\partial \Phi}{\partial y} \frac{\partial \xi}{\partial y} \quad (2.9)$$

where the suffice  $\xi$  refers to quantities at the free surface. Another condition is that the pressure at both sides of the free surface could differ only as a results of surface tension. This condition is called the dynamic condition and it is found by applying Bernoulli's equation (Eq. 2.6) to both sides of the free surface:

$$\left( \frac{\partial \Phi}{\partial t} \right)_\xi + \frac{1}{2} (\nabla \Phi)_\xi^2 + \frac{p}{\rho} + g\xi = 0 \quad (2.10)$$

where the arbitrary function  $C(t)$  is incorporated into  $\Phi$ . Since

$$p = p_a + \gamma (R_1^{-1} + R_2^{-1}) \quad (2.11)$$

where  $p_a$  is the atmospheric pressure,  $\gamma$  is the surface tension to density ratio of the liquid and  $R_1$  and  $R_2$  are the radii of curvature of the free surface in the  $\mathbf{e}_x$  and  $\mathbf{e}_y$  directions. Together, Eq. 2.10 and Eq. 2.11 constitute the dynamic condition at the free surface, as far as  $p_a$  is defined.

The free surface dynamic and kinematic boundary conditions could be combined by computing the material derivative of Eq. 2.10, in order to obtain a non-linear free surface boundary condition:

$$\left( \frac{\partial}{\partial t} + \mathbf{q} \cdot \nabla \right) \cdot \left( \frac{\partial \Phi}{\partial t} + \frac{1}{2} |\mathbf{q}|^2 + \frac{p}{\rho} + g\xi \right) = 0$$

$$\frac{\partial^2 \Phi}{\partial t^2} + \mathbf{q} \cdot \nabla \frac{\partial \Phi}{\partial t} + \frac{1}{2} \frac{\partial |\mathbf{q}|^2}{\partial t} + \frac{1}{2} \mathbf{q} \cdot \nabla |\mathbf{q}|^2 + \frac{\partial}{\partial t} \frac{p}{\rho} + \mathbf{q} \cdot \nabla \frac{p}{\rho} + g \frac{\partial \xi}{\partial t} + g \mathbf{q} \cdot \nabla \xi = 0, \quad (2.12)$$

which is valid at the free surface  $z = \xi(x, y, t)$ . Thus, neglecting the influence of the surface tension, for constant atmospheric pressure  $p_a$  ( $\nabla p_a = 0$  and  $\partial p_a / \partial t = 0$ ) and using Eq. 2.9 we obtain:

$$\frac{\partial^2 \Phi}{\partial t^2} + \frac{\partial |\mathbf{q}|^2}{\partial t} + \frac{1}{2} \mathbf{q} \cdot \nabla |\mathbf{q}|^2 + g \frac{\partial \Phi}{\partial z} = 0 \quad \text{at } z = \xi(x, y, t). \quad (2.13)$$

The Stokes' approach consists in expanding the free surface condition in a Taylor series around

## Chapter 2. Analytical approach

---

$z = 0$ :

$$\begin{aligned} & \left[ \frac{\partial^2 \Phi}{\partial t^2} \right]_{z=0} + \xi \left[ \frac{\partial}{\partial z} \frac{\partial^2 \Phi}{\partial t^2} \right]_{z=0} + \left[ \frac{\partial |\mathbf{q}|^2}{\partial t} \right]_{z=0} + \xi \left[ \frac{\partial}{\partial z} \frac{\partial |\mathbf{q}|^2}{\partial t} \right]_{z=0} + \frac{1}{2} [\mathbf{q} \cdot \nabla |\mathbf{q}|^2]_{z=0} \\ & + \frac{1}{2} \xi \left[ \frac{\partial}{\partial z} \mathbf{q} \cdot \nabla |\mathbf{q}|^2 \right]_{z=0} + g \left[ \frac{\partial \Phi}{\partial z} \right]_{z=0} + g \xi \left[ \frac{\partial^2 \Phi}{\partial z^2} \right]_{z=0} + \dots = 0. \end{aligned} \quad (2.14)$$

The expansion parameter is the wave slope  $ak$  where  $a$  is the wave amplitude and  $k$  the wave number. The expansion parameter will become evident as the solutions of the potential and free surface elevation will be given. The convergence of the expansion series has been demonstrated for small steepness (low values of  $ak$ ) in infinite [67] and finite depth [102] waves [86].

The velocity potential  $\Phi$ , as well as the velocity  $\mathbf{q}$  and the free surface position  $\xi$  are expanded in a perturbation series of the form  $\Phi = \epsilon \Phi_1 + \epsilon^2 \Phi_2 + \epsilon^3 \Phi_3 + \dots$ . The free surface kinematic boundary condition (Eq. 2.9) is thus expressed as:

$$\epsilon \left( \frac{\partial \Phi_1}{\partial z} \right)_\xi + \epsilon^2 \left( \frac{\partial \Phi_2}{\partial z} \right)_\xi + O(\epsilon^3) = \epsilon \frac{\partial \xi_1}{\partial t} + \epsilon^2 \left( \frac{\partial \xi_2}{\partial t} + \frac{\partial \Phi_1}{\partial x} \frac{\partial \xi_1}{\partial x} + \frac{\partial \Phi_1}{\partial y} \frac{\partial \xi_1}{\partial y} \right) + O(\epsilon^3) \quad (2.15)$$

while the combined free surface boundary condition (Eq. 2.14) becomes:

$$\begin{aligned} & \epsilon \left[ \frac{\partial^2 \Phi_1}{\partial t^2} + g \frac{\partial \Phi_1}{\partial z} \right] \\ & + \epsilon^2 \left[ \frac{\partial^2 \Phi_2}{\partial t^2} + g \frac{\partial \Phi_2}{\partial z} + \xi_1 \frac{\partial}{\partial z} \frac{\partial^2 \Phi_1}{\partial t^2} + g \xi_1 \frac{\partial^2 \Phi_1}{\partial z^2} + \frac{\partial |\mathbf{q}_1|^2}{\partial t} \right] \\ & + O(\epsilon^3) = 0 \quad \text{at } z = 0. \end{aligned} \quad (2.16)$$

According to perturbation techniques, solutions are found for each order of  $\epsilon$ , starting from the lower one, and each solution is used in the following order.

For the first order, the set of equations that has to be solved is:

$$\nabla^2 \Phi_1 = 0, \quad \text{and} \quad \mathbf{q}_1 = \nabla \Phi_1 \quad (2.17a)$$

$$\frac{\partial \Phi_1}{\partial n} = 0 \quad \text{at the solid surfaces} \quad (2.17b)$$

$$\frac{\partial^2 \Phi_1}{\partial t^2} + g \frac{\partial \Phi_1}{\partial z} = 0 \quad \text{at } z = 0 \quad (2.17c)$$

$$\frac{\partial \xi_1}{\partial t} = \frac{\partial \Phi_1}{\partial z} \quad \text{at } z = 0 \quad (2.17d)$$

where we look for a solution of Laplace equation (Eq. 2.17a) respecting the boundary conditions (Eqs. 2.17b-d). Instead of the kinematic boundary condition, it is possible to use the

dynamic boundary condition, thus substituting Eq. 2.17d with the first term of the perturbation expansion of Eq. 2.10.

Without loss of generality, the solution for the free surface is expressed in the form of a Fourier series:

$$\xi = \sum_{n=1}^{\infty} a_n \cos(n(\mathbf{k} \cdot \mathbf{x} - \omega \cdot t)) \quad (2.18)$$

where  $a_n$  is the wave amplitude,  $\omega$  is the wave frequency and  $\mathbf{k}$  is the wave numbers vector. If we limit the resolution to the first order, we obtain the solutions for linear waves, or Airy's waves.\* Solutions for the free surface and the potential, respecting Eqs. 2.17b and 2.17c are (dropping the suffice <sub>1</sub>):

$$\xi = a \cos(\mathbf{k} \cdot \mathbf{x} - \omega \cdot t). \quad (2.19)$$

$$\Phi = \frac{\omega a \cosh(k(z + H_0))}{k \sinh(kH_0)} \sin(\mathbf{k} \cdot \mathbf{x} - \omega t). \quad (2.20)$$

Those results are injected into Eq. 2.17d to satisfy the kinematic boundary condition, thus obtaining the relation of dispersion between the wave number and the frequency:

$$\omega^2 = gk \tanh kH_0, \quad (2.21)$$

where  $k = \|\mathbf{k}\|$ . The wave period is  $T = 2\pi/\omega$ . The speed at which any phase (e.g. the crest) of the wave travels is called phase velocity and is given by  $c_p = \omega/k$  or, according to Eq. 2.21:

$$c_p = \sqrt{\frac{g}{k} \tanh kH_0}, \quad (2.22)$$

while the wavelength (the distance between two equivalent phases, say the crests) is given by

$$\lambda = \frac{2\pi}{k} = \frac{2\pi c_p}{\omega}. \quad (2.23)$$

In the case of a bi-dimensional flow propagating along the  $\mathbf{e}_x$  direction, the wave number becomes  $\mathbf{k} = (k, 0, 0)$  and the velocity fields are found integrating the potential  $\Phi_1$  (Eq. 2.20):

$$q_x = \frac{dx}{dt} = \frac{\omega a \cosh(z_0 + H_0)}{\sinh(kH_0)} \cos(kx - \omega t) \quad (2.24a)$$

$$q_z = \frac{dz}{dt} = \frac{\omega a \sinh(z_0 + H_0)}{\sinh(kH_0)} \sin(kx - \omega t). \quad (2.24b)$$

---

\*The first order is usually obtained from perturbation expansion of the kinematic and dynamic boundary condition without need of introducing the combined boundary condition and its expression as a Taylor series.

It is possible to compute the trajectories followed by hypothetical liquid particles released into the liquid from an initial location  $\mathbf{x}_0 = (x_0, y_0, z_0)$  calculating iteratively their position after each increment of time  $dt$  as:

$$\begin{aligned} x(t + dt) &= x(t) + q_x(x(t), y(t), z(t), t) \cdot dt \\ y(t + dt) &= y(t) + q_y(x(t), y(t), z(t), t) \cdot dt \\ z(t + dt) &= z(t) + q_z(x(t), y(t), z(t), t) \cdot dt, \end{aligned} \quad (2.25)$$

where  $dt$  is small enough not to influence the result of the trajectory computations. Three examples of trajectories followed in different wave conditions are depicted in Fig. 2.1. We observe that the magnitude of the velocity field as well as the amplitude of the trajectories rapidly decrease with the depth, while the rate of this reduction depends on the wave characteristics  $H_0$  and  $k$ . Although the velocity fields have a mean value along  $\mathbf{e}_x$  equivalent to zero,

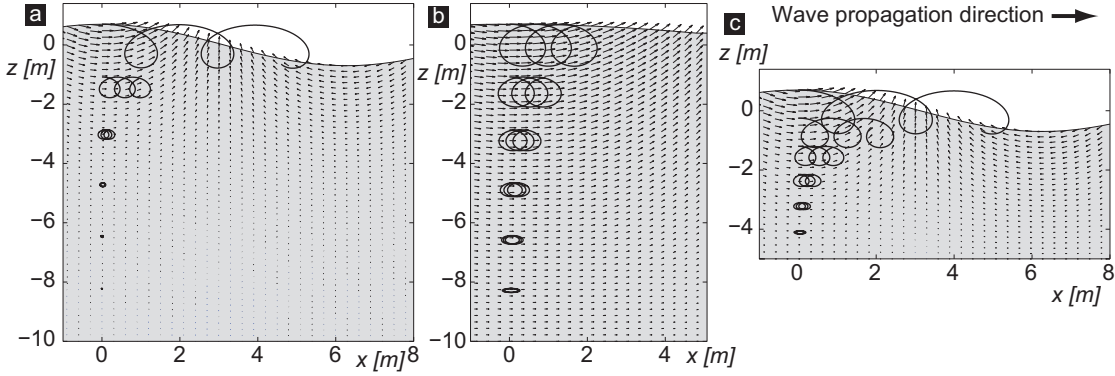


**Figure 2.1** | Linear wave velocity fields and trajectories followed by groups of particles released at  $x_0 = 0$  and various  $z_0$  during three periods of the waves, for waves with different characteristics. The free surface height and the velocity fields are depicted at  $t = 3T$ . **a:** the wave has the following characteristics:  $H_0 = 10\text{m}$ ,  $k = 0.5$ ,  $a = 0.7\text{m}$ . **b:**  $H_0 = 10\text{m}$ ,  $k = 0.2$ ,  $a = 0.7\text{m}$ . **c:**  $H_0 = 2\text{m}$ ,  $k = 0.5$ ,  $a = 0.7\text{m}$ .

the particles experience a motion in the direction of propagation of the wave, hence displaying the trochoidal trajectories typical of the wave motion. This displacement in the direction of the wave propagation is commonly known as the Stokes drift [100]: while the velocity fields average on a horizontal line is zero, the particles are not moving along horizontal lines. Because of the definition of the velocity fields, the positive horizontal velocity they experience in the upper part of the trajectory is greater (in magnitude) than the negative velocity in the lower part, thus they move in the positive  $\mathbf{e}_x$  direction.

Hence, in order to estimate the value of the Stokes drift, is necessary to estimate the Lagrangian velocity, which is the velocity experienced by an liquid particle moving with the flow. By contrast, the velocity of the flow at a fixed location is known as Eulerian velocity of the flow. The latter description was used throughout the preceding developments.

If at  $t = 0$  a particle is at the initial position  $\mathbf{x}_0 = (x_0, y_0, z_0)$ , its position at a time  $t > 0$  is calculated as:

$$\mathbf{x} = \mathbf{x}_0 + \int_0^t \mathbf{q}_L(\mathbf{x}_0, t') dt'. \quad (2.26)$$

where the suffice  $_L$  indicates the Lagrangian velocity. At any given location and at the same moment, the Lagrangian  $\mathbf{q}_L(\mathbf{x}_0, t)$  and Eulerian  $\mathbf{q}(\mathbf{x}, t)$  velocities must be equivalent. Using Eq. 2.26 we have then:

$$\mathbf{q}_L(\mathbf{x}_0, t) = \mathbf{q}\left(\mathbf{x}_0 + \int_0^t \mathbf{q}_L(\mathbf{x}_0, t') dt', t\right). \quad (2.27)$$

Equation 2.27 could be expressed as a Taylor series expansion around  $\mathbf{x}_0$ , and using Eq. 2.26 for  $\mathbf{x} - \mathbf{x}_0$  we obtain:

$$\mathbf{q}_L(\mathbf{x}_0, t) = \mathbf{q}(\mathbf{x}_0, t) + (\mathbf{x} - \mathbf{x}_0) \cdot \nabla \mathbf{q}(\mathbf{x}_0, t) + \dots \quad (2.28)$$

$$\mathbf{q}_L(\mathbf{x}_0, t) = \mathbf{q}(\mathbf{x}_0, t) + \int_0^t \mathbf{q}_L(\mathbf{x}_0, t') dt' \cdot \nabla \mathbf{q}(\mathbf{x}_0, t) + \dots \quad (2.29)$$

We notice that at the first order the two velocities are equivalent, thus the Lagrangian velocity in the second term in the right hand side of Eq. 2.29 is approximated at the first order [86], leading to:

$$\mathbf{q}_L(\mathbf{x}_0, t) = \mathbf{q}(\mathbf{x}_0, t) + \int_0^t \mathbf{q}(\mathbf{x}_0, t') dt' \cdot \nabla \mathbf{q}(\mathbf{x}_0, t). \quad (2.30)$$

The average of the Lagrangian velocity, calculated by using Eq. 2.30 with the Eulerian velocity fields given by Eq. 2.24, is:

$$\bar{q}_{L,x} = \frac{\omega k a^2 \cosh(2k(z_0 + H_0))}{2 \sinh^2(kH_0)} \quad \text{and} \quad (2.31a)$$

$$\bar{q}_{L,z} = 0, \quad (2.31b)$$

explaining the drift of the particles. The distribution of the drift velocity as a function of the depth is shown in Fig. 2.2b, along with the evolution of the Eulerian average.

First order solutions provide an accurate estimation of the wave shape and velocity fields, also extending to cases of varying liquid depth and wave interaction, as long as the amplitude of the wave remains small compared to the wavelength [86]. However, as the wave increases in steepness and approaches the breaking, higher orders are required. The solutions have been obtained by Stokes [101] up to the fifth order  $O((ak)^5)$  for deep water waves and up to the third order for finite depth, when the expansion parameter  $ak$  remains small. Solutions have been obtained also for waves where the wavelength is large compared to the amplitude (known as cnoidal waves) and waves of infinite wavelength (solitary waves) [94]. As the order of resolution

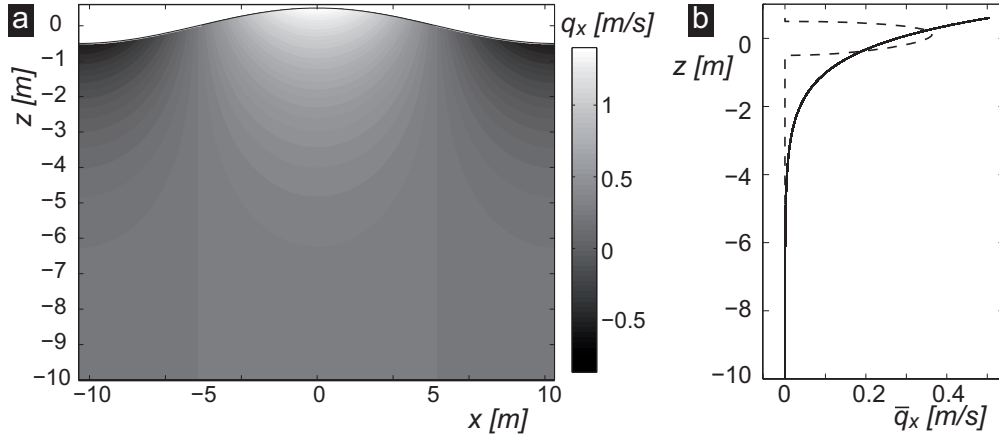


**Figure 2.2** | **a:** field of the horizontal velocity  $u$  in a wave with  $H_0 = 10$ ,  $k = 0.5$ . **b:** the solid line represents the evolution of the mean Lagrangian velocity  $\bar{q}_{L,z}$  calculated according to Eqs. 2.31a, the dashed line is the mean velocity  $\bar{q}_z$  computed only for the liquid phase. We considered that in the gas phase (above the surface)  $u=0\text{m/s}$ .

increases, several (and sometimes discording) solutions have been proposed, using different approaches [91, 35], while numerical solutions have also been suggested [26, 36]. Besides the increased precision of the estimations, higher order solutions provide estimation of the limiting steepness of the wave, usually defined as  $H/\lambda \approx 0.1412$ , where  $H$  is the crest-to-trough amplitude [95, 41]. Overviews of the issues mentioned above are found in [94, 113].

## 2.3 Sloshing dynamics

In case of free surface motion in a confined vessel, the development is somehow similar to the one followed for gravity waves, but with additional boundary conditions taking into account the moving walls. A large number of publications present the wave motion of an inviscid incompressible fluid in a rigid circular tank, e.g. a comprehensive review is found in [50].

The equations of motion derived in the previous section are given for an inertial frame of reference, e.g.  $O'\mathbf{e}'_x\mathbf{e}'_y\mathbf{e}'_z$  in Fig. 2.3a. In case of a moving container, we define a reference frame  $O\mathbf{e}_x\mathbf{e}_y\mathbf{e}_z$  moving with the container. Any time-change in the inertial reference frame has to be expressed in terms of total derivatives in the moving one:

$$\left. \frac{\partial \Phi}{\partial t} \right|_O = \left( \frac{\partial}{\partial t} - \dot{\mathbf{X}}_0 \cdot \nabla \right) \Phi \Big|_{O'} \quad (2.32)$$

where  $\dot{\mathbf{X}}_0$  is the velocity of  $O$  in the  $O'$  frame of reference. The velocity fields in the moving reference frame are expressed in  $O\mathbf{e}_x\mathbf{e}_y\mathbf{e}_z$  as

$$\mathbf{q}|_O = \mathbf{q}|_{O'} - \dot{\mathbf{X}}_0 = \nabla \Phi - \dot{\mathbf{X}}_0 \quad (2.33)$$

The orbital shaking motion may be described as a combination of two sinusoidal translations with a  $\pi/2$  phase shift (Fig.2.3a), which leads to the following equations for the motion of the wall:

$$\mathbf{X}_0(t) = \begin{cases} \frac{d_s}{2} \cdot \cos(\Omega t) \cdot \mathbf{e}_x \\ \frac{d_s}{2} \cdot \sin(\Omega t) \cdot \mathbf{e}_y \end{cases} \quad (2.34a)$$

$$\mathbf{X}_0(t) = \begin{cases} \frac{d_s}{2} [\cos(\Omega t) \cos(\theta) + \sin(\Omega t) \sin(\theta)] \mathbf{e}_r = \frac{d_s}{2} \cos(\Omega t - \theta) \mathbf{e}_r \\ \frac{d_s}{2} [-\cos(\Omega t) \sin(\theta) + \sin(\Omega t) \cos(\theta)] \mathbf{e}_\theta = \frac{d_s}{2} \sin(\Omega t - \theta) \mathbf{e}_\theta. \end{cases} \quad (2.34b)$$

where the displacements are expressed in Cartesian ( $\mathbf{x} = (x, y, z)$ ) and cylindrical ( $\mathbf{x} = (r, \theta, z)$ ) coordinates system, as depicted in Fig. 2.3b. The forcing expressed in term of velocity is:

$$\dot{\mathbf{X}}_0(t) = \begin{cases} -\frac{d_s \Omega}{2} \cdot \sin(\Omega t) \cdot \mathbf{e}_x \\ \frac{d_s \Omega}{2} \cdot \cos(\Omega t) \cdot \mathbf{e}_y \end{cases} \quad (2.35a)$$

$$\dot{\mathbf{X}}_0(t) = \begin{cases} -\frac{d_s \Omega}{2} \sin(\Omega t - \theta) \mathbf{e}_r \\ \frac{d_s \Omega}{2} \cos(\Omega t - \theta) \mathbf{e}_\theta. \end{cases} \quad (2.35b)$$

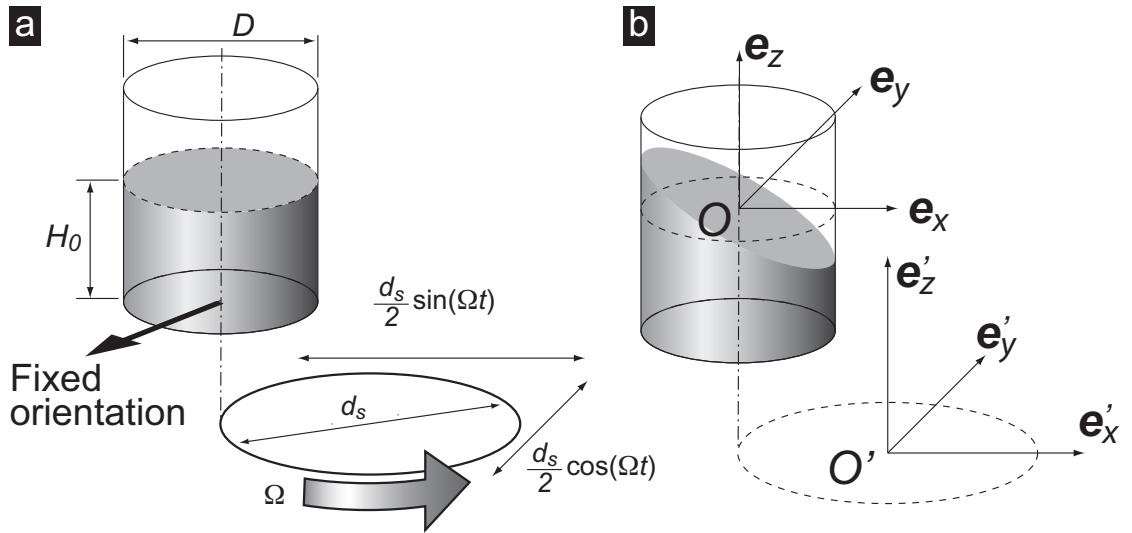


**Figure 2.3 | a:** decomposition of the orbital shaking into two sinusoidal translations, with reminder of the definition of the shaking parameters  $D$ ,  $H_0$ ,  $d_s$  and  $\Omega$ . **b:** position of the two frame of references,  $O$  fixed to an inertial frame of reference,  $O'$  fixed to the moving container.

## Chapter 2. Analytical approach

---

In the moving reference frame the kinematic (Eq. 2.9) and dynamic (Eq. 2.10) boundary conditions become respectively:

$$\frac{\partial \Phi}{\partial z} = \frac{\partial \xi}{\partial t} + (\nabla \Phi - \dot{\mathbf{X}}_0) \cdot \nabla \xi \quad \text{at } z = \xi(r, \theta, t) \quad (2.36)$$

$$\frac{\partial \Phi}{\partial t} + \frac{1}{2} (\nabla \Phi)^2 + \frac{p}{\rho} + g\xi - \dot{\mathbf{X}}_0 \cdot \nabla \Phi = 0 \quad \text{at } z = \xi(r, \theta, t) \quad (2.37)$$

while the conditions at the container walls are, according to Eqs. 2.7 and 2.35b:

$$\frac{\partial \Phi}{\partial r} = -\frac{d_s \Omega}{2} \sin(\Omega t - \theta) \quad \text{at } r = D/2 \quad (2.38)$$

$$\frac{\partial \Phi}{\partial z} = 0 \quad \text{at } z = -H_0. \quad (2.39)$$

It is usual to separate the potential function  $\Phi$  into a liquid motion component  $\tilde{\Phi}$  and a container motion component  $\Phi_0$ :

$$\Phi = \tilde{\Phi} + \Phi_0. \quad (2.40)$$

The container displacement potential  $\Phi_0$  is determined integrating Eq. 2.38 in cylindrical coordinates:

$$\nabla \Phi_0 = \dot{\mathbf{X}}_0 \quad (2.41)$$

$$\Phi_0 = -\frac{d_s \Omega r}{2} \sin(\Omega t - \theta) - \frac{1}{2} \int (\dot{\mathbf{X}})^2 dt. \quad (2.42)$$

We observe that  $\partial \Phi_0 / \partial z = 0$ . The free surface boundary conditions (expressed in Eq. 2.37 and 2.36) are modified according to Eq. 2.40, 2.41 and 2.42, and become:

$$\frac{\partial \tilde{\Phi}}{\partial t} - \frac{d_s \Omega^2 r}{2} \cos(\Omega t - \theta) + \frac{1}{2} \nabla \tilde{\Phi}^2 + \frac{p}{\rho} + g\xi = 0 \quad (2.43)$$

$$\frac{\partial \tilde{\Phi}}{\partial z} = \frac{\partial \xi}{\partial t} - \frac{\partial \xi}{\partial r} \frac{\partial \tilde{\Phi}}{\partial r} - \frac{1}{r^2} \frac{\partial \xi}{\partial \theta} \frac{\partial \tilde{\Phi}}{\partial \theta}. \quad (2.44)$$

To obtain solutions at the first order the boundary conditions are linearized, typically by perturbation expansion of the quantities  $\tilde{\Phi}$ ,  $\mathbf{q}$  and  $\xi$ , as described for gravity waves, or according



to the expressions detailed in the next section. The linearized set of equations is:

$$\nabla^2 \tilde{\Phi} = 0 \quad (2.45a)$$

$$\frac{\partial \tilde{\Phi}}{\partial r} = 0 \quad \text{at } r = D/2 \quad (2.45b)$$

$$\frac{\partial \tilde{\Phi}}{\partial z} = 0 \quad \text{at } z = -H_0 \quad (2.45c)$$

$$\frac{\partial \tilde{\Phi}}{\partial t} - \frac{d_s \Omega^2 r}{2} \cos(\Omega t - \theta) + g \xi = 0 \quad \text{at } z = \xi(r, \theta, t) \quad (2.45d)$$

$$\frac{\partial \tilde{\Phi}}{\partial z} = \frac{\partial \xi}{\partial t} \quad \text{at } z = \xi(r, \theta, t) \quad (2.45e)$$

A general solution for Laplace's equation in cylindrical coordinates is usually obtained by combination of separate solutions for each variable, which are composed of exponential functions in the axial solution, of harmonics functions in the tangential solution and of Bessel's functions of the first and second kind in the radial one [51]. Characteristics and proprieties of the Bessel's functions are given in Annexe B. In order to obtain finite values of the potential within the limits of the container, the Bessel's function of the second kind are dropped. Moreover, to respect boundary conditions 2.45b and 2.45c the solution takes the following form:

$$\tilde{\Phi}(r, \theta, z, t) = \sum_{m=0}^{\infty} \sum_{n=1}^{\infty} [\alpha_{mn}(t) \cos m\theta + \beta_{mn}(t) \sin m\theta] J_m(\lambda_{mn} r) \frac{\cosh[\lambda_{mn}(z + H_0)]}{\cosh \lambda_{mn} H_0} \quad (2.46)$$

where  $\alpha_{mn}$  and  $\beta_{mn}$  are time dependent functions to be determined,  $J_m$  is the Bessel's function of the first kind,  $\lambda_{mn} = \varepsilon_{mn}/(D/2)$  are the roots of  $\partial J_m(\lambda_{mn} r)/\partial r = 0$  at  $r = D/2$ , needed to satisfy the boundary condition of the velocity at the vertical wall (Eq. 2.45b). Those roots are reported in Annexe B. The free surface conditions Eq. 2.45d and Eq. 2.45e could be combined in one equation by time differentiating once the dynamic boundary condition and by using the kinematic boundary condition to obtain:

$$\frac{\partial^2 \tilde{\Phi}}{\partial t^2} + g \frac{\partial \tilde{\Phi}}{\partial z} = -\frac{d_s \Omega^3 r}{2} \sin(\Omega t - \theta). \quad (2.47)$$

The natural frequencies of the flow are found supposing  $\alpha_{mn} = a_{mn} \cos \omega_{mn} t$  and  $\beta_{mn} = b_{mn} \sin \omega_{mn} t$  and are obtained injecting Eq. 2.46 into Eq. 2.47 in the case of non forced motion ( $\Omega = 0$ ):

$$\omega_{mn}^2 = g \lambda_{mn} \tanh(\lambda_{mn} H_0) = \frac{2g\varepsilon_{mn}}{D} \tanh\left(\frac{2\varepsilon_{mn} H_0}{D}\right). \quad (2.48)$$

The natural modes of the free surface  $\xi$  are represented in Fig. 2.4, as seen from the top of the container: black and white regions pulsate in the vertical direction ( $\mathbf{e}_z$  direction), while the grey regions remains at  $z = 0$  - they are the nodal lines or circles. Depending on the forcing,

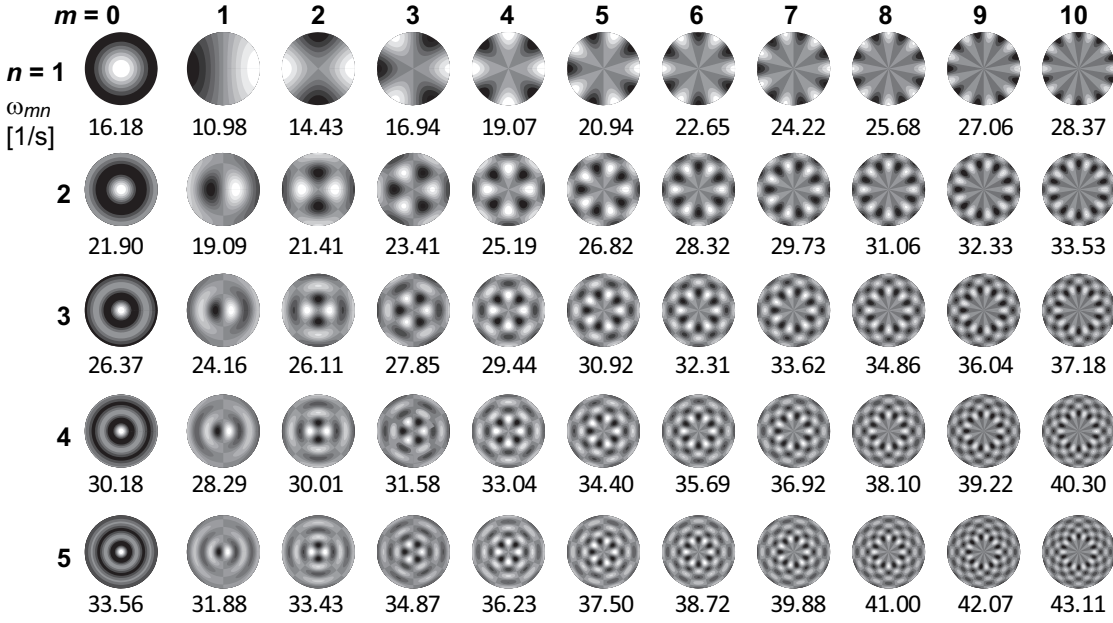


**Figure 2.4** | Visualization of the natural modes of the free surface  $\xi$ . The natural frequencies  $\omega_{mn}$  are also given as a way of example, for a container of a diameter  $D$  of 0.287m, and a liquid filling  $H_0$  of 0.15m.

different modes are excited, e.g. vertical pulsation is likely to generate  $m=0$  modes, while lateral acceleration is expected to excite the  $m=1$ . In an iconic scene of the film Jurassic Park, the appearance of concentric wavelets in a glass of water (mode  $m=0$  or 1,  $n=6-7$ ) is the first sign of the approaching T-Rex.<sup>†</sup> An usual way to define a mode, employed throughout the current work, is to identify it as  $(m, n)$ .

The orbital shaking generates a displacement of the liquid toward the external wall of the container, thus exciting the first non-axisymmetric mode,  $m=1$ . These modes, with  $n=1, 2, \dots$ , have also the lowest natural frequencies. Moreover,  $r \in [0; D/2]$  has to be expressed in terms of Fourier-Bessel series (see Annexe B.1) as:

$$r = \sum_{n=1}^{\infty} c_n J_1(\lambda_{1n} r) \quad (2.49)$$

$$\text{where } c_n = \frac{D}{(\varepsilon_{1n}^2 - 1) J_1(\varepsilon_{1n})}$$

<sup>†</sup>According to the interview to the film's special effects supervisor, appearing in the extras of the DVD trilogy (2011), the effect was achieved playing a guitar string to excite the wanted natural frequency of the glass.

When introducing Eq. 2.46 and Eq. 2.49 into Eq. 2.47 we obtain:

$$\begin{aligned} \sum_{n=1}^{\infty} \left[ \ddot{\alpha}_{1n}(t) + \omega_{1n}^2 \alpha_{1n}(t) + \frac{d_s \Omega^3 c_n \sin \Omega t}{2} \right] J_1(\lambda_{1n} r) \cos \theta \\ + \left[ \ddot{\beta}_{1n}(t) + \omega_{1n}^2 \beta_{1n}(t) - \frac{d_s \Omega^3 c_n \cos \Omega t}{2} \right] J_1(\lambda_{1n} r) \sin \theta = 0 \end{aligned} \quad (2.50)$$

where  $\omega_{1n}$  is defined according to Eq. 2.48. Each function  $\alpha_{1n}(t)$  and  $\beta_{1n}(t)$  must satisfy the linear set of differential equations. The steady state solutions of this are:

$$\alpha_{1n}(t) = -\frac{d_s \Omega^3 c_n}{2(\omega_{1n}^2 - \Omega^2)} \sin \Omega t \quad (2.51a)$$

$$\beta_{1n}(t) = +\frac{d_s \Omega^3 c_n}{2(\omega_{1n}^2 - \Omega^2)} \cos \Omega t. \quad (2.51b)$$

Introducing Eqs. 2.51a and 2.51b in Eq. 2.46 we obtain:

$$\begin{aligned} \tilde{\Phi}(r, \theta, z, t) = -\frac{d_s}{2} \Omega [\sin \Omega t \cos \theta - \cos \Omega t \sin \theta] \\ \cdot \sum_{n=1}^{\infty} \left[ \frac{D}{(\varepsilon_{1n}^2 - 1)} \frac{\Omega^2}{(\omega_{1n}^2 - \Omega^2)} \frac{J_1(2\varepsilon_{1n} r / D)}{J_1(\varepsilon_{1n})} \frac{\cosh(2\varepsilon_{1n}(z + H_0)/D)}{\cosh(2\varepsilon_{1n} H_0 / D)} \right]. \end{aligned} \quad (2.52)$$

The potential is the sum of the liquid motion potential and of the container motion potential (Eq. 2.40), which is defined by Eq. 2.42. We have then:

$$\begin{aligned} \Phi(r, \theta, z, t) = -\frac{d_s}{2} \Omega \sin(\Omega t - \theta) \\ \cdot \left\{ r + \sum_{n=1}^{\infty} \left[ \frac{D}{(\varepsilon_{1n}^2 - 1)} \frac{\Omega^2}{(\omega_{1n}^2 - \Omega^2)} \frac{J_1(2\varepsilon_{1n} r / D)}{J_1(\varepsilon_{1n})} \frac{\cosh(2\varepsilon_{1n}(z + H_0)/D)}{\cosh(2\varepsilon_{1n} H_0 / D)} \right] \right\} \end{aligned} \quad (2.53)$$

The free surface elevation is obtained by using Eq. 2.45d:

$$\xi(r, \theta, t) = \frac{d_s \Omega^2}{2g} \cos(\Omega t - \theta) \cdot \left\{ r + \sum_{n=1}^{\infty} \left[ \frac{D}{(\varepsilon_{1n}^2 - 1)} \frac{\Omega^2}{(\omega_{1n}^2 - \Omega^2)} \frac{J_1(2\varepsilon_{1n} r / D)}{J_1(\varepsilon_{1n})} \right] \right\}. \quad (2.54)$$

We observe that the free surface height increases radially as a combination of a linear and of a Bessel's function, while tangentially it has sine distribution. The evolution of the free surface, for arbitrary experimental setup, is shown in Fig. 2.5, along with the evolution of the liquid height at the most external location at the container wall  $\xi(D/2, 0, 2\pi/\Omega)$  and of the crest-to-through amplitude as a function of the shaking frequency. During orbital shaking the depicted waves rotate around the  $\mathbf{e}_z$  axis, while maintaining a constant shape.

As the shaking frequency is increased toward a natural frequency  $\omega_{1n}$  the amplitude grows dramatically, reaching infinite values at the natural frequencies, e.g. at  $\omega_{11}$  it is a vertical plane,

a clearly non-physical solution. It is also interesting to notice that when  $\Omega > \omega_{1n}$  the model predicts a liquid distribution at the wall which is in opposition to the inertial forces - higher at the internal than at the external wall.

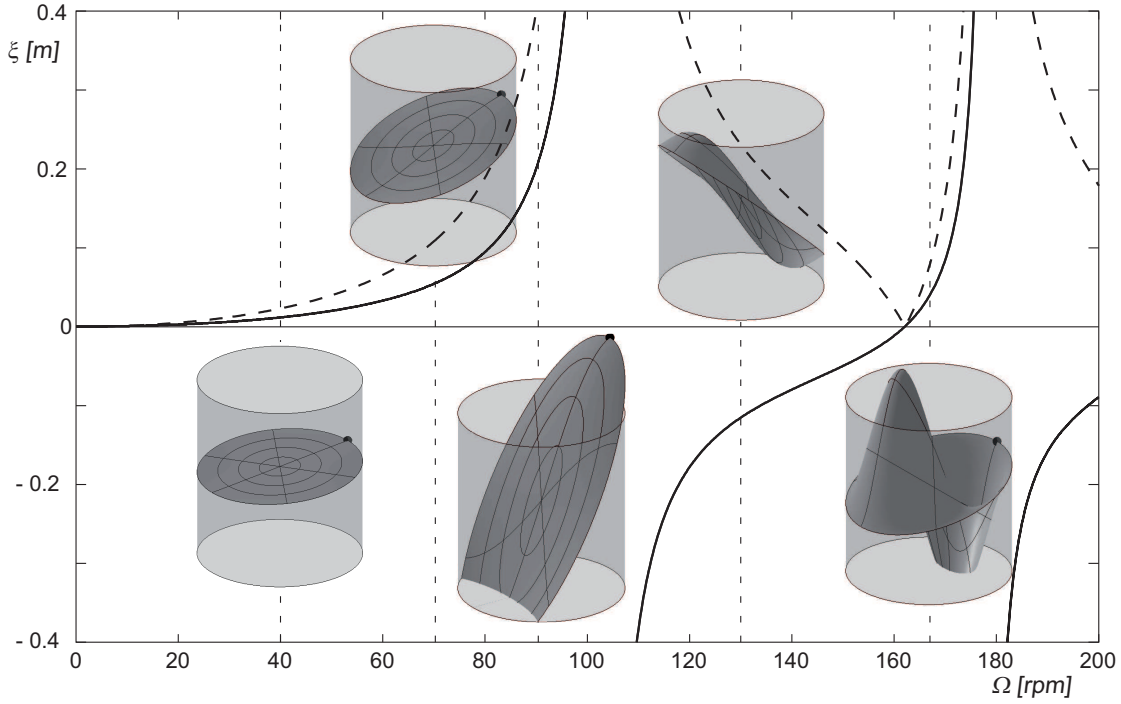


**Figure 2.5** | Examples of free surface shapes for  $D = 300\text{mm}$ ,  $d_s = 75\text{mm}$ ,  $H_0 = 150\text{mm}$  at  $\Omega = 40, 70, 92, 130, 167$  rpm. The solid line is the vertical displacement of a particle situated at the most external point of the container  $\xi(D/2, 0, 2\pi/\Omega)$ , depicted on the free surface as a black dot. The dashed line is the evolution of the crest-to-trough amplitude of the wave at the wall.

Considering the forces acting on the liquids, one may expect the free surface to be planar, tilted with respect to the vertical direction by the balance between the inertial ( $\Omega^2 d_s$ ) and the gravitational ( $g$ ) acceleration. We notice that the linear result includes this intuitive solution, but it also takes into account the existence of natural modes and it respects the boundary condition at the walls. Figure 2.6 depicts the solution of the potential model  $\xi(r, \theta)$  and the wave created by the balance of accelerations in a vertical  $x - z$  plane, thus from a lateral point of view. Hence, we observe that at low shaking frequency the free surface is indeed close to a tilted plane, but with a different slope. Moreover, the free surface potential solution has a greater slope at the bulk of the liquid (at some distance from the wall) than at the wall.

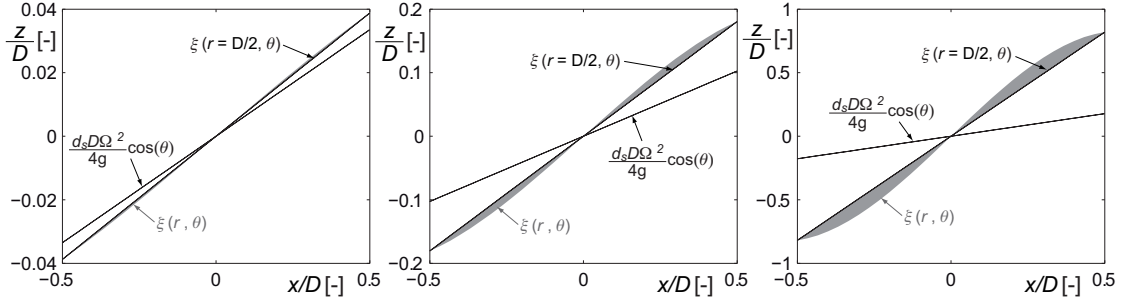


**Figure 2.6** | Free surface elevation according to the potential model and according only to the balance of forces. The elevation at the wall is shown as a solid line, while the liquid bulk is depicted in grey.

The velocity fields of the liquid are found differentiating Eq. 2.52:

$$q_r(r, \theta, z, t) = \frac{\partial \tilde{\Phi}}{\partial r} = -\frac{d_s \Omega}{2} \sin(\Omega t - \theta) \cdot \sum_{n=1}^{\infty} \frac{2\varepsilon_{1n}}{(\varepsilon_{1n}^2 - 1)} \frac{\Omega^2}{(\omega_{1n}^2 - \Omega^2)} \frac{J'_1(2\varepsilon_{1n}r/D)}{J_1(\varepsilon_{1n})} \frac{\cosh(2\varepsilon_{1n}(z + H_0)/D)}{\cosh(2\varepsilon_{1n}H_0/D)}, \quad (2.55a)$$

$$q_\theta(r, \theta, z, t) = \frac{1}{r} \frac{\partial \tilde{\Phi}}{\partial \theta} = \frac{d_s \Omega}{2} \cos(\Omega t - \theta) \cdot \sum_{n=1}^{\infty} \frac{D}{r(\varepsilon_{1n}^2 - 1)} \frac{\Omega^2}{(\omega_{1n}^2 - \Omega^2)} \frac{J_1(2\varepsilon_{1n}r/D)}{J_1(\varepsilon_{1n})} \frac{\cosh(2\varepsilon_{1n}(z + H_0)/D)}{\cosh(2\varepsilon_{1n}H_0/D)}, \quad (2.55b)$$

$$q_z(r, \theta, z, t) = \frac{\partial \tilde{\Phi}}{\partial z} = -\frac{d_s \Omega}{2} \sin(\Omega t - \theta) \cdot \sum_{n=1}^{\infty} \frac{2\varepsilon_{1n}}{(\varepsilon_{1n}^2 - 1)} \frac{\Omega^2}{(\omega_{1n}^2 - \Omega^2)} \frac{J_1(2\varepsilon_{1n}r/D)}{J_1(\varepsilon_{1n})} \frac{\sinh(2\varepsilon_{1n}(z + H_0)/D)}{\cosh(2\varepsilon_{1n}H_0/D)}. \quad (2.55c)$$

The velocity fields are depicted in Fig.2.7 for four vertical and four horizontal planes in a stationary wave ( $t$  is fixed). It has to be noted that the colours depict the off-plane velocity, which is  $q_\theta \cdot \text{sgn}(r)$  in vertical planes and  $q_z$  in horizontal ones. We note that the magnitude of the velocity is similar for the three components, and that the highest velocities are predicted near the free surface. While in vertical planes the velocity field resembles the one observed in bi-dimensional waves, in horizontal planes it is similar to the one generated by a potential dipole. As the container is shaken, the velocity fields rotate around the revolution axis of the container ( $\mathbf{e}_z$ ). Consequently, it is necessary to compute the trajectories followed by liquid particles to better understand the motion of the liquid.

The Lagrangian trajectories of liquid parcels submitted to this velocity field are computed

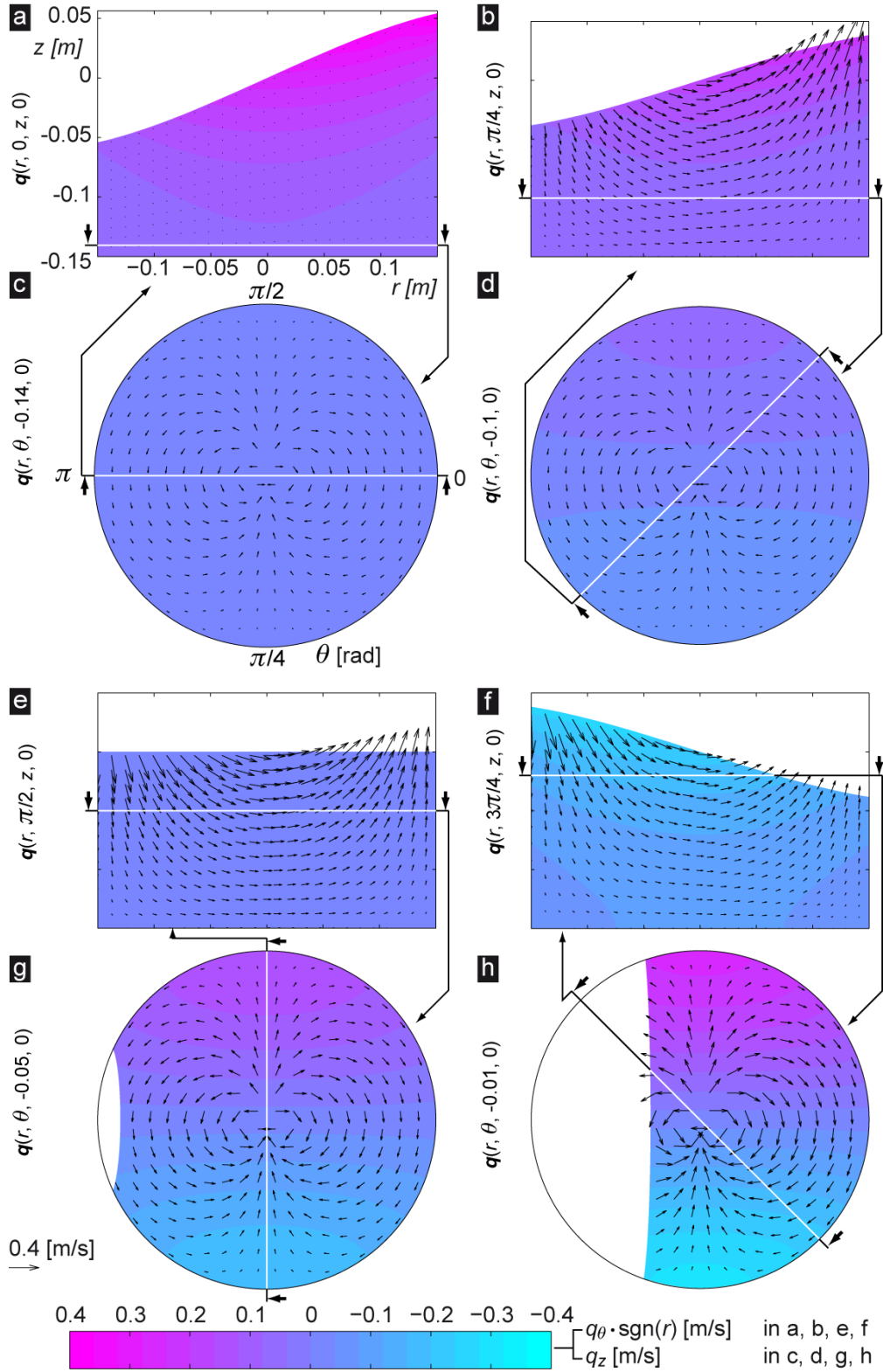


**Figure 2.7** | Examples of velocity fields in the liquid for  $D = 300\text{mm}$ ,  $d_s = 75\text{mm}$ ,  $H_0 = 150\text{mm}$ ,  $\Omega = 70\text{rpm}$ . The velocity fields are displayed at four different vertical and four horizontal planes. Each vertical plane displays also the position of a horizontal plane, and vice versa. Colours indicate the off-plane velocity component.

iteratively using Eqs. 2.25 in cylindrical coordinates:

$$\begin{aligned} r(t+dt) &= r(t) + q_r(r(t), \theta(t), z(t), t) \cdot dt \\ \theta(t+dt) &= \theta(t) + \frac{1}{r(t)} q_\theta(r(t), \theta(t), z(t), t) \cdot dt \\ z(t+dt) &= z(t) + q_z(r(t), \theta(t), z(t), t) \cdot dt. \end{aligned} \quad (2.56)$$

An example of trajectories followed during five revolutions by particles starting from  $\theta_0=0$  at several  $r_0$  and  $z_0$  is depicted in Fig. 2.8, for  $D=300\text{mm}$ ,  $d_s=50\text{mm}$ ,  $H_0=150\text{mm}$  and  $\Omega=70\text{rpm}$ . Since the motion of the particles is three-dimensional and sometimes difficult to understand from a single point of view, the trajectories are depicted in a three-dimensional space (Fig. 2.8a)

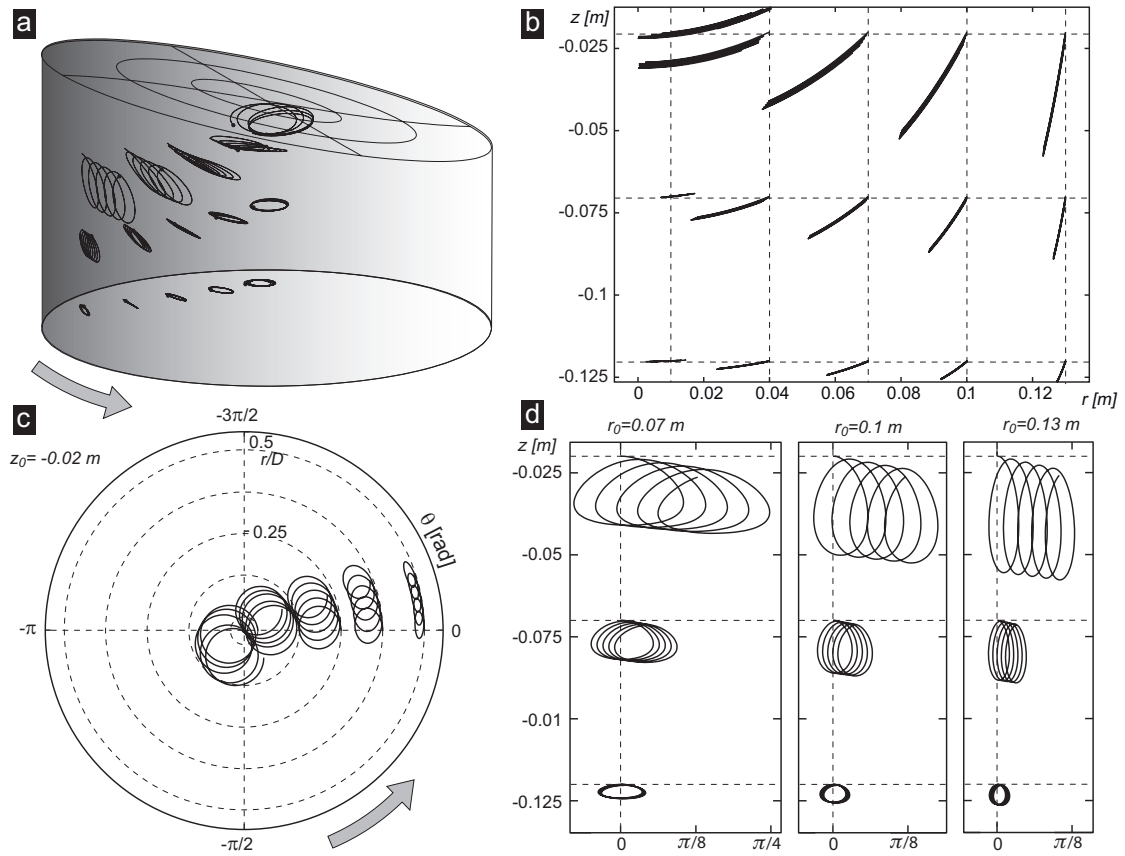


**Figure 2.8** | Trajectories followed by particles during five vessel revolutions, from potential velocity fields, for  $D=300\text{mm}$ ,  $d_s=50\text{mm}$ ,  $H_0=150\text{mm}$  and  $\Omega=70\text{rpm}$ . The initial positions of the particles  $\mathbf{x}_0$  are at the intersections of the dashed lines ( $r_0=0.01, 0.04, 0.07, 0.1, 0.13\text{m}$ ,  $\theta_0=0$  and  $z_0=-0.02, -0.07, -0.12\text{m}$ ). **a**: Three-dimensional trajectories from starting locations identical to those given in **b**. The free surface shape is also depicted, and the final position of the particles is depicted as a black dot **b**: projection of the trajectories in the  $r-z$  plane. **c**: projection of the trajectories starting from  $z_0=-0.02\text{m}$  in the  $r-\theta$  plane. **d**: projections in the  $\theta-z$  plane, of the trajectories starting at  $r_0=0.07, 0.1, 0.13$ .

and as projections in different planes (Fig. 2.8b-d). We observe that the particles draw tilted trochoidal trajectories, moving in the three dimensions as they drift in the direction of the wave propagation. The motion is almost vertical at the wall, while it becomes increasingly horizontal as we approach the axis of the container (Fig. 2.8b), thus increasing the amplitude of the radial and tangential motions to the detriment of the vertical one (Fig. 2.8c-d). The dispersion of the gas exchanged at the free surface is supposed to be due mainly to the transport of gas by the liquid. These trajectories suggest that the gas exchanged at the free surface descends into the liquid near the wall and is subsequently advected to the centre of the container.

Analogously to the bi-dimensional waves velocity fields (Eq. 2.24), the trajectories of the particles display a significant drift in the direction of propagation of the wave. We quantify it by computing the difference between Lagrangian and Eulerian velocities.

$$\bar{\mathbf{q}}_L = \frac{1}{2} \frac{d_s^2 \Omega}{4r_0} \left[ (A^2 + C^2) - \frac{D}{r_0} AB + \frac{D^2}{r_0^2} B^2 \right] \mathbf{e}_\theta, \quad (2.57)$$

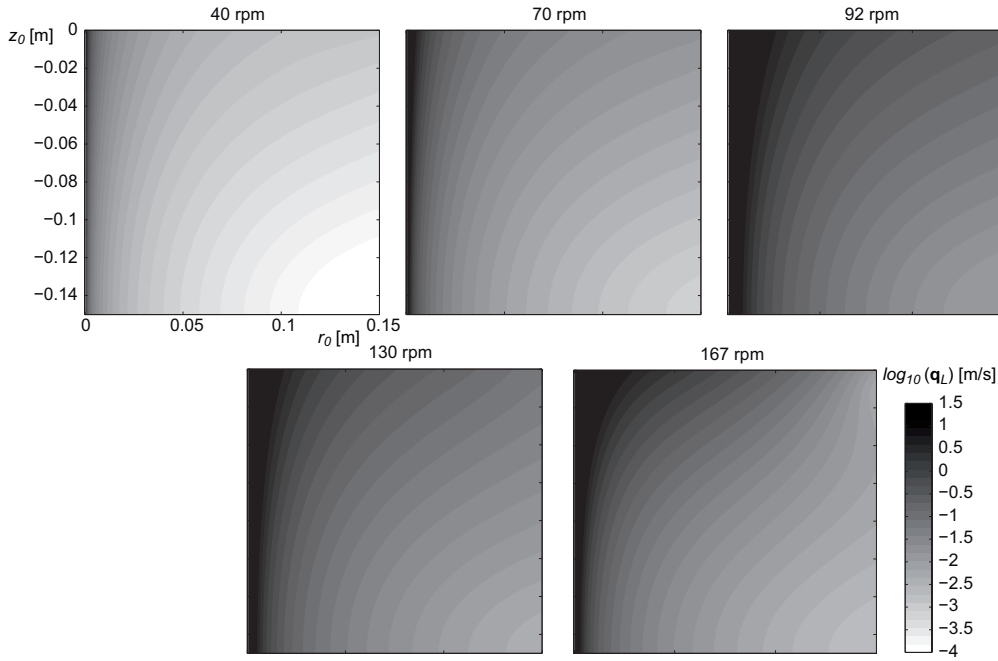


**Figure 2.9** | Stokes drift computed according to Eq. 2.57 for  $D=300\text{mm}$ ,  $d_s=75\text{mm}$ ,  $H_0=150\text{mm}$  and  $\Omega=40, 70, 92, 130, 167\text{rpm}$ . The shaking configurations are the same as the one used to obtain the wave shapes in Fig. 2.5. The drift is displayed as a function of the starting position  $r_0 \in [0, D/2]$ ,  $z_0 \in [0, -H_0]$ , and is given in logarithmic scale.



where:

$$\begin{aligned}
 A &= \sum_{n=1}^{\infty} \frac{2\varepsilon_{1n}}{(\varepsilon_{1n}^2 - 1)} \frac{\Omega^2}{(\omega_{1n}^2 - \Omega^2)} \frac{J_1'(2\varepsilon_{1n}r_0/D)}{J_1(\varepsilon_{1n})} \frac{\cosh(2\varepsilon_{1n}(z_0 + H_0)/D)}{\cosh(2\varepsilon_{1n}H_0/D)}, \\
 B &= \sum_{n=1}^{\infty} \frac{1}{(\varepsilon_{1n}^2 - 1)} \frac{\Omega^2}{(\omega_{1n}^2 - \Omega^2)} \frac{J_1(2\varepsilon_{1n}r_0/D)}{J_1(\varepsilon_{1n})} \frac{\cosh(2\varepsilon_{1n}(z + H_0)/D)}{\cosh(2\varepsilon_{1n}H_0/D)}, \\
 C &= \sum_{n=1}^{\infty} \frac{2\varepsilon_{1n}}{(\varepsilon_{1n}^2 - 1)} \frac{\Omega^2}{(\omega_{1n}^2 - \Omega^2)} \frac{J_1(2\varepsilon_{1n}r_0/D)}{J_1(\varepsilon_{1n})} \frac{\sinh(2\varepsilon_{1n}(z_0 + H_0)/D)}{\cosh(2\varepsilon_{1n}H_0/D)}.
 \end{aligned}$$

The steps leading to Eq.2.57 are given in Annexe C, and an example of drift encountered by the particles, as a function of their starting position  $(r_0, z_0)$ , is shown in logarithmic scale in Fig. 2.9 for the same shaking configurations giving the free surface shapes in Fig. 2.5. We observe that the drift decreases with the depth and with the radius, as already seen in the trajectories followed by the particles, in Fig. 2.8. Moreover, we notice that the shaking configuration displaying an overall greater drift is the one closer to the natural frequency (92rpm,  $\omega_{11}=104$ rpm). At shaking frequencies above the first natural frequency, the influence of the second mode is visible in the deformation of the velocity contours at  $r \rightarrow D$ .

### 2.3.1 Dimensionless formulation

It is possible to rewrite Eq. 2.54 in a scale independent way by introducing the following dimensionless quantities:  $\tilde{r} = r/D$ ,  $\tilde{z} = z/D$  and  $\tilde{\xi} = \xi/D$ . Moreover it is usual in waves dynamics to identify the Froude number  $Fr$  as root of the ratio between a characteristic velocity and the gravitational wave celerity. In the present case, we define the  $Fr^2 = d_s \Omega^2 / g$ . Accordingly, we define the following dimensionless operating parameters:  $\tilde{d}_s = d_s/D$  and  $\tilde{H}_0 = H_0/D$ . The free surface height is hence defined as:

$$\tilde{\xi}(\tilde{r}, \theta) = \frac{Fr^2}{2} \cos(\theta - \Omega t) \cdot \left\{ \tilde{r} + \sum_{n=1}^{\infty} \left[ \frac{1}{(\varepsilon_{1n}^2 - 1)} \frac{Fr^2}{(Fr_{1n}^2 - Fr^2)} \frac{J_1(2\varepsilon_{1n}\tilde{r})}{J_1(\varepsilon_{1n})} \right] \right\} \quad (2.59)$$

where  $Fr_{1n}$  is found according to Eq. 2.48:

$$Fr_{mn}^2 = 2\varepsilon_{mn}\tilde{d}_s \tanh(2\varepsilon_{mn}\tilde{H}_0). \quad (2.60)$$

We see therefore that  $\tilde{d}_s$ ,  $\tilde{H}_0$  and  $Fr$  are sufficient to determine unequivocally the shape of the free surface. This result is used throughout the rest of this work to describe the behaviour of the wave in a dimensionless way.

The components of the velocity fields are normalized by the tangential velocity of displacement

of the shaker:  $\tilde{q}_i = q_i / (d_s \Omega)$  where  $i = r, \theta, z$ . Hence, we have:

$$\begin{aligned} \tilde{q}_r(\tilde{r}, \theta, \tilde{z}) &= -\frac{1}{2} \sin(\theta - \Omega t) \\ &\cdot \sum_{n=1}^{\infty} \frac{2\varepsilon_{1n}}{(\varepsilon_{1n}^2 - 1)} \frac{Fr^2}{(Fr_{1n}^2 - Fr^2)} \frac{J_1'(2\varepsilon_{1n}\tilde{r})}{J_1(\varepsilon_{1n})} \frac{\cosh(2\varepsilon_{1n}(\tilde{z} + \tilde{H}_0))}{\cosh(2\varepsilon_{1n}\tilde{H}_0)}, \end{aligned} \quad (2.61a)$$

$$\begin{aligned} \tilde{q}_\theta(\tilde{r}, \theta, \tilde{z}) &= \frac{1}{2\tilde{r}} \cos(\theta - \Omega t) \\ &\cdot \sum_{n=1}^{\infty} \frac{1}{(\varepsilon_{1n}^2 - 1)} \frac{Fr^2}{(Fr_{1n}^2 - Fr^2)} \frac{J_1(2\varepsilon_{1n}\tilde{r})}{J_1(\varepsilon_{1n})} \frac{\cosh(2\varepsilon_{1n}(\tilde{z} + \tilde{H}_0))}{\cosh(2\varepsilon_{1n}\tilde{H}_0)}, \end{aligned} \quad (2.61b)$$

$$\begin{aligned} \tilde{q}_z(\tilde{r}, \theta, \tilde{z}) &= -\frac{1}{2} \sin(\theta - \Omega t) \\ &\cdot \sum_{n=1}^{\infty} \frac{2\varepsilon_{1n}}{(\varepsilon_{1n}^2 - 1)} \frac{Fr^2}{(Fr_{1n}^2 - Fr^2)} \frac{J_1(2\varepsilon_{1n}\tilde{r})}{J_1(\varepsilon_{1n})} \frac{\sinh(2\varepsilon_{1n}(\tilde{z} + \tilde{H}_0))}{\cosh(2\varepsilon_{1n}\tilde{H}_0)}. \end{aligned} \quad (2.61c)$$

### 2.3.2 Weakly non-linear solution

The results presented in the previous sections are valid for linear waves, i.e. as long as the amplitude remains small compared to the wavelength. They are therefore not suitable to describe the flow near the natural frequencies. Several higher order resolutions, inspired by Stokes expansion method, exist in the case of linear excitation [33, 84], and may be found in [50] Chap. 4. Those solutions allow a better estimation of the forces acting on the container [4], as well as a closer agreement to the non-linear behaviour of the wave near the natural frequencies [92]. Our experimental results suggest that in most cases the linear solution provides sufficient precision and, knowing its limitations, it is often used throughout this paper. There are, however, specific phenomena that the linear solution is unable to predict. Therefore, we present here a solution of the potential model taking into account the non-linearity of the free surface boundary conditions, based on the development of the cited works.

The boundary conditions (Eqs. 2.43 and 2.44) are expressed in terms of a Taylor expansion

around  $z = \xi = 0$ . We obtain:

$$\begin{aligned}
 & \frac{1}{2} \left[ \left( \frac{\partial \tilde{\Phi}}{\partial r} \right)^2 + \left( \frac{1}{r} \frac{\partial \tilde{\Phi}}{\partial \theta} \right)^2 + \left( \frac{\partial \tilde{\Phi}}{\partial z} \right)^2 \right] + \frac{\partial \tilde{\Phi}}{\partial t} - \frac{d_s \Omega^2 r}{2} \cos(\Omega t - \theta) \\
 & + \xi \left[ g + \frac{\partial \tilde{\Phi}}{\partial r} \frac{\partial}{\partial z} \frac{\partial \tilde{\Phi}}{\partial r} + \frac{1}{r^2} \frac{\partial \tilde{\Phi}}{\partial \theta} \frac{\partial}{\partial z} \frac{\partial \tilde{\Phi}}{\partial \theta} + \frac{\partial \tilde{\Phi}}{\partial z} \frac{\partial^2 \tilde{\Phi}}{\partial z^2} + \frac{\partial}{\partial z} \frac{\partial \tilde{\Phi}}{\partial t} \right] \\
 & + \frac{\xi^2}{2} \left[ \frac{\partial \tilde{\Phi}}{\partial r} \frac{\partial^2}{\partial z^2} \frac{\partial \tilde{\Phi}}{\partial r} + \left( \frac{\partial}{\partial z} \frac{\partial \tilde{\Phi}}{\partial r} \right)^2 + \frac{1}{r^2} \frac{\partial \tilde{\Phi}}{\partial \theta} \frac{\partial^2}{\partial z^2} \frac{\partial \tilde{\Phi}}{\partial \theta} + \frac{1}{r^2} \left( \frac{\partial}{\partial z} \frac{\partial \tilde{\Phi}}{\partial \theta} \right)^2 \right. \\
 & \quad \left. + \frac{\partial \tilde{\Phi}}{\partial z} \frac{\partial^3 \tilde{\Phi}}{\partial z^3} + \left( \frac{\partial^2 \tilde{\Phi}}{\partial z^2} \right)^2 + \frac{\partial^2}{\partial z^2} \frac{\partial \tilde{\Phi}}{\partial t} \right] \\
 & + O(\xi^3) = 0
 \end{aligned} \tag{2.62}$$

and

$$\begin{aligned}
 & \frac{\partial \tilde{\Phi}}{\partial z} - \frac{\partial \xi}{\partial t} - \frac{\partial \xi}{\partial r} \frac{\partial \tilde{\Phi}}{\partial r} - \frac{1}{r^2} \frac{\partial \xi}{\partial \theta} \frac{\partial \tilde{\Phi}}{\partial \theta} + \xi \left[ \frac{\partial^2 \tilde{\Phi}}{\partial z^2} - \frac{\partial \xi}{\partial r} \frac{\partial}{\partial z} \frac{\partial \tilde{\Phi}}{\partial r} - \frac{1}{r^2} \frac{\partial \xi}{\partial \theta} \frac{\partial}{\partial z} \frac{\partial \tilde{\Phi}}{\partial \theta} \right] \\
 & + \frac{\xi^2}{2} \left[ \frac{\partial^3 \tilde{\Phi}}{\partial z^3} - \frac{\partial \xi}{\partial r} \frac{\partial^2}{\partial z^2} \frac{\partial \tilde{\Phi}}{\partial r} - \frac{1}{r^2} \frac{\partial \xi}{\partial \theta} \frac{\partial^2}{\partial z^2} \frac{\partial \tilde{\Phi}}{\partial \theta} \right] + O(\xi^3) = 0.
 \end{aligned} \tag{2.63}$$

We have seen that the linear solutions for the velocity potential and free surface height are of the following form:

$$\begin{aligned}
 \tilde{\Phi}(r, \theta, z, t) &= \sum_{m=0}^{\infty} \sum_{n=1}^{\infty} [\alpha_{mn}(t) \cos(m\theta) + \beta_{mn}(t) \sin m\theta] J_m(\lambda_{mn} r) \frac{\cosh[\lambda_{mn}(z + H_0)]}{\cosh \lambda_{mn} H_0} \\
 \xi(r, \theta, t) &= \sum_{m=0}^{\infty} \sum_{n=1}^{\infty} [a_{mn}(t) \cos m\theta + b_{mn}(t) \sin m\theta] J_m(\lambda_{mn} r)
 \end{aligned}$$

where  $\alpha_{mn}$ ,  $\beta_{mn}$ ,  $a_{mn}$  and  $b_{mn}$  are time dependent coefficients to be determined,  $J_m$  is the Bessel's function of the first kind,  $m^{th}$  order and  $\lambda_{mn}$  is the normalized  $n^{th}$  root of  $J'_m(r)$ . In order to keep a finite number of terms in the solution, we consider only the waves at shaking frequencies below the first natural frequency,  $\Omega < \omega_{11}$ . We suppose the dominant mode to be the (1, 1) and the secondary ones to be the (0, 1) and (1, 2). Thus, the potential and free surface

solutions are:

$$\begin{aligned}\tilde{\Phi}(r, \theta, z, t) = & [\alpha_{11}(t) \cos \theta + \beta_{11}(t) \sin \theta] J_1(\lambda_{11} r) \frac{\cosh[\lambda_{11}(z + H_0)]}{\cosh \lambda_{11} H_0} \\ & + \alpha_{01}(t) J_0(\lambda_{01} r) \frac{\cosh[\lambda_{01}(z + H_0)]}{\cosh \lambda_{01} H_0} \\ & + [\alpha_{21}(t) \cos 2\theta + \beta_{21}(t) \sin 2\theta] J_2(\lambda_{21} r) \frac{\cosh[\lambda_{21}(z + H_0)]}{\cosh \lambda_{21} H_0}\end{aligned}\quad (2.64)$$

$$\begin{aligned}\xi(r, \theta, t) = & [a_{11}(t) \cos \theta + b_{11}(t) \sin \theta] J_1(\lambda_{11} r) + a_{01}(t) J_0(\lambda_{01} r) \\ & + [a_{21}(t) \cos 2\theta + b_{12}(t) \sin 2\theta] J_2(\lambda_{21} r)\end{aligned}\quad (2.65)$$

Injecting this solution in the boundary conditions and keeping only the order up to  $O(a_{11}^2) = O(a_{01}) = O(a_{21})$  we obtain, expressing  $r$  in a Bessel-Fourier series as expressed in Eq. 2.49:

$$\begin{aligned}& \frac{1}{2} \left[ \lambda_{11}^2 [\alpha_{11}^2 \cos^2(\theta) + 2\alpha_{11}\beta_{11} \cos \theta \sin \theta + \beta_{11}^2 \sin^2(\theta)] J_1'^2(\lambda_{11} r) \right. \\ & \quad + \frac{1}{r^2} [\alpha_{11}^2 \sin^2(\theta) - 2\alpha_{11}\beta_{11} \cos \theta \sin \theta + \beta_{11}^2 \cos^2(\theta)] J_1^2(\lambda_{11} r) \\ & \quad \left. + \lambda_{11}^2 [\alpha_{11}^2 \cos^2(\theta) + 2\alpha_{11}\beta_{11} \cos \theta \sin \theta + \beta_{11}^2 \sin^2(\theta)] J_1^2(\lambda_{11} r) \tanh^2(\lambda_{11} H_0) \right] \\ & + [\dot{\alpha}_{11} \cos \theta + \dot{\beta}_{11} \sin \theta] J_1(\lambda_{11} r) + \dot{\alpha}_{01} J_0(\lambda_{01} r) \\ & + [\dot{\alpha}_{21} \cos 2\theta + \dot{\beta}_{21} \sin 2\theta] J_2(\lambda_{21} r) - \frac{d_s \Omega^2 c_1 J_1(\lambda_{11} r)}{2} [\cos(\Omega t) \cos(\theta) + \sin(\Omega t) \sin(\theta)] \\ & + g[a_{11} \cos \theta + b_{11} \sin \theta] J_1(\lambda_{11} r) + g a_{01} J_0(\lambda_{01} r) \\ & + g[a_{21} \cos 2\theta + b_{12} \sin 2\theta] J_2(\lambda_{21} r) + \lambda_{11} \left[ \dot{\alpha}_{11} a_{11} \cos^2 \theta + \dot{\alpha}_{11} b_{11} \sin \theta \cos \theta \right. \\ & \quad \left. + \dot{\beta}_{11} a_{11} \sin \theta \cos \theta + \dot{\beta}_{11} b_{11} \sin^2 \theta \right] J_1^2(\lambda_{11} r) \tanh(\lambda_{11} H_0) = 0\end{aligned}\quad (2.66)$$

or

$$\begin{aligned}
 & \frac{1}{4} \left[ \lambda_{11}^2 J_1'^2(\lambda_{11} r) + \frac{1}{r^2} J_1^2(\lambda_{11} r) + \lambda_{11}^2 J_1^2(\lambda_{11} r) \tanh^2(\lambda_{11} H_0) \right] (\alpha_{11}^2 + \beta_{11}^2) \\
 & + \frac{1}{4} \left[ \lambda_{11}^2 J_1'^2(\lambda_{11} r) - \frac{1}{r^2} J_1^2(\lambda_{11} r) + \lambda_{11}^2 J_1^2(\lambda_{11} r) \tanh^2(\lambda_{11} H_0) \right] (\alpha_{11}^2 - \beta_{11}^2) \cos 2\theta \\
 & + \frac{1}{2} \left[ \lambda_{11}^2 J_1'^2(\lambda_{11} r) - \frac{1}{r^2} J_1^2(\lambda_{11} r) + \lambda_{11}^2 J_1^2(\lambda_{11} r) \tanh^2(\lambda_{11} H_0) \right] \alpha_{11} \beta_{11} \sin 2\theta \\
 & + [\dot{\alpha}_{11} \cos \theta + \dot{\beta}_{11} \sin \theta] J_1(\lambda_{11} r) + \dot{\alpha}_{01} J_0(\lambda_{01} r) \\
 & + [\dot{\alpha}_{21} \cos 2\theta + \dot{\beta}_{21} \sin 2\theta] J_2(\lambda_{21} r) - \frac{d_s \Omega^2 c_1 J_1(\lambda_{11} r)}{2} [\cos(\Omega t) \cos(\theta) + \sin(\Omega t) \sin(\theta)] \\
 & + g[a_{11} \cos \theta + b_{11} \sin \theta] J_1(\lambda_{11} r) + g a_{01} J_0(\lambda_{01} r) \\
 & + g[a_{21} \cos 2\theta + b_{12} \sin 2\theta] J_2(\lambda_{21} r) + \frac{\lambda_{11}}{2} (\dot{\alpha}_{11} a_{11} + \dot{\beta}_{11} b_{11}) J_1^2(\lambda_{11} r) \tanh(\lambda_{11} H_0) \\
 & + \frac{\lambda_{11}}{2} (\dot{\alpha}_{11} a_{11} - \dot{\beta}_{11} b_{11}) \cos 2\theta J_1^2(\lambda_{11} r) \tanh(\lambda_{11} H_0) \\
 & + \frac{\lambda_{11}}{2} (\dot{\alpha}_{11} b_{11} + \dot{\beta}_{11} a_{11}) \sin 2\theta J_1^2(\lambda_{11} r) \tanh(\lambda_{11} H_0) = 0
 \end{aligned} \tag{2.67}$$

and the kinematic boundary condition becomes:

$$\begin{aligned}
 & \lambda_{11} (\alpha_{11} \cos \theta + \beta_{11} \sin \theta) J_1(\lambda_{11} r) \tanh(\lambda_{11} H_0) + \lambda_{01} \alpha_{01} J_0(\lambda_{01} r) \tanh(\lambda_{01} H_0) \\
 & + \lambda_{21} (\alpha_{21} \cos 2\theta + \beta_{21} \sin 2\theta) J_2(\lambda_{21} r) \tanh(\lambda_{21} H_0) - (\dot{\alpha}_{11} \cos \theta + \dot{\beta}_{11} \sin \theta) J_1(\lambda_{11} r) \\
 & - \dot{\alpha}_{01} J_0(\lambda_{01} r) - (\dot{\alpha}_{21} \cos 2\theta + \dot{\beta}_{21} \sin 2\theta) J_2(\lambda_{21} r) \\
 & - \lambda_{11}^2 J_1'^2(\lambda_{11} r) (\alpha_{11} a_{11} \cos^2 \theta + \alpha_{11} b_{11} \cos \theta \sin \theta + \beta_{11} a_{11} \cos \theta \sin \theta + \beta_{11} b_{11} \sin^2 \theta) \\
 & - \frac{J_1^2(\lambda_{11})}{r^2} (\alpha_{11} a_{11} \sin^2 \theta - \alpha_{11} b_{11} \cos \theta \sin \theta - \beta_{11} a_{11} \cos \theta \sin \theta + \beta_{11} b_{11} \cos^2 \theta) \\
 & + \lambda_{11}^2 J_1^2(\lambda_{11} r) (\alpha_{11} a_{11} \cos^2 \theta + \alpha_{11} b_{11} \cos \theta \sin \theta \\
 & + a_{11} \beta_{11} \cos \theta \sin \theta + \beta_{11} b_{11} \sin^2 \theta) = 0
 \end{aligned} \tag{2.68}$$

or

$$\begin{aligned}
& \lambda_{11}(\alpha_{11} \cos \theta + \beta_{11} \sin \theta) J_1(\lambda_{11} r) \tanh(\lambda_{11} H_0) + \lambda_{01} \alpha_{01} J_0(\lambda_{01} r) \tanh(\lambda_{01} H_0) \\
& + \lambda_{21}(\alpha_{21} \cos 2\theta + \beta_{21} \sin 2\theta) J_2(\lambda_{21} r) \tanh(\lambda_{21} H_0) - (\dot{\alpha}_{11} \cos \theta + \dot{b}_{11} \sin \theta) J_1(\lambda_{11} r) \\
& - \dot{\alpha}_{01} J_0(\lambda_{01} r) - (\dot{\alpha}_{21} \cos 2\theta + \dot{b}_{21} \sin 2\theta) J_2(\lambda_{21} r) \\
& - \frac{\lambda_{11}^2 J_1'^2(\lambda_{11} r)}{2} (\alpha_{11} a_{11} + \beta_{11} b_{11}) - \frac{\lambda_{11}^2 J_1'^2(\lambda_{11} r)}{2} (\alpha_{11} b_{11} + \beta_{11} a_{11}) \sin 2\theta \\
& - \frac{\lambda_{11}^2 J_1'^2(\lambda_{11} r)}{2} (\alpha_{11} a_{11} - \beta_{11} b_{11}) \cos 2\theta - \frac{J_1^2(\lambda_{11} r)}{2r^2} (\alpha_{11} a_{11} + \beta_{11} b_{11}) \\
& + \frac{J_1^2(\lambda_{11} r)}{2r^2} (\alpha_{11} b_{11} + \beta_{11} a_{11}) \sin 2\theta + \frac{J_1^2(\lambda_{11} r)}{2r^2} (\alpha_{11} a_{11} - \beta_{11} b_{11}) \cos 2\theta \\
& + \frac{\lambda_{11}^2 J_1^2(\lambda_{11} r)}{2} (\alpha_{11} a_{11} + \beta_{11} b_{11}) + \frac{\lambda_{11}^2 J_1^2(\lambda_{11} r)}{2} (\alpha_{11} b_{11} + \beta_{11} a_{11}) \sin 2\theta \\
& + \frac{\lambda_{11}^2 J_1^2(\lambda_{11} r)}{2} (\alpha_{11} a_{11} - \beta_{11} b_{11}) \cos 2\theta = 0.
\end{aligned} \tag{2.69}$$

Each linear set of differential equations defined by the trigonometric functions has to be solved independently. For the order  $\cos(\theta)$  or  $\sin(\theta)$  we have:

$$\dot{\alpha}_{11} + g a_{11} = \frac{d_s \Omega^2 c_1}{2} \cos(\Omega t) \tag{2.70a}$$

$$\lambda_{11} \alpha_{11} \tanh(\lambda_{11} H_0) = \dot{\alpha}_{11} \tag{2.70b}$$

$$\dot{\beta}_{11} + g b_{11} = \frac{d_s \Omega^2 c_1}{2} \sin(\Omega t) \tag{2.70c}$$

$$\lambda_{11} \beta_{11} \tanh(\lambda_{11} H_0) = \dot{\beta}_{11}. \tag{2.70d}$$

Injecting Eqs. 2.70b and 2.70d in the time derivation of respectively Eqs. 2.70a and 2.70c; and using the definition of the natural frequencies  $\omega_{11}$  given in Eq. 2.48, we obtain the equations for  $a_{1n}$  and  $b_{1n}$  equivalent to the first term of the linear solution, in Eq. 2.50. The solutions (given in Eqs. 2.51a and 2.51b) are:

$$\alpha_{11}(t) = - \frac{d_s \Omega^3}{2(\omega_{11}^2 - \Omega^2)} \frac{D}{(\varepsilon_{11}^2 - 1)J(\varepsilon_{11})} \sin \Omega t \tag{2.71a}$$

$$\beta_{11}(t) = + \frac{d_s \Omega^3}{2(\omega_{11}^2 - \Omega^2)} \frac{D}{(\varepsilon_{11}^2 - 1)J(\varepsilon_{11})} \cos \Omega t \tag{2.71b}$$

and the values of  $a_{11}$  and  $b_{11}$  are found injecting these solutions in the corresponding equa-

tions of Eq. 2.70:

$$a_{11}(t) = \frac{\lambda_{11} d_s \Omega^2 D \tanh(\lambda_{11} H_0)}{2(\omega_{11}^2 - \Omega^2)(\varepsilon_{11}^2 - 1)J(\varepsilon_{11})} \cos \Omega t = \frac{d_s \Omega^2 c_1}{2g} \cos \Omega t + \frac{d_s \Omega^4 c_1}{2g(\omega_{11}^2 - \Omega^2)} \cos \Omega t \quad (2.72a)$$

$$b_{11}(t) = \frac{\lambda_{11} d_s \Omega^2 D \tanh(\lambda_{11} H_0)}{2(\omega_{11}^2 - \Omega^2)(\varepsilon_{11}^2 - 1)J(\varepsilon_{11})} \sin \Omega t = \frac{d_s \Omega^2 c_1}{2g} \sin \Omega t + \frac{d_s \Omega^4 c_1}{2g(\omega_{11}^2 - \Omega^2)} \sin \Omega t \quad (2.72b)$$

Those results lead to the linear solution for the potential  $\tilde{\Phi}$  and the free surface  $\xi$  given in Eqs. 2.53 and 2.54, if all the  $n=1$  dots  $\infty$  modes are considered. In the other orders, several combinations of those time dependent coefficients appear and are given in Appendix D. The equations of the order  $m=0$  are:

$$\begin{aligned} & \frac{1}{4} \left[ \lambda_{11}^2 J_1'^2(\lambda_{11} r) + \frac{1}{r^2} J_1^2(\lambda_{11} r) + \lambda_{11}^2 J_1^2(\lambda_{11} r) \tanh^2(\lambda_{11} H_0) \right] (\alpha_{11}^2 + \beta_{11}^2) \\ & + \dot{\alpha}_{01} J_0(\lambda_{01} r) + g a_{01} J_0(\lambda_{01} r) \\ & + \frac{\lambda_{11}}{2} (\dot{\alpha}_{11} a_{11} + \dot{\beta}_{11} b_{11}) J_1^2(\lambda_{11} r) \tanh(\lambda_{11} H_0) = 0 \end{aligned} \quad (2.73a)$$

$$\lambda_{01} \alpha_{01} J_0(\lambda_{01} r) \tanh(\lambda_{01} H_0) = \dot{\alpha}_{01} J_0(\lambda_{01} r). \quad (2.73b)$$

Using the relations between  $\alpha_{11}$ ,  $\beta_{11}$ ,  $a_{11}$  and  $b_{11}$  given in Appendix D, we rewrite the previous equations as:

$$\begin{aligned} & \dot{\alpha}_{01} J_0(\lambda_{01} r) + g a_{01} J_0(\lambda_{01} r) = \\ & - \frac{1}{4} \left[ \lambda_{11}^2 J_1'^2(\lambda_{11} r) + \frac{1}{r^2} J_1^2(\lambda_{11} r) - \frac{\omega_{11}^4}{g^2} J_1^2(\lambda_{11} r) \right] (\alpha_{11}^2 + \beta_{11}^2) \end{aligned} \quad (2.74a)$$

$$\frac{\omega_{01}^2}{g} \alpha_{01} = \dot{\alpha}_{01}. \quad (2.74b)$$

The right hand terms in Eq. 2.74a are expanded in a Fourier-Bessel series of  $J_0$ , where only the

## Chapter 2. Analytical approach

---

first term is retained, all the others being considerably smaller:

$$\dot{\alpha}_{01} J_0(\lambda_{01} r) + g a_{01} J_0(\lambda_{01} r) = c_{01} J_0(\lambda_{01} r) \quad (2.75a)$$

$$\text{where } c_{01} = \frac{\int_0^{D/2} r F J_0(\lambda_{01} r) dr}{\int_0^{D/2} J_0(\lambda_{01} r) J_0(\lambda_{01} r) dr} \quad (2.75b)$$

$$F = -\frac{1}{4} \left[ \lambda_{11}^2 J_1'^2(\lambda_{11} r) + \frac{1}{r^2} J_1^2(\lambda_{11} r) - \frac{\omega_{11}^4}{g^2} J_1^2(\lambda_{11} r) \right] (\alpha_{11}^2 + \beta_{11}^2) \quad (2.75c)$$

$$\frac{\omega_{01}^2}{g} \alpha_{01} = \dot{a}_{01} \quad (2.75d)$$

the  $c_{01}$  coefficient is determined by applying the definition of the Dini series (Annexe B.1):

$$c_{01} = -\frac{(\alpha_{11}^2 + \beta_{11}^2)}{2D^2} \int_0^{D/2} r \left[ \lambda_{11}^2 J_1'^2(\lambda_{11} r) + \frac{1}{r^2} J_1^2(\lambda_{11} r) - \frac{\omega_{11}^4}{g^2} J_1^2(\lambda_{11} r) \right] dr. \quad (2.76)$$

All the terms are expressed in dimensionless form ( $\tilde{r} = r/D$ ) in order to obtain a scale independent numerical evaluation of the integrals of the Bessel's functions.

$$\begin{aligned} c_{01} = & -\frac{(\alpha_{11}^2 + \beta_{11}^2)}{2D^2} \left[ 4\varepsilon_{11}^2 \int_0^{1/2} \tilde{r} J_1'^2(2\varepsilon_{11} \tilde{r}) d\tilde{r} \right. \\ & \left. + \int_0^{1/2} \frac{1}{\tilde{r}} J_1^2(2\varepsilon_{11} \tilde{r}) d\tilde{r} - \frac{\omega_{11}^4 D^2}{g^2} \int_0^{1/2} \tilde{r} J_1^2(2\varepsilon_{11} \tilde{r}) d\tilde{r} \right] \end{aligned} \quad (2.77)$$

After numerical evaluation of the integrals to the 15<sup>th</sup> decimal, we have

$$c_{01} = -\frac{(\alpha_{11}^2 + \beta_{11}^2)}{2D^2} \left[ 0.404580526766959 - 0.029836701676641 \cdot \frac{\omega_{11}^4 D^2}{g^2} \right] \quad (2.78)$$

thus the following solutions are found:

$$\alpha_{01} = 0, \quad (2.79a)$$

$$a_{01} = \frac{c_{01}}{g} = -\frac{d_s^2 \Omega^6 c_1^2}{8gD^2(\omega_{11}^2 \Omega^2)^2} \left[ 0.41 - 0.03 \frac{\omega_{11}^2 D^2}{g^2} \right]. \quad (2.79b)$$



The equations for the order of  $\cos 2\theta$  in Eqs. 2.67 and 2.69 are:

$$\begin{aligned} & \frac{1}{4} \left[ \lambda_{11}^2 J_1'^2(\lambda_{11} r) - \frac{1}{r^2} J_1^2(\lambda_{11} r) + \lambda_{11}^2 J_1^2(\lambda_{11} r) \tanh^2(\lambda_{11} H_0) \right] (\alpha_{11}^2 - \beta_{11}^2) \cos 2\theta \\ & + \dot{a}_{21} \cos 2\theta J_2(\lambda_{21} r) + g a_{21} \cos 2\theta J_2(\lambda_{21} r) \\ & + \frac{\lambda_{11}}{2} (\dot{\alpha}_{11} a_{11} - \dot{\beta}_{11} b_{11}) \cos 2\theta J_1^2(\lambda_{11} r) \tanh(\lambda_{11} H_0) = 0 \end{aligned} \quad (2.80)$$

$$\begin{aligned} & \lambda_{21} \alpha_{21} \cos 2\theta J_2(\lambda_{21} r) \tanh(\lambda_{21} H_0) - \dot{a}_{21} \cos 2\theta J_2(\lambda_{21} r) \\ & - \frac{\lambda_{11}^2 J_1'^2(\lambda_{11} r)}{2} (\alpha_{11} a_{11} - \beta_{11} b_{11}) \cos 2\theta + \frac{J_1^2(\lambda_{11} r)}{2r^2} (\alpha_{11} a_{11} - \beta_{11} b_{11}) \cos 2\theta \\ & + \frac{\lambda_{11}^2 J_1^2(\lambda_{11} r)}{2} (\alpha_{11} a_{11} - \beta_{11} b_{11}) \cos 2\theta = 0. \end{aligned} \quad (2.81)$$

This equation is rewritten taking into account the relations between the time dependent coefficients of the dominant mode (1, 1) (Appendix D):

$$\begin{aligned} & \dot{a}_{21} J_2(\lambda_{21} r) + g a_{21} J_2(\lambda_{21} r) = \\ & - \frac{1}{4} \left[ \lambda_{11}^2 J_1'^2(\lambda_{11} r) - \frac{1}{r^2} J_1^2(\lambda_{11} r) + 3 \frac{\omega_{11}^4}{g^2} J_1^2(\lambda_{11} r) \right] (\alpha_{11}^2 - \beta_{11}^2) \end{aligned} \quad (2.82)$$

$$\begin{aligned} & \frac{\omega_{21}^2}{g} \alpha_{21} J_2(\lambda_{21} r) - \dot{a}_{21} J_2(\lambda_{21} r) = \\ & \frac{1}{2} \left[ \lambda_{11}^2 J_1'^2(\lambda_{11} r) - \frac{J_1^2(\lambda_{11} r)}{r^2} - \lambda_{11}^2 J_1^2(\lambda_{11} r) \right] (\alpha_{11} a_{11} - \beta_{11} b_{11}). \end{aligned} \quad (2.83)$$

The left hand side term of both equations is expressed in Fourier-Bessel series of  $J_2$  and, again, only the first term of the series is retained:

$$\dot{a}_{21} J_2(\lambda_{21} r) + g a_{21} J_2(\lambda_{21} r) = c_{21} J_2(\lambda_{21} r) \quad (2.84)$$

$$\frac{\omega_{21}^2}{g} \alpha_{21} J_2(\lambda_{21} r) - \dot{a}_{21} J_2(\lambda_{21} r) = d_{21} J_2(\lambda_{21} r) \quad (2.85)$$

and the coefficients are determined according to the definition given in Appendix B.1 and with

## Chapter 2. Analytical approach

---

the usual normalization of the radius  $\tilde{r} = r/D$ :

$$c_{21} = -\frac{2\varepsilon_{21}^2(\alpha_{11}^2 - \beta_{11}^2)}{D^2(\varepsilon_{21}^2 - 4)J_2^2(\varepsilon_{21})} \cdot \left[ 4\varepsilon_{11}^2 \int_0^{1/2} \tilde{r} J_2(2\varepsilon_{21}\tilde{r}) J_1'^2(2\varepsilon_{11}\tilde{r}) d\tilde{r} \right. \\ \left. - \int_0^{1/2} J_2(2\varepsilon_{21}\tilde{r}) \frac{J_1^2(2\varepsilon_{11}\tilde{r})}{\tilde{r}} d\tilde{r} + 3 \frac{\omega_{11}^4 D^2}{g^2} \int_0^{1/2} \tilde{r} J_2(2\varepsilon_{21}\tilde{r}) J_1^2(2\varepsilon_{11}\tilde{r}) d\tilde{r} \right] \quad (2.86)$$

$$d_{21} = \frac{4\varepsilon_{21}^2(\alpha_{11}a_{11} - \beta_{11}b_{11})}{D^2(\varepsilon_{21}^2 - 4)J_2^2(\varepsilon_{21})} \cdot \left[ 4\varepsilon_{11}^2 \int_0^{1/2} \tilde{r} J_2(2\varepsilon_{21}\tilde{r}) J_1'^2(2\varepsilon_{11}\tilde{r}) d\tilde{r} \right. \\ \left. - \int_0^{1/2} J_2(2\varepsilon_{21}\tilde{r}) \frac{J_1^2(2\varepsilon_{11}\tilde{r})}{\tilde{r}} d\tilde{r} - 4\varepsilon_{11}^2 \int_0^{1/2} \tilde{r} J_2(2\varepsilon_{21}\tilde{r}) J_1^2(2\varepsilon_{11}\tilde{r}) d\tilde{r} \right]. \quad (2.87)$$

The numerical solution is:

$$c_{21} = \frac{(\alpha_{11}^2 - \beta_{11}^2)}{D^2} \cdot \left[ 0.894001759862218 - 0.526203772391958 \frac{\omega_{11}^4 D^2}{g^2} \right] \quad (2.88)$$

$$d_{21} = -6.544826289756327 \frac{(\alpha_{11}a_{11} - \beta_{11}b_{11})}{D^2}. \quad (2.89)$$

Consequently, the differential equations become (keeping only the first two decimals of the numerical component, to shorten the notation):

$$\dot{\alpha}_{21} + g a_{21} = \frac{(\alpha_{11}^2 - \beta_{11}^2)}{D^2} \left[ 0.89 - 0.53 \frac{\omega_{11}^4 D^2}{g^2} \right] \quad (2.90)$$

$$\frac{\omega_{21}^2}{g} \alpha_{21} + 6.55 \frac{(\alpha_{11}a_{11} - \beta_{11}b_{11})}{D^2} = \dot{a}_{21} \quad (2.91)$$

Time differentiating once the first equation, and inserting the second one in the first we obtain:

$$\ddot{\alpha}_{21} + \omega_{21}^2 \alpha_{21} = -\frac{(\alpha_{11}a_{11} - \beta_{11}b_{11})}{D^2} \left[ 6.55g + 1.79 \frac{g\Omega^2}{\omega_{11}^2} - 1.05 \frac{\omega_{11}^2 \Omega^2 D^2}{g} \right] \quad (2.92)$$

thus the solutions are:

$$\alpha_{21} = \frac{d_s^2 \Omega^5 c_1^2 \omega_{11}^2}{(\omega_{11}^2 - \Omega^2)^2 D^2 (\omega_{21}^2 - 4\Omega^2)} \left[ 1.64 + 0.45 \frac{\Omega^2}{\omega_{11}^2} - 0.26 \frac{\omega_{11}^2 \Omega^2 D^2}{g^2} \right] \sin 2\Omega t \quad (2.93)$$

and

$$\begin{aligned} \dot{a}_{21} &= \frac{d_s^2 \Omega^5 c_1^2 \omega_{11}^2 \omega_{21}^2 \sin 2\Omega t}{g D^2 (\omega_{11}^2 - \Omega^2)^2 (\omega_{21}^2 - 4\Omega^2)} \left[ 1.64 + 0.45 \frac{\Omega^2}{\omega_{11}^2} - 0.26 \frac{\omega_{11}^2 \Omega^2 D^2}{g^2} - 1.64 \frac{(\omega_{21}^2 - 4\Omega^2)}{\omega_{21}^2} \right] \\ a_{21} &= \frac{-d_s^2 \Omega^4 c_1^2 \omega_{11}^2 \omega_{21}^2 \cos 2\Omega t}{2g D^2 (\omega_{11}^2 - \Omega^2)^2 (\omega_{21}^2 - 4\Omega^2)} \\ &\quad \cdot \left[ 1.64 + 0.45 \frac{\Omega^2}{\omega_{11}^2} - 0.26 \frac{\omega_{11}^2 \Omega^2 D^2}{g^2} - 1.64 \frac{(\omega_{21}^2 - 4\Omega^2)}{\omega_{21}^2} \right] \end{aligned} \quad (2.94)$$

where the numerical values to the 15<sup>th</sup> digit are in order of appearance: 1.636206572439082, 0.447000879931109, -0.263101886195979 and -1.636206572439082.

The order of  $\sin 2\theta$  are:

$$\begin{aligned} \dot{\beta}_{21} \sin 2\theta J_2(\lambda_{21} r) + g b_{12} J_2(\lambda_{21} r) = \\ -\frac{1}{2} \left[ \lambda_{11}^2 J_1'^2(\lambda_{11} r) - \frac{1}{r^2} J_1^2(\lambda_{11} r) + 3 \frac{\omega_{11}^4}{g^2} J_1^2(\lambda_{11} r) \right] \alpha_{11} \beta_{11} \end{aligned} \quad (2.95)$$

$$\begin{aligned} \frac{\omega_{21}^2}{g} \beta_{21} J_2(\lambda_{21} r) - \dot{b}_{21} J_2(\lambda_{21} r) = \\ \left[ \frac{\lambda_{11}^2 J_1'^2(\lambda_{11} r)}{2} - \frac{J_1^2(\lambda_{11} r)}{2r^2} - \frac{\lambda_{11}^2 J_1^2(\lambda_{11} r)}{2} \right] (\alpha_{11} b_{11} + \beta_{11} a_{11}). \end{aligned} \quad (2.96)$$

The expansion is done equivalently to the one for the term in  $\cos 2\theta$  and the coefficients of the Fourier-Bessel series are:

$$\dot{\beta}_{21} J_2(\lambda_{21} r) + g b_{21} J_2(\lambda_{21} r) = e_{21} J_2(\lambda_{21} r) \quad (2.97)$$

$$\frac{\omega_{21}^2}{g} \beta_{21} J_2(\lambda_{21} r) - \dot{b}_{21} J_2(\lambda_{21} r) = f_{21} J_2(\lambda_{21} r) \quad (2.98)$$

$$e_{21} = \frac{\alpha_{11} \beta_{11}}{D^2} \cdot \left[ 1.788003519724436 - 1.052407544783917 \frac{\omega_{11}^4 D^2}{g^2} \right] \quad (2.99)$$

$$f_{21} = -6.544826289756327 \frac{(\alpha_{11} b_{11} + \beta_{11} a_{11})}{D^2}. \quad (2.100)$$

## Chapter 2. Analytical approach

The found solutions are as follows:

$$\beta_{21} = -\frac{d_s^2 \Omega^5 c_1^2 \omega_{11}^2}{(\omega_{11}^2 - \Omega^2)^2 D^2 (\omega_{21}^2 - 4\Omega^2)} \left[ 1.64 + 0.45 \frac{\Omega^2}{\omega_{11}^2} - 0.26 \frac{\omega_{11}^2 \Omega^2 D^2}{g^2} \right] \cos 2\Omega t \quad (2.101)$$

$$b_{21} = \frac{d_s^2 \Omega^4 c_1^2 \omega_{11}^2 \omega_{21}^2 \sin 2\Omega t}{2g D^2 (\omega_{11}^2 - \Omega^2)^2 (\omega_{21}^2 - 4\Omega^2)} \cdot \left[ 1.64 + 0.45 \frac{\Omega^2}{\omega_{11}^2} - 0.26 \frac{\omega_{11}^2 \Omega^2 D^2}{g^2} - 1.64 \frac{(\omega_{21}^2 - 4\Omega^2)}{\omega_{21}^2} \right]. \quad (2.102)$$

Summarizing the previous results, the order (order  $O(a_{11}^2)$ ) free surface solution, of the weakly non-linear expansion of the free surface boundary condition is given by:

$$\xi(r, \theta, t) = A_{11} \cos(\Omega t - \theta) J_1(\lambda_{11} r) + A_{01} J_0(\lambda_{01} r) + A_{21} \cos(2(\Omega t - \theta)) J_2(\lambda_{21} r) \quad (2.103)$$

where the amplitudes are calculated as:

$$A_{11} = \frac{d_s D \Omega^2 \omega_{11}^2}{2g(\omega_{11}^2 - \Omega^2)(\varepsilon_{11}^2 - 1)J(\varepsilon_{11})} \quad (2.104a)$$

$$A_{01} = -\frac{d_s^2 \Omega^6}{8g(\omega_{11}^2 \Omega^2)^2 (\varepsilon_{11}^2 - 1)J(\varepsilon_{11})^2} \left[ n_{01,1} - n_{01,2} \frac{\omega_{11}^2 D^2}{g^2} \right] \quad (2.104b)$$

$$A_{21} = -\frac{d_s^2 \Omega^4 \omega_{11}^2 \omega_{21}^2}{2g(\omega_{11}^2 - \Omega^2)^2 (\omega_{21}^2 - 4\Omega^2)(\varepsilon_{11}^2 - 1)J(\varepsilon_{11})^2} \cdot \left[ n_{21,1} + n_{21,2} \frac{\Omega^2}{\omega_{11}^2} - n_{21,3} \frac{\omega_{11}^2 \Omega^2 D^2}{g^2} - n_{21,1} \frac{(\omega_{21}^2 - 4\Omega^2)}{\omega_{21}^2} \right]. \quad (2.104c)$$

and the numerical values  $n$  have the following value:

$$\begin{aligned} n_{01,1} &= 0.404580526766959 \\ n_{01,2} &= 0.029836701676641 \\ n_{21,1} &= 1.636206572439082 \\ n_{21,2} &= 0.447000879931109 \\ n_{21,3} &= 0.263101886195979 \end{aligned} \quad (2.105)$$

We observe that, since the linear solution presented in Eq.2.54 is a series on all  $m=1$ ,  $n = 1, 2, \dots, \infty$ , the expansion of the radius  $r$  is equivalent to  $r$ . On the other hand, Eq. 2.103 is not a series on all  $n$ , thus the radius is replaced by the first term of its expansion in a Fourier-Bessel series:  $c_1 = D/(\varepsilon^2 - 1)$ .

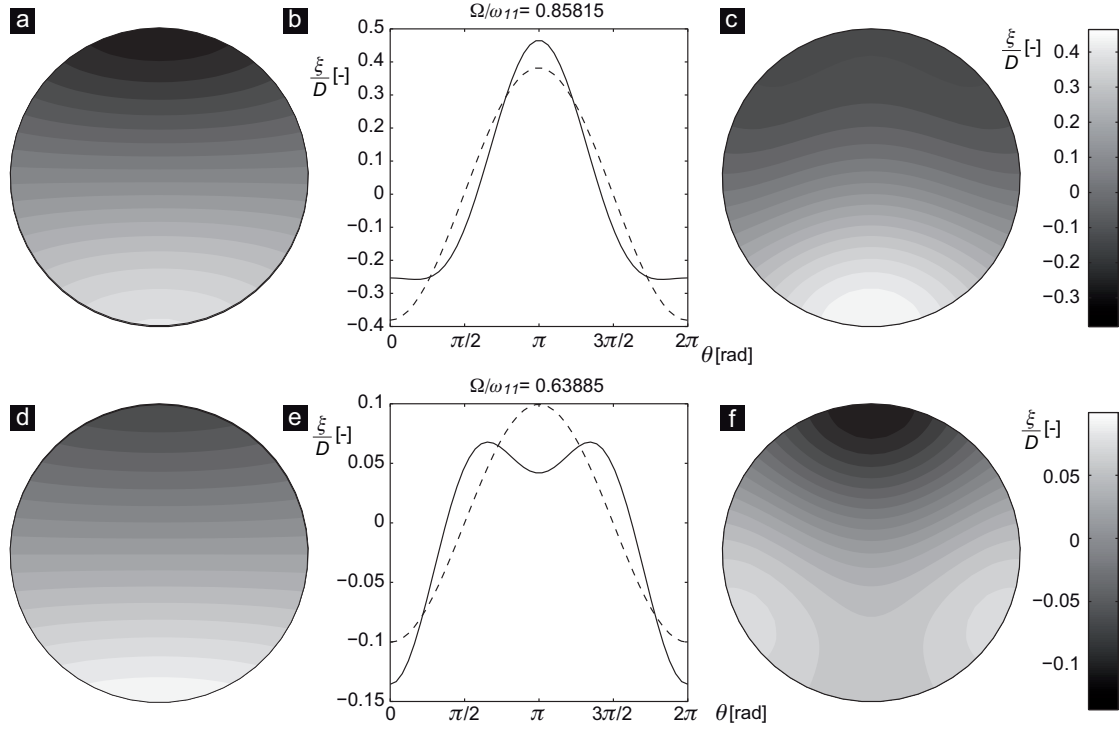


**Figure 2.10** | Examples of elevation of the free surface according to the linear (a and d) and non-linear solution (c and f) at  $\Omega/\omega_{11} = 0.85815$  (for a, b, and c) and  $\Omega/\omega_{11} = 0.63885$  (for figures d, e, and f). Figures b and e depict the amplitude at the wall of the container, where the dashed line is the linear solution, according to Eq. 2.54, while the solid line is the weakly non-linear solution according to Eq. 2.103.

Figure 2.10 compares the free surface height obtained according to the linear and the non-linear solution, in situations where a difference between the two is expected. We notice that, close to the first natural frequency  $\omega_{11}$  (Fig. 2.10a-c), the second order terms of Eq. 2.103 increase the slope of the wave, in a behaviour similar to the one observed in breaking gravitational waves, where the non-linear terms increase the slope until the wave breaks. Furthermore, in the time coefficients of the second order,  $a_{21}$  and  $b_{21}$ , we observe a resonance behaviour of this mode to the sub-harmonic of the natural frequency  $\omega_{21}$ : as the shaking frequency  $\Omega$  approaches  $\omega_{21}/2$  the amplitude increases. This situation is depicted in Fig. 2.10d-f, where we clearly observe the appearance of a dominant term in  $\cos(2(\Omega t - \theta))$ , which is not predicted by the linear solution.

## 2.4 Considerations

The potential approach has already proved its validity by correctly predicting several phenomena, both in waves and sloshing dynamics. It is however based on a very strong hypothesis: the absence of viscosity in the flow. The model is therefore unable to predict the viscous damping, which will necessarily appear to bound the amplitude of the waves to finite values.

## Chapter 2. Analytical approach

---

The viscosity acts creating boundary layer at all solid walls of the container: regions where the dissipation takes place. Depending on the ratio between the boundary layer thickness and the container size, the influence of the viscous boundary layer becomes non negligible. Our study, not taking into account the viscosity, is therefore implicitly limited to large scale containers. A summary of the influence of the viscosity in sloshing flows may be found in [50], Chapter 3, while a thorough discussion of our observation is given in Sec. 5.1.3.

## 3 Experimental setup

The study of liquid sloshing within an orbital shaken container requires several specifically designed equipments. This chapter describes the tools and methods used to obtain suitable shaking configurations, to measure the elevation of the free surface and the velocity fields, and to estimate the mixing efficiency.

### 3.1 The orbital shaker

To obtain a smooth and steady orbital motion, with minimum shocks and jerks, we made use of a Kuhner Es-X shaker, which is commonly employed in bioengineering for cell cultivations. The rotatory motion of an electrical motor is transmitted to the shaken table (420 x 420mm, 25kg of maximum load) through a ball bearings pivot, whose eccentricity from the motor axis determines the shaking diameter (Fig. 3.1). Partial disassembly of the shaker is necessary to adjust the shaking diameter to one of the three allowed values (12.5, 25 and 50mm). Four metallic elastic strips maintain the table to a fixed orientation during operation. The shaking velocity may be varied between 20 and 500 revolutions per minute (for  $d_s=12.5\text{mm}$ ) with an accuracy of 0.1 rpm.

The original shaker was modified to allow a continuous adjustment of the eccentricity during operation. The pivot was substituted with a linear rail mounted on the rotor, actioned by a stepper motor and controlled by a linear potentiometer. The rotary connection to the shaken table is mounted on the carriage of the linear rail (Fig. 3.2a), and its rotation is ensured by a couple of ball bearings. Since the whole system rotates with the motor, the power supply and the control signals are transmitted through a slip ring located in the pivot. Several components of the shaker had to be adapted to the new system, e.g. the strips structure maintaining the table orientation was expanded and elevated (the distance between the motor and the table with the moving pivot system is 90mm, whereas with the original pivot was 48mm).

With this improvement, the shaking diameter could be set at values between 0.1 and 60mm, with a precision of  $\pm 0.05\text{mm}$ , greatly increasing the number of attainable configurations.

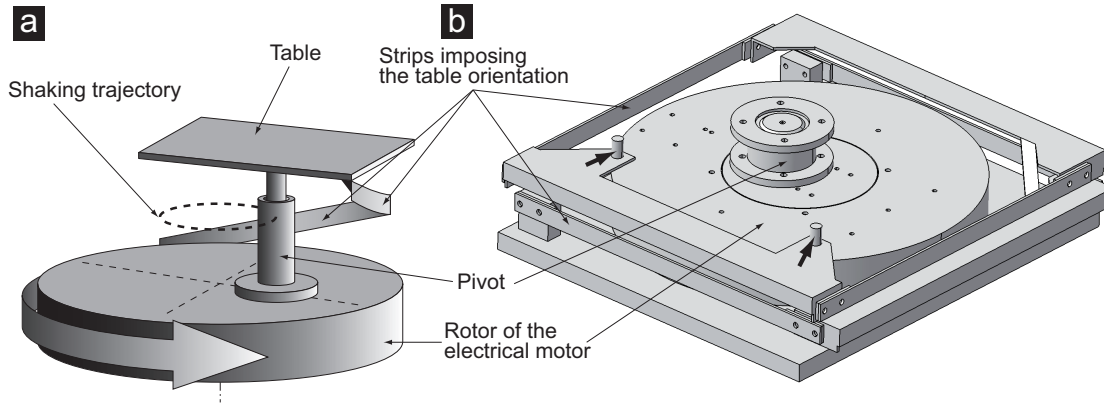


**Figure 3.1 | a:** schematic functioning of the Kuhner ES-X Shaker. **b:** drawing of the shaker, without the shaking table and the protecting coverage. Note that the structure with the blades, maintaining the orientation of of the shaken table, is connected to the latter through the two screw support marked by black arrows.

Although further increase of the range of operation would have been technically feasible, the maximum diameter and speed have been limited (to 60mm and 200rpm respectively) to reduce structural failure risks and parasitic vibrations. During the modification process several electro-mechanical and magnetic switches were added to provide trigger signals for the acquisition of data or images. The shaken table was modified in order to host the equipment used to measure the free surface height and the velocity fields.

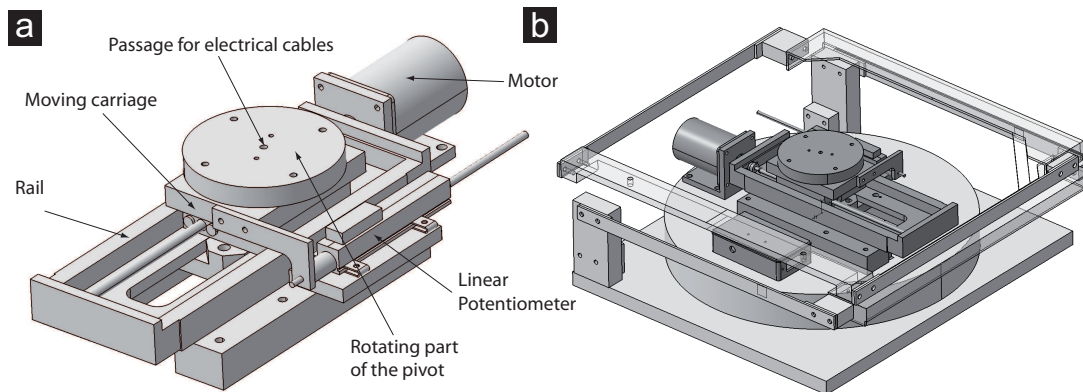


**Figure 3.2 | a:** Drawing of the linear rail with its different components. The slip ring is inside the pivot, hence not visible. **b:** Positioning of the shaking diameter control system (dark gray) in the shaker. Note also the differences between the current strips structures and the one in Fig. 3.1b.



## 3.2 Free surface visualization and measurement

The most visible effect of the orbital shaking on a liquid is the deformation of its free surface, creating a wave-like motion. Moreover, according to the potential model, a free surface shape uniquely defines a velocity field in the liquid. It is thus necessary to achieve a measurement of the free surface motion. Several existing optical methods use the diffraction of light to reconstruct the free surface of a transparent medium [53, 120, 118]. Their application to the case of orbital shaker (described in Appendix A) is nevertheless hampered by the presence of bubbles and very short but steep surface wavelets, which increase the number of reflections and diffractions of the light behind any reconstruction possibility [62]. The measurement of the free surface elevation is therefore performed only at the container wall, where higher precision could be achieved.

### 3.2.1 Wall liquid elevation measurement

The motion of the free surface is filmed with a high speed camera (Photron SA 1.1), while the contrast of the liquid is increased by the addition of a small amount of white dye. The external wall of the container is enveloped in a cover leaving only a vertical slit while the liquid is illuminated at the wall by a narrow beam spotlight. From each frame a column of pixels, optically centred on the vertical slit, is extracted. Setting side by side those columns of pixels leads to a reconstruction of the motion of the free surface at a single location of the container wall (Fig. 3.3). The columns width (in pixels) is adapted as a function both of the shaking frequency and of the number of frames per seconds in order to obtain images with a constant number of pixels per revolution.

Moreover, by using an appropriate processing of the images, it is possible to measure the elevation of the free surface. Light intensity and contrast are analysed in order to identify the

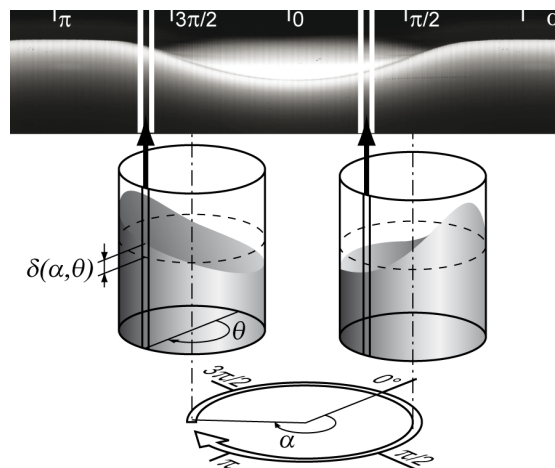


**Figure 3.3** | Procedure used to retrieve a single image from a movie of the wave obtained with a fixed camera. From the images it is also possible to recover the free surface elevation  $\delta(\alpha, \theta)$ .

### Chapter 3. Experimental setup

interface of the liquid at the wall. It has to be noted that in Fig. 3.3 the whole free surface is illuminated (it is thus possible to see the wave on the farthest side of the wall), while the employ of a narrower beam of light illuminating only the front wall results in easier processing of the images. Moreover, the number of frames captured by the camera per second (fps) is adapted to the shaking frequency in order to guarantee a maximum angular distance between two consecutive frames of  $1.5^\circ$  on the shaking trajectory. Since the camera allows only predefined values (in our range of operations: 125, 250, 500 and 1000 fps), the actual angle between two successive measurements varies between  $0.68^\circ$  and  $1.35^\circ$ .

We note that, if the free surface is a rigid shape rotating around the revolution axis of the container at the shaking frequency, the image reconstructed from the frames of the movie is equivalent to an image obtained instantaneously at the whole circumference of the container. We may therefore consider the images obtained with the procedure described above as reconstructed snapshots of the wave. Similarly, the measurement of the free surface elevation is assimilated to the measurement of the entire wave at the wall at a specific moment. Hence measurements taken at the same angular position may be phase averaged: the container circular trajectory is divided into 90 angular sectors, also called bins, of  $4^\circ$  each, and the average is computed of all the measurements in each bin. Obviously this procedure given deceitful results if the wave is changing in shape while rotating.

Because of the motion of the shaker, the distance and angle of viewing are constantly changing

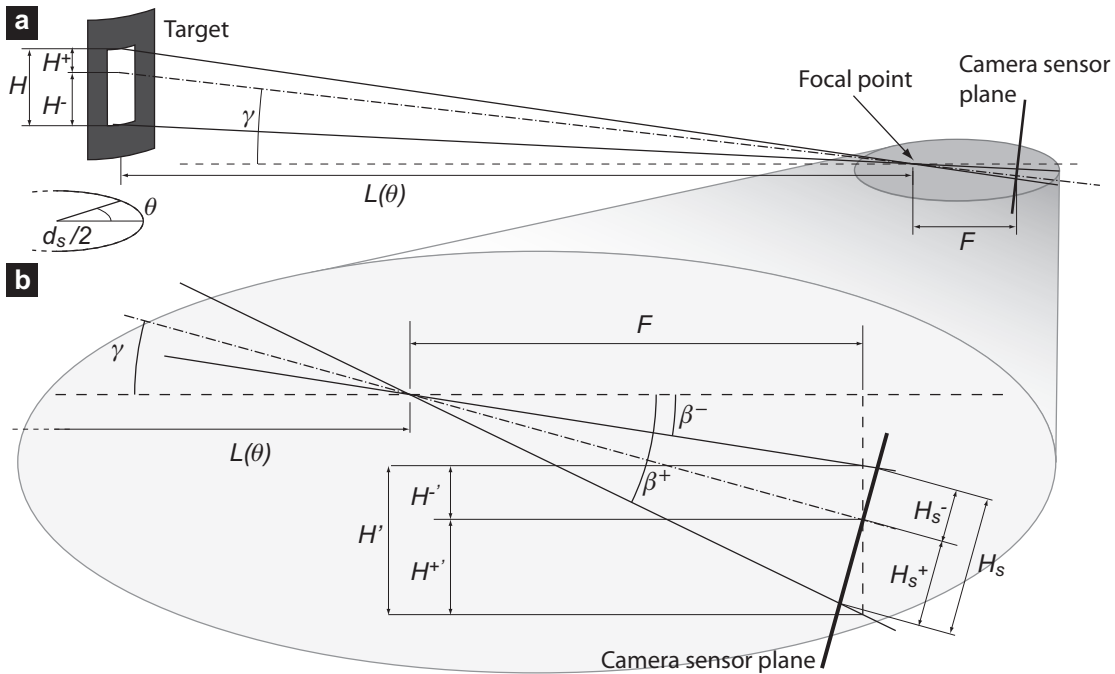


**Figure 3.4** | Relations between the height of a target  $H$  and the dimension of its projection on the camera sensor  $H_s$  when the direction of observation of the camera has an angle of  $\gamma$  with the direction perpendicular to the target.

during operation both in vertical and horizontal direction. Figure 3.4 depicts the configuration of an object and its reproduction on the sensor of the camera. Neglecting the non-linear deformations that could be introduced by the objective, it is possible to geometrically relate the dimension of the target to the dimension of its image on the sensor plane as:

$$H_s = \frac{F}{\cos \gamma} \left[ \tan \left( \gamma - \arctan \left( \sin \gamma - \frac{H^-}{L(\theta)} \right) \right) + \tan \left( \arctan \left( \sin \gamma + \frac{H^+}{L(\theta)} \right) - \gamma \right) \right] \quad (3.1)$$

if the target is located at a distance  $L(\theta)$  from the focal point of the optics, is not centred on the direction of observation ( $H^+$  is not necessary equivalent to  $H^-$ ) and the sensor plane is located at a distance  $F$  from the focal point (note that  $F$  is not the focal distance of the objective), as shown in Fig. 3.4. For vanishing angles of visualization  $\gamma$ , we have:

$$H_s \approx \frac{F(H^- + H^+)}{L} = \frac{F H}{L}. \quad (3.2)$$

In a typical setup we have a distance  $L$  of 1m, a target of 150mm (camera centred on the target:  $H^+ = H^- = 75$ mm), a vertical displacement of the camera compared to the centre of the target of 100mm (thus giving  $\gamma \cong 0.1511$  radians) and a length  $F$  of 60mm. In this case, by using Eq. 3.1 we obtain  $H_s \cong 8.9561$ mm, while approximating for  $\gamma=0$  we obtain  $H' = 9$ mm. Thus the error introduced assuming  $\gamma=0$  is less than 0.5%.

The distance  $L$  is related to the experimental setup according to  $L = L_0 - d_s \cdot \cos(\theta(t))$ , where  $L_0$  is the distance from the focal point to the axis of the motor of the orbital shaker. The relation between the elevation measured in pixels on the image  $H_s^p$  and the physical dimension  $H$  is:

$$H = H_s^p \cdot p_p \cdot \frac{L_0 - d_s \cos(\theta)}{F} \quad (3.3)$$

where  $p_p$  is the pixel pitch. Since the exact values of  $L_0$  and  $F$  are difficult to measure with sufficient precision, they are determined by calibration on a target (rectangle of known  $H$ ), followed during one revolution at two different shaking diameters  $d_s$ , and fitting Eq. 3.3 (in least mean squares sense) to retrieve the values of  $F$  and  $L_0$ . The results are used to convert all measurements as long as the position of the camera with respect to the shaker is unchanged. On the other hand, a new calibration is performed before each new set of measurements. As a way of example, the resolution obtained during the measurement of a 287mm container is 3 to 4 pixels per millimetre.

### 3.2.2 Automated measurements

To allow autonomous measurements of a large amount of shaking configurations in an efficient way, we have developed a fully automated procedure in Matlab environment, controlling the agitation rate  $\Omega$  through a CAN-BUS network, the high speed camera through Gigabit Ethernet connection and the shaking diameter  $d_s$  through USB connection as depicted in Fig. 3.5a.

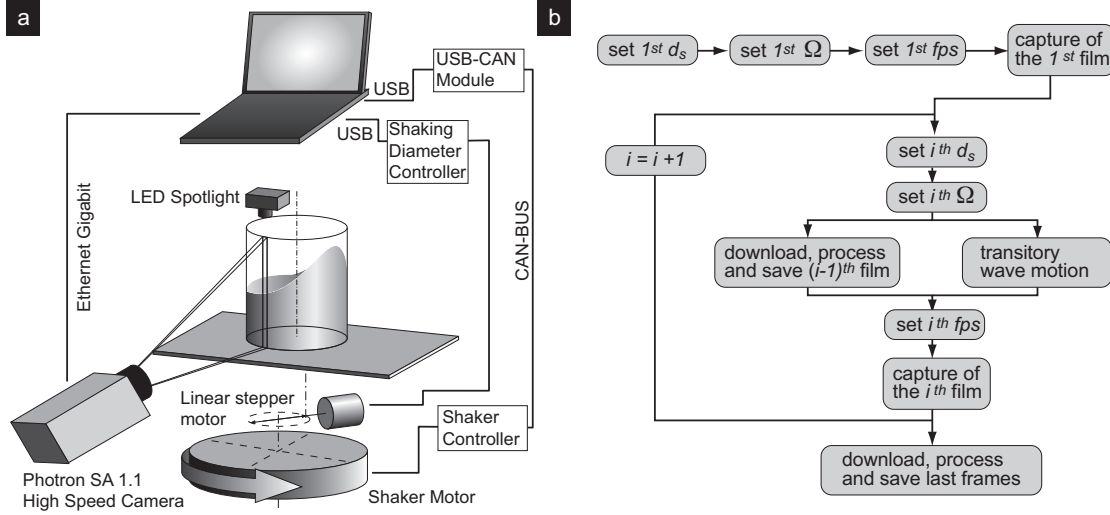


**Figure 3.5 | a:** communication principle of the control of the rotation speed, the shaking diameter and the high speed camera. **b:** Schematic flow chart of the measurement routine.

When an operating parameter is changed, the motion of the wave experiences a transitory behaviour until the new steady motion is established. The transient usually vanishes after 60 to 90 seconds, depending on the start and target conditions. The routine controlling the acquisition uses this transitory time to download and process the images of the previous operating parameters, giving the procedure depicted in Fig. 3.5b. Initially, the first operating parameters ( $d_s$ ,  $\Omega$ ) and the appropriate number of frames per seconds (fps) of the camera are set, then the movie is acquired. After the second set of operating parameters is set, the frames of the first movie are downloaded and processed, while the flow goes through the transitory motion. The image and the measurement of the free surface displacement  $\delta(\theta, t)$  obtained from the processing of the frame are saved. This operation necessitates typically between 90 and 150 seconds, allowing the motion to reach the steady state. Since most of the phenomena observed have a period equivalent to the shaking period, the measurements are phase averaged. Every wave was typically recorded during 3 to 4 revolutions, thus each bin of the phase average contains between 10 and 20 measurements.

### 3.2.3 Free surface measurements operating conditions

Thanks to the automated procedure, the free surface has been measured on a total of 6'612 shaking configurations, which is equivalent (considering a realistic average time of two minutes for measurement) to nearly 9 days and 4 hours of round-the-clock operation. Besides the container diameter  $D$ , the filling level  $H_0$ , the shaking diameter  $d_s$  and the shaking frequency  $\Omega$ , we have also varied the viscosity of the liquid, using different glycerol dilutions. The tested configurations are depicted in Fig. 3.6, with a separate graph for every value of viscosity, vessel diameter and liquid height at rest. Each dot represents a set of operating parameters. The viscosity is given as a ratio to the water viscosity  $\mu_w$ . The ranges of the tested configurations are given in Table 3.1.

$\mu/\mu_w$	$D$ [mm]	$H_0$ [mm]	$d_s$ [mm]	$\Omega$ [rpm]	Measurements
1	74	37	2.96 - 44.4	22 - 200	504
1	144	45	5.76 - 57.6	22 - 200	465
1	144	60	5.76 - 57.6	20 - 200	873
1	144	75	2.88 - 57.6	20 - 200	1818
1	144	100	2.88 - 57.6	20 - 200	582
1	287	150	2.87 - 57.4	20 - 200	1586
1	750	355	50	30 - 59	6
2.5	144	75	2.88 - 43.2	21 - 200	293
6	144	75	2.88 - 57.6	20 - 200	485

**Table 3.1** | Range of operating conditions whose free surface displacement  $\delta(\theta, t)$  has been measured. The viscosity of the liquid is given as a ratio to the viscosity of the water  $\mu_w$ . The measurements with  $D=750\text{mm}$  have been performed with a Kuhner SB200-X(OrbShake) with fixed  $d_s$ .

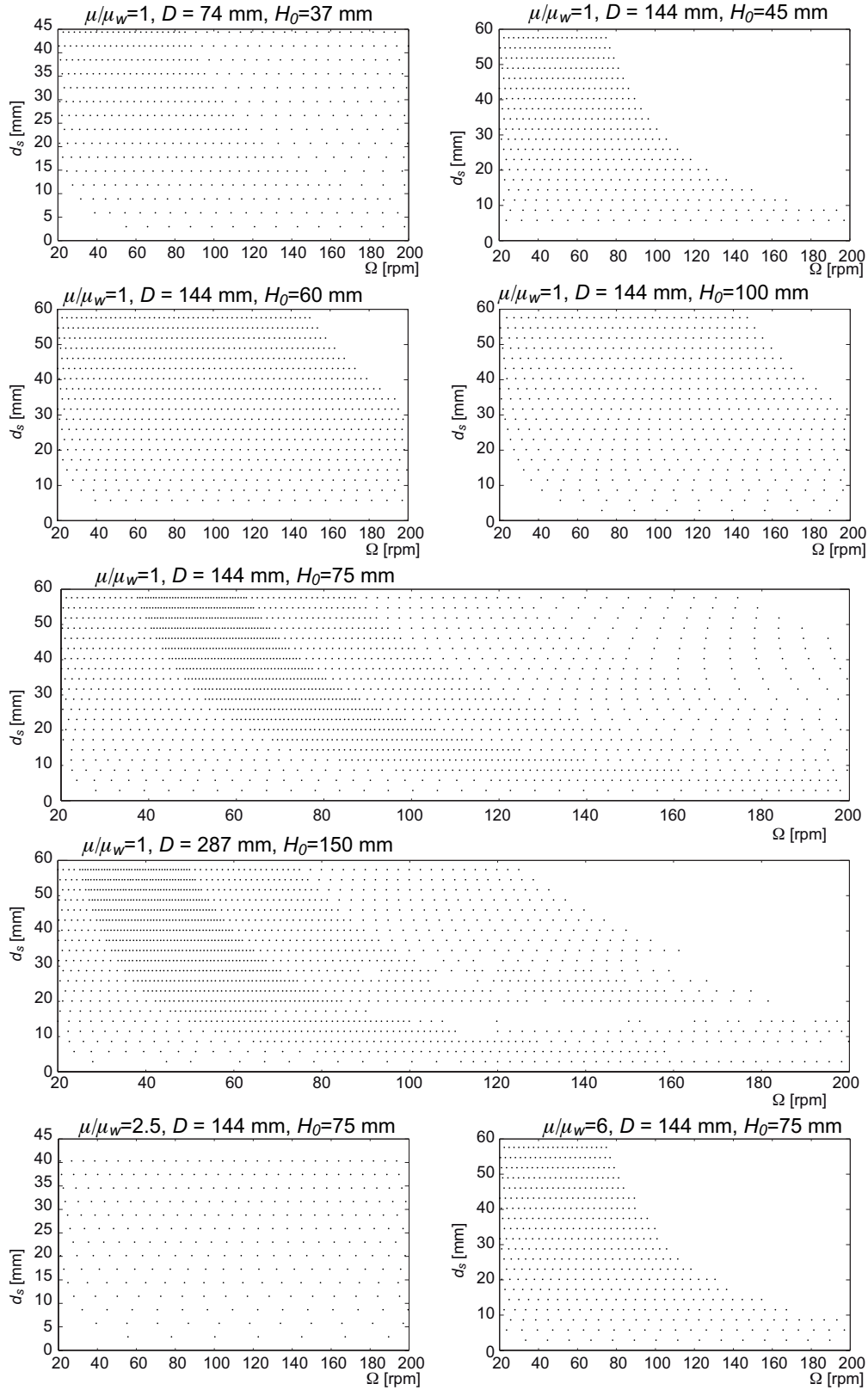


**Figure 3.6** | List of shaking configurations whose wave displacement at the wall  $\delta(\theta, t)$  has been measured. The viscosity of the liquid is given as a ratio to the viscosity of the water  $\mu_w$ .

### 3.2.4 Instantaneous visualization of the free surface height at the entire wall

The method previously presented provides high reliability measurements and images in case of free surface shapes that are stationary in a frame of reference rotating at the shaking frequency  $\Omega$ . In fact, most of the observed waves do respect this hypothesis. We have nevertheless identified cases of waves continuously changing in shape as they rotate. A different setup, allowing the simultaneous visualization of the entire wall is thus required. As depicted in Fig. 3.7, four mirrors are placed around the container, reflecting the image of the free surface shape to a camera placed on top.

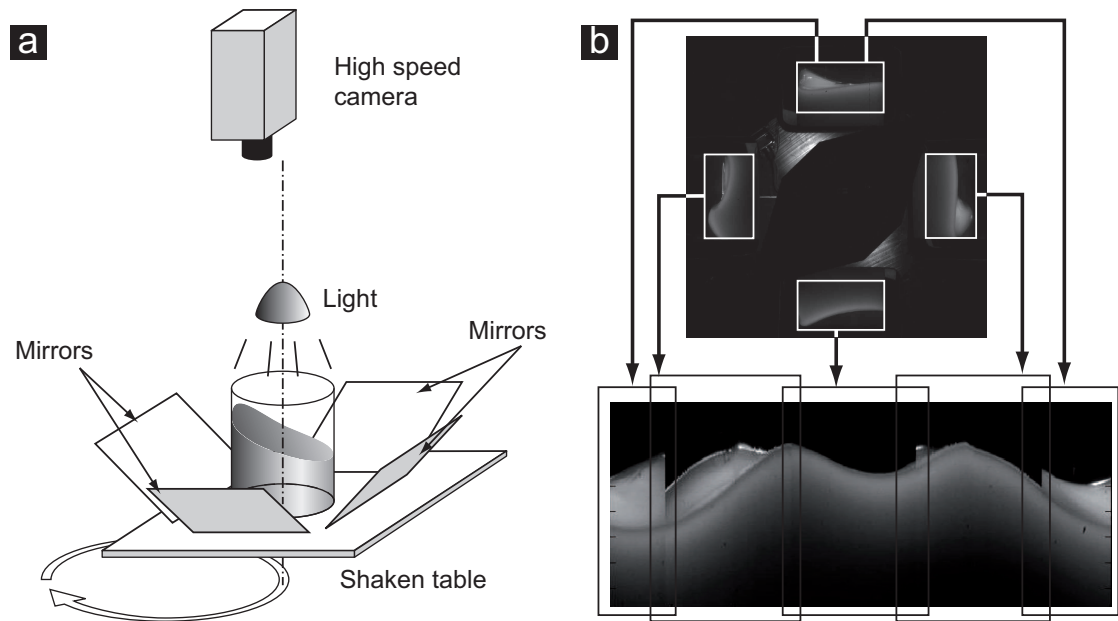


**Figure 3.7 | a:** positioning of the camera and mirrors for the capture of images of waves whose shape is changing while rotating. **b:** example of reconstruction of the wave from the image captured by the camera above the vessel.

The images reflected by the mirrors are extracted from the camera image, de-warped (to account for the circular shape of the container), rotated and assembled to create a single unfolded view of the wave (Fig. 3.7b). The use of four mirrors guarantees the overlapping of some observations regions, thus simplifying the reconstruction of a single image from the four mirror reflections.

Due to limitations of the images resolution and to the deformations introduced by the use of mirrors, high precision measurements could not be achieved. Furthermore, the use of illumination on the whole surface increases the difficulty of correct capture of the interface at the wall. Hence, this method is used only to visualize the waves, without measuring their elevation.

### 3.3 Velocity fields measurements

The velocity field of the liquid within the vessel was measured using both Laser Doppler Velocimetry (LDV) and Particle Image Velocimetry (PIV). Those methods were chosen for their precision, non-intrusivity and flexibility. Both measurement techniques are described in the following sections.

#### 3.3.1 Laser Doppler Velocimetry

The LDV is based on the analysis of the light scattered by seeding particles, which are supposed to follow the motion of the fluid without perturbing it [7]. The crossing of two converging polarized laser beams creates a region (called measurement volume) where a series of superposed high and low light intensity planes (fringes) appears. Knowing the distance between the fringes, which is imposed by the laser wavelength, the velocity of a particle crossing the measurement volume is measured by the analysis of the intensity of the scattered light (Fig. 3.8a). The velocity component in the direction perpendicular to the fringes is thus measured. The use of couples of laser beams with different wavelengths converging from different planes at the same location allows the simultaneous measurement of more than one velocity component.

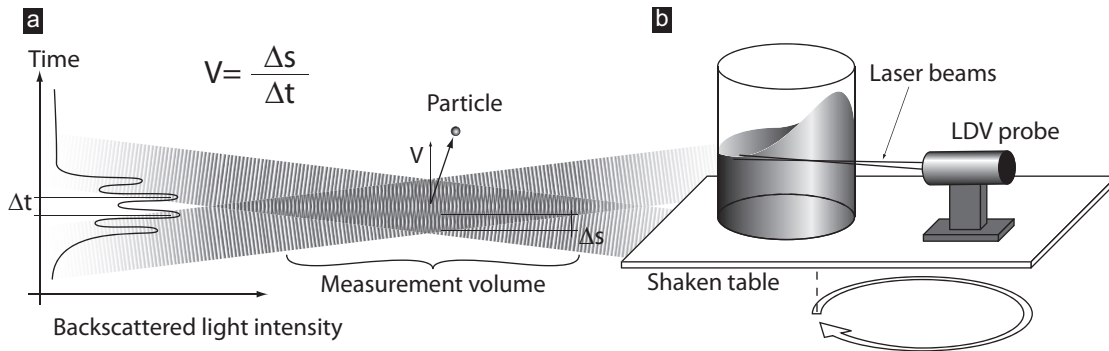


**Figure 3.8 | a:** principle of measurement of the LDV: at the crossing of the two laser beams the measurement volume, with fringes of high and low light intensity, is created. The analysis of the light scattered by the particles crossing this region allows retrieving the velocity of the particle perpendicular to the fringes. **b:** schematic illustration of the positioning of the LDV probe on the shaken table.

A two components Dantec LDV probe was used, with a 250mm focal length lens, giving a control volume of nearly  $1.3 \times 0.07 \times 0.07$ mm in water. We used  $10 \mu\text{m}$  hollow glass spheres, with a density of  $1100\text{kg/m}^3$ , as seeding particles. The probe was mounted on the shaking table, and moved with the vessel (Fig. 3.8b). The radial component was measured from the bottom of the container, using a mirror to redirect the laser beams, while the axial and tangential component were measured with the probe fixed laterally, as depicted in Fig. 3.8b. The measurement location was determined by adjusting the position of the probe with respect to the container. The four laser beams (two for each component) are disposed on two perpendicular planes, in order to measure perpendicular components of the velocity. However, crossing



the container curved walls, each couple of laser beams is diffracted with different angles, thus converging at different locations. Simultaneous measurements of two components are therefore impossible. Only one couple of beams was used, taking into account the diffraction, to measure independently each component of the velocity at a single location.

The sampling provided by LDV measurements is irregular, and depends on the number of particles crossing the measurement volume. For this reason the measurements were phase averaged. The typical angular sector width is  $4^\circ$ , giving averaged measurements on 90 phases of the trajectory. This average is representative of the velocity field only if the latter is stationary in a reference frame rotating at the shaking frequency (see more details in Sec. 4.1.1).

#### 3.3.2 Particle Image Velocimetry

PIV is another optical, non intrusive measurement technique that allows instantaneous reconstruction of the velocity field in a planar region illuminated by a laser light [5].

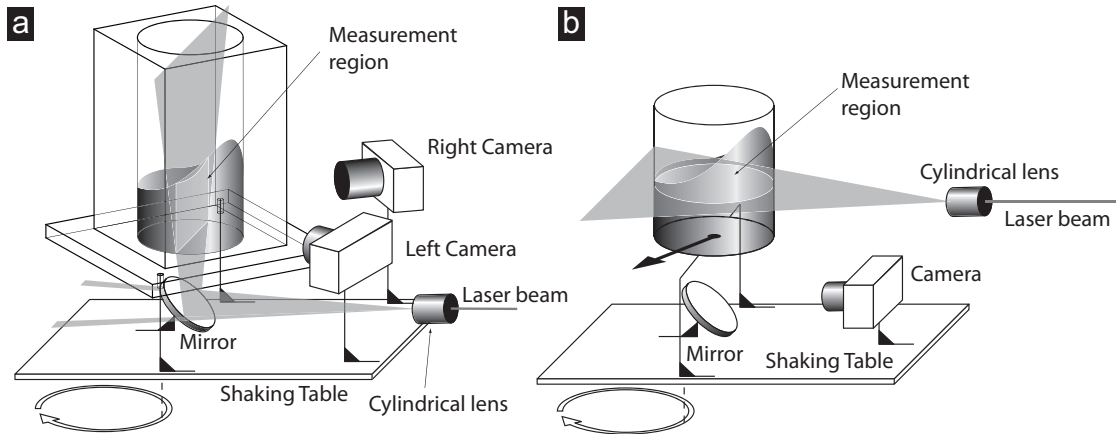


**Figure 3.9** | Setup used for the measurement of the velocity fields with Particle Image Velocimetry. **a**: three components of the velocity are measured on a bidimensional plane (2D3C-PIV). **b**: two components of the velocity (2D2C-PIV).

Two images are captured in succession using a double pulsed laser sheet to illuminate the particles in the flow. The images are then divided into a large number of small portions, called interrogation areas. The displacements of the particles in each area is computed by cross-correlation on the other image. Knowing the time between the two images, the displacement of each interrogation area, and the relation between pixels and millimetres it is possible to calculate the velocity of the flow at each interrogation window. When this method is used in several small interrogation windows, the local velocities are measured in the whole field of view of the cameras. Thus, we obtain two dimensional measurements (the measurement region is a plane) of two component of the velocity (horizontal and vertical): 2D2C-PIV. On the other hand, by using two cameras synchronized to take the pictures at the same moment from different locations it is possible to reconstruct by stereoscopy the three components of

the velocity [8, 88]. We refer to this measurements as 2D3C-PIV.

In the present study we used a couple of Dantec FlowSense EO 4M cameras (resolution 2048 X 2048 pixels, 8 to 12 bits intensity depth) and a Litron Dual Power 200-15 laser (pulse power 2x200 mJ, wavelength 532 nm). In both 2D2C and 2D3C measurements the cameras are mounted on the shaken table, while the laser and the cylindrical lens used to obtain the sheet of light remain outside it (Fig. 3.9). In 2D3C setup the cameras use Scheimpflug mounts (not depicted in Fig. 3.9a) to tilt the focal plane and adjust it to be coincident to the laser plane. The laser sheet is wide enough to ensure the illumination despite the motion of the vessel and mirror. Since stereo PIV measurements are largely dependent on the quality of the images, it is preferred to avoid optical deformations due to the refraction while capturing the images through a non-planar wall. For this reason, a vessel with square external walls and cylindrical internal wall has been designed and realized. The proximity of the refractive indexes  $n$  of Poly(methyl methacrylate) used for the vessel and of water ( $n=1.4914$  [87] and  $n=1.33$  [43] respectively) ensures minimal distortion as the light scattered by the particles reaches the cameras. In order to convert the pixels of the images into physical dimensions a calibration of the measurement field is necessary. This was performed using dotted targets with third-order polynomial calibration, which provided the most reliable results in our case.\*

The presence of the free surface increases the reflections of the laser in all direction, potentially misleading the measurements. For this reason, the tracking particles (polyamide particles, 5 - 35 $\mu\text{m}$  diameter, density 1.03kg/m<sup>3</sup>) have been treated with a fluorescent dye (Rhodamine B), which emits orange light at 625nm when excited at 540nm [60]. This was achieved by submerging the particles during several months in saturated solutions of rhodamine and water, in a warm environment (80°C). Both cameras have been equipped with a long pass filter, cutting all wavelength shorter than 570nm. Therefore the cameras capture only the light scattered by the particles and not from other reflections such as bubbles, free surface and walls.

In most cases, the velocity field rotates with the wave, i.e. it is constant in a reference frame rotating at the shaking frequency. Measurements on a vertical plane at a fixed position with respect to the container, along a complete revolution of the vessel, give the velocity field of the entire liquid (Fig. 3.10a). The measurement location is determined by the delay from a trigger signal based on the position of the shaker motor. We performed 45 measurements of the whole vertical plane for each vessel revolution, that is, one every 4°. Furthermore, the presence of a free surface may, depending on the shaking configuration, mask a portion of the measurement plane to one of the two cameras, as depicted in Fig. 3.10b). For this reason, the velocity field of the upper part of the wave is missing in waves with large amplitude.

---

\*The calibration takes into account also the diffraction deformations that are not entirely corrected by the vessel geometry.

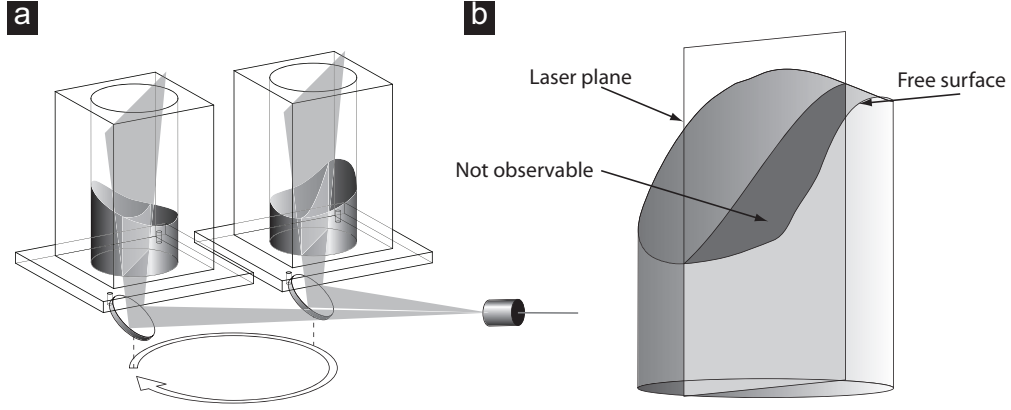


**Figure 3.10** | **a:** measurements on a vertical plane at a fixed position with respect to the container, performed at different position of the container on its shaking trajectory give the velocity field of the entire liquid. **b:** obstruction of a region of the measurement field by the wave.

#### 3.3.3 Proper Orthogonal Decomposition

Proper Orthogonal Decomposition (POD) is a powerful method extracting the most energetic coherent structures from a turbulent or unsteady flow [48]. It could also be seen as an inhomogeneous low pass filter [47, 6]. POD is successfully used in the analysis of various turbulent flows, such as boundary layer [6], vortices [40, 121] and even stirred tanks [46].

Since the POD deals with the velocity fluctuations, the velocity field at any location  $\mathbf{x}$  may be decomposed as:

$$\mathbf{u} = \bar{\mathbf{u}} + \mathbf{u}' \quad (3.4)$$

where  $\bar{\mathbf{u}}$  is the time average velocity and  $\mathbf{u}'$  is the fluctuating part. Without loss of generality the fluctuating part could be expressed as [98, 48]:

$$\mathbf{u}'(\mathbf{x}, t) = \sum_{n=1} a_n(t) \boldsymbol{\phi}_n(\mathbf{x}) \quad (3.5)$$

where  $a_n(t)$  are the time-dependent coefficients of the expansion and  $\boldsymbol{\phi}_n(\mathbf{x})$  are the orthogonal basis of each component of the velocity. The POD method that we used to extract the modes is embedded in the Dantec PIV software package, and uses the snapshot method proposed by Sirovich [97]. In order to determine the POD modes the fluctuations  $\mathbf{u}'(\mathbf{x}, t) = (u'(\mathbf{x}, t), v'(\mathbf{x}, t), w'(\mathbf{x}, t))$  of all the measurements (snapshots) taken at each time  $t$  are

arranged in a matrix of the following form:

$$U = \begin{bmatrix} u'(\mathbf{x}_1, t_1) & u'(\mathbf{x}_1, t_2) & \cdots & u'(\mathbf{x}_1, t_N) \\ \vdots & \vdots & & \vdots \\ u'(\mathbf{x}_M, t_1) & u'(\mathbf{x}_M, t_2) & \cdots & u'(\mathbf{x}_M, t_N) \\ v'(\mathbf{x}_1, t_1) & v'(\mathbf{x}_1, t_2) & \cdots & v'(\mathbf{x}_1, t_N) \\ \vdots & \vdots & & \vdots \\ v'(\mathbf{x}_M, t_1) & v'(\mathbf{x}_M, t_2) & \cdots & v'(\mathbf{x}_M, t_N) \\ w'(\mathbf{x}_1, t_1) & w'(\mathbf{x}_1, t_2) & \cdots & w'(\mathbf{x}_1, t_N) \\ \vdots & \vdots & & \vdots \\ w'(\mathbf{x}_M, t_1) & w'(\mathbf{x}_M, t_2) & \cdots & w'(\mathbf{x}_M, t_N) \end{bmatrix} \quad (3.6)$$

so that each column contains all the measurements of the velocity fluctuations at a given time  $t_1 \dots t_N$  while each row contains all the successive measurements at a given location  $\mathbf{x}_1 \dots \mathbf{x}_M$ .  $N$  is the number of measurements in time and  $M$  is the number of measurements locations. The eigenvalues  $\lambda_i$  and the eigenvectors  $\Xi_i$  of the auto-covariance of the matrix  $U$  are computed as:

$$C\Xi_i = \lambda_i \Xi_i \quad \text{where} \quad C = U^T U. \quad (3.7)$$

The POD modes are then computed as the normalized eigenfunctions:

$$\phi_i = \frac{U\Xi_i}{\|U\Xi_i\|} \quad (3.8)$$

Since the total kinetic energy of each mode is proportional to its eigenvalue [9] it is possible to order the POD modes ensuring that the most contributing in terms of energy are the first. Moreover, the time dependent coefficients (or POD coefficients) are determined for each snapshot as the projection of the fluctuating velocities into the corresponding POD mode:

$$\mathbf{a}_n = \Psi^T \mathbf{u}'_n \quad (3.9)$$

where  $\Psi$  is the tensor composed by all the POD modes  $\phi_i$ :  $\Psi = [\phi_1 \phi_2 \dots \phi_{N-1}]$ . Since the mean  $\bar{\mathbf{u}}(\mathbf{x}, t)$  is calculated from the snapshots themselves, the  $N^{th}$  mode is equivalent to zero and is usually neglected. The vector  $\mathbf{a}_n$  contains the time dependent coefficients  $a_n(t)$  of all the snapshots for the  $n^{th}$  mode.

The velocity, filtered at the  $n^{th}$  mode is therefore determined as:

$$\mathbf{u}^{(n)}(\mathbf{x}, t) = \bar{\mathbf{u}}(\mathbf{x}, t) + \sum_{i=1}^n a_i(t) \phi(\mathbf{x}) \quad (3.10)$$

and it is equivalent to the velocity of the snapshot if all the modes are included:  $n = N - 1$ .

#### 3.3.4 Operating conditions of the measurements

The velocity fields have been measured with several shaking configurations: in Table 3.2 are given the operating parameters of the LDV measurements, while the ones of the PIV measurements are given in Table 3.3.

$D$ [mm]	$H_0$ [mm]	$d_s$ [mm]	$\Omega$ [rpm]
144	100	25	85
144	100	25	113
287	200	50	60
287	200	50	80
287	200	50	100

**Table 3.2** | Operating parameters of the LDV measurements.

$D$ [mm]	$H_0$ [mm]	$d_s$ [mm]	$\Omega$ [rpm]
150	75	15	85
150	75	15	100
150	75	15	120
150	75	15	160
150	75	30	85
150	75	30	100
150	75	30	120
150	75	30	140
150	75	30	160

**Table 3.3** | Operating parameters of the PIV measurements.

### 3.4 Mixing measurement

The mixing efficiency of the shaker is estimated measuring the number of revolutions required to homogenize an initially heterogeneous condition. This is usually achieved by releasing a dye or a chemical reagent (e.g. in Dual Indicator For Mixing Time [24, 104, 108]) in the flow and following the change in coloration of the liquid. A main drawback of this technique is the average in the observation direction which is introduced when only one observation location is used. More accurate measurements are obtained by using tomographic techniques, e.g. if the concentration of the dye is known in a specific plane inside the liquid bulk. This is usually achieved by Laser Induced Fluorescence (LIF) [57], an optical measurement technique based on fluorescent dyes.

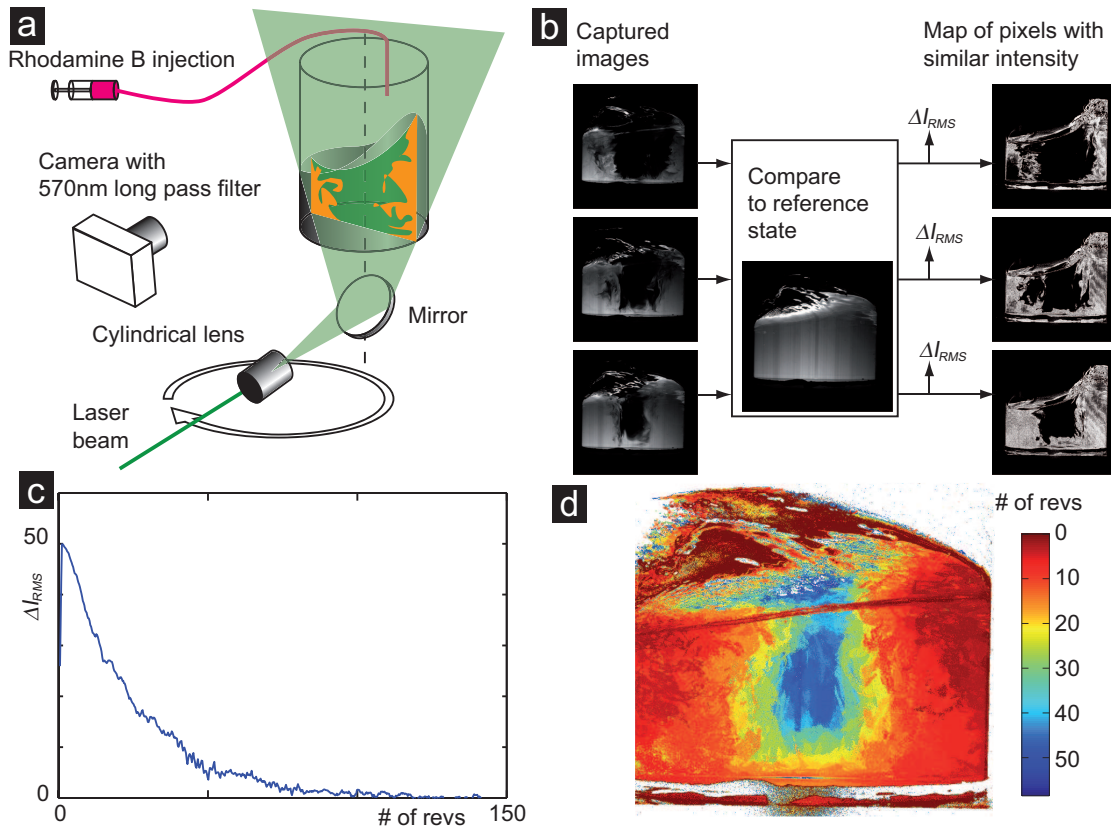


**Figure 3.11** | **a:** setup used to measure the fluorescent dye concentration in a vertical plane. **b:** all images are compared to a reference state, and the root mean square difference of the intensity ( $\Delta I_{RMS}$ ) is calculated. Moreover, regions having the same concentration as the reference state (pixels with similar values) are identified. **c:**  $\Delta I_{RMS}$  evolution as a function of the number of revolutions of the vessel. **d:** example of mixing map obtained superposing the maps of similar concentration.

The fluorescent dye, Rhodamine B (for properties see Sec. 3.3.2) has a fluorescent quantum yield depending both on the concentration and the temperature [56]. The PIV pulsed laser was used to create a vertical plane of light in which the concentration was measured. The Rho-

damine, in water solutions near saturation ( $\sim 50\text{g/L}$ ), was introduced in the flow by injection at the free surface (Fig. 3.11a), and its transport in the liquid was followed by a FlowSense camera equipped with a long pass filter (Sec. 3.3.2). The dye was injected at the wall slightly above the crest of the wave. Quick injection is likely to generate strong jets of dye perturbing the wave motion, while slow injection may affect initial heterogeneous conditions, thus leading to misleading results. A good compromise was found injecting 1ml in 3 seconds. Electromechanical triggers were used to acquire the images at four fixed locations on the trajectory of the orbital shaker. The use of multiple acquisitions per revolution ensured the monitoring of the tangential homogeneity of the dye dispersion.

The images acquired at each time step are compared to the corresponding reference state (Fig. 3.11b), i.e. when no perceivable change in concentration is observed over time, at the end of the experiment. The comparison to the reference state at the end of the mixing has the advantage of overriding experimental errors introduced by the use of different concentration or quantities of dye or changes in the temperature of the liquid. During the comparison the root mean squared difference of the intensity (hereafter called  $\Delta I_{RMS}$ ) is computed using the following relation:

$$\Delta I_{RMS} = \left[ \frac{1}{N^2} \sum_{i=1}^N \sum_{j=1}^N (I(i, j) - I_{ref}(i, j))^2 \right]^{\frac{1}{2}} \quad (3.11)$$

where  $N$  is the horizontal and vertical number of pixels of the images (in the case of the FlowSense are  $N=2048$ );  $I(i, j)$  and  $I_{ref}(i, j)$  are the intensity of the pixel in the  $i^{th}$  column and  $j^{th}$  row, of the current and of the reference image respectively. Since the reference state is homogeneous,  $\Delta I_{RMS}$  provides a quantitative assessment of the inhomogeneity of the flow at each moment, thus decreasing with time (Fig. 3.11c). After the injection the value of  $\Delta I_{RMS}$  increases due to the high fluorescence of the saturated rhodamine solution.

Furthermore, at each time step the regions having a concentration of dye comparable to the reference state are identified. We establish thus mixing maps, graphically depicting the number of revolutions necessary to the dye in order to attain the final concentration in each location (Fig. 3.11d). It has to be noted that mixing maps as defined here do not show regions where there is better mixing; they assess the velocity at which the dye, from its initial location, reaches each region.

Obviously, only measurements obtained with equivalent experimental setup are comparable: changing the injection site of the dye lead to different number of revolutions necessary to obtain homogeneity.





## 4 Dynamics of waves induced by orbital shaking

### 4.1 Observations

The motion of the container along its shaking trajectory generates a deformation of the free surface, hereafter called wave pattern, which rotates around the revolution axis of the container. According to the potential model, each set of operating parameters  $D$ ,  $d_s$ ,  $H_0$  and  $\Omega$  leads to a peculiar free surface shape and flow.

The observation of the free surface shape for more than 6000 sets of operating parameters reveals a remarkable richness of wave patterns, largely outreaching the predictions of the potential model. We present in Fig. 4.1 the visualizations of the waves reconstructed from the high speed movies. The images are composed of narrow vertical portions of the frames, taken at a fixed location on the container periphery as the waves rotate, as described in Sec. 3.2.1.

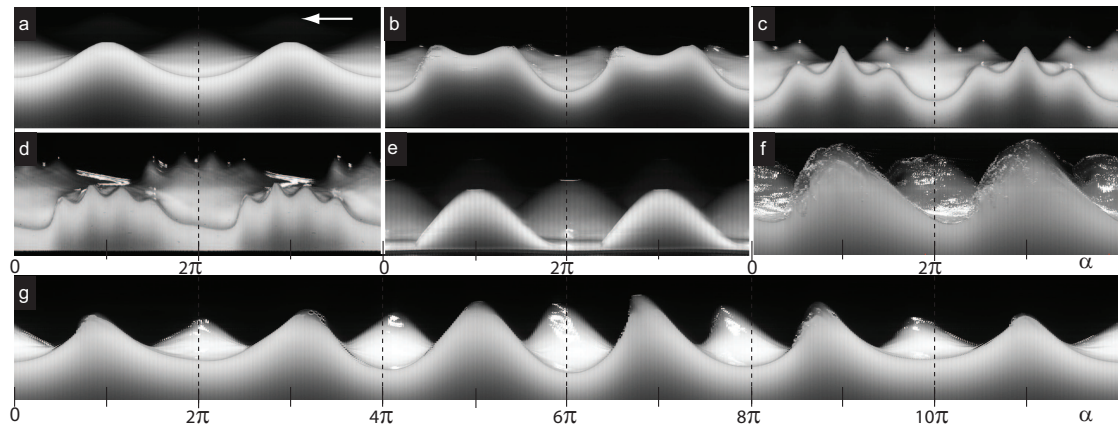


**Figure 4.1** | Wave patterns reconstructed from high speed movies as described in Sec. 3.2.1, depicted for two (a-f) or six (g) revolutions of the vessel. All waves are travelling from right to left. **a**: single crested wave, the most usually observed. **b**: double crested wave. **c**: triple crested wave. **d**: quadruple crested wave. **e**: wave drying a portion of the vessel bottom. **f**: breaking single crested wave. **g**: wave whose wave pattern it is not constant in a reference frame rotating at the shaking frequency.

## Chapter 4. Dynamics of waves induced by orbital shaking

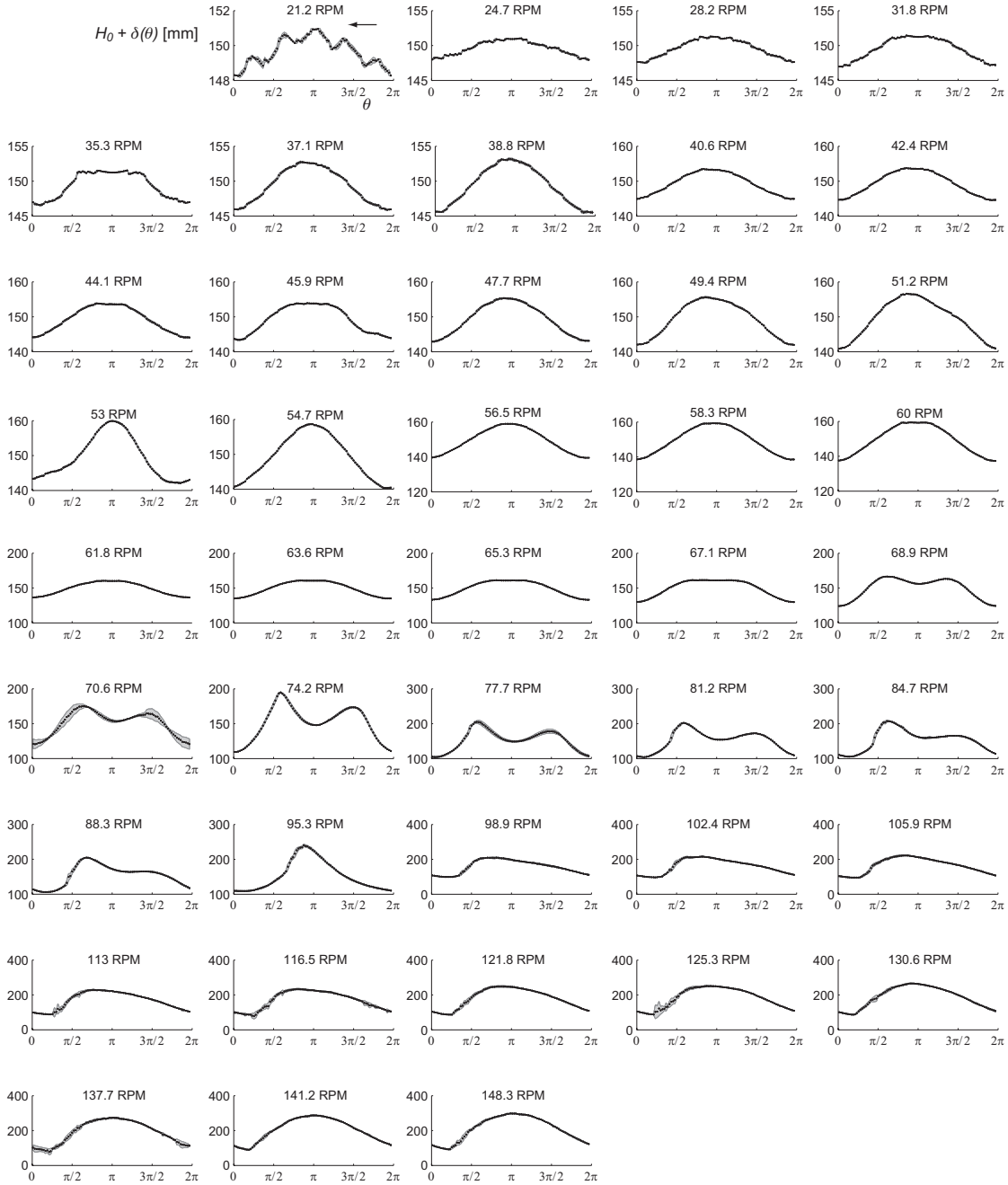


**Figure 4.2** | Evolution of the interface height at the container wall ( $H_0 + \delta(\theta)$  in mm) measured from movies, as described in Sec. 3.2.1, for a vessel having  $D = 287\text{mm}$ ,  $H_0 = 150\text{mm}$  and  $d_s = 28.7\text{mm}$ , the shaking frequencies are specified in the image (in rpm). The measurements are phase averaged over three revolutions: black dots are mean values, the standard deviation is depicted as the grey surface (e.g. at 70.6rpm). The scale in the vertical direction is not constant to highlight shape differences. The waves are travelling from right to left.

The images are thus reconstructed snapshots of the wave at the entire periphery (if the wave is rotating as a fixed shape at the shaking frequency). Although single crested waves, with one crest and one trough (Fig. 4.1a) are the most common, more complex shapes featuring multiple crests and troughs are also observed: double (Fig. 4.1b), triple (Fig. 4.1c) and quadruple crest waves (Fig. 4.1d). Under specific conditions, the wave may “dry” a portion of the vessel bottom (Fig. 4.1e) or break (Fig. 4.1f). Another characteristic of a wave is its symmetry: for three dimensional waves as those encountered in cylindrical containers, we define “symmetric” a wave having a vertical plane of symmetry, usually passing through the crest and the trough. The waves depicted in Figs. 4.1a-b are symmetric, while those in Figs. 4.1d and f clearly are not. Moreover, not all patterns are rigid shapes rotating around the vertical axis of the vessel: Fig. 4.1g depicts a wave whose amplitude increases over several revolutions, eventually breaks and returns to a smaller amplitude, repeating this cycle indefinitely.

In Fig. 4.2 we illustrate an example of the evolution of the free surface height at the wall for  $D=287\text{mm}$ ,  $d_s=28.7\text{mm}$ ,  $H_0=150\text{mm}$  and  $\Omega$  varied between 21.2 and 148.3rpm. Note that the measurements, retrieved from the high speed movies, are phase averaged over 3 to 4 revolutions, while the scale in the vertical direction is adapted to magnify the features of each wave. The standard deviations of the averaging is depicted as a grey surface, highlighting the wave steadiness. To further illustrate the wave pattern, a subset of the measurements shown in Fig. 4.2 is depicted in Fig. 4.3 projected on its principal planes of inertia, thus giving a side and a front view of the wave at the wall. Note that in case of symmetric waves one of the planes of inertia is the symmetry plane. The measurements at the wall are not continuous between  $\alpha=0$  and  $2\pi$ , hence the phase shift of the principal planes of inertia with respect to the container is directly visible in the images.

At low shaking frequencies the waves are mostly planar, with a slope increasing with the shaking frequency, giving a sinusoid distribution of the liquid at the wall (Figs. 4.2 and 4.3). We may nevertheless discern rare but stable waves with higher number of crests (e.g. five crests at 21.2rpm) and asymmetric waves (e.g. at 35.3, 45.9 and 53rpm). As the shaking frequency is further increased we notice flattening of the crest (63.6 to 67.1rpm) which evolves into a persistent double crested wave (68.9rpm). At  $\Omega=70.6\text{rpm}$  the wave exhibits a peculiar behaviour with its shape changing constantly as it rotates, which explains the significant increase of the standard deviation (in Fig 4.2). Although the wave remains periodic, its period is different from the shaking one. From 74.2 to 88.3rpm the wave is double crested, asymmetric and breaking at its front crest. As the shaking frequency is increased (from 95.3rpm) the wave recover its single crested shape, but it is neither sinusoid nor symmetric: it is more similar to a jet of liquid impinging at the wall, with enhanced entrainment of air in the liquid phase (as shown also in Fig 4.1f), whose amplitude increases with the shaking frequency. Changing one of the operating parameters  $D$ ,  $d_s$  or  $H_0$  and increasing the shaking frequency would yield to similar but not identical behaviour: at low shaking frequency we would observe single crested and discontinued multiple crested waves, whose number of crests decreases with increasing shaking frequency. At higher shaking frequency we would obtain higher amplitude waves with occasional persistent triple or double crested waves, followed by breaking and finally

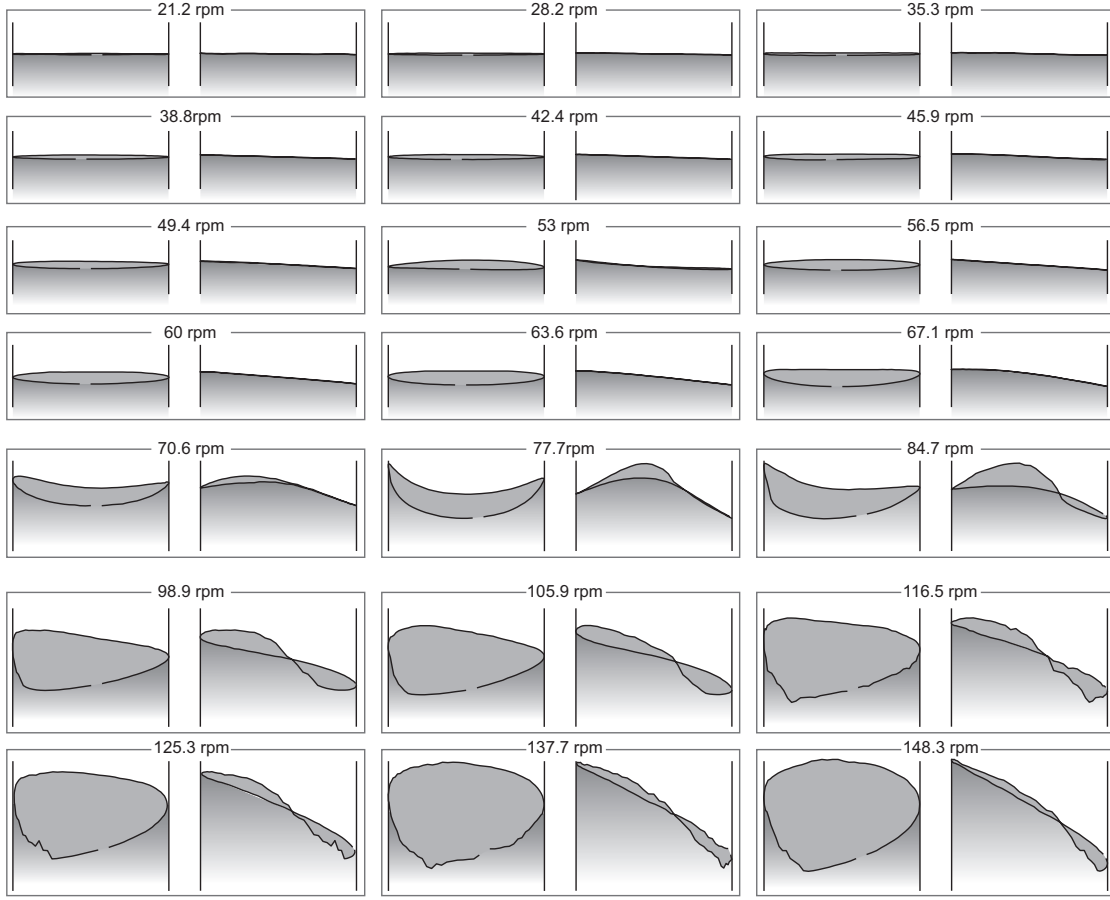


**Figure 4.3** | Evolution of the average interface height at the wall  $\delta(\alpha)$  projected on the symmetry plane of the wave, and on the plane perpendicular to the symmetry one, passing through the revolution axis of the container (right and left respectively in each couple of images). The measurements are intentionally not continuous between  $\alpha = 0$  and  $2\pi$ , thus visually assessing rotation of the symmetry plane with respect to the container.

splashing at the wall.

To illustrate the effect of the operating parameters other than the shaking frequency, we depict in Fig. 4.4a-b the measurements of the free surface height at the wall  $\delta(\theta)$  as the shaking diameter  $d_s$  is changed, while  $H_0$ ,  $D$  and  $\Omega$  are kept constant. Although the amplitude changes, the pattern is conserved: single crested waves do not evolve into multiple crested and vice-versa. In some cases the wave may break as  $d_s$  is increased, but the number of crests is always preserved. On the other hand, modifications of the unperturbed height of liquid  $H_0$  may influence the wave pattern. In Fig. 4.4c-d we observe that low  $H_0$  values affect the wave patterns especially for multiple crested waves, completely changing the wave morphology and occasionally breaking the wave (in Fig. 4.4d the almost vertical wave front of  $H_0=45\text{mm}$  is breaking). Single crested waves seem less dependant on the value of  $H_0$  (Fig. 4.4c).

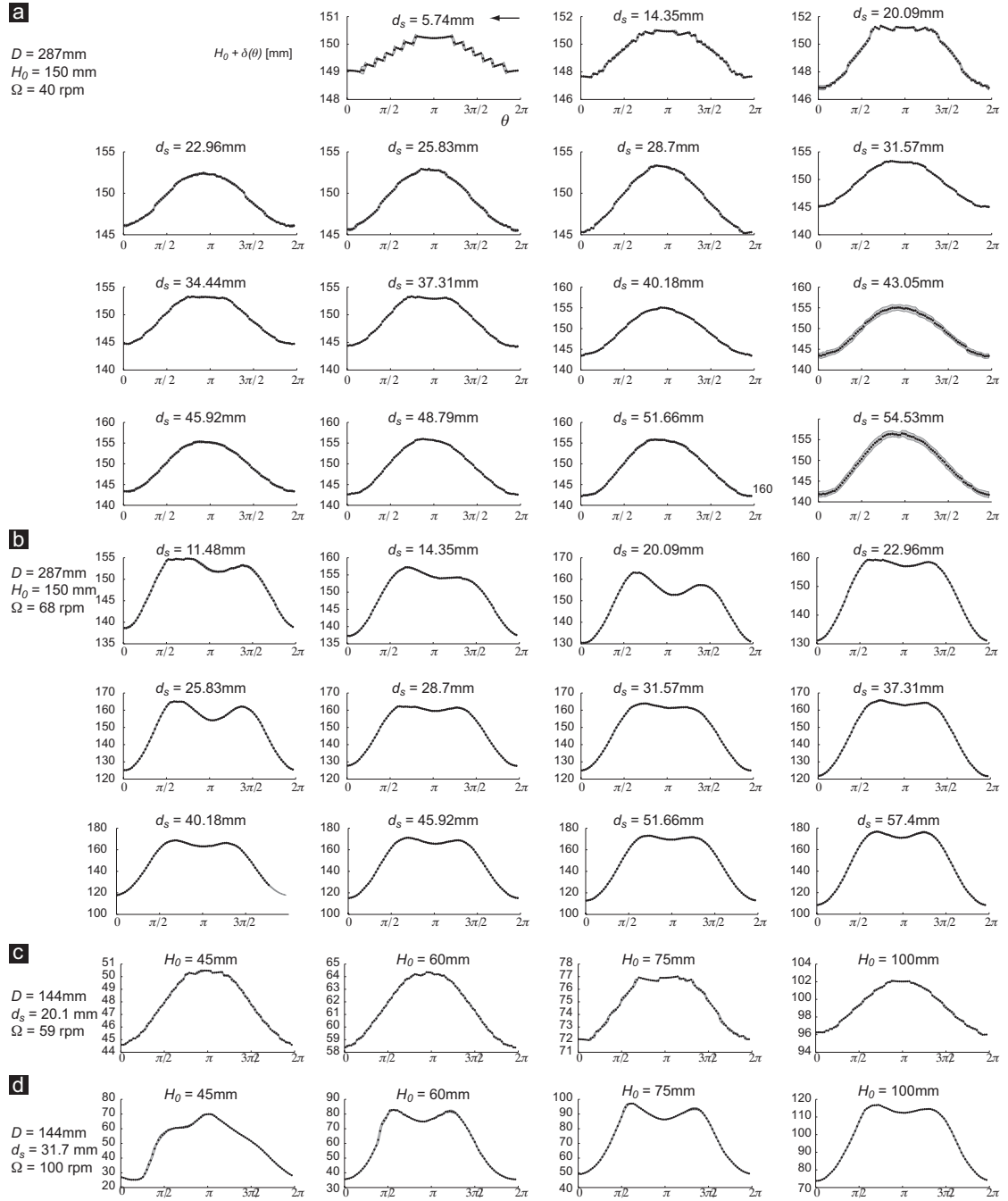


**Figure 4.4** | Evolution of the interface height at the wall ( $H_0 + \delta(\theta)$  in mm) phase averaged from measurements from movies, as described in Sec. 3.2.1. Black dots are mean values, the standard deviation is depicted as the grey surface. The scale in the vertical direction is adapted to highlight pattern differences. **a-b**: the shaking diameter  $d_s$  is changed while the other operating parameters are kept constant. **c,d**: the unperturbed liquid height at rest  $H_0$  is varied.

### 4.1.1 The periodicity of the waves

Besides the obvious differences in shape, a main characteristic of the waves is their periodicity, or synchronicity to the shaking excitation. While most of the waves (Fig. 4.1a-f) are constant in a frame of reference rotating around the container revolution axis at the shaking frequency, others (Fig. 4.1g) have a shape continually changing while rotating. The free surface height and velocity fields of waves of the former kind are related at different arbitrary instants  $t$  and  $t + \tau$  by the following equations:

$$\begin{aligned} \delta(r, \theta, t) &= \delta(r, \theta + \Omega\tau, t + \tau) & \text{and} \\ \mathbf{v}(r, \theta, t) &= \mathbf{v}(r, \theta + \Omega\tau, t + \tau) & \forall r \in [0, D/2], \forall \theta \in [0, 2\pi[ \end{aligned} \quad (4.1)$$

We define “synchronous” the waves respecting Eqs. 4.1, and “non-synchronous” those not respecting them. The potential model predicts only synchronous waves. Moreover, in synchronous waves, measurements of physical quantities at an angular location, fixed with respect to the container along a complete revolution of the vessel, give the instantaneous value of the physical quantities at all angular locations. Thus, the measurements of the wave height as a function of the container position  $\delta(\alpha)$  are equivalent to  $\delta(\theta, t)$ , and the images, such as those depicted in Fig. 4.1a-f, are equivalent to unfolded views of the wave at the container wall. This is not the case in non-synchronous waves, since the wave changes in shape as it rotates.

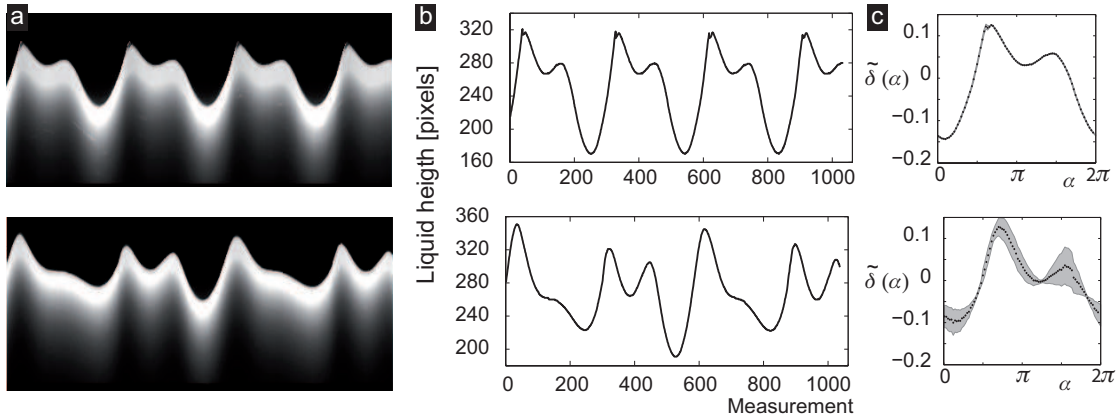


**Figure 4.5** | **a:** image and **b:** height in pixels of two waves, the upper one respecting Eqs. 4.1, the lower one not. **c:** phase average of the dimensionless wave height at the wall  $\tilde{\delta}(\alpha) = \delta(\alpha)/D$  of the waves (black dots), standard deviation is shown in grey.

In synchronous waves the measurements are phase averaged to reduce errors: Fig. 4.5c depicts the phase averaging of a synchronous and of a non-synchronous wave. We observe that the overall standard deviation is significantly lower in the former case.

### 4.1.2 Wave classification

Considering the variety of the wave patterns, and their discontinuous evolution while the operating parameters are changed, they are most appropriately analysed by categorizing them according to their morphology, i.e. the number of their crests, their period and their “breaking state”.

Wave patterns are first subdivided according to their periodicity into synchronous and non-synchronous. Three main behaviours are identified in synchronous waves: non-breaking waves, waves at the inception of the breaking (where the breaker is localized at the crest), and waves where the breaking is generalized to the entire liquid, which impinges at the wall. Usually, this coarse categorisation corresponds to the evolution of the patterns with increasing shaking frequency  $\Omega$  and constant  $D$ ,  $d_s$  and  $H_0$ . Moreover, non-breaking and inception breaking waves may be single or multiple crested, while spaleshing waves are only observed single crested. Non-synchronous waves may also be single or multiple crested. The categorisation is summarized in Fig.4.6 and the structure of the next sections will follow this classification.

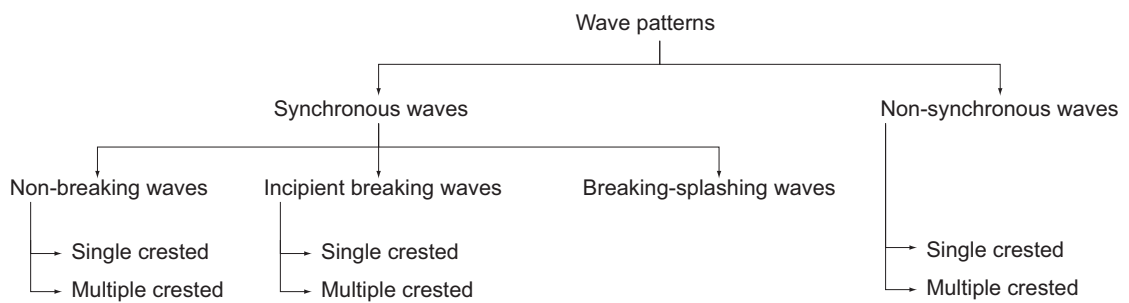


**Figure 4.6** | Summary of the wave patterns categories.

## 4.2 Synchronous waves motion

In this section we present the behaviour of synchronous waves, following their evolution as the shaking frequency is increased. The influence of the operating parameters is investigated and the measurements are compared to the solutions of the potential model.

We remind the reader that, under potential hypothesis, the flow equations have been solved with linear approximation of the free surface boundary conditions (Sec. 2.3) and to the second order of non-linear free surface boundary conditions (Sec. 2.3.2). The solutions of this eigenvalues problem are found for a series of two-dimensional natural modes, identified by two integers  $(m, n)$ , with associated natural frequencies  $\omega_{mn}$ . The first index  $m$  defines the number of the mode in the tangential direction, and is equivalent to the number of nodal diameters, whereas  $n$  is the number of nodal circles and defines the mode number in the radial direction.\* The linear solution is a sum of all the  $(1, n)$  modes, where the  $(1, 1)$  mode is the first non-axisymmetric mode and the dominant as long as  $\Omega < \omega_{11}$ . The non-linear solution is obtained considering the  $(1, 1)$  mode as dominant, with  $(0, 1)$  and  $(2, 1)$  as secondary. The solution shows that the  $(2, 1)$  is the most important of the secondary modes. The experiments have been obtained in the ranges listed in Table. 3.1 and, since most of the phenomena are found to be scale independent, the measurements are presented by using the normalizations introduced in Sec. 2.59.

### 4.2.1 Non-breaking waves

Figure 4.7 shows the crest-to-trough amplitude of non-breaking waves measured at the wall with respect to the shaking frequency  $\Omega$  (normalized by the natural frequency  $\omega_{11}$ ), for five values of the shaking diameter  $\tilde{d}_s$ . The amplitude  $\tilde{A}_\delta$  is computed as  $\tilde{A}_\delta \equiv \max(\tilde{\delta}(\theta, t)) - \min(\tilde{\delta}(\theta, t))$  where  $\tilde{\delta}(\theta, t) = \delta(\theta, t)/D$ . Those measurements are compared to the amplitude predicted by the linear solution of the potential model, which is derived from Eq. 2.59 as follows:

$$\tilde{A}_\xi = \frac{d_s \Omega^2}{g} \cdot \left\{ \frac{1}{2} + \sum_{n=1}^{\infty} \left[ \frac{1}{(\epsilon_{1n}^2 - 1)} \frac{\Omega^2}{(\omega_{1n}^2 - \Omega^2)} \right] \right\}, \quad (4.2)$$

and depicted as a solid line for each shaking diameter in Fig.4.7.

Despite the strong hypothesis used in the linear solution of the potential model, we observe that the experiments and the model agree remarkably well at most of the shaking frequencies, as far as the wave does not break, and for all shaking diameters. We may also notice regions where the measured amplitudes are sensibly larger than the model, namely at  $\Omega/\omega_{11}=0.5$ , corresponding to shaking frequencies at which multiple crested waves are observed (described and discussed in Sec. 4.2.1.2). To further analyse the liquid dynamics, we will first focus on single-crested non-breaking waves.

---

\*A graphical representation of the modes is given in Fig. 2.4 on page 18.



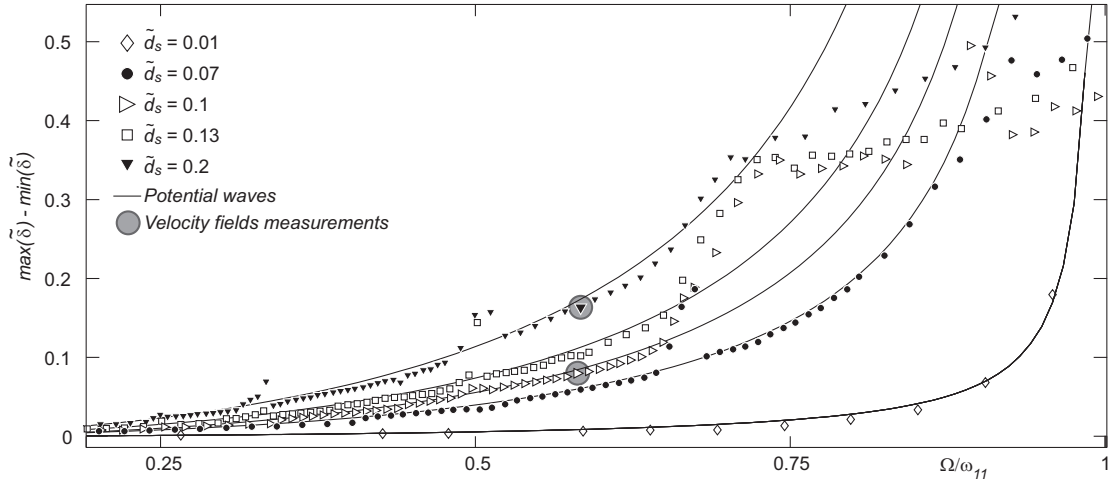


**Figure 4.7** | Measured waves amplitudes  $\tilde{A}_\delta$ , depicted as markers, compared to the predictions of the linear potential model depicted as solid lines, for five different shaking diameters  $\tilde{d}_s$ , at shaking frequencies below the first natural frequency  $\omega_{11}$ ,  $\tilde{H}_0 = 0.5$ . The amplitudes of the waves whose velocity fields have been measured and used to compute the trajectories shown in Fig. 4.9 are highlights by grey circles.

#### 4.2.1.1 Single crest waves

The waves with one crest, one trough and sinusoid liquid height at the wall, follow the predictions of the linear potential model, both concerning the amplitude of the free surface (Fig. 4.7) and the velocity fields. In Fig. 4.8 we show the radial, tangential and axial velocity components as functions of angular position  $\theta$ , measured using Laser Doppler Velocimetry (LDV, see Sec. 3.3.1) at two fixed values of radius and depth:  $r/D=0.348$ ,  $z/H_0=0.5$  and  $r/D=0.104$ ,  $z/H_0=0.25$ . We observe a good agreement between the measured velocity fields  $\tilde{\mathbf{v}}$  and the potential predictions  $\tilde{\mathbf{q}}$ , and we also notice several characteristic features of the potential motion: the vertical velocity decreases with the depth (it is zero at the tank bottom to respect the impermeability conditions), while the tangential velocity increases with the radius. The radial velocity decreases with the radius and the depth, and it is almost equivalent at the two measurement locations depicted in Fig. 4.8.

A deeper understanding of the motion is obtained by computing the Lagrangian trajectories followed by liquid particles released into the flow at the initial location  $\mathbf{x}_0 = (r_0, \theta_0, z_0)$ . The positions are calculated iteratively at each successive time  $t$  as follows:

$$\begin{aligned} r(t+dt) &= r(t) + v_r(r(t), \theta(t), z(t), t) \cdot dt \\ \theta(t+dt) &= \theta(t) + \frac{1}{r(t)} v_\theta(r(t), \theta(t), z(t), t) \cdot dt \\ z(t+dt) &= z(t) + v_z(r(t), \theta(t), z(t), t) \cdot dt, \end{aligned} \quad (4.3)$$

where  $dt$  is the time interval, whose value has to be small enough not to influence the solution.

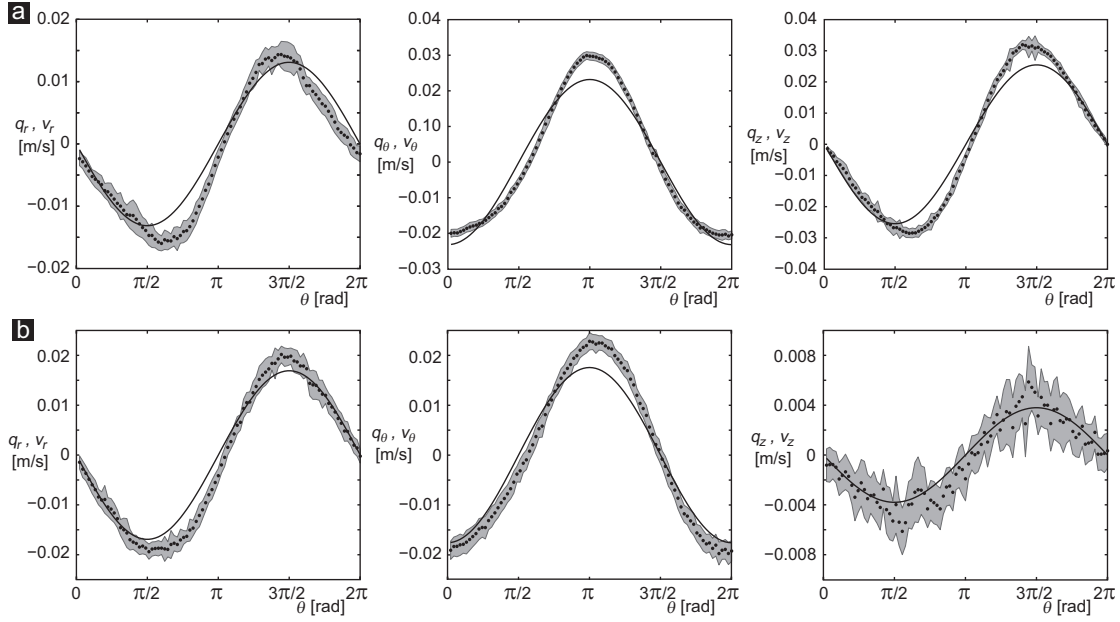


**Figure 4.8** | Phase averaged LDV measurements of the three components of the velocity, for  $\tilde{d}_s = 0.174$ ,  $\tilde{H}_0 = 0.7$  and  $Fr = 0.45$  ( $\Omega/\omega_{11} = 0.56$ ). The black dots are the phased means of the measurements, while the grey area depicts the standard deviation. Velocity predicted by the potential model are depicted as solid lines. **a:** measurements at  $r/D = 0.348$  and  $z/H_0 = 0.5$ . **b:** measurements at  $r/D = 0.104$  and  $z/H_0 = 0.25$ .

The values of  $v_r$ ,  $v_\theta$  and  $v_z$  are determined at each time step by linear interpolation of the velocity fields measured by Particle Image Velocimetry (see Sec. 3.3.2). Velocities obtained by PIV are preferred to those obtained by the LDV since they have a finer measurement locations grid, decreasing the interpolation errors, and are defined in the whole liquid domain, thus preventing excessive extrapolations. The amplitude corresponding to the waves whose trajectories are computed are highlighted in Fig. 4.7.

The trajectories followed during two revolutions by a group of liquid particles are shown in Fig. 4.9, along with trajectories obtained from linear potential velocity fields (Eqs. 2.56), for  $\tilde{d}_s = 0.1$  and  $0.2$ . We observe a good agreement of the amplitudes of the motion between the measurements and the potential model prediction, although at  $\tilde{d}_s = 0.1$  the measurements show a large displacement of the particles in direction of propagation of the wave, exceeding the predicted drift. The trajectories reveal other typical features of wave motion when projected on the  $\theta - z$  and on the  $r - z$  planes, as shown in Figs. 4.9b-c. As predicted by the potential model the liquid particles follow trochoidal paths, the amplitude of their motion depends on the shaking diameter  $\tilde{d}_s$  and decreases with the depth. Moreover, while the motion at the wall is nearly vertical, it is more circular around  $\tilde{r} = 0.25$  and almost horizontal at the centre of the container.

Nevertheless, the trajectories also reveal discrepancies between the potential prediction and the measurements. The tangential motion has opposite directions depending on the shaking

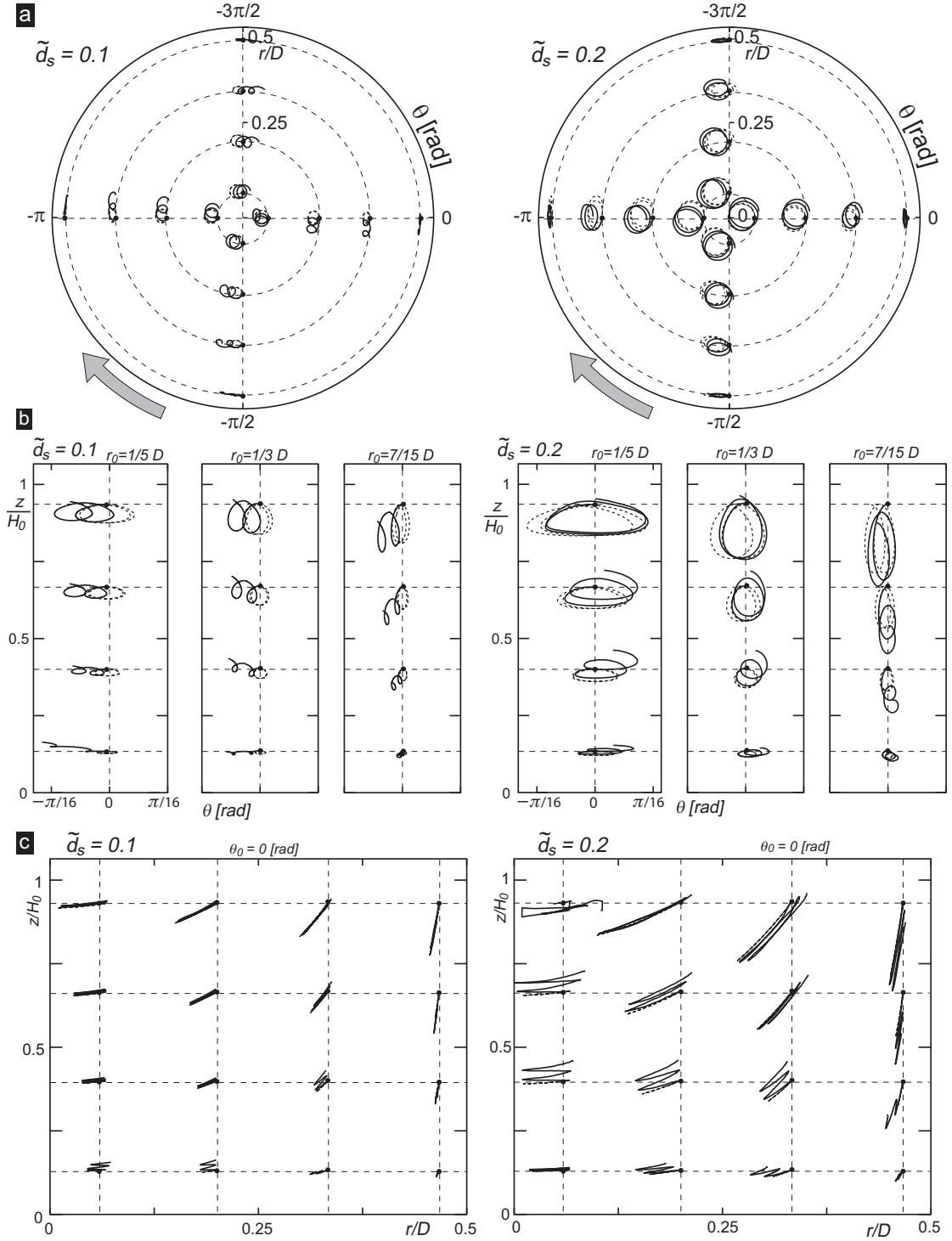


**Figure 4.9** | Trajectories of liquid particles from PIV measurements (solid lines) and from linear potential velocity fields (thin dashed lines),  $\tilde{d}_s=0.1$  on the left and  $\tilde{d}_s=0.2$  on the right, for  $\Omega/\omega_{11} = 0.59$ . **a:** view from above, projected in the  $r-\theta$  plane,  $r_0/D=1/15, 1/5, 1/3$  and  $7/15$ ,  $\theta_0=0, \pi/2, \pi$  and  $3\pi/2$ ,  $z_0/D=1/4$ . **b:** projection in the  $\theta-z$  plane,  $r_0/D=1/5, 1/3$  and  $7/15$ ,  $\theta_0=0, \pi/2, \pi$  and  $3\pi/2$ ,  $z_0/D=1/15, 1/5, 1/3$  and  $7/15$ . **c:** projection in the  $r-z$  plane,  $r_0/D=1/5, 1/3$  and  $7/15$ ,  $\theta_0=0, \pi/2, \pi$  and  $3\pi/2$ ,  $z_0/D=1/15, 1/5, 1/3$  and  $7/15$ .

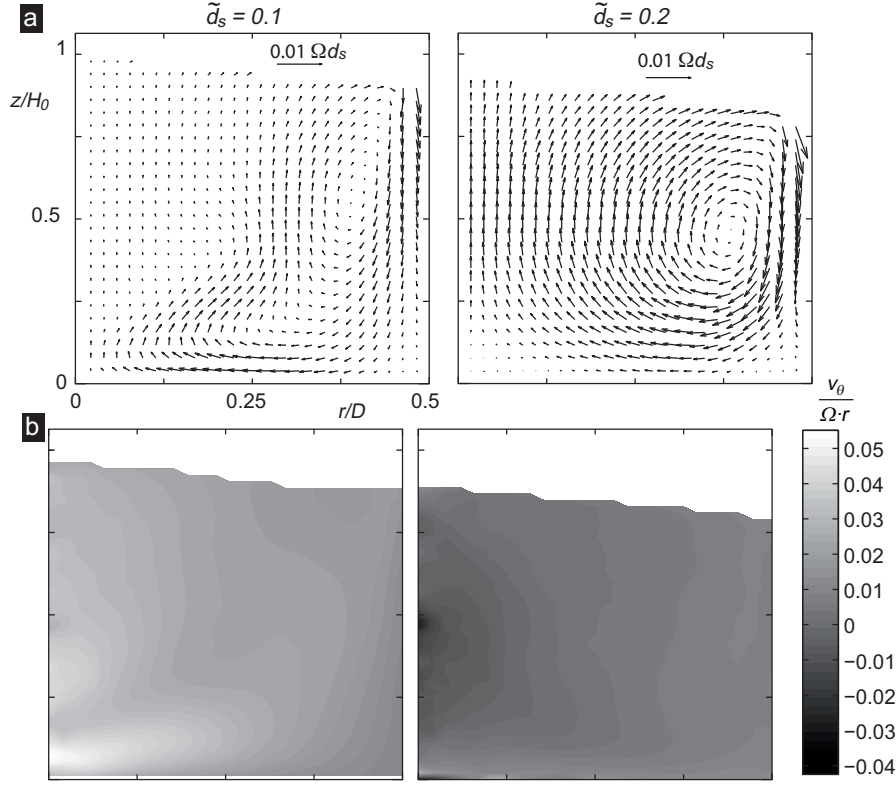


**Figure 4.10** | Averaged velocity components, calculated for  $\tilde{d}_s=0.1$ ,  $\tilde{H}_0=0.5$  and  $Fr = 0.348$  ( $\Omega/\omega_{11} = 0.59$ ) on the left and  $\tilde{d}_s=0.2$ ,  $Fr = 0.492$  ( $\Omega/\omega_{11} = 0.59$ ) on the right. **a:** velocity field calculated using the averages of the radial and axial velocity components ( $\bar{v}_r$  and  $\bar{v}_z$ ). **b:** Values of  $\bar{v}_\theta$  normalized by the tangential velocity of the container - this ratio could be understood as the average ratio of rotation of the flow.

diameter: it is negative at  $\tilde{d}_s = 0.2$ , while it is positive at  $\tilde{d}_s = 0.1$ . In addition to this, a slow upward motion is observed near the container axis, while an even more pronounced downward motion is detected at the periphery.

This unexpected motion appears both at  $\tilde{d}_s = 0.1$  and  $\tilde{d}_s = 0.2$ , and is highlighted by averaging the velocity components over one revolution:

$$\bar{v}_i(r, z) = \frac{1}{2\pi} \int_0^{2\pi} v_i(r, \theta, z) d\theta \quad (4.4)$$

where  $i = r, \theta, z$ . Only the regions having a valid measurement over a complete revolution are taken into account to compute the average: i.e. all the portion of the velocity fields that are partially hidden by the wave or that are not in the liquid phase for a portion of the vessel motion do not contribute to the computation of the averages. Average radial and axial velocities are shown in Fig. 4.10a as a vector field, for both values of  $\tilde{d}_s$ . The average tangential velocities in Fig. 4.10b are normalized by the velocity of the shaker,  $r\Omega$ , hereafter called the “synchronous velocity”, since it is the velocity the flow would have at solid rotation synchronous with the

shaker. Although the potential model predicts average velocities equal to zero, we observe that the experiments display small but well defined average flows. An important downward motion of the liquid at the wall is observed, generating convective motions of different size depending on the shaking diameter. Although this convective flow also reminds the secondary motion of rotating liquids, phenomenon also known as the “tea leaf paradox”, already explained by Einstein [34], the absence of any primary rotary motion waken this hypothesis. We expect this flow to be generated by the existence of a viscous boundary layer at the external wall of the container. Moreover, a tangential motion, of the order of 5% of the solid rotation motion, is observed in opposite direction: positive for  $\tilde{d}_s=0.1$  and negative for  $\tilde{d}_s=0.2$ , in line with the trajectories followed by the liquid particles depicted in Fig. 4.10.

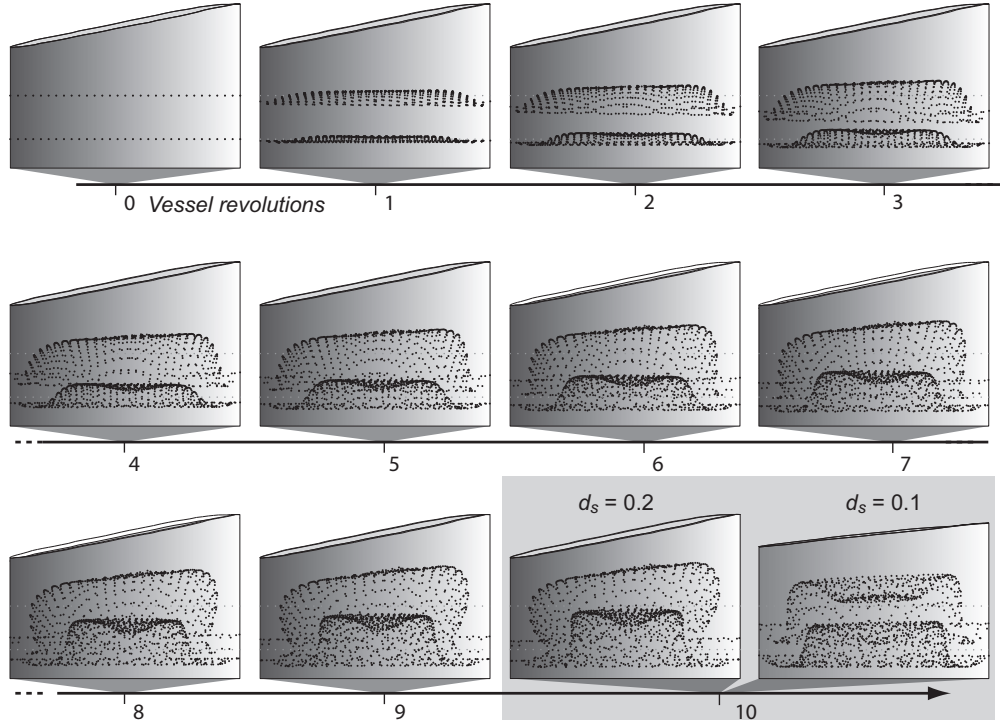


**Figure 4.11** | Positions of a large number of particles (black dots) after each vessel revolution.  $\tilde{d}_s=0.2$ ,  $\tilde{H}_0=0.5$  and  $Fr = 0.492$  ( $\Omega/\omega_{11} = 0.59$ ). The particles are released at  $t=0$  from two horizontal planes at  $z_0/H_0=0.2$  and  $z_0/H_0=0.4$ , depicted in the upper left image. The tenth revolution compares the position of the particles to those obtained with  $\tilde{d}_s=0.1$ ,  $Fr = 0.348$  (bottom right). The free surfaces shown above are retrieved from the measurements of the liquid height at the wall (Sec. 3.2).

The contribution of the average velocity fields to the motion of the liquid is emphasized in Fig. 4.11, where positions of liquid particles are followed for several revolutions of the vessel. The starting positions are on two horizontal planes, clearly visible in the first image at zero revolutions. The position after each revolution is shown for  $\tilde{d}_s=0.2$ , while only the positions at the tenth revolution are shown for  $\tilde{d}_s=0.1$ . According to the potential model predictions, the particles should return to the initial plane after each complete revolution. The formation of a mushroom cloud of particles highlights the motion of the slow convection cell.

### 4.2.1.2 Multiple crested waves

Although the linear potential solution captures the main phenomena of the single crested waves, it is unable to predict multiple crested waves, as those shown in Fig. 4.1b-d. They appear at very specific shaking configurations, and may change shape or disappear when the operating parameters are modified. We observe that the number of crests generally decreases as the shaking frequency is increased - an example is given in Fig. 4.1.

Amplitude spectra of the raw measurements of the liquid elevation at the wall are depicted in Fig. 4.12 for several waves with the arbitrarily chosen operating conditions  $\tilde{d}_s=0.13$ ,  $\tilde{H}_0=0.5$  and  $\Omega/\omega_{11}$  between 0.19 and 0.75. The amplitudes are normalized by the value at  $f=\Omega$ . The

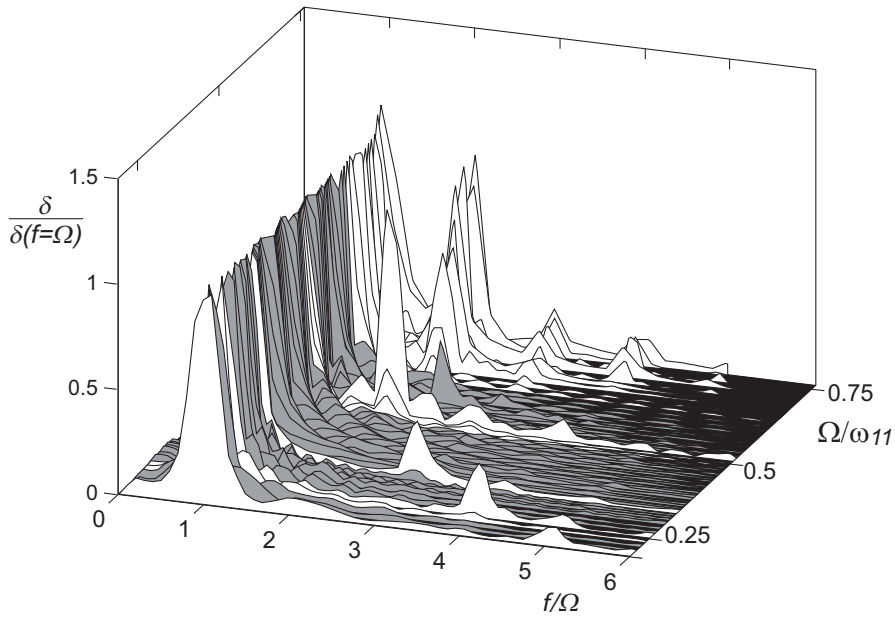


**Figure 4.12** | Amplitudes spectra of wave amplitudes measured at the container wall,  $\tilde{d}_s=0.13$ ,  $\tilde{H}_0=0.5$ . Spectra of visually recognised multiple crested and asymmetric waves are highlighted in white. We observe that their spectra show an increase of the amplitude at multiples of the shaking frequency.

spectra of the asymmetric and multiple crests waves are highlighted in white and clearly show the appearance of peaks at frequencies multiple of the shaking frequency  $\Omega$ . Therefore, multiple crested and asymmetric waves may be seen as the superposition of two or more sinusoidal waves with frequencies that are multiple of the shaking frequency.

However, we have presented in Sec. 2.3.2 the non-linear resolution of the potential model obtained considering the first non-axisymmetric mode (1, 1) as dominant. The solution predicts a sub-harmonic response of the mode (2, 1) at a half of the natural frequency  $\omega_{21}$ , with an amplitude of the order of  $A_{11}^2$  (where  $A_{11}$  is the amplitude of the main mode), as displayed in Fig. 2.10. Our analysis of the weakly non-linear waves is limited to  $O(A_{11}^2)^\dagger$ , and

<sup>†</sup>We use the notation  $O(\dots)$  to express the order of magnitude of a variable.

only the sub-harmonic at a half of the natural frequency  $\omega_{21}$  appears. This double crested wave is the most stable and the one displaying the most important amplitudes.

To determine the dominant modes, and their most relevant sub-harmonics, the waves measured at the wall  $\delta(\theta, t)$  are decomposed into a single crested part  $\xi_{1n}(D/2, \theta, t)$ , computed according to the linear prediction, and a sub-harmonic contribution:  $\delta_{sh}(\theta, t)$ , fitted (in the least squares sense) with the following generic wave expression:

$$\delta_{sh}(\theta, t) = \frac{A_{sh,p}}{2} \cos(p(\Omega t - \theta) + \phi_{sh,p}), \quad (4.5)$$

where  $p$  is an integer. The fitting determines the value of  $p$  best approximating the experimental data (smallest value of fitting residuals), and the corresponding amplitude  $A_{sh,p}/D$  and phase shift  $\phi_{sh,p}$ . In this way we identify the amplitude and phase shift of the most important secondary component of the wave. Several examples of the decomposition are given in dimensionless form in Fig. 4.13 where the measurements are depicted as black dots (with in grey the standard deviation), the linear solution of the potential model  $\tilde{\xi}_{1n}(D/2, \theta, \pi/\Omega)$  is a dotted line, the sub-harmonic wave ( $\tilde{\delta}_{sh} = \delta_{sh}(\theta, \pi/\Omega)/D$ ) is a dashed line and the composition of the two is a solid line. We observe a large variety of wave patterns, generated by different sub-harmonics of two modes, each with specific value of  $p$ ,  $A_{sh,p}$  and  $\phi_{sh,p}$ . It is also interesting to notice that equivalent values of  $p$  may result in completely different wave patterns, as illustrated by comparing Figs. 4.13a and 4.13b.

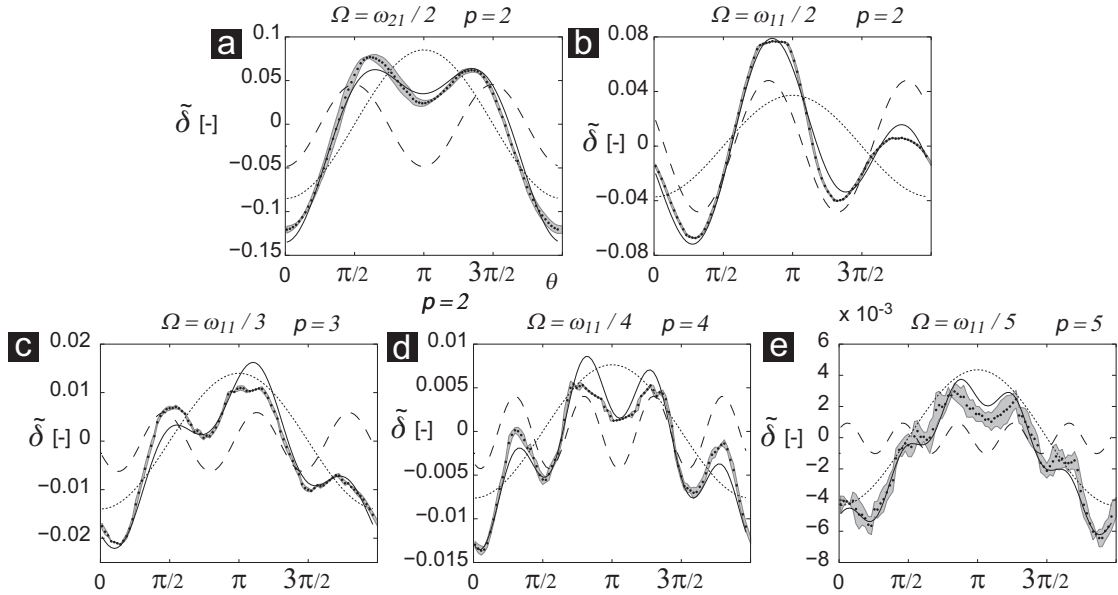


**Figure 4.13** | Phase averaged measurements of the free surface displacement ( $\tilde{\delta}$ , black dots and grey surface to depict the standard deviation) are compared with potential predictions (dotted lines), sub-harmonic waves (dashed line) and composition of both (continuous line). Amplitude  $A_{sh,p}$  and phase shift  $\phi_{sh,p}$  of the sub-harmonic waves are determined by fitting to the experimental data.



Figure 4.14 shows the value of  $A_{sh,p}$  corresponding to the value of  $p$  giving the best fitting to the measured wave, as a function of the shaking frequency, for  $\tilde{d}_s$  between 0.01 and 0.4. Note that the graph has three abscissae: corresponding to the shaking frequency  $\Omega$  normalized by three natural frequencies ( $\omega_{11}$ ,  $\omega_{21}$  and  $\omega_{12}$ ).

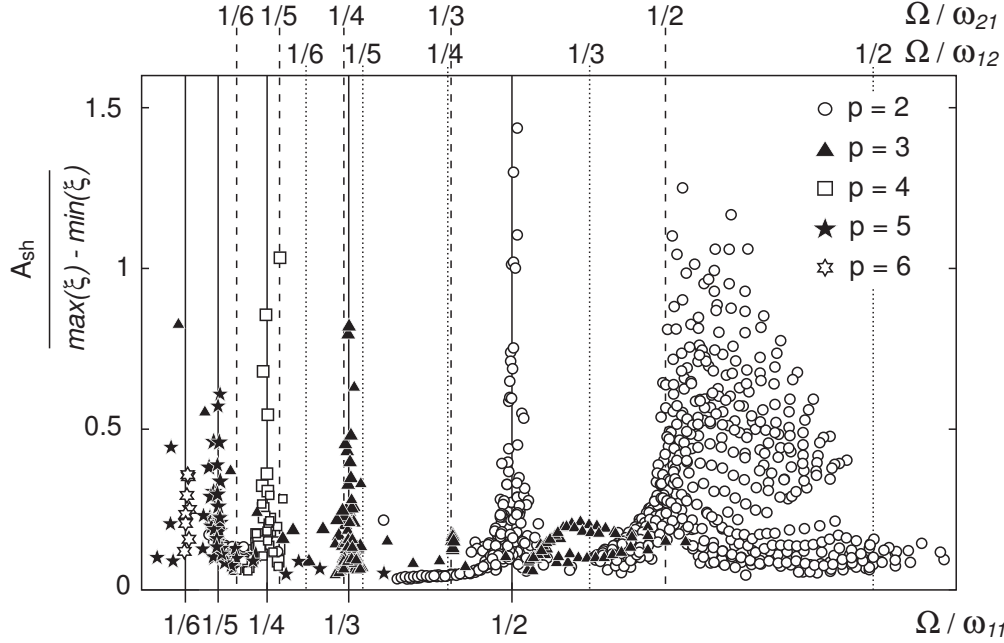


**Figure 4.14** | Amplitude of sub-harmonic waves as a function of  $\Omega$ , for  $\tilde{d}_s \in [0.01, 0.4]$  and  $\tilde{H}_0 = 0.5$ , expressed as a ratio to the amplitudes predicted by the linear potential model at the same shaking frequency. Two vessel sizes are represented here:  $D=144$  and  $287$  mm. The value of  $p$  is determined as the one giving the best fitting of Eq. 4.5 to the experimental data.

We notice that not only the sub-harmonics of the secondary mode (2, 1) are excited but also those of the main mode (1, 1) and of the mode (1, 2). In fact, the sub-harmonics of the lowest natural frequency  $\omega_{11}$  are excited as far as the sixth sub-harmonics. In several cases the sub-harmonic of a mode is close to sub-harmonic of another one, e.g.  $\omega_{11}/3$  and  $\omega_{21}/4$ . In this case we observe that the lowest natural frequency (i.e.  $\omega_{11}$ ) has a dominant amplitude, but both sub-harmonics are nevertheless excited. Figure 4.15 shows the amplitude spectra of the waves around  $\Omega = \omega_{11}/3$ , and clearly reveals the presence of both sub-harmonics at very close values of the shaking frequencies.

The evolution of the phase shift  $\phi_{sh,p}$  is illustrated in Fig. 4.16, at shaking frequencies close to the sub-harmonics of the first natural frequency, for  $\tilde{d}_s$  between 0.01 and 0.4. We note that the phase shift value experiences a  $\pi$  change as the shaking frequency crosses a sub-harmonic frequency, as it is expected from the response of a system excited around its resonance frequency. However, the value before and after the fraction of the natural frequency appears to be different in each case: e.g.  $\phi_{sh,p}$  changes from  $-\pi/3$  to  $-4\pi/3$  for the double crests waves at  $\omega_{11}/2$  while it changes from 0 to  $-\pi$  for the triple crests waves at  $\omega_{11}/3$ .



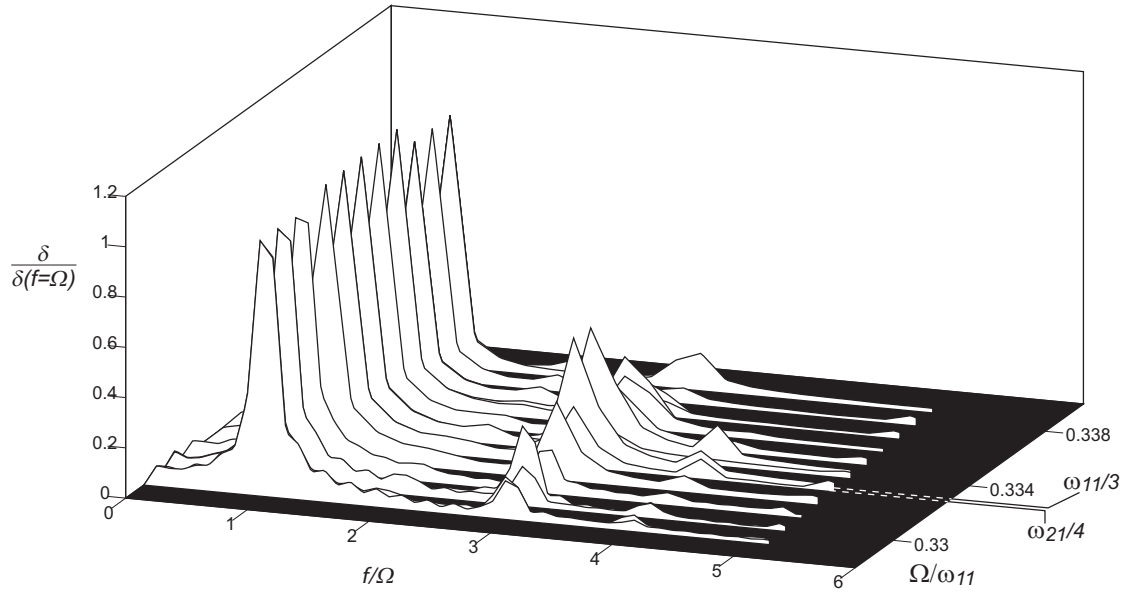


**Figure 4.15** | Amplitude spectra of waves at shaking frequencies around  $\Omega = \omega_{11}/3$  and  $\omega_{21}/4$ , for  $\tilde{d}_s$  ranging from 0.02 to 0.2,  $\tilde{H}_0=0.52$ . Both sub-harmonics are excited at very similar frequencies, creating waves (Fig. 4.13c) where the  $\omega_{11}/3$  perturbation dominates and the  $\omega_{21}/4$  is also present, with a smaller amplitude.

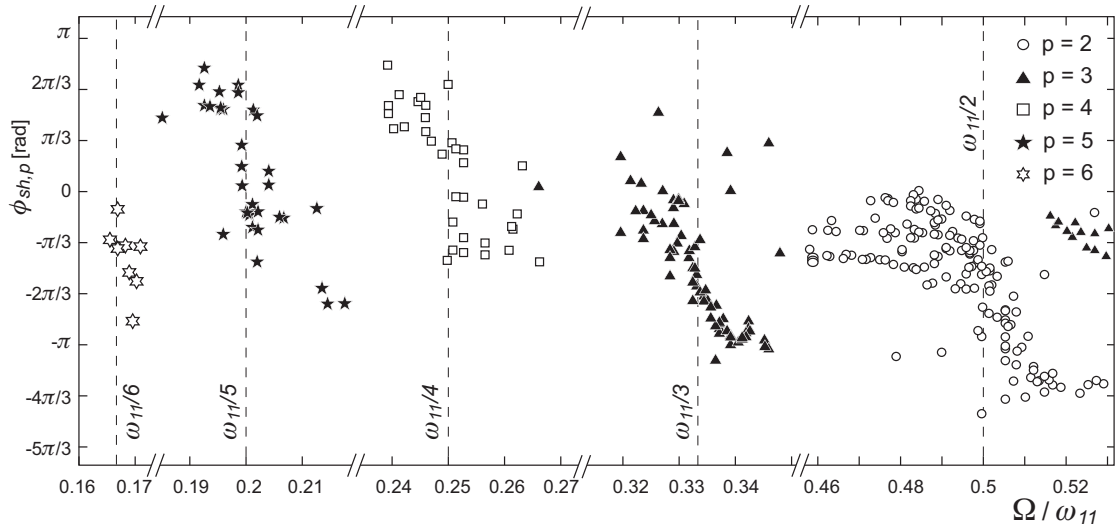


**Figure 4.16** | Phase shift  $\phi_{sh,p}$  of sub-harmonic waves as a function of  $\Omega/\omega_{11}$ , for  $\tilde{d}_s \in [0.01, 0.4]$ ,  $\tilde{H}_0=0.5$  and  $D=144$  and  $287$ mm. The value of  $p$  is determined as the one giving the best fitting of Eq. 4.5 to the experimental data. Note that the abscissa is not continuous in order to enhance readability of the data.

Having demonstrated that the multiple crested waves originate from the combination of sub-harmonics of the natural modes, and having identified the most dominant modes (namely (1, 1), (2, 1) and to a less extent (1, 2)), we are able to compare their behaviour with the predictions of the non-linear model. Figure 4.17 compares the measured wave height at the wall with the linear (dashed line) and non-linear (solid line) results of the potential model. We observe that at low shaking diameter ( $\tilde{d}_s=0.06$ , Fig. 4.17a-d) the non-linear model correctly predicts the amplitude of the sub-harmonic wave at shaking frequencies both below and above  $\omega_{21}/2$ . On

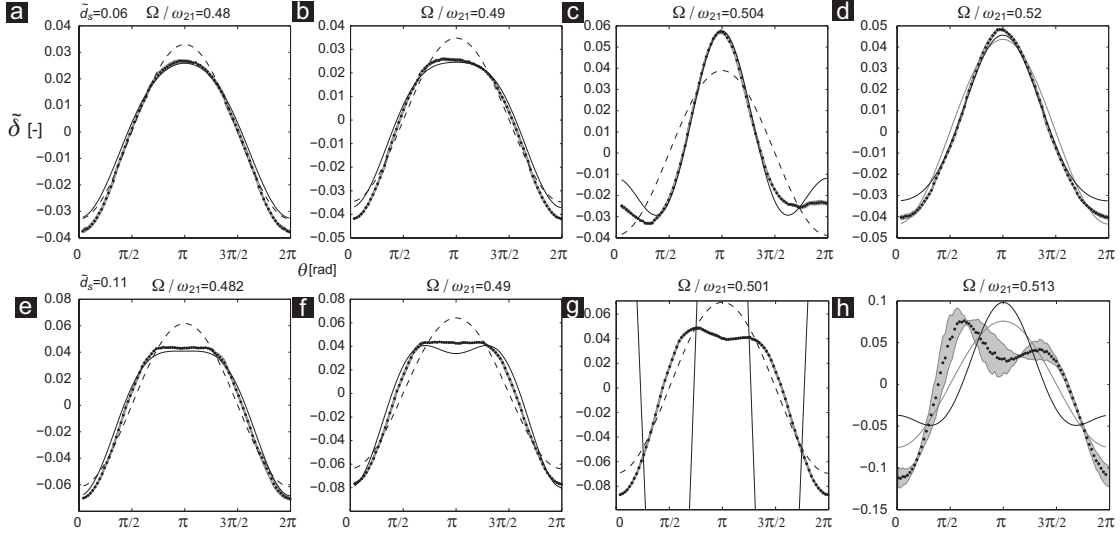


**Figure 4.17** | Measurements of sub-harmonic waves at  $\Omega$  around  $\omega_{21}/2$  (depicted as black dots, with standard deviation depicted in gray) compared to the prediction of the linear (dashed line) and of the non-linear model (solid line), with  $\tilde{H}_0=0.5$ . **a:**  $\tilde{d}_s=0.06$ ,  $\Omega = 0.478\omega_{21}$ . **b:**  $\tilde{d}_s=0.06$ ,  $\Omega = 0.489\omega_{21}$ . **c:**  $\tilde{d}_s=0.06$ ,  $\Omega = 0.504\omega_{21}$ , note the change of phase of the wave and the increase. **d:**  $\tilde{d}_s=0.06$ ,  $\Omega = 0.521\omega_{21}$ . **e:**  $\tilde{d}_s=0.11$ ,  $\Omega = 0.482\omega_{21}$ . **f:**  $\tilde{d}_s=0.11$ ,  $\Omega = 0.49\omega_{21}$ . **g:**  $\tilde{d}_s=0.11$ ,  $\Omega = 0.501\omega_{21}$ , the non-linear amplitude tends to infinity, hence giving the almost vertical line depicted. **h:**  $\tilde{d}_s=0.11$ ,  $\Omega = 0.513\omega_{21}$ , note that the measured wave does not change phase.

the other hand, as  $\tilde{d}_s$  is increased, the non-linear model predicts only the behaviour of the wave at shaking frequencies below the sub-harmonic one, as shown in Fig. 4.17e-f, whereas above  $\omega_{21}/2$  the wave displays a persistence of double crested shape (Fig. 4.17h), and the change of sign of the amplitude of the sub-harmonic wave predicted by the model is not observed. The shaking frequency until which the wave remains double crested depends also on the shaking diameter.

As we have already stated, the non-linear solution of the potential model predicts only one of the several multiple crested waves observed. We expect the others (namely the subharmonics of the mode (1, 1)), to be predicted solving the non-linear equations using different hypothesis on the dominant and secondary modes, and to an higher order.

Considering the influence of the operating parameters on the sub-harmonics waves we notice that, according to the potential model, the amplitudes of the sub-harmonics are of the order of the square of the amplitude of the main wave. They hence increase with  $\tilde{d}_s^2$ . On the other

hand, the filling ratio  $\tilde{H}_0$  has not a direct influence on the amplitude, but affects the value of the natural frequencies (according to Eq. 2.48). This influence is especially effective when  $2\varepsilon_{mn}\tilde{H}_0 < 2$ , whereas above this limit the natural frequencies are almost independent of the filling ratio.

The influence of the sub-harmonic wave is clearly visible in the trajectories followed by the particles, computed from PIV measurements, as depicted in Fig. 4.18: the upper part of the trajectories is deformed by the superposition of linear and sub-harmonic velocity fields. At the shaking frequency of this wave ( $\Omega > \omega_{21}/2$ ) the potential model predicts a single crested wave with a very high crest, as the one shown in Fig. 4.17c. The trajectories (and the wave pattern) are nevertheless those of a double crested wave at shaking frequencies smaller than  $\omega_{21}/2$ .

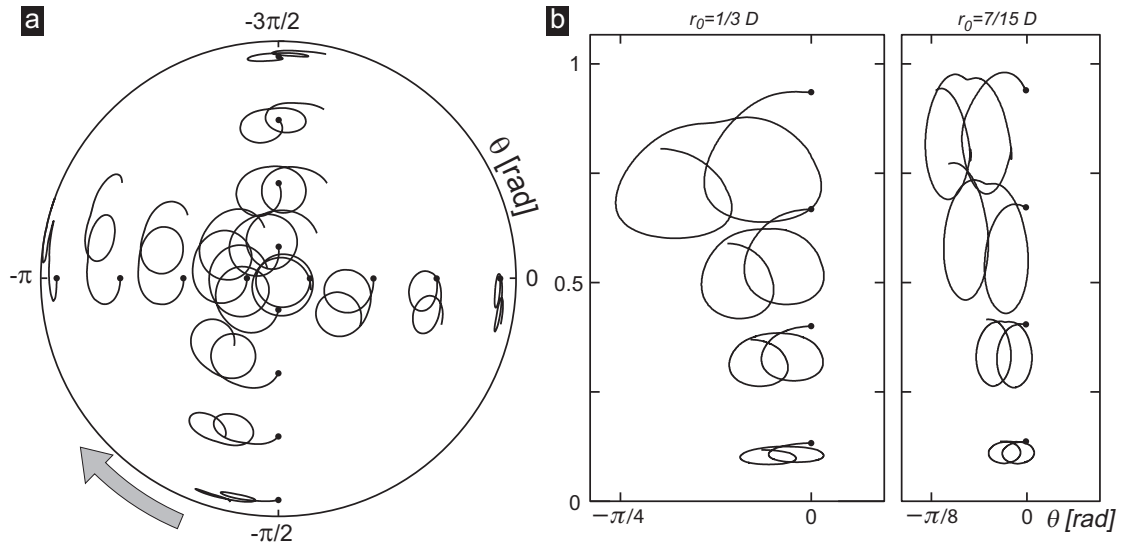


**Figure 4.18** | Trajectories from PIV measurements followed by particles at  $\tilde{d}_s=0.2$ ,  $\tilde{H}_0=0.5$ ,  $Fr=0.58$  ( $\Omega/\omega_{11}=0.692$ ,  $\Omega/\omega_{21}=0.52$ ). Starting points are identified by a black dot. **a:** view from above, projected in the  $r-\theta$  plane,  $r_0/D=1/15, 1/5, 1/3$  and  $7/15$ ,  $\theta_0=0, \pi/2, \pi$  and  $3\pi/2$ ,  $z_0/D=1/4$ . **b:** projection in the  $\theta-z$  plane,  $r_0/D=1/3$  and  $7/15$ ,  $\theta_0=0$ ,  $z_0/D=1/15, 1/5, 1/3$  and  $7/15$ .

As the shaking frequency is increased above a value of  $\omega_{mn}/p$ , the sub-harmonic wave should experience the reported phase shift, then decreases and disappears - the flow returns usually to the linear behaviour. This is not always the case. Indeed, the most flagrant example is observed at  $\Omega > \omega_{21}/2$ . For  $\tilde{d}_s$  below 0.1 the wave returns to potential behaviour, while for  $\tilde{d}_s > 0.1$  remains double crested and increases in amplitude, as we clearly see in Fig. 4.19.

In fact, we are approaching a boundary between two very distinct flow behaviours: non-breaking and breaking waves. Depending on the value of  $\tilde{d}_s$ , the wave reaches a breaking condition, which changes the regime of the flow, and prevents the wave to return to potential behaviour. The breaking of the waves is thoroughly discussed in the next section.

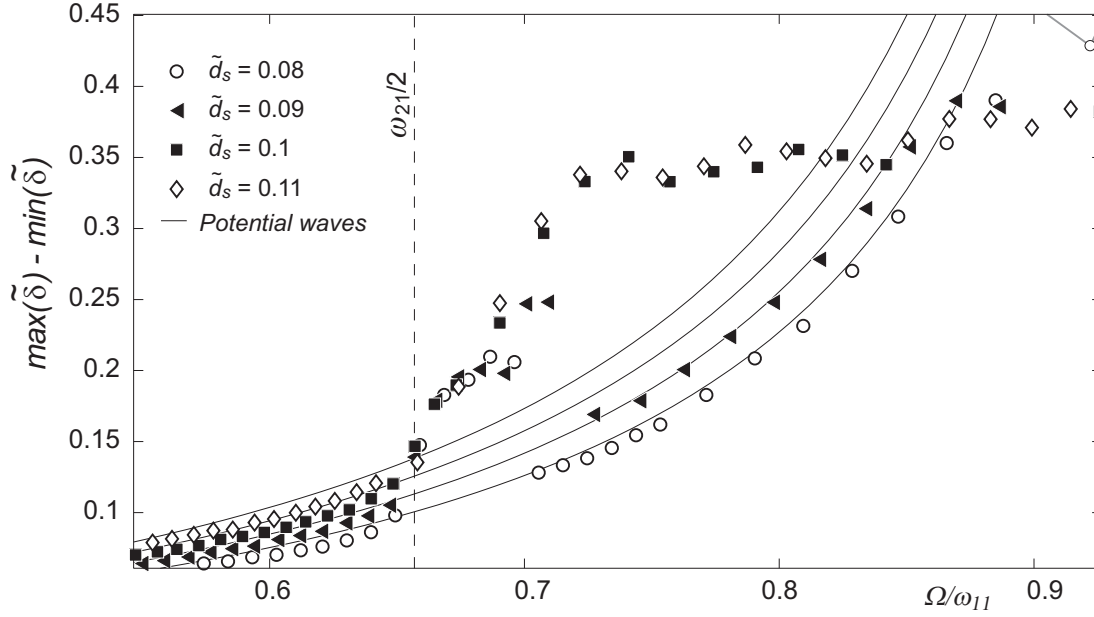


**Figure 4.19** | Amplitude of waves between the apparition of sub-harmonic double crested waves ( $\omega_{21}/2$ , vertical dashed line) and the first natural frequency ( $\omega_{11}$ ). Four values of  $\tilde{d}_s$  are represented with different markers. The black solid lines are the amplitudes given by the linear potential model.

#### 4.2.2 Toward breaking waves

The breaking of water gravity waves has been extensively studied, from mathematical [101, 41], experimental [20, 90] and numerical points of view. The resolution of the gravity waves equations at orders higher than the first demonstrates the existence of a limiting steepness beyond which no gravity wave can exist, thus introducing a threshold for the breaking of the wave [95, 41]. As research on wave breaking progressed, it was found that various instabilities are liable to develop before this limit is attained [105, 71, 85, 72]. Breaking is traditionally categorized into three types: collapsing (occurring at the water's edge), spilling (as the wave steepens, it becomes unstable, with turbulent and aerated water spilling down over the front face) and plunging (where the upper part of the crest forms a jet plunging ahead of the wave, the surfer's waves) [10, 11]. Wave breaking is also an important phenomenon in air-liquid interaction [76], a consideration which is very interesting in the light of increasing the gas exchange between the liquid and the surrounding atmosphere.

The theoretical limiting steepness for gravity waves is  $H/\lambda \cong 0.1412$ , where  $H$  is the crest-to-trough amplitude and  $\lambda$  is the wavelength [94]. In the specific case of our orbitally shaken container we have:

$$\frac{H}{\lambda} = \frac{\max(\delta) - \min(\delta)}{\pi D} \cong 0.1412 \quad \Rightarrow \quad \max(\tilde{\delta}) - \min(\tilde{\delta}) \cong 0.443. \quad (4.6)$$

This is the upper limit at which waves should break. Figure 4.20a, which is a zoomed view of

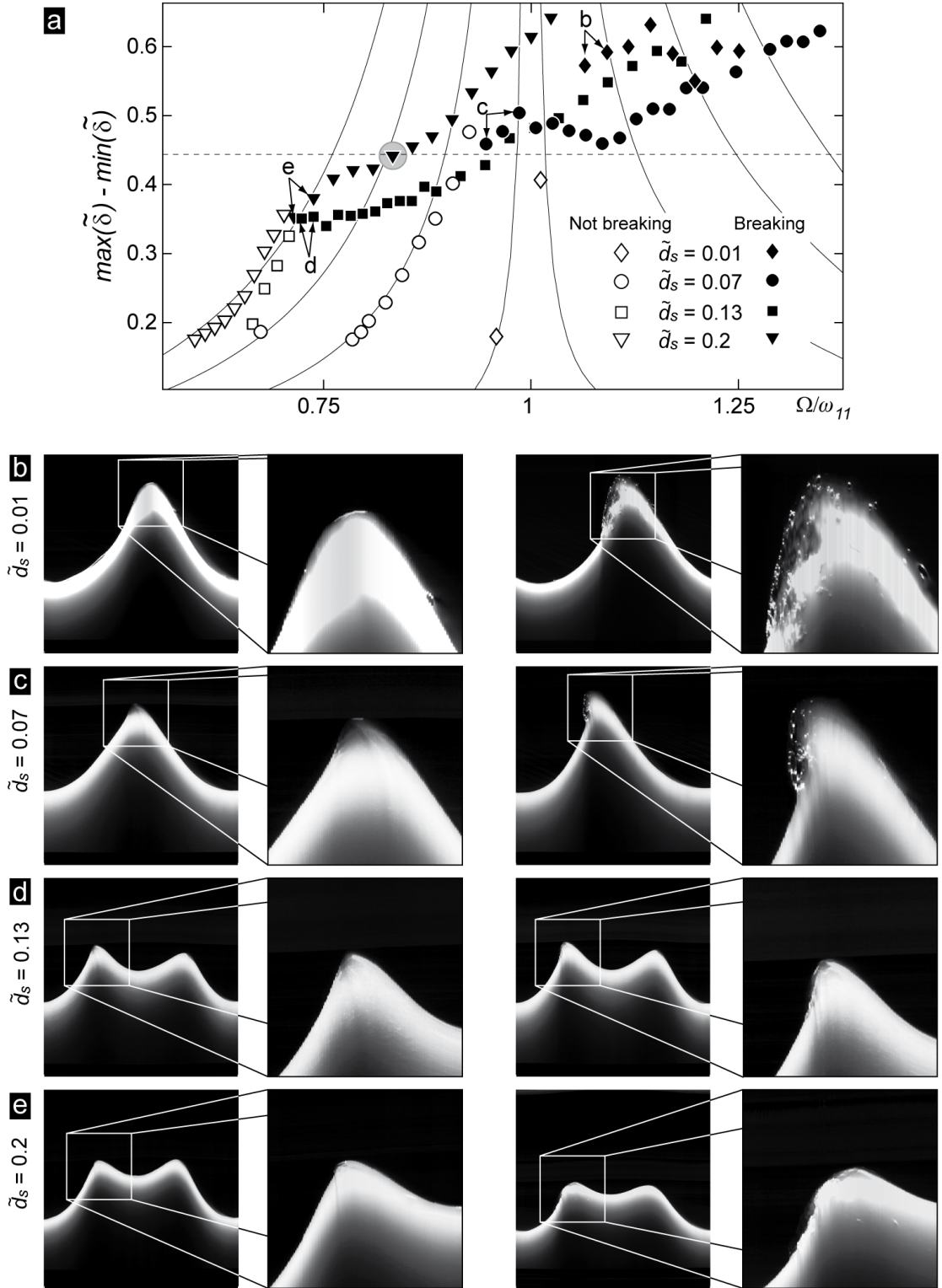


**Figure 4.20** | **a**: dimensionless amplitude of the waves around the transition to the breaking, at four  $\tilde{d}_s$ . Breaking waves are depicted with black markers, while non-breaking with white markers. The predicted amplitude limit (Eq. 4.6) is depicted as a dashed line. **b**: images of the wave, and details of the crest, at the inception (right) and breaking (left).  $\tilde{d}_s=0.01$ ,  $\Omega/\omega_{11}=1.07$  (left),  $\Omega/\omega_{11}=1.09$  (right). **c**:  $\tilde{d}_s=0.07$ ,  $\Omega/\omega_{11}=0.926$  (left),  $\Omega/\omega_{11}=0.966$  (right). **d**:  $\tilde{d}_s=0.13$ ,  $\Omega/\omega_{11}=0.708$  (left),  $\Omega/\omega_{11}=0.724$  (right). **e**:  $\tilde{d}_s=0.2$ ,  $\Omega/\omega_{11}=0.714$  (left),  $\Omega/\omega_{11}=0.738$  (right).

Fig. 4.7, depicts the amplitude of the wave as a function of the shaking frequency. A change of behaviour is clearly visible when the wave reaches amplitudes between 0.35 and 0.45, hence when the waves break. The wave breaking is initially visible only at the wave crest (Fig. 4.20b-e left), in the form of a small splash of water at the wall. In multiple crested waves the breaking appears at the steepest crest, usually the front one (Fig. 4.20d-e). The breaking then becomes more generalized (Fig. 4.20b-e right), and we observe spilling breakers, with entrainment of large air bubbles into the liquid. As  $\Omega$  is further increased the “white water” at the crest spreads down over the front slope and the wave loses its symmetry. The breaking starts at the wall, where the wave is steeper, and propagates to a limited extent (usually less than one third of the radius) toward the centre of the container.

We observe that multiple crested waves break at amplitudes lower than single crested ones. Moreover, although both kinds of waves display similar behaviours at the crest, the liquid bulk has somehow different reactions to the breaking. It is therefore more convenient to distinguish between single and multiple crested waves.

### 4.2.2.1 Breaking of single crested waves

We have seen how the waves are composed by the sum of a main sinusoidal wave (the linear solution of the potential equations) and several other waves, with amplitude of the order of a power of the main wave, and with a wavelength which is a fraction of the one of the main wave. The non-linear solution of the potential model, solved to the second order, predicts one of those smaller waves, with an amplitude  $O(A_{11}^2)$  and a wavelength equivalent to half of the main wave. As the wave increases in amplitude the ratio between the amplitudes of smaller waves and of the main one increases. The composition of waves with different wavelengths and increasing amplitudes leads to a singularity of the free surface, thus to breaking. It is with this approach that the limiting steepness was estimated in water waves. Figure 4.21 depicts the liquid height at the wall compared to the linear (dashed line) and non-linear (solid line) predictions.

We observe (in Fig. 4.21b) that, approaching the natural frequency, the wave becomes steeper than the linear sinusoid solution. As  $\Omega$  is further increased, the second-order non-linear prediction also loses its agreement with the measurements (Fig. 4.21c), and the wave breaks. When we are even closer to the natural frequency (Fig. 4.21d), the amplitude of both potential solutions tends to infinity, hence they are visualized in the graph as almost vertical lines. The wave is clearly breaking. We notice also that after the inception of the breaking the amplitude of the wave is slightly reduced, e.g. in Fig. 4.20a for  $\tilde{d}_s=0.07$ . This is due to the increased dissipation in the breaker [106, 10]. As the shaking frequency is further increased the amplitude restarts growing.

Although during breaking most of the flow remains potential, a rotational region is created at the crest with a motion in the direction of the wave propagation [80]. Due to the viscosity, the liquid bulk is also entrained. In the present case of orbital shaken liquids, we observe

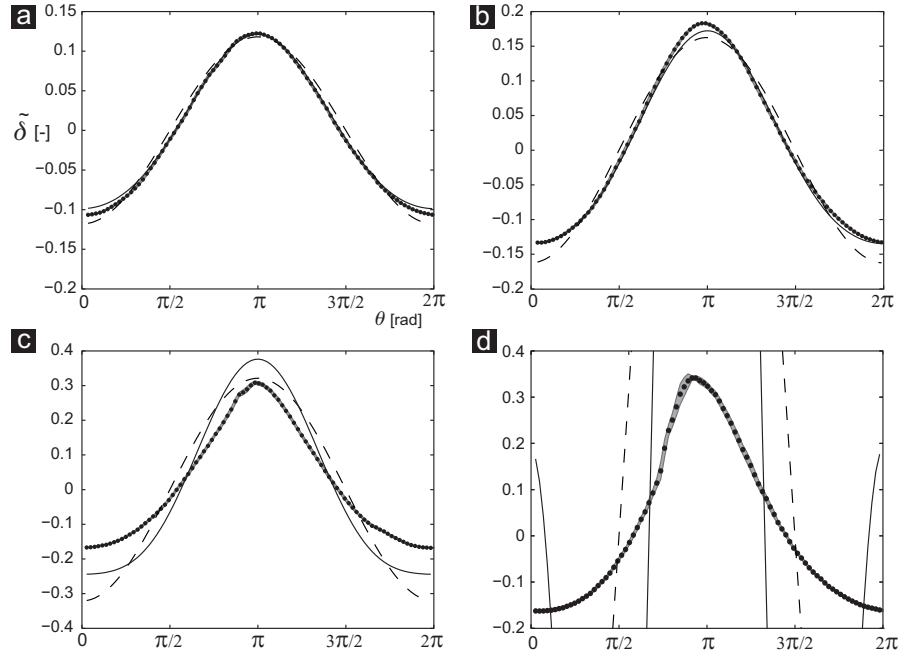


**Figure 4.21** | Wave measurements (black dots) compared with linear solution prediction (dashed line) and second order non-linear prediction (solid line) at  $\tilde{d}_s=0.07$ ,  $\tilde{H}_0=0.5$ , **a:**  $\Omega/\omega_{11}=0.825$ . **b:**  $\Omega/\omega_{11}=0.865$ . **c:**  $\Omega/\omega_{11}=0.925$ . **d:**  $\Omega/\omega_{11}=0.986$ .

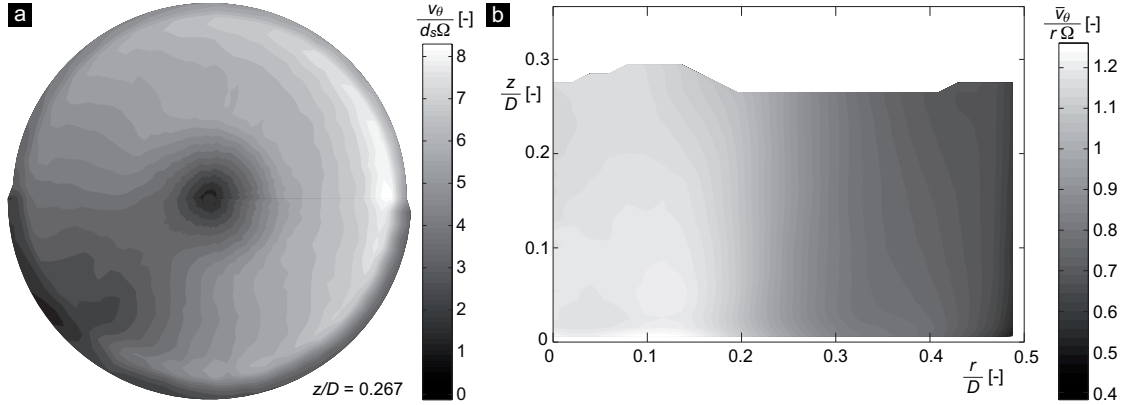


**Figure 4.22** | Tangential velocity at the breaking of a single crested wave, from PIV measurements, at  $\tilde{d}_s=0.1$ ,  $\tilde{H}_0=0.5$ ,  $Fr=0.401$ ,  $\Omega/\omega_{11}=0.83$ . **a:** tangential velocity normalized by the shaking tangential velocity, measured on a horizontal plane at  $z/D=0.267$ . **b:** tangential velocity averaged over one revolution, normalized by the solid rotation velocity, in vertical-radial plane. Note that the grey shading does not correspond to the same values in both graphs.

that a swirling motion is imposed to the whole flow. Figure 4.22 shows the tangential velocity  $v_\theta$  at the transition to the breaking, from PIV measurements. As the tangential velocity is depicted on a horizontal plane (Fig. 4.22a), we observe a strong rotational (or swirl) motion that superposes to the sinusoid velocity field of the wave motion, which in turn disappears toward the axis of the container. The rotation is so strong that the motion of the flow is unidirectional in the tangential direction: the whole liquid rotates in the direction of the propagation of the wave, at angular velocities depending on the radius. Figure 4.22b shows the tangential velocity averaged over one revolution (as described in Eq.4.4) and normalized by the velocity of solid rotation  $d_s\Omega$ . The values are shown on a vertical plane and we observe that the rotation is nearly linear from the container revolution axis to  $r \cong d_s$ , where it attains its maximum and then decreases with increasing radius. The rotation is very strong: in average it surprisingly exceeds the velocity of synchronous rotation.

### 4.2.2.2 Breaking of multiple crested waves

Breaking of multiple crested waves is observed particularly at the first sub-harmonic of the (2, 1) mode: the double crested wave at  $\Omega = \omega_{21}/2$ . The sub-harmonic perturbation maintains the double crested shape after  $\omega_{21}/2$  if  $\tilde{d}_s > 0.07$  (see also Sec. 4.2.1.2). As the shaking frequency is increased, those waves display a steepness at the front crest that is larger than the one of single crested wave at the close operating conditions. The breaking phenomena described for the single crested wave are thus noticed only at the first crest.

Since the breaking is localized at crest, the rotational part has a smaller influence than in single crested waves: Fig. 4.23 depicts the LDV measured velocities of a double crested wave whose front crest is breaking. We clearly observe the perturbation of the velocity fields due to the sub-harmonic, especially near the free surface (Fig 4.23a), where the velocity profile is given by the superposition of two sine waves, one having a smaller amplitude and a wavelength double than the other one. Moreover, we notice that the tangential velocity  $v_\theta$  has a non-zero mean component. However, the tangential velocity fields (Fig. 4.23c) show that the wave motion is not completely dominated by the rotation, since we have both positive and negative values. Moreover, the average tangential velocity (Fig. 4.23d) has values considerably smaller than those measured at the breaking of the single crest wave.

Figure 4.24 illustrates the trajectories followed by liquid particles in the case of a single crested at the inception of the breaking (dashed line). We superpose also the trajectories of a double crested wave (solid line), at a shaking frequency slightly above the breaking threshold. We notice the strong rotation of the liquid induced by the single crested wave, but also the large displacement it imposes to the particles in the vertical direction near the container vertical axis (Fig. 4.24b). Moreover, the radial motion is almost suppressed, while it remains visible in the double crested wave (Fig. 4.24a). This confirms again the dominance of the swirl motion on the breaking of single crested waves.

According to the solutions of the potential model, at every sub-harmonic of a natural fre-



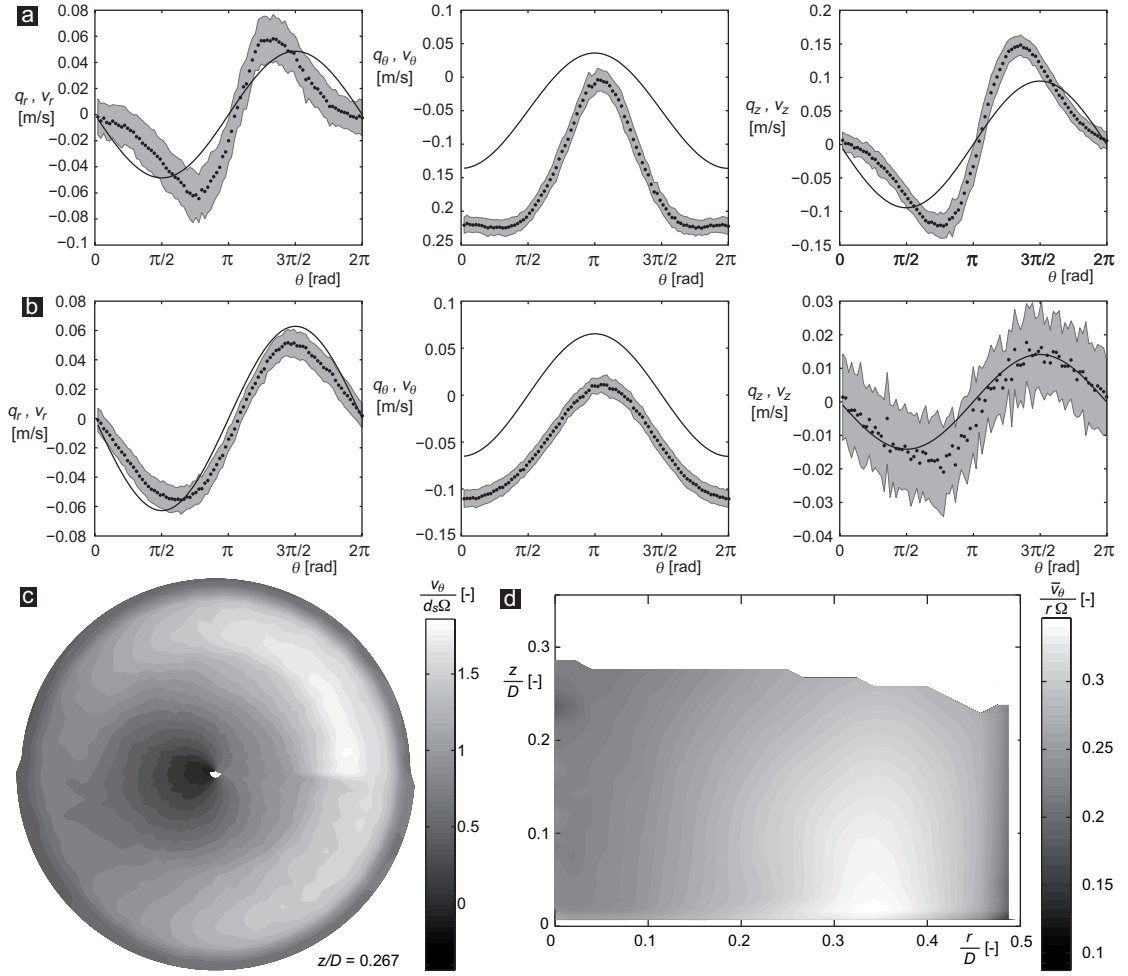


**Figure 4.23** | Velocity measurements of double crested wave at breaking inception **a:** LDV velocity fields measurements of the three component of the velocity, phase averaged over several vessel revolution (black dots) and linear potential predictions (solid line), for  $\tilde{d}_s = 0.174$ ,  $\tilde{H}_0 = 0.7$  and  $Fr = 0.6$  ( $\Omega/\omega_{11} = 0.75$ ), at  $r/D = 0.348$  and  $z/H_0 = 0.5$ . **b:** LDV measurements at  $r/D = 0.104$  and  $z/H_0 = 0.25$ . **c:** dimensionless tangential velocity  $\tilde{v}_\theta$  from PIV measurements in a horizontal plane at  $z/D=0.26$ , for  $\tilde{d}_s = 0.2$ ,  $\tilde{H}_0 = 0.5$  and  $Fr = 0.695$  ( $\Omega/\omega_{11} = 0.83$ ). **d:** average tangential velocity  $\bar{v}_\theta$ .

quency the amplitude of the concerned mode should increase to infinity, hence we should observe breaking at every sub-harmonic frequency. However, due to the viscous damping, the amplitude is (luckily) less than infinity, thus only multiple crested waves with sufficient amplitude break. We have identified a critical shaking diameter  $\tilde{d}_{s,\omega_{21}/2}$  below which the double crested wave generated by the sub-harmonics at  $\Omega = \omega_{11}/2$  disappears and the wave breaks as a single crested one. Conversely, for shaking diameters above this value the wave breaks as double crested. Similar behaviour is observed for the double crested waves generated at

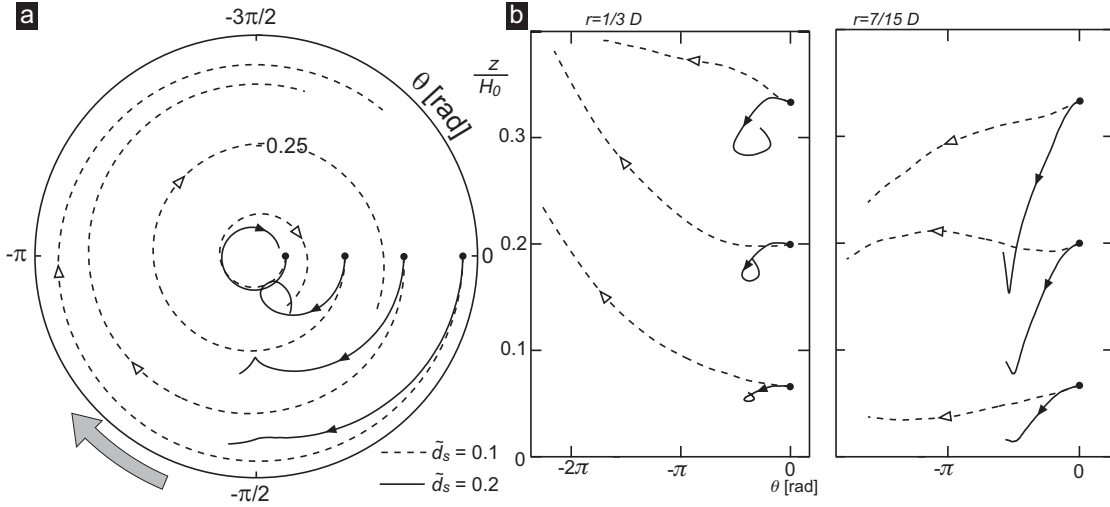


**Figure 4.24** | Trajectories from PIV measurements followed by particles released at black dots locations, followed during one revolution of the container. Solid line are from double crested wave:  $\tilde{d}_s=0.2$ ,  $\tilde{H}_0=0.5$ ,  $Fr=0.695$  ( $\Omega/\omega_{11}=0.83$ ), while dashed lines are from single crested wave:  $\tilde{d}_s=0.1$ ,  $\tilde{H}_0=0.5$ ,  $Fr=0.491$ ,  $\Omega/\omega_{11}=0.83$ . **a:** projection of the trajectories in a horizontal plane at  $z_0/D=0.25$ . **b:** projections on the  $r-\theta$  plane, from two different starting points:  $r_0/D=1/3$  and  $r_0/D=7/15$ .

$\Omega = \omega_{11}/2$ . According to our investigation, these limits may be empirically predicted as:

$$\tilde{d}_{s,\omega_{21}/2} = 0.1349 \cdot \tanh^2(2.5\tilde{H}_0) \quad \text{and} \quad (4.7)$$

$$\tilde{d}_{s,\omega_{11}/2} = 0.4281 \cdot \tanh^2(2.82\tilde{H}_0). \quad (4.8)$$

Moreover, low filling values reduce the first natural frequency, thus causing the wave to break at lower  $\Omega$ .

Although all the previous considerations are generally valid regardless the dimension of the experiment, we have observed that, at those particular transitions, the size of the container may affect the threshold values. Figure 4.25 compares the measurements of the wave amplitude  $\tilde{\delta}(\theta)$  at  $D=144$  and at  $287\text{mm}$ , with a filling ratio  $\tilde{H}_0=0.52$  and a shaking diameter  $\tilde{d}_s=0.1$ , which is the limit between waves returning to single crested and waves breaking as double crested. In the smaller experiment ( $D=144\text{mm}$ ) the wave returns single crested before breaking, hence following the behaviour of a wave having  $\tilde{d}_s < \tilde{d}_{s,\omega_{21}/2}$ , while in the larger experiment we observe a persistence of the double crests wave, which breaks. It should be noted that both waves are non-synchronous at  $\Omega$  slightly above  $\omega_{21}/2$  before becoming synchronous but different.

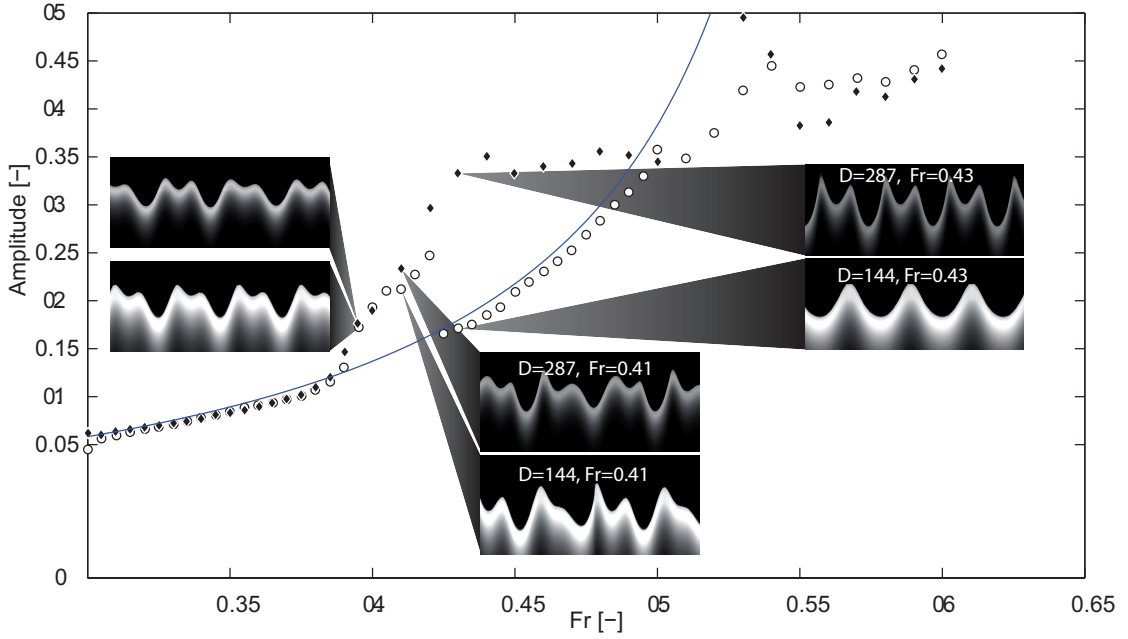


**Figure 4.25** | Behaviour of the wave at two different scales of the experiment:  $D=144$  and  $287\text{mm}$ , with  $\tilde{d}_s=0.1$  and  $\tilde{H}_0=0.5$ . The wave in smaller experiment ( $D=144\text{mm}$ ) returns to single crested before breaking, whereas in the bigger one we observe a persistence of the double crests wave, which breaks. Both waves are also observed non-synchronous before reaching their respective synchronous conditions.

### 4.2.3 After the breaking of the waves

After the breaking of the wave crest, the liquid motion (free surface and bulk) undergoes deep changes. To highlight the contrast with the potential model, which describes the flow at shaking frequencies below the breaking inception and appears to be inappropriate above it, we define the present regime as rotational or swirling.

Figure 4.26a depicts the evolution of the wave amplitude at the wall for four values of  $\tilde{d}_s$  corresponding to single crested ( $\tilde{d}_s=0.04$  and  $0.07$ ) and double crested ( $\tilde{d}_s=0.13$  and  $0.2$ ) waves, while in Figs. 4.26b-c are shown the images of the waves at  $\tilde{d}_s=0.04$  and  $0.2$ . As already reported, the amplitude of single crested waves slightly decreases after the breaking, then monotonously increases with the shaking frequency. Multiple crested waves break at lower amplitudes, and the amplitude monotonously increases with the shaking frequencies. At shaking frequencies above the natural frequency  $\omega_{11}$  the breaking of single crested wave spreads to the entire front slope, and the liquid at the wall has a distribution more similar to a splash than a wave (Fig. 4.26b). On the other hand, the sub-harmonic wave giving the double crests gradually disappears (Fig. 4.26c), and completely vanishes before reaching  $\omega_{11}$ . At the natural frequency  $\omega_{11}$  the amplitude of multiple crested waves do not increase, confirming that the flow is not following the prediction of the potential model. As the shaking frequency increases, the morphology of single and multiple crested waves becomes similar notwithstanding the number of crests at the breaking transition. The crest and especially the trough of the wave experience a

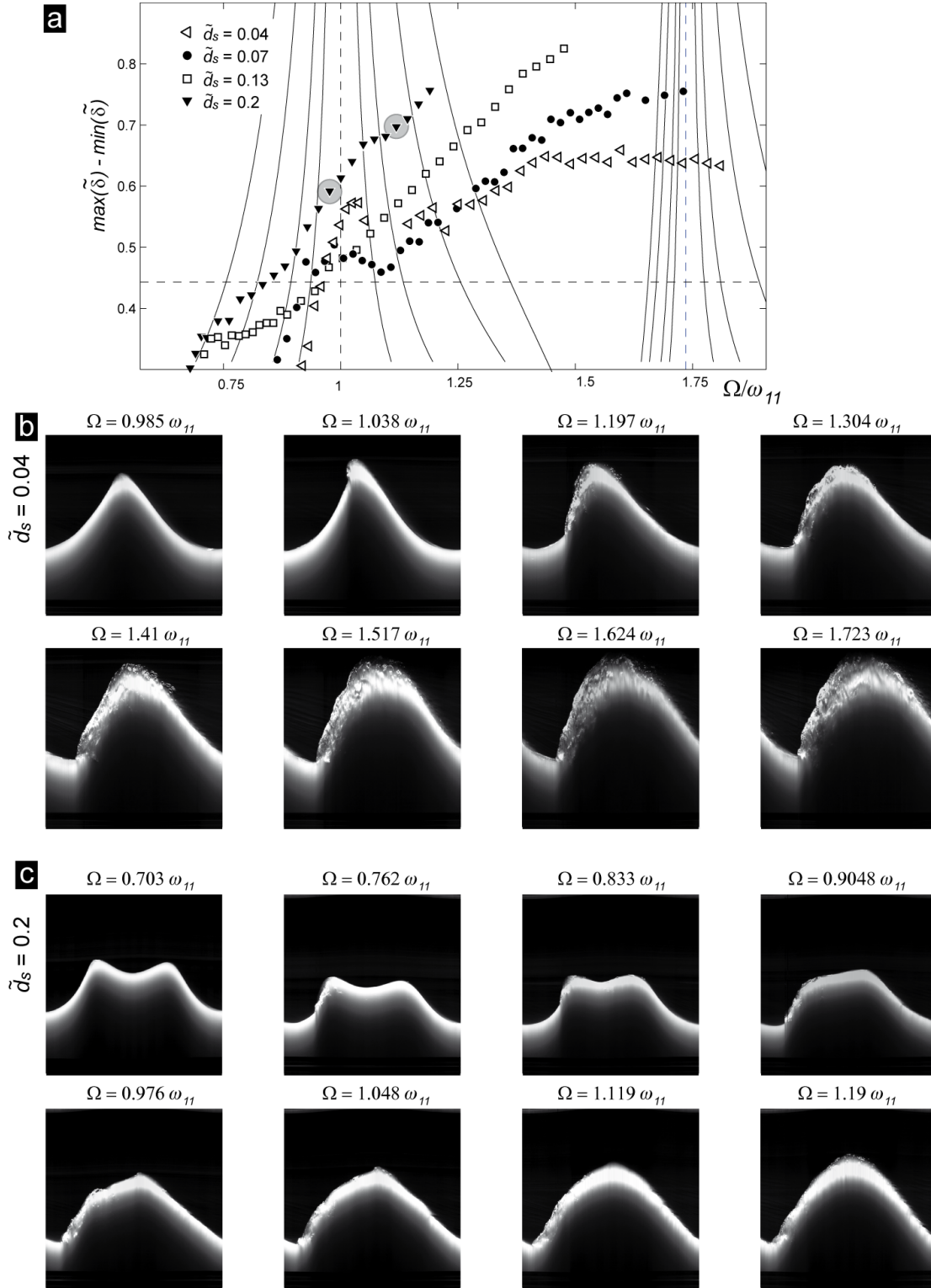


**Figure 4.26 | a:** dimensionless amplitude of breaking waves, at four  $\tilde{d}_s$ . The predicted amplitude limit (Eq. 4.6) is depicted as a dashed line, and the amplitudes of the waves whose trajectories are shown in Fig. 4.29 are highlighted by grey circles. **b:** evolution of the breaking wave with  $\tilde{d}_s=0.4$  and **c:**  $\tilde{d}_s=0.2$ .

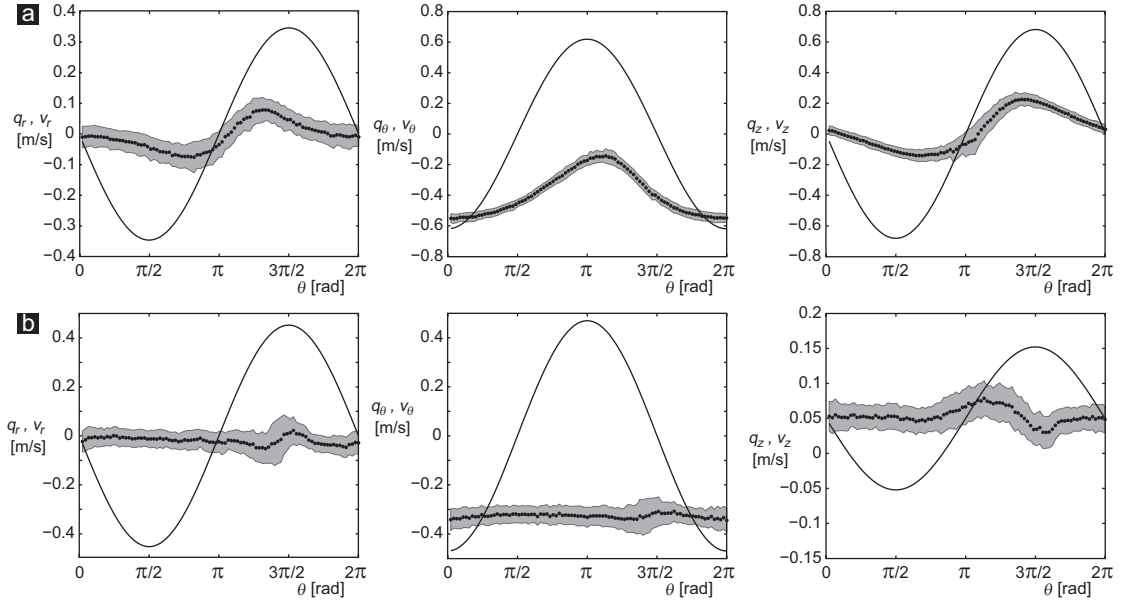


**Figure 4.27** | Phase averaged LDV measurement (black dots) and potential prediction (solid line) of the three component of the velocity at  $\tilde{d}_s = 0.174$ ,  $\tilde{H}_0 = 0.7$  and  $Fr = 0.748$  ( $\Omega/\omega_{11} = 0.939$ ). **a:** Measurements at  $r/D = 0.348$  and  $z/H_0 = 0.5$ . **b:** Measurements at  $r/D = 0.104$  and  $z/H_0 = 0.25$ .

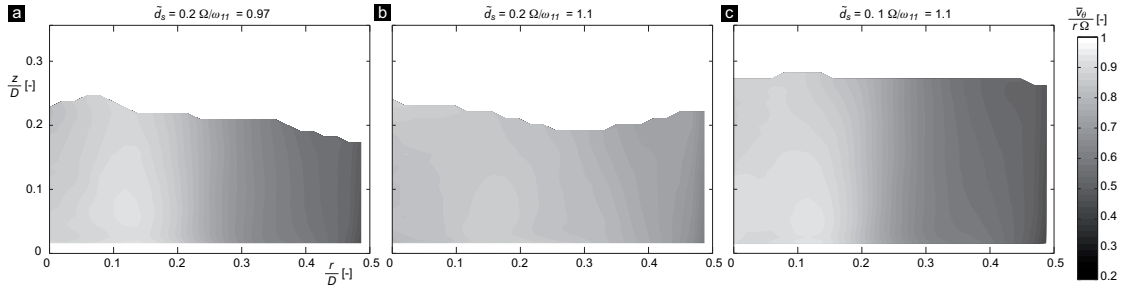


**Figure 4.28** | The averaged tangential velocity  $\bar{v}_\theta$  distribution on  $r-z$  plane, for  $\tilde{H}_0 = 0.5$ , **a:**  $\tilde{d}_s = 0.2$ ,  $\Omega/\omega_{11} = 0.969$ . **b:**  $\tilde{d}_s = 0.2$ ,  $\Omega/\omega_{11} = 1.1$ . **c:**  $\tilde{d}_s = 0.1$ ,  $\Omega/\omega_{11} = 1.1$ .

phase shift, as the propagating front becomes steeper and steeper. The liquid is now mostly at the wall, and the free surface at the centre of the container is depressed.

Concerning the velocity fields, we notice in Fig. 4.27 that the amplitude of each component decreases significantly, and the most important velocity is the average of the tangential velocity, which account for most of the motion of the flow. The rotation of the flow continually increases with the shaking frequency, as the averages of the tangential velocity, normalized by the solid rotation velocity, clearly depicts in Fig. 4.28. We observe that the rotation is stronger at a distance of nearly  $r = \tilde{d}_s$  from the container revolution axis, and rapidly decreases along the radius toward the external wall. The maximum rotation for multiple crested waves is observed near the natural frequency, but is nevertheless lower than the one observed at the breaking of single crested waves. Above the first shaking frequency, the average tangential velocities of the flow are similar in both single crested and multiple crested waves. Eventually, complete solid

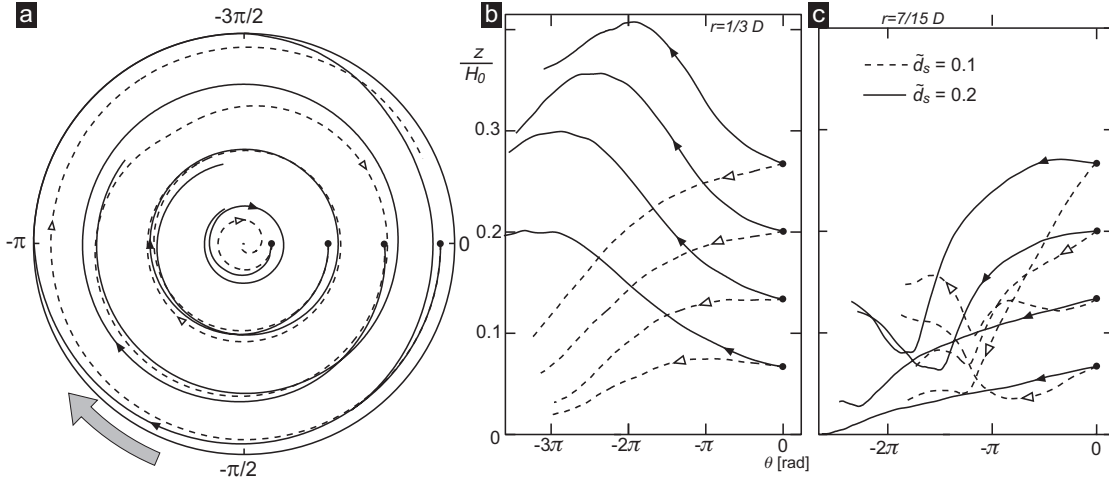


**Figure 4.29** | Trajectories reconstructed from the PIV measurements, followed during two vessel revolutions at  $\Omega/\omega_{11}=1.1$  by liquid particles starting from the black dots. Dashed line:  $\tilde{d}_s=0.1$ , solid lines:  $\tilde{d}_s=0.2$ . **a:** trajectories at  $z_0/H_0=0.5$ , in the  $r-z$  plane, **b:** trajectories at  $r_0/D=1/3$

rotation of the flow is expected, particularly when a portion of the container bottom is dried by the motion of the flow (Fig. 4.1g). In this case the free surface is expected to be described by a parabolic shape, due to the balance of inertial and centrifugal forces on the liquid, as observed in Erlenmeyer flasks [23].

From the analyses of trajectories followed during two revolutions by the particles, reconstructed from the PIV measurements (Fig. 4.29) we observe that the radial motion nearly disappears - the particles travel along circles. Moreover, since the liquid is advected by the rotation, it remains in regions of overall upward or downward motion. As a result the path of the particles is not limited by the wave amplitude: they may be carried from the bottom of the container to the free surface in less than one revolution. We notice also that the particles at  $r_0=1/3D$  have a completely different behaviour after the breaking than at the inception (shown for one vessel revolution in Fig. 4.24b): at the transition to the breaking the single crested wave ( $\tilde{d}_s=0.1$ ) depicts trajectories with an upward movement, while after the breaking the particles move downward, and it is the multiple crested wave ( $\tilde{d}_s=0.2$ ) that has an upward movement. Apart from this difference the amplitude of both motions are comparable after the natural frequency  $\omega_{11}$ .

A final surprise awaits us at the end of this journey through the wave behaviours: the behaviour of the flow after the breaking may depend on the shaking diameter  $\tilde{d}_s$ . A persistence of high amplitude, rotating regime is observed for  $\tilde{d}_s > 0.02$  - the wave amplitude increases, and so does the average tangential velocity. On the other hand for small values of the shaking diameter ( $\tilde{d}_s < 0.02$ ) the wave eventually resumes the potential behaviour before reaching the second natural frequency. The evolution of the crest-to-trough amplitude of the wave at the wall for  $\tilde{d}_s < 0.2$  is shown in Fig. 4.30, along with four measured liquid elevations at the wall  $\tilde{\delta}(\theta)$ . We remind that according to the linear solution of the potential model, for  $\Omega > \omega_{11}$  the wave at

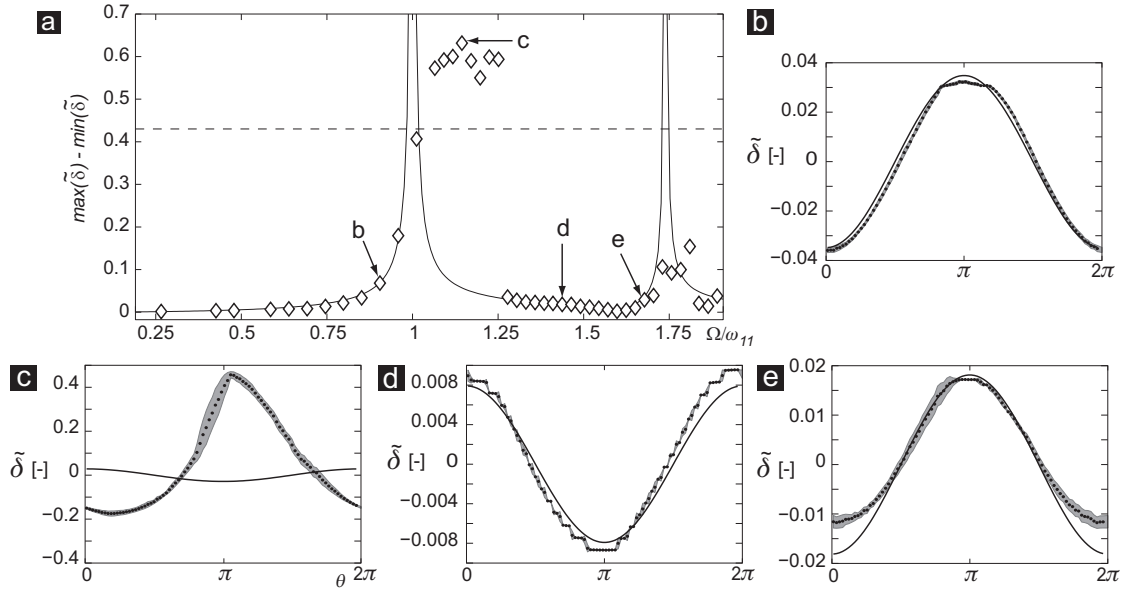


**Figure 4.30** | Evolution of free surface amplitude of a wave with  $\tilde{d}_s=0.01$ ,  $\tilde{H}_0=0.5$ , and varying  $\Omega$ .

the wall has its maximum in the direction of the axis of the shaker motor, in opposition to the inertial forces direction (see also Fig. 2.5). Indeed, we observe (Fig. 4.30d) that the free surface behaves like predicted, after a persistence of high amplitude rotation waves it returns to potential regime. Visual observations show that this transition from high to low amplitude is subject to hysteresis, depending on the increase or decrease of the shaking frequency. Hence, the transition to swirling regime is not only in one direction, and high shaking frequency does not necessary entail large amplitude waves.



### 4.3 Non-synchronous waves

In the previous section we have listed and described the behaviour of flows whose velocity field and free surface height are constant in a frame of reference rotating with the wave, at the shaking frequency  $\Omega$ , around the revolution axis of the container. As we have mentioned at the beginning of this chapter, this is not always the case. Obviously, after each change of the operating conditions a certain time is necessary before the flow returns steady. This transitory motion is not considered here, since its existence is limited in time. We will relate only about those waves whose motion remains indefinitely non-synchronous - waves that are not unsteady, but have period different from the shaking one.

#### 4.3.1 Continuously changing waves

When measured at a single location, non-synchronous waves are not periodic over one revolution of the vessel, thus their phase averaging is meaningless, as detailed in Sec. 4.1.1. However, the time evolution of the liquid height at a single location, shown in Fig. 4.31, already suggests that various non-synchronous phenomena are possible. We have indeed single (Fig. 4.31a-c) as well as double crested (Fig. 4.31d-f) non-synchronous waves. Moreover, the period of those waves may vary, if some have a period of four revolutions or more (Fig. 4.31a-d), others seem to have a period of nearly two revolutions (Fig. 4.31e-f).

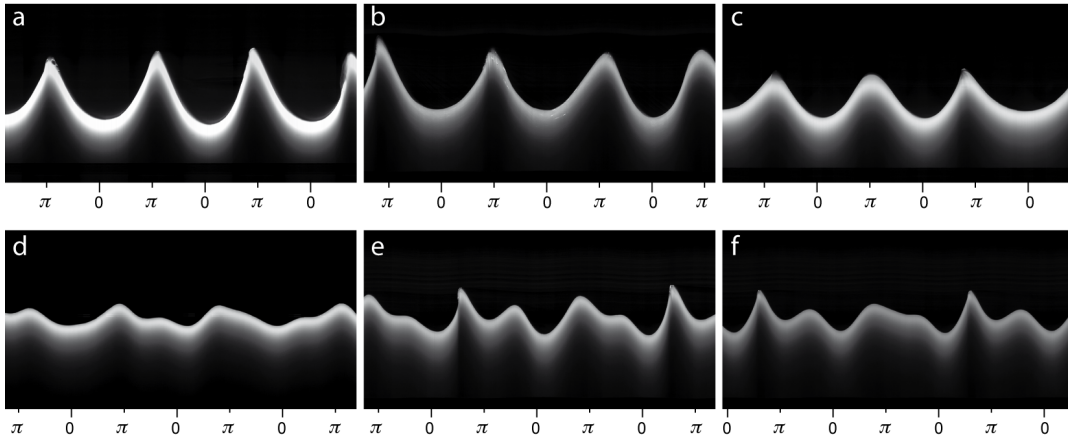


**Figure 4.31** | Several examples of visualization of non-synchronous waves from a fixed location at the container wall, reconstructed from high speed movies (Sec. 3.2.1). Since the shape is constantly changing, the images are not unfolded views of the wave, but the evolution of the free surface height at a single location. **a:**  $\tilde{d}_s=0.08$ ,  $\tilde{H}_0=0.42$ ,  $Fr=0.4801$  or  $\Omega/\omega_{11}=0.927$  ( $D=144\text{mm}$ ). **b:**  $\tilde{d}_s=0.09$ ,  $\tilde{H}_0=0.52$ ,  $Fr=0.4997$  or  $\Omega/\omega_{11}=0.8867$  ( $D=287\text{mm}$ ). **c:**  $\tilde{d}_s=0.1$ ,  $\tilde{H}_0=0.7$ ,  $Fr=0.52$  or  $\Omega/\omega_{11}=0.862$  ( $D=144\text{mm}$ ). **d:**  $\tilde{d}_s=0.13$ ,  $\tilde{H}_0=0.52$ ,  $Fr=0.38$  or  $\Omega/\omega_{11}=0.56$  ( $D=287\text{mm}$ ). **e:**  $\tilde{d}_s=0.09$ ,  $\tilde{H}_0=0.52$ ,  $Fr=0.4$  or  $\Omega/\omega_{11}=0.71$  ( $D=287\text{mm}$ ). **f:**  $\tilde{d}_s=0.09$ ,  $\tilde{H}_0=0.52$ ,  $Fr=0.365$  or  $\Omega/\omega_{11}=0.687$  ( $D=287\text{mm}$ )

We have observed, in the section dedicated to the wave breaking (sec. 4.2.2), that at the breaking inception the amplitude of single crested waves decreases. An equilibrium is created



between the energy provided by the shaking and the energy dissipated by the breaker, therefore the amplitude of the wave is adapted to this new balance. If the breaking dissipates more energy than it requires to be maintained, it disappears and the wave returns to non-breaking state. Non-synchronous waves are observed to be at this limit. After the disappearing of the breaker, they require several revolutions to attain the breaking steepness again. It is thus not uncommon to observe a wave growing in amplitude until it breaks, and restarting to grow, repeating this cycle indefinitely. The number of revolutions required to the wave to gather enough energy to break depends on the proximity, in terms of shaking frequency, of the wave regime to one of the two stable situations.

Although this behaviour is expected at every transition to the breaking, in most of the shaking configurations the non-synchronous waves occur at a very thin range of shaking frequencies, and are usually not observable. On the other hand they are observable on a wider range of shaking frequencies when the breaking mixes with other phenomena: e.g. the transition of double crested waves to single before breaking. We have reported (Sec. 4.2.2.2) that below a critical value of the shaking diameter ( $\tilde{d}_{s,\omega_{11}/2}$ ) the wave break as single crested, while above this value they break as multiple crested. Non-synchronous waves are observed at  $\tilde{d}_s \cong \tilde{d}_{s,\omega_{11}/2}$  when the wave is “hesitating” not only between breaking and non breaking, but also between different number of crests.

An example of single crested non-synchronous wave is depicted in Fig. 4.32a, where the wave is shown at fifteen positions  $\alpha$  of the shaker on its circular trajectory, during two complete vessel revolutions. The images are reconstructed from the reflection of four mirrors to a high speed camera placed above the setup, as described in Sec. 3.2.4. We observe not only a change in the amplitude of the wave, but also a displacement of the crest and, to a less extent, of the trough. The wave has an advancing movement when increasing in amplitude, and a backward one during the breaking. The spilling breaker, localized at the crest, may be noticed in the second ( $\alpha = 2/7\pi$ ) and the last ( $\alpha = 4\pi$ ) images. The first image is similar (but not identical) to the last one, hence the periodicity of this particular wave is close to half the shaking frequency.

In the case of double crested waves (Fig. 4.32b) the phenomenon is slightly more complex, since the increase in amplitude of the first crest leads to a reduction of the second one. We notice the same forward movement of the wave as the amplitude increases before breaking ( $\alpha$  from  $2\pi$  to  $4\pi$ ), while the second crest decreases. This behaviour may not be explained simply by the change in phase shift of two waves with different wavelengths, since this would not account for the advance and backward motion of the first crest. The period of this surface perturbation is also close to two revolutions, (a more precise estimation is given in the following section).

#### 4.3.2 Liquid motion

In synchronous waves the velocity fields are obtained by phase averaging the measurements at each position of the container on the shaking trajectory. The same procedure in non-

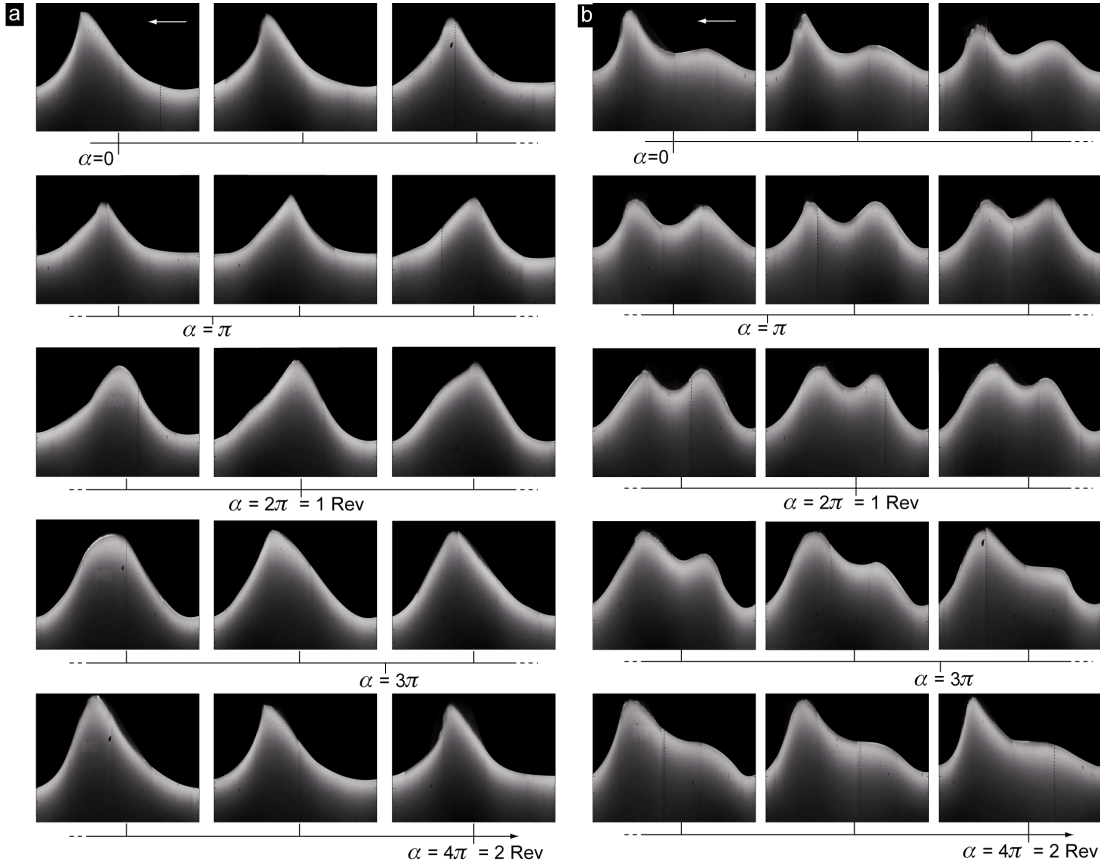


**Figure 4.32** | Non-synchronous waves visualized during two revolutions of the container, using the method described in Sec. 3.2.4. The wave at the farthest wall has been hidden by a black cover manually added. **a:**  $\tilde{d}_s=0.1$ ,  $\tilde{H}_0=0.5$ ,  $Fr = 0.4975$  or  $\Omega/\omega_{11} = 0.838$ . **b:**  $\tilde{d}_s=0.1$ ,  $\tilde{H}_0=0.5$ ,  $Fr = 0.0421$  or  $\Omega/\omega_{11} = 0.0709$ .

synchronous waves would give misleading results, since the velocity fields are different from one revolution to the next, due to the continuously changing motion. It is therefore necessary to use the proper orthogonal decomposition (POD, see Sec. 3.3.3) to investigate the flow motion.

The analyses of non-synchronous velocity fields is performed on the double crested wave depicted in Fig. 4.32b. As for synchronous waves, the velocity fields are measured on vertical planes passing through the vessel revolution axis, every  $4^\circ$ . Separate POD decomposition is performed on the fluctuating velocity field of each set of measurements. Figure 4.33a depicts the energy fraction of each POD mode, computed as the ratio between the eigenvalue of the POD mode and the sum of the eigenvalues, for an arbitrary plane of measurement. From the analyses of the energy of the modes we observe that in almost all measurement locations the first two modes account for 35 to 45 % of the energy of the perturbations. All the other modes add singularly less than 5% of the energy.

Furthermore, Fig. 4.33b depicts the variation of the value of the time dependent parameters

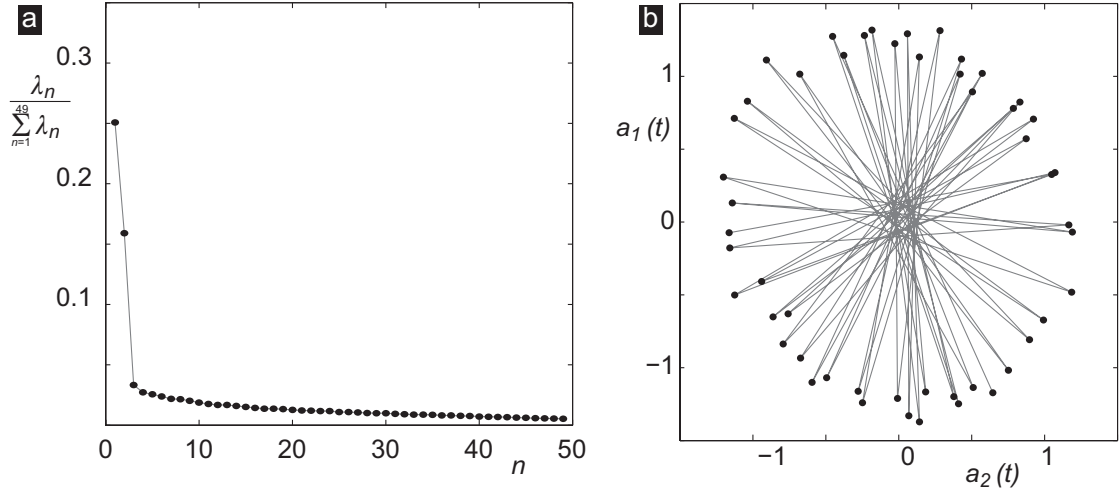


**Figure 4.33** | **a:** energy fraction of each POD mode  $n$ , expressed as the ratio between the mode eigenvalue ( $\lambda_n$ ) and the sum of the eigenvalues. Since 50 measurements were effectuated, the first 49 modes are computed, the 50<sup>th</sup> being composed by zeros. **b:** relation between the value of the time dependent coefficients  $a_n(t)$  of the first two modes, for the 50 measurements. The grey line connects the measurements chronologically.

$a_n(t)$  of the first two modes. We notice that they depend sinusoidally on time, with a phase shift of  $\pi/2$  between them. To compute the trajectories followed by liquid particles in the non-synchronous velocity fields we generated synthetic velocity fields using the mean velocity and the first two modes. The other modes were neglected because their contribution is small compared to the first two, and because the value of their coefficients may be difficult to determine with sufficient precision. Each measurement position within the container has its own POD modes  $\phi_1(\theta)$  and  $\phi_2(\theta)$  and time coefficients  $a_1(t, \theta)$  and  $a_2(t, \theta)$ . Moreover, we suppose the intensity of each mode to increase or decrease simultaneously in the whole liquid domain - the time coefficients are synchronous. The synthetic velocity field filtered to the second order is determined as:

$$\mathbf{v}_{POD} = \bar{\mathbf{v}}(\theta) + a_1(t, \theta)\phi_1(\theta) + a_2(t, \theta)\phi_2(\theta) = \bar{\mathbf{v}}(\theta) + \hat{a}_1(\theta) \cos(\eta t)\phi_1 + \hat{a}_2(\theta) \sin(\eta t)\phi_2 \quad (4.9)$$

where  $a_1(t, \theta)$  and  $a_2(t, \theta)$  are expressed as trigonometric functions with amplitudes  $\hat{a}_1(\theta)$  and  $\hat{a}_2(\theta)$  and frequency  $\eta$ , whose values are determined fitting  $\hat{a}_1(\theta) \cos(\eta t)$  to  $a_1(t, \theta)$  at each measurement location  $\theta$ . In the present wave the frequency of the POD coefficients is slightly below half of the shaking frequency ( $\Omega=10.472$  1/s,  $\eta= 5.07$  1/s). It is interesting to notice that, if  $\eta = \Omega/2$ , the reconstruction of the values of  $\hat{a}_1(t)$  and  $\hat{a}_2(t)$  would be more difficult: in Fig.4.33b only two opposing points on the circle would be identified.

To highlight the effect of the non-synchronous motion we compare trajectories followed by particles in synchronous velocity fields (only the average flow,  $\bar{\mathbf{v}}(t)$ , is taken into account) and those in non-synchronous velocity fields, reconstructed according to Eq. 4.9. The results are depicted in Fig. 4.34 for particles released at  $\tilde{r}_0=1/15, 1/5, 1/3$  and  $7/15, \theta_0=0, \tilde{z}_0=1/15, 1/5, 1/4,$

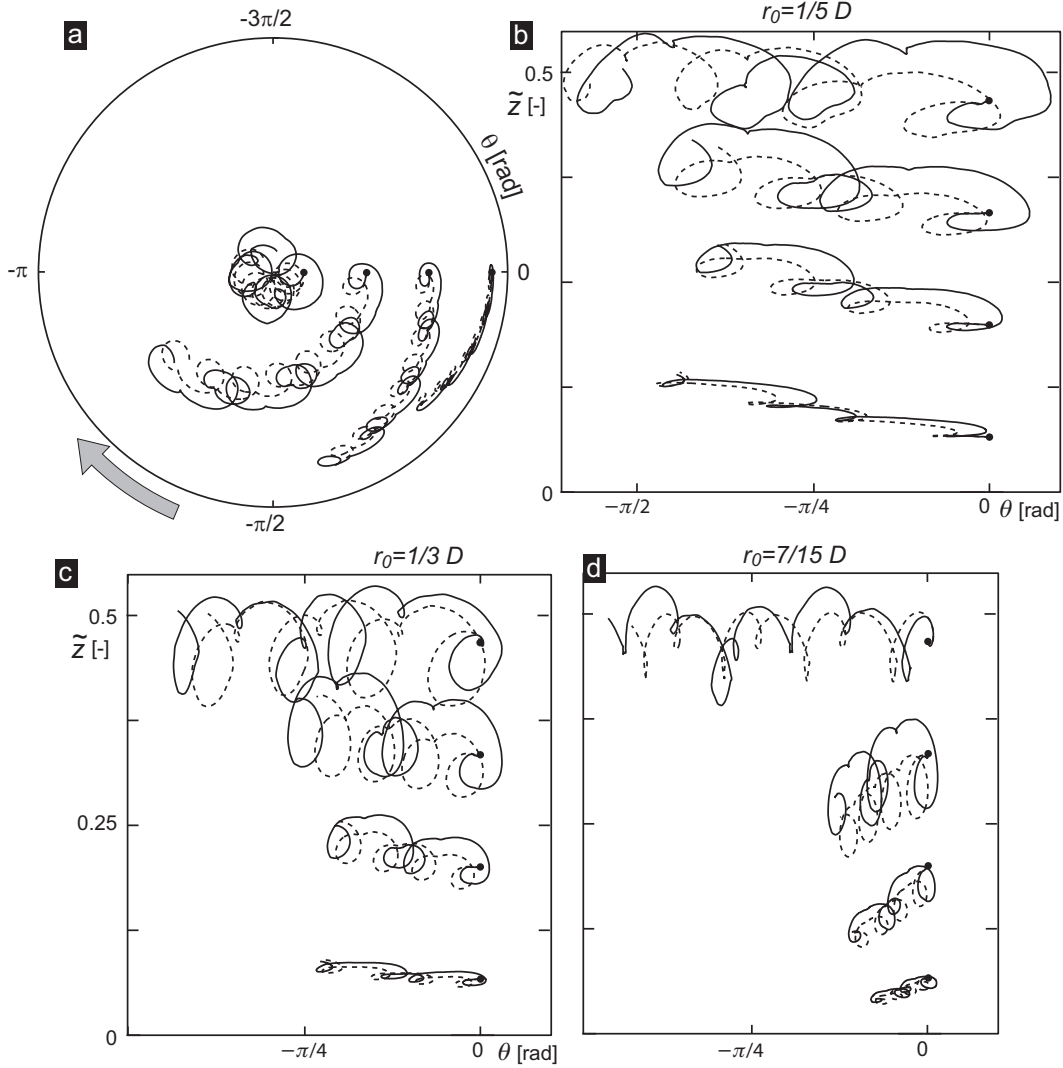


**Figure 4.34** | Trajectories followed during eight (a) or four b-d revolutions by liquid particles for synchronous (dashed lines) and non-synchronous waves (solid lines),  $\bar{d}_s=0.1$ ,  $\bar{H}_0=0.5$ ,  $Fr = 0.0421$  or  $\Omega/\omega_{11} = 0.0709$ . Particles released from the black dots. **a:**  $\bar{r}_0=1/15, 1/5, 1/3$  and  $7/15$ ,  $\theta_0=0$ ,  $\bar{z}_0=1/4$ , projected on  $r-z$  plane. **b, c, d:**  $\bar{r}_0$  is given in each image,  $\theta_0=0$ ,  $\bar{z}_0=1/15, 1/5, 1/3$  and  $7/15$ , projected on  $\theta-z$  plane.

1/3 and 7/15, during three revolutions. We observe that the multiple crested behaviour dominates - there is no strong rotation of the flow, and both synchronous and non-synchronous trajectories depict the deformation in the upper part, typical of multiple waves. However, the non-synchronous motion stretches and compresses the trajectories in the tangential direction, especially in the internal part of the container. Indeed, we notice in Fig. 4.34b-d that the distance between the “loops” of the non-synchronous trajectories is not constant. Moreover, in non-synchronous velocity fields the amplitudes of the motion are increased, especially in the vertical direction. The eventual enhancing of the mixing due to this motion will be assessed in the following chapter.

## 5 Application to orbital shaken bioreactors

Having presented and thoroughly discussed the wave behaviours and regimes, we apply, in this chapter, those findings to the industrial case of cells cultivation in suspension in orbital shaken bioreactors. The cells are living organisms, interacting with the surrounding environment and responding to the stimuli they receive. They are usually fed with nutrient (from the culture medium) and oxygen (through the surrounding atmosphere) to multiply and produce the required protein, whereas the carbon dioxide they produce is evacuated. Most of these exchange phenomena are directly linked to the motion of the liquid medium. Therefore, although our investigation was not directly involved with the cells welfare, growth and productivity, we are able to contribute to several aspects of the cultivation, namely the scale-up, the evaluation of the mixing efficiency, and the prediction of the flow behaviour. Moreover, in the light of our study we are able to point out the wave patterns ensuring, from the hydrodynamics point of view, the most promising results in term of mixing.

### 5.1 Scale-up

Increasing in size the cell cultures is obviously more complex than simply using a bigger container: the operating parameters have to be adapted to ensure the required oxygenation and mixing without harming the cells [77, 119, 108, 107]. Several parameters may be taken into account, e.g. the gas transfer coefficient [116, 109], the geometric proportions, the power input [55, 73] or the mixing time [116, 55]. However, enforcing the value of one of the these parameters during scale-up is likely to generate unsuitable conditions for the cells [65]. From the hydrodynamics point of view, the flow is maintained in exact hydrodynamic similarity between two scales (i.e. it is equivalent in a scale-independent representation) if the dimensionless parameters governing the flow are kept constant.

### 5.1.1 Dimensionless parameters

The liquid motion in an orbitally shaken bioreactor is governed by the dimensions and forces ratios. We define therefore the following dimensionless parameters:

$$\begin{aligned} \tilde{d}_s &\equiv \frac{d_s}{D} & \tilde{H}_0 &\equiv \frac{H_0}{D} \\ Fr^2 &\equiv \frac{(\Omega^2 d_s)}{g} & Re &\equiv \frac{\rho \Omega d_s^2}{\nu}. \end{aligned} \quad (5.1)$$

where  $d_s$ ,  $D$ ,  $H_0$  and  $\Omega$  are the shaking diameter, the vessel diameter, the height of the unperturbed liquid and the shaking angular velocity,  $\nu$  is the liquid viscosity and  $\rho$  the liquid density. The first two dimensionless parameters are dimensional ratios,  $Fr$  is the Froude number, which expresses the ratio between gravity and centrifugal forces,  $Re$  is the Reynolds number expressing the ratio between inertial and viscous forces. We note that the characteristic velocity used in  $Fr$  and  $Re$  numbers is the tangential velocity of the container  $\Omega \cdot d_s$ , the only velocity imposed in the entire setup. Those dimensionless groups were identified also in the potential model in Sec. 2.3.1, except for  $Re$  number, since the viscosity is not considered in potential flows.

The same dimensionless groups are obtained also performing a dimensional analysis on the physical quantities controlling, for example, the free surface height at the wall:  $D$ ,  $d_s$ ,  $H_0$ ,  $\Omega$ ,  $\nu$ ,  $\rho$  and the gravitational acceleration  $g$ . Viscosity and density of the gas phase are not taken into account, playing a minor role in the phenomena. The surface tension is supposed to have limited influence in macroscopic flow, and it is therefore intentionally omitted.\*

The physical quantities measured in the container are normalized according to the above relations, as described in the potential model (in Sec. 2.3.1).

$$\tilde{\delta} \equiv \frac{\delta}{D} \quad \tilde{\mathbf{v}} \equiv \frac{\mathbf{v}}{d_s \Omega} \quad (5.2)$$

Moreover, in cell cultures a main issue is the control of the shear stress  $\tau_{ij}$  in the flow, since it appears to negatively influence the size and viability of the cells [59, 82]. The shear stress is defined by:

$$\tau_{ij} = \mu \frac{\partial v_i}{\partial x_j} \quad \text{with } i \neq j \quad (5.3)$$

The evolution of the shaking velocity between two culture scales  $D_1$  and  $D_2$  in hydrodynamic similarity goes as  $\Omega_1 = \Omega_2 \sqrt{D_2/D_1}$  and consequently the ratio between two velocities at the same location is  $v_1 = v_2 \sqrt{D_1/D_2}$ . If adapted, the viscosity scales as  $\mu_1 = \mu_2 (D_1/D_2)^{3/2}$ . Thus

---

\*Obviously when sloshing in small containers is considered (such as in tube spins, Fig. 1.3 on page 3) the surface tension must be taken into account.

the shear stress evolves as:

$$\tau_{ij,2} = \frac{D_2}{D_1} \tau_{ij,1} \quad (5.4)$$

It has to be considered that the resistance of the cells to the shear stress does not change with the culture scale. For this reason configurations proving to be optimal for cell cultures at small scale may reveal themselves catastrophic at larger scale.

Another parameter typically used in the field of shaking cultures is the mixing time, i.e. the time required to homogenize an initially heterogeneous condition. However, in order to emphasize the hydrodynamic similarity, it is more appropriate to characterize the mixing by the number of revolutions required to attain homogeneity, thus adimensionalizing the mixing time by multiplying it by the shaking frequency. Hence, two shakers in hydrodynamic similarity will attain the homogeneity after the same amount of revolutions, but not necessarily after the same lapse of time. More considerations about the mixing efficiency of the different wave patterns are found in Sec. 5.2.

### 5.1.2 Parameters validation

The validity of the dimensionless parameters is confirmed by comparing the values of physical quantities, such as  $\tilde{\delta}$  and  $\tilde{v}$ , measured at various experimental configurations and scales. The similarity between two measurements  $\tilde{\delta}_i$  and  $\tilde{\delta}_j$ , associated with two different experimental configurations  $i$  ( $D=144\text{mm}$ ) and  $j$  ( $D=287\text{mm}$ ), is evaluated as the root-mean-square (RMS) of the difference between  $\tilde{\delta}_i$  and  $\tilde{\delta}_j$  at each measurement location, weighted by the average crest to trough amplitude of the corresponding waves ( $\tilde{A}_i$  and  $\tilde{A}_j$ ):

$$R_{ij} = \frac{2}{(\tilde{A}_i + \tilde{A}_j)} \sqrt{\frac{1}{N} \sum_{k=1}^N (\tilde{\delta}_i(\alpha_k) - \tilde{\delta}_j(\alpha_k))^2}, \quad (5.5)$$

where  $N$  is the number of angular measurement locations. Figure 5.1 shows the values of  $R_{ij}$  calculated for selected pairs of experimental configurations. This matrix is arranged so that on the diagonal are compared configurations with nearly identical dimensionless parameters  $\tilde{a}_s$ ,  $\tilde{H}_0$  and  $Fr$  (yet different overall scales), while off-diagonal are compared configurations with different dimensionless parameters. The  $Re$  values are not kept constant on the diagonal: all experiments are performed with the same liquid. This is done on one hand because it is impractical to adapt the viscosity at each experiment, on the other hand because we expect the  $Re$  number to play a minor role in the similarity of the large scale flow. Thorough discussion of the latter hypothesis is given in the following section.

The diagonal values of  $R_{ij}$  are much smaller compared to the off-diagonal ones. The dimensionless parameters  $\tilde{a}_s$ ,  $\tilde{H}_0$ ,  $Fr$  are thus appropriate to describe the behaviour of the free surface at the wall in a scale-invariant way, despite the non respect of  $Re$  similarity. Furthermore, we observe that the similarity is ensured for both potential and swirling regime after the

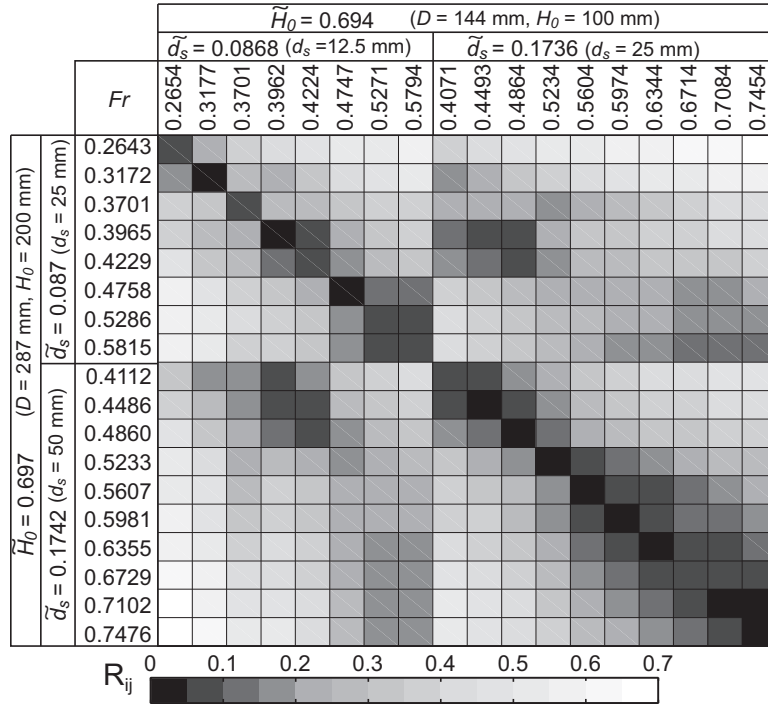


**Figure 5.1** | Values of RMS difference between measurements  $R_{ij}$  obtained at distinct configurations and scales. We observe a good good agreement (low value of  $R_{ij}$ ) when  $\tilde{d}_s$ ,  $\tilde{H}_0$  and  $Fr$  are identical, i.e. at the diagonal of the matrix. The  $Re$  number values are not adapted to be equivalent on the diagonal.

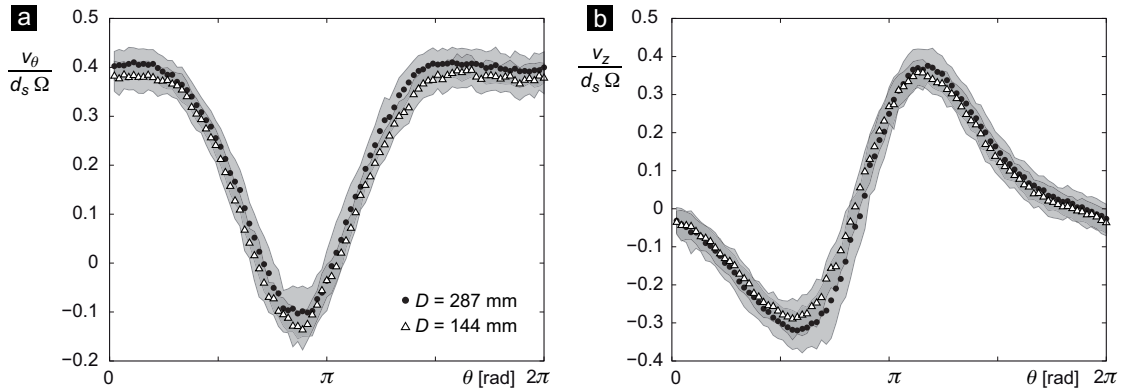


**Figure 5.2** | Comparison of LDV velocity measurements obtained at different scales ( $D=144\text{mm}$  as white triangles,  $D=287\text{mm}$  as black dots) but equivalent dimensionless parameters. The standard deviations are depicted as grey surfaces, overlapping regions are darker grey.  $\tilde{d}_s=0.17$ ,  $\tilde{H}_0=0.695$ ,  $Fr=0.597$ ,  $\Omega/\omega_{11}=0.75$ , measurement effectuated at  $\tilde{r}=0.38$ ,  $\tilde{z}=0.348$ . Note that this wave is double crested although  $\Omega > \omega_{21}/2$ , a situation described in Sec. 4.2.1.2 not predicted by the potential model. **a:** normalized tangential velocity. **b:** normalized axial velocity.



wave breaking.

In Fig. 5.2 are compared the tangential and axial velocities of two different containers ( $D=144$  and  $287$  mm) with similar  $\tilde{d}_s$ ,  $\tilde{H}_0$  and  $Fr$ , measured at the same dimensionless location  $\tilde{r} = r/D$  and  $\tilde{z} = z/D$ . Comparing the dimensionless velocity fields we find very close values, confirming the similarity not only of the free surface but of the whole flow field.

### 5.1.3 Influence of the Reynolds number

While maintaining constant values of  $\tilde{d}_s$ ,  $\tilde{H}_0$  and  $Fr$  between two scales is relatively easy, matching the  $Re$  number requires viscosity adjustment, which might be difficult in bioengineering implementations. The influence of this dimensionless parameter has thus to be assessed. The value of the  $Re$  number may be controlled by changing the viscosity of the flow (using glycerol-water solutions), or by changing the scale of the experiments while  $\tilde{d}_s$ ,  $\tilde{H}_0$  and  $Fr$  are kept constant.

Figure 5.3a displays the amplitude of the wave measured at the wall as a function of the  $Re$  number, for three sets of operating parameters  $\tilde{d}_s$ ,  $\tilde{H}_0$  and  $Fr$ . We observe that the wave behaviour is affected by  $Re$  numbers below  $4'000$ - $6'000$ . Moreover, the effect of low  $Re$  numbers depends on the wave pattern: e.g. for non-breaking waves ( $Fr=0.54$ ,  $\tilde{d}_s=0.18$ ) the increased viscosity reduces the wave amplitude. This is expected, since the higher viscosity increases the

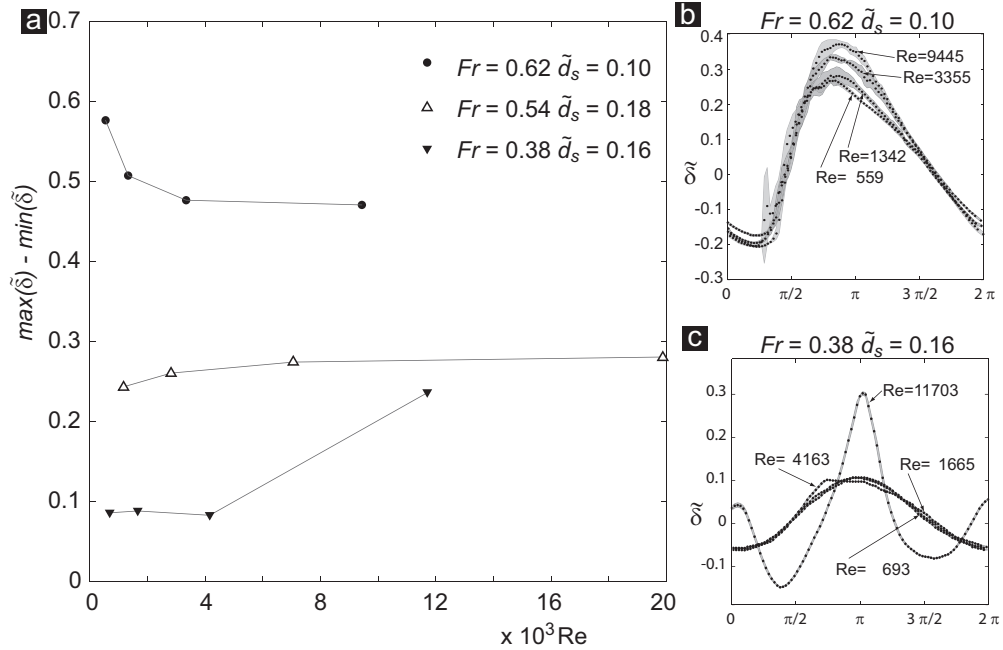


**Figure 5.3** | Influence of the  $Re$  number on the wave,  $\tilde{H}_0=0.5$ . **a:** amplitude of selected waves with fixed  $\tilde{d}_s$ ,  $\tilde{H}_0$ ,  $Fr$  as a function of  $Re$ . **b:** non-dimensional liquid elevation at the wall  $\tilde{\delta}(\alpha)$  for selected breaking waves. **c:**  $\tilde{\delta}(\alpha)$  of selected non-breaking waves, where the change in behaviour (appearance of multiple crested wave) is highlighted.

resistance of the flow to the agitation forces. On the other hand, for breaking waves ( $Fr=0.62$ ,  $d_s=0.1$ ) an increase of the viscosity, hence a reduction of the  $Re$  number, leads to smaller breaking regions and therefore larger amplitudes (Fig. 5.3b). We may be tempted to attribute this reduction of the breaking to an increase of the surface tension, reducing the intensity of the spilling. However, the fact that glycerol has a surface tension slightly lower than the one of water discards this hypothesis. We explain this increase of the amplitudes by a partial relaminarisation of the breaking region, due to the increase of viscosity, leading to lower dissipation in the breaker. Furthermore, another phenomenon is observed for multiple crested waves generated by sub-harmonics of natural frequencies  $\omega_{mn}$  ( $Fr=0.38$ ,  $d_s=0.16$ ). They tend to disappear as the  $Re$  number is reduced. We display an example in Fig. 5.3c, where a single crested wave at  $Re$  values below 5'000 becomes a multiple crested wave above 10'000.

Another interesting effect of low  $Re$  numbers is the increased phase shift between the principal plane of inertia (which, we remind, is the symmetry plane in case of symmetrical waves) and the direction of the centripetal force: the direction connecting the revolution axis of the container to the rotation axis of the shaker motor. The measured values are given in Fig. 5.4 for a large range of operating parameters ( $\tilde{d}_s$  from 0.02 to 0.4,  $\tilde{H}_0=0.52$ ,  $\Omega/\omega_{11}$  from 0.136 to 1.345) and three different viscosities expressed as a ratio to the water viscosity  $\mu/\mu_w=1$ , 2.5 and 6. We remind that, according to the potential model this value should be always equal

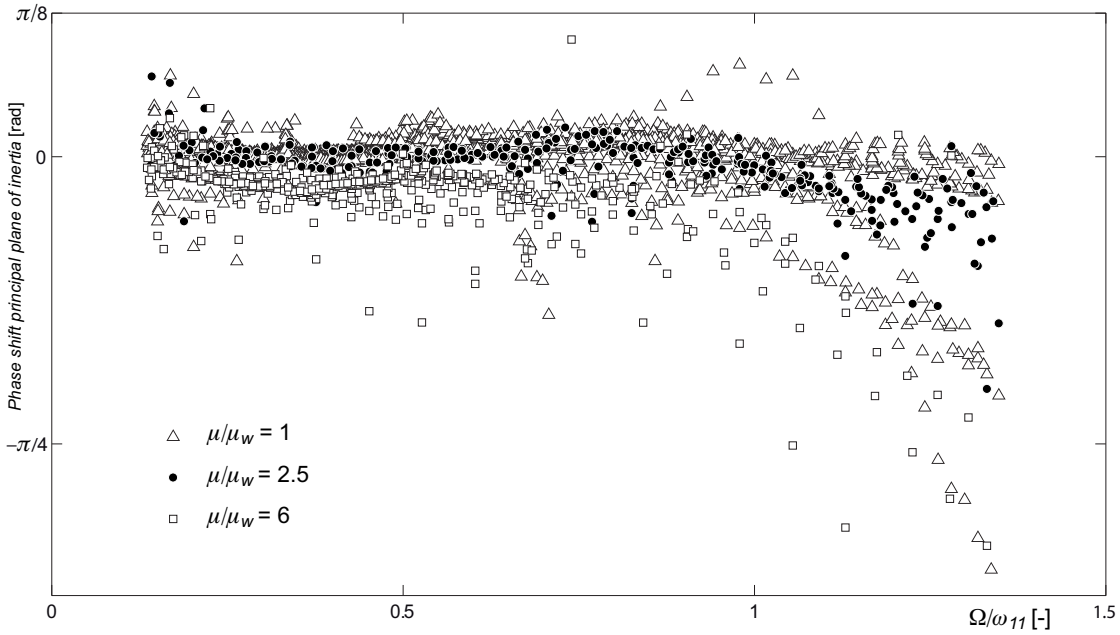


**Figure 5.4** | Phase shift of the principal plane of inertia with respect to the centripetal force direction, for nearly 2600 sets of operating parameters:  $\tilde{d}_s$  from 0.02 to 0.4,  $\tilde{H}_0=0.52$ ,  $\Omega/\omega_{11}$  from 0.136 to 1.345, and three different viscosities:  $\mu/\mu_w=1$ , 2.5 and 6, where  $\mu_w$  is the water viscosity.

to zero. We observe here an increasing phase shift especially at shaking frequencies above the first natural frequency, for the impinging wave (Sec. 4.1 and Fig. 4.3). This behaviour is noticed also in Fig. 5.4. Moreover we observe a general tendency of the phase shift to increase

with the viscosity. Visual observations of very high viscosity liquids confirmed this trend.

For the above mentioned reasons it is not possible to compare directly experiments at very small scale (e.g. in tube spins) with large scale cultures, while similar results are expected scaling from middle (some litres) to large sizes (thousands of litres).

## 5.2 Mixing

Mixing is fundamental in cell cultures, since it ensure homogeneity of the cells distribution [77, 107]. Moreover, we expect the gas dispersion within the container to be ensured mostly by liquid transport (rather than by diffusion), thus mixing also ensures homogeneity of the gasses. However, achieving complete homogeneity, especially in large scale bioreactors, is very unlikely [65, 116].

The analysis of the liquid motion, reported in the previous chapter, shows that the mixing is guaranteed by a three dimensional periodic wave motion, which ensures an exchange of liquid in all directions. We evaluate the global mixing efficiency of the shaker by monitoring the dispersion of a fluorescent dye (released at the free surface) on a vertical plane passing through the revolution axis of the container, as described in Sec. 3.4. From the measurements, we establish maps depicting the number of revolutions necessary to attain the final concentration in each region of the measurement plane, defined as mixing maps. Figure 5.5a illustrates the mixing map of a wave in potential regime, single crested, whereas Fig. 5.5b is the mixing map of a single crested breaking wave, at the natural frequency  $\omega_{11}$ .

We observe that the transport is very slow in the potential wave, without a clear path followed by the dye as it moves from the top to the bottom of the liquid phase. On the other hand, in breaking waves we notice that the dye descend from the free surface along the external walls of the container, travels to the centre and rises to the top. The number of revolutions required to attain homogeneity is also considerably lower compared to the non-breaking wave. We have seen (in Fig. 4.24) that the trajectories of single crested breaking waves reveal a strong vertical motion at the periphery of the container, explaining the fast advection in this region. Moreover, we have noticed (in Fig. 4.22) that the flow is in solid rotation in its central part ( $\tilde{r} < 0.2\tilde{d}_s$ ). Due to the strong (and solid) rotation of the central part of the liquid, exchanges in the radial direction are less efficient, and the dye reaches the central rotating part only through the motion near the bottom.

Moreover, interesting considerations may be drawn from the comparison of snapshot of the dye diffusion in the liquid (Figs. 5.5c-d). While in the potential regime (Figs. 5.5c) the diffusion is mostly done by slow, large eddies and a seemingly laminar motion, at the breaking (Figs. 5.5d) the presence of small, fast and very likely turbulent eddies homogenizes the concentration, in those regions that have been reached by the dye. The PIV velocity fields measurements allow to distinguish between the mixing due to the average velocity field from the mixing due to the fluctuations, as we will detail in the following sections.

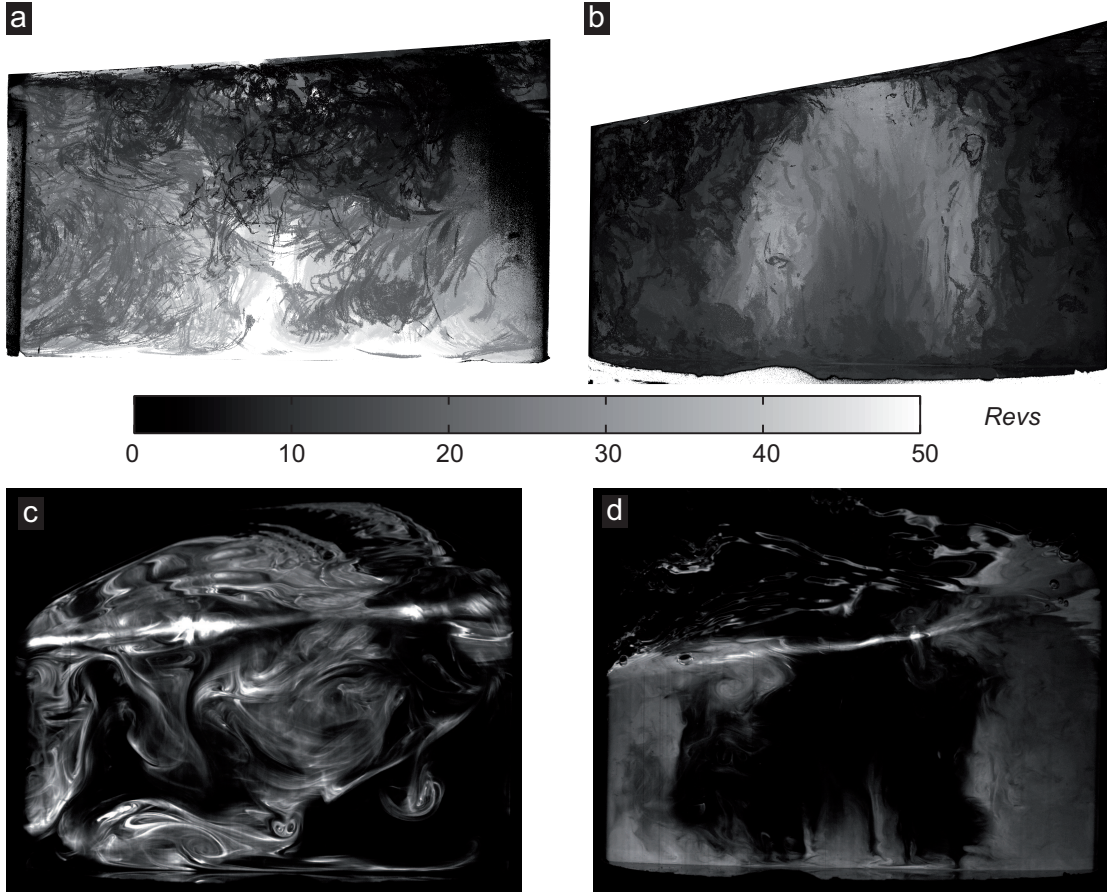


**Figure 5.5 | a:** Examples of advection of fluorescent dye from the free surface into the liquid bulk. The shading indicates the number of revolutions necessary to reach the final (homogeneous) concentration of dye at any location in the measurement plane, in a single crest non breaking wave:  $\tilde{d}_s=0.087$ ;  $\tilde{H}_0=0.52$ ,  $Fr=0.467$ ,  $\Omega/\omega_{11}=0.845$ . **b:** single crest breaking wave at  $\tilde{d}_s=0.087$ ;  $\tilde{H}_0=0.52$ ,  $Fr=0.5569$  ( $\Omega/\omega_{11}=1$ ). **c:** concentration of the dye at the 20<sup>th</sup> vessel revolution of the wave in **a** whereas in **d:** is depicted the dye concentration at the 9<sup>th</sup> vessel revolution of the wave in **b**.

### 5.2.1 Average flow mixing

During the measurements of the velocity fields, the three component of the velocities are measured repeatedly (usually 50 times) at each successive revolution of the vessel (see Sec. 3.3.2). At each measurement location we obtain a field of average velocities and a corresponding field of standard deviations of the measurements. The mixing induced by the average velocity field is evaluated computing the increase in distance between the particles of a group released from a specific location<sup>†</sup>. Moreover, since the gas exchange occur at the free surface, the vertical mixing of the flow is the most important to achieve homogeneous concentrations in the liquid bulk and is therefore estimated computing the mean of the vertical distance between the

<sup>†</sup>The motion of the particles is computed as Lagrangian trajectories, see more details in Sec. 4.2.1.1.

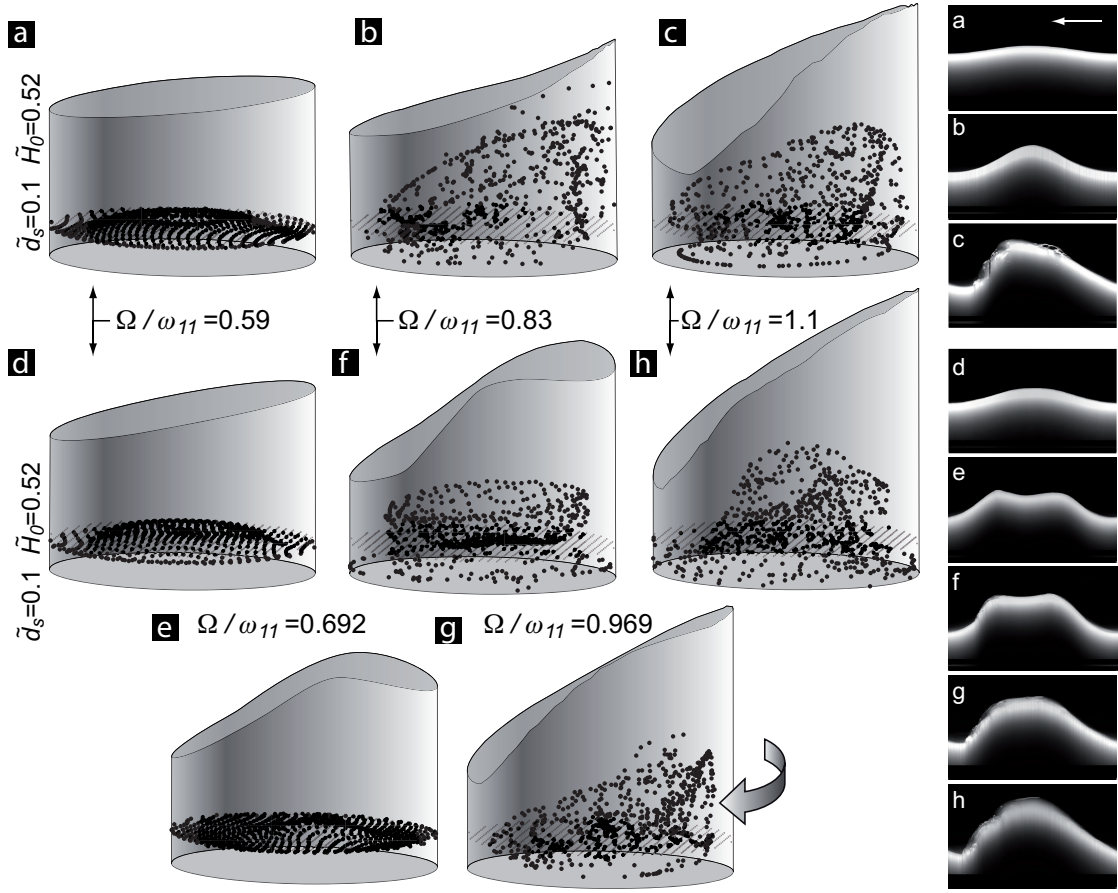


**Figure 5.6** | Positions reached by particles, released on a horizontal plane at  $z_0/H_0=0.2$  after three container revolutions,  $\tilde{H}_0=0.52$  **d**:. The waves at the wall are shown on the right hand side of the figure. **a**:  $\tilde{d}_s=0.1$ ,  $Fr = 0.348$  ( $\Omega/\omega_{11} = 0.59$ ); **b**:  $\tilde{d}_s=0.1$ ,  $Fr = 0.49$  ( $\Omega/\omega_{11} = 0.83$ ); **c**:  $\tilde{d}_s=0.1$ ,  $Fr = 0.655$  ( $\Omega/\omega_{11} = 1.1$ ); **d**:  $\tilde{d}_s=0.2$ ,  $Fr = 0.492$  ( $\Omega/\omega_{11} = 0.59$ ); **e**:  $\tilde{d}_s=0.2$ ,  $Fr = 0.58$  ( $\Omega/\omega_{11} = 0.692$ ); **f**:  $\tilde{d}_s=0.2$ ,  $Fr = 0.695$  ( $\Omega/\omega_{11} = 0.83$ ); **g**:  $\tilde{d}_s=0.2$ ,  $Fr = 0.81$  ( $\Omega/\omega_{11} = 0.969$ ); **h**:  $\tilde{d}_s=0.2$ ,  $Fr = 0.9265$  ( $\Omega/\omega_{11} = 1.1$ )

particles of a group released from a horizontal plane:

$$\overline{||\Delta_z||} = \frac{1}{N^2} \sum_{i=1}^N \sum_{j=1(j \neq i)}^N ||z_i - z_j|| \quad (5.6)$$

where  $z_i$  and  $z_j$  are the vertical position of the  $i^{th}$  and  $j^{th}$  particles and  $N$  is the total number of particles. To highlight the relation between the vertical displacement and the liquid height, the average vertical distance is normalized by  $H_0$ .

The position after three revolutions of 709 particles released at  $z_0/H_0 = 0.2$  with several shaking configurations are depicted Fig. 5.6. while the associated values of  $\overline{||\Delta_z||}$  are shown, normalized by the liquid filling level at rest  $H_0$ , in Fig. 5.7. We notice that the potential behaviour, with or

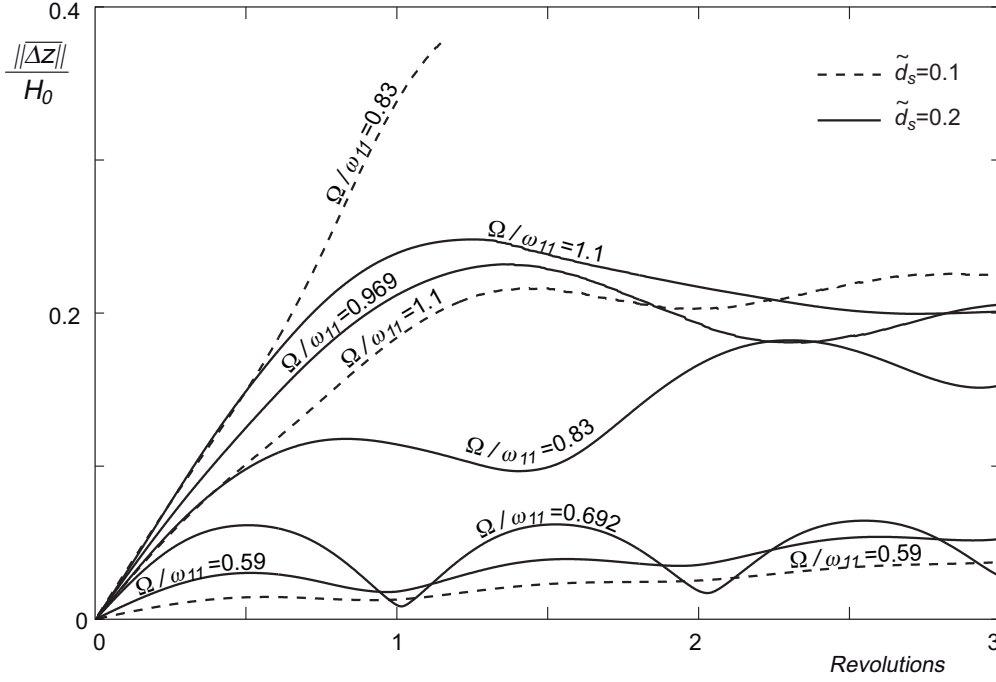


**Figure 5.7** | Average vertical distance  $\overline{||\Delta z||}$  between the liquid particles of each group released into the flow at  $z_0/H_0=0.2$  during three container revolutions, normalized by  $H_0$ , at  $\tilde{H}_0=0.52$ . Dashed lines are for  $\tilde{d}_s=0.1$ , while solid lines are for  $\tilde{d}_s=0.2$ . The shaking frequencies are given in the figure.

without the sub-harmonic double crest (respectively Fig. 5.7a and Fig. 5.7d-e), generates very low mixing. In the potential regime the dispersion of the particles increases with the shaking frequency: at  $\Omega/\omega_{11}=0.83$ , the first crest of the double wave (Fig. 5.6f) is breaking, and we observe a larger dispersion. Moreover, the single crested wave slightly before the incipient breaking (Fig. 5.6b) displays the larger dispersion of the particles, as depicted in Fig. 5.7. Note that after one revolution some particles leave the measurement domain, and the vertical dispersion  $\overline{||\Delta z||}$  in Fig. 5.7 is not shown after this point (particles exiting the measurement regions are not shown in Fig. 5.6 either). After the breaking ( $\Omega > \omega_{11}$ ) the dispersion of particles is somehow similar in all configurations: in the case of single crested waves it is smaller than the one observed at  $\Omega/\omega_{11}=0.83$ , while for double crested waves there is only a small increase between the mixing at  $\Omega/\omega_{11}=0.969$  and 1.1. We observe therefore that, from a mixing point of view, increasing the shaking frequency does not necessarily entail better results.

The very large dispersion of particles observed for single crested breaking waves is explained by two factors. First, the maximum velocities of the flow increase approaching the natural frequency, and are larger for single crested waves than for double crested ones. Indeed, the composition of various waves reduces the maximum values of the velocities. Secondly, the swirling behaviour, while not contributing directly to the vertical mixing, enhances the vertical dispersion of the particles, advecting some of them in regions of upward or downward motion. Indeed, the maximum mixing is achieved when the swirling motion is at its maximum:



respectively at the breaking inception for single crested waves and at the first natural frequency  $\omega_{11}$  for multiple crested ones.

### 5.2.2 Turbulent mixing

Beside the laminar mixing, the particles are dispersed also by the velocity fluctuations. To estimate this turbulent contribution a large number of particles is released simultaneously from a single location. The velocity  $\mathbf{v}(\mathbf{x}_i, t)$  at each location  $\mathbf{x}_i$  and each time  $t$  is assumed to be as follows:

$$\mathbf{v}(\mathbf{x}_i, t) = \bar{\mathbf{v}}(\mathbf{x}_i, t) + \mathbf{f}(\mathbf{x}_i, t) \cdot \sigma(\mathbf{x}_i, t) \quad (5.7)$$

where  $\bar{\mathbf{v}}(\mathbf{x}_i, t)$  and  $\sigma(\mathbf{x}_i, t)$  are the interpolated average and standard deviation values of the velocities at the position  $\mathbf{x}_i$  at the time  $t$  (from PIV measurements), and  $\mathbf{f}(\mathbf{x}_i, t)$  is a vector of three pseudo-random normal distributed values, determined at each time  $t$  and at each position  $\mathbf{x}_i$ .<sup>‡</sup>

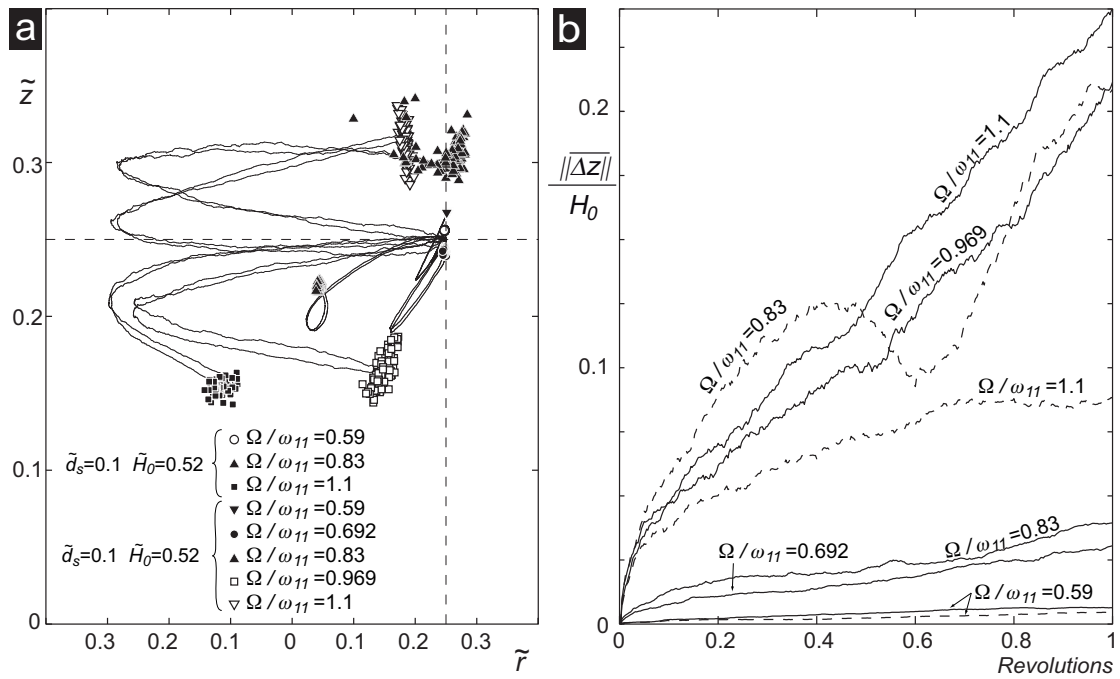


**Figure 5.8 | a:** positions reached by the particles, released at the same location  $z_0/H_0=0.5$ ,  $r_0/D=0.25$  (the crossing of the dashed lines), after one container revolution, projected on a vertical plane passing through the revolution axis of the container. The trajectories of two particles of each group are depicted as solid lines. **b:** average vertical distance  $\|\Delta z\|$  between each group of particles normalized by the unperturbed liquid height  $H_0$ .

<sup>‡</sup>The pseudo-random values are determined by the computation software (Matlab). Large quantities of these values respect thus a normal distribution with average equal to zero and standard deviation equivalent to one.

The dispersion of the particles subject to these velocity fields is representative of the turbulence only if short time intervals are considered: once the distance between the particles increases, they become subject to different average velocity fields, thus their relative distance is increased from the action of both the average and fluctuating velocity fields. For this reason, the dispersion of the particles is computed only during one revolution of the vessel. The position of 100 particles, starting from  $z_0/H_0=0.5$  and  $r_0/D=0.25$  after one revolution of the container are shown in Fig. 5.8a, for  $\tilde{H}_0=0.52$ ,  $\tilde{d}_s=0.1$  and  $\tilde{d}_s=0.2$  and several shaking frequencies. The average vertical distance between the particles of each group is given in Fig. 5.8b. We observe two distinct behaviours for breaking and non breaking waves, especially in the first tenth of revolution. This is not surprising, since the breaking of the wave is known to be a source of turbulence [12]. On the other hand, no particular difference is noticed between single or multiple crested waves, and between waves at the incipient breaking or strong swirling waves.

### 5.2.3 Mixing in non-synchronous waves

Non-synchronous waves, thoroughly described in Sec. 4.3, have a motion of the wave continuously changing as it rotates, due to the transition of the wave pattern between two different synchronous situations. We have identified two main kind of non synchronous waves: single and double crested. Using the PIV velocity measurements and POD analysis we were able to reconstruct the motion of the particles in a double crested non-synchronous wave. The dispersion of a group of particles, released from an horizontal plane at  $z_0/H_0=0.2$ , during three revolutions of the container is compared in Fig. 5.9 to the dispersions of the particles in synchronous waves, discussed above.

The mixing is not enhanced in non-synchronous waves: and the overall dispersion is similar to the one observed for synchronous double crested waves ( $\Omega/\omega_{11} = 0.692$ ,  $\tilde{d}_s=0.1$ ). On the other hand, the mixing efficiency of single crested non-synchronous wave was evaluated using the fluorescent dye technique, described in Sec. 3.4, which gives both mixing map and measurement of the inhomogeneity of the flow:  $\Delta I_{RMS}(R)$ . The latter value is computed at each revolution of the vessel calculating the RMS difference between the dye concentration at a given moment and the homogeneous state, at the end of the experience. Therefore the number of revolutions necessary to attain homogeneity (defined as  $R_h(\tilde{d}_s, \tilde{H}_0, Fr)$ ) may be estimated as  $\Delta I_{RMS}(R_h) < 0.05 \cdot \max(\Delta I_{RMS})$ . Since images of the dye dispersion were taken in four positions of the vessel on its trajectory, and three measurements were performed for each shaking configuration ( $\tilde{d}_s, \tilde{H}_0, Fr$ ), the number of revolutions to homogeneity is obtained as the average of these twelve  $R_h$  values, and defined as  $\bar{R}_h$ . Figure 5.10 depicts the values of  $\bar{R}_h$  measured for a vessel with  $\tilde{d}_s=0.087$ ,  $\tilde{H}_0=0.52$  and  $Fr$  varying between 0.467 and 0.55 or,  $\Omega/\omega_{11}$  between 0.84 and 1.

We observe that the mixing in non-synchronous waves is 20 to 50% better than the one of synchronous waves with slightly different shaking configurations. Therefore, although the



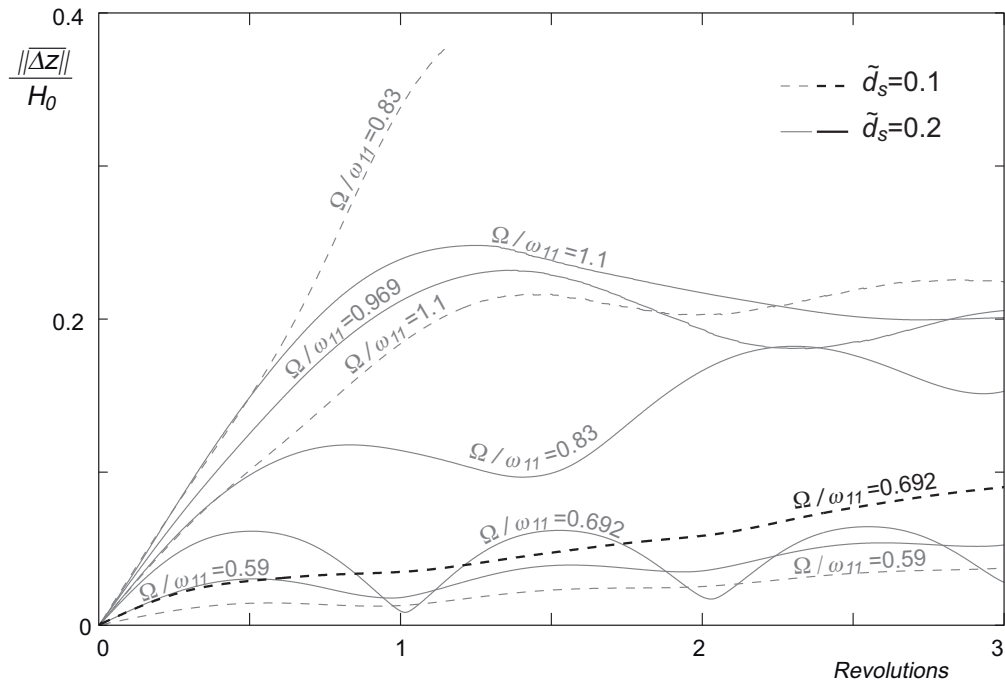


**Figure 5.9** | Average vertical distance  $\overline{||\Delta z||}$ , normalized by the unperturbed liquid height  $H_0$ , between the particles of a group released from a horizontal plane at  $z_0/H_0=0.2$ , during three vessel revolutions, with  $\tilde{d}_s=0.1$ ,  $\tilde{H}_0=0.52$ ,  $Fr = 0.409$  and  $\Omega/\omega_{11} = 0.692$ , giving a non-synchronous double crested wave (dashed black line), compared to the dispersions of synchronous waves (dashed and solid grey lines), already shown in Fig.5.7.

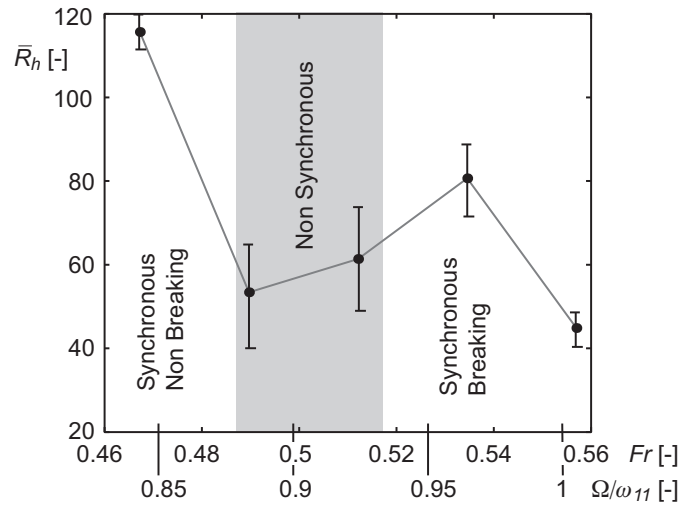


**Figure 5.10** | Average number of rotations necessary to homogenize the dye, for  $\tilde{d}_s=0.087$ ,  $\tilde{H}_0=0.52$ , and several shaking frequencies, depicted as black dots. The errorbars represent the standard deviation on four measurement locations on the vessel, three tests for each shaking configuration. The grey line is intended to guide the eye, whereas the wave pattern is also shown in the figure.

non-synchronous motion was not bringing any enhancement of the mixing for double crested waves, we notice that it greatly improves the mixing for single crested waves. It has to be noted that synchronous single crested waves approaching the breaking, e.g. the one observed at  $\tilde{d}_s=0.1$  and  $\Omega/\omega_{11} = 0.83$  (see Fig.5.7) have the best mixing efficiency observed in the present investigation. It is therefore for these ranges of operating conditions, with synchronous or non-synchronous waves that the best mixing efficiencies are reached.

### 5.3 Optimal wave pattern

Two main phenomena are crucial in large scale cell cultures: the mixing and the oxygenation. While the former has been estimated directly from the velocity fields measurements, the latter depends on the exchange of gas at the free surface and on the homogenization of the gas concentration within the liquid, which is ensured by mixing. The gas exchange is influenced by several parameters: the partial pressure of gas near the interface both in the gas and liquid phase [54] (which is, once again, influenced by mixing), the inclusion of water bubbles in the liquid phase due to breaking waves [63] and the explosion of bubbles at the surface [19]. Moreover, we have seen in the previous sections that the wave pattern and its performances does not depend monotonously on any shaking parameter. The optimum conditions are therefore dictated by the wave pattern rather than by a single shaking parameter (e.g. the shaking frequency).

Taking into account all these aspects, we expect the best conditions for cell cultivations to be reached by single crested waves at shaking frequencies slightly above the breaking inception, to take advantage both of the enhanced mixing and gas exchange. Below this agitation rate non-breaking waves are not suitable since they have too small values of mixing and gas exchange, while swirling regimes (at very high shaking frequencies) may have good gas exchange but insufficient mixing to homogenize the concentrations within the container. To obtain the desired wave pattern, the flow has to be predicted for any set of arbitrary operating parameters.

#### 5.3.1 Prediction of the wave pattern and flow regimes

Summarizing the mathematical and experimental results exposed in the previous chapters, we describe here a “recipe” to predict the breaking inception, expected to be the most efficient pattern in terms of mixing and oxygenation. Given a set of shaking parameters  $D$ ,  $d_s$ ,  $H_0$  and  $\Omega$ , the natural frequencies are calculated using Eq. 2.48:

$$\omega_{mn}^2 = g\lambda_{mn} \tanh(\lambda_{mn}H_0) = \frac{2g\varepsilon_{mn}}{D} \tanh\left(\frac{2\varepsilon_{mn}H_0}{D}\right). \quad (5.8)$$

The most dominant modes are the (1,1), (2,1) and (1,2) thus the corresponding values of the roots  $\varepsilon_{mn}$  are<sup>§</sup>:

$$\varepsilon_{11} = 1.84118378134065$$

$$\varepsilon_{21} = 3.05423692822714$$

$$\varepsilon_{12} = 5.33144277352503$$

The amplitude of single crested wave at the wall is calculated, as long as  $\Omega < \omega_{11}$ , with sufficient precision using the linear solution of the potential problem (Eq. 2.54), considering only the first non-axisymmetric mode (1,1) as dominant:

$$A = \frac{d_s D \Omega^2}{g} \cdot \left( \frac{1}{2} + \frac{1}{(\varepsilon_{11}^2 - 1)} \frac{\Omega^2}{(\omega_{11}^2 - \Omega^2)} \right). \quad (5.9)$$

or, in dimensionless form, according to Eq.4.2:

$$\tilde{A} = Fr^2 \cdot \left( \frac{1}{2} + \frac{1}{(\varepsilon_{11}^2 - 1)} \frac{Fr^2}{(Fr_{11}^2 - Fr^2)} \right), \quad (5.10)$$

where  $Fr_{11}^2 = 2\varepsilon_{11} \tilde{d}_s \tanh(2\varepsilon_{11} \tilde{H}_0)$ .

The wave pattern at the breaking depends on the shaking diameter  $\tilde{d}_s$ : the wave is single crested if  $\tilde{d}_s < \tilde{d}_{s,\omega_{21}/2}$ , where  $\tilde{d}_{s,\omega_{21}/2}$  is defined as (Eq. 4.7):

$$\tilde{d}_{s,\omega_{21}/2} = 0.1349 \cdot \tanh^2(2.5 \tilde{H}_0), \quad (5.11)$$

whereas it is double crested if  $\tilde{d}_s > \tilde{d}_{s,\omega_{21}/2}$ . At shaking diameters very close to the critical one the wave is liable to be non-synchronous at the breaking inception. The dimensionless amplitude of incipient breaking ( $\tilde{A}_b$ ) is computed as

$$\tilde{A}_b = \begin{cases} 0.43 & \text{if } \tilde{d}_s < \tilde{d}_{s,\omega_{21}/2} \\ 0.35 & \text{if } \tilde{d}_s > \tilde{d}_{s,\omega_{21}/2} \end{cases} \quad (5.12)$$

Using this relations it is possible to fix the operating conditions of each scale to obtain a wave at the inception of the breaking, which we expect to be the most favourable regime.

More generally, when the wave is not breaking the height of the free surface, as well as the velocity fields, are predicted in each location within the container using the linear (for single crested waves) or the non-linear (for multiple crested waves) solution of the potential model developed in Chap. 2. The wave is subject to the sub-harmonics excitation, hence a multiple crested wave with  $p$  crest and troughs is expected at each  $\omega_{11}/p$ ,  $\omega_{21}/p$  and to a less extent  $\omega_{12}/p$ , where  $p=1, 2, \dots 6$ .

<sup>§</sup>The list of the  $n^{th}$  root of  $J'_m$  for  $m=0, 1, \dots 5$  and  $n=1, 2, \dots 5$  is given in Appendix B.

### 5.3.2 Engineering considerations

The relations given in the previous section allow to determine the inception of the breaking with any set of operating parameters. However, they do not specify in which ranges of the operating parameters it is more convenient, easy or favourable to obtain a wave at the transition to the breaking. Several other consideration have thus to be taken into account.

According to both the linear and non-linear solutions of the potential model, the velocity fields of all the modes composing the solution depend on the dimensionless unperturbed liquid height  $\tilde{H}_0$  as follows:

$$\begin{aligned} q_r(r, \theta, z, t) &\propto \frac{\cosh(2\varepsilon_{mn}(\tilde{z} + \tilde{H}_0))}{\cosh(2\varepsilon_{mn}\tilde{H}_0)} \\ q_\theta(r, \theta, z, t) &\propto \frac{\cosh(2\varepsilon_{mn}(\tilde{z} + \tilde{H}_0))}{\cosh(2\varepsilon_{mn}\tilde{H}_0)} \\ q_z(r, \theta, z, t) &\propto \frac{\sinh(2\varepsilon_{mn}(\tilde{z} + \tilde{H}_0))}{\cosh(2\varepsilon_{mn}\tilde{H}_0)}, \end{aligned} \quad (5.13)$$

where  $\tilde{z} = z/D$ . Figure 5.11a depicts the evolution of the radial and tangential velocities of the dominant mode (1,1) with the normalized depth ( $z/H_0$ ), for  $\tilde{H}_0 = 0.2, 0.5, 1, 2$  and  $5$ , while in Fig. 5.11b are shown the distribution of the axial velocity. We observe that the value of the tangential and radial velocity at the bottom is determined by  $\tilde{H}_0$ , while the axial velocity is always equivalent to zero (to respect the impermeability condition). We note incidentally

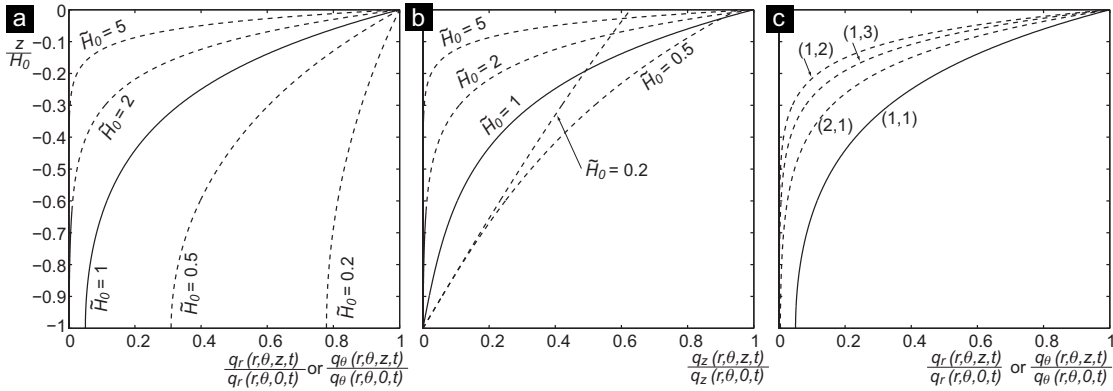


**Figure 5.11** | **a:** evolution of the radial and tangential velocities, normalized by the velocity at  $z = 0$ , with the depth (expressed as the ratio to  $H_0$ ), according to the linear solution of the potential model, for several values of  $\tilde{H}_0$ . **b:** evolution of the axial (vertical) velocity. **c:** Tangential and radial velocities evolution of several of the lowest  $(m, n)$  modes.

that in actual flow, which are viscous, the velocity components at all solid walls are zero, and a boundary layer develops. We neglect here this effect, since the boundary layer thickness is supposed small compared to the size of all phenomena involved, especially when the potential velocity at the wall tends to zero.

The contribution of each mode  $(m, n)$  decreases with the depth also as a function of the value of the  $n^{th}$  root of the derivative of the Bessel's function of the first kind,  $m^{th}$  order, as depicted in Fig. 5.11c. Moreover, evaluating the amplitude of the secondary modes and of the sub-harmonic waves we found them to be smaller than the dominant one. Therefore, the radial and tangential velocity at the bottom may be estimated with good approximation considering only the dominant (1,1) mode. We estimate that at the container bottom the lowest radial and tangential velocities ensuring adequate mixing must be 5% of the velocity at the unperturbed free surface ( $z=0$ ). The maximum acceptable filling ratio  $\tilde{H}_{0,max}$  is therefore:

$$\frac{q_i(r, \theta, -H_0, t)}{q_i(r, 0, z, t)} = \frac{1}{\cosh(2\varepsilon_{11}\tilde{H}_0)} = 0.05 \quad i = r, \theta \quad \text{thus } \tilde{H}_{0,max} \cong 1 \quad (5.14)$$

Furthermore, for each couple of  $\tilde{d}_s$  and  $\tilde{H}_0$  values a shaking frequency  $\Omega$  may be found to have the wave the breaking inception. However, if the unperturbed liquid height  $\tilde{H}_0$  is smaller than half of the dimensionless breaking amplitude  $\tilde{A}_b$  the wave would dry the bottom of the container before breaking. We expect this situation to be undesired for several reasons: first because a drying bottom wave necessarily entails a very strong rotation of the flow, which does not contribute to the mixing. Secondly because this kind of wave generate a large displacement of the liquid centre of mass farther from the axis of the shaker motor. This considerably increases the eccentric forces, hence requiring stronger mechanical constructions, without increasing the mixing and oxygenation efficiencies. To avoid the drying of the bottom a minimum value of  $\tilde{H}_0$  is identified:

$$\tilde{H}_{0,min} = \frac{1}{2}\tilde{A}_b \cong 0.16 - 0.22. \quad (5.15)$$

To identify narrower ranges of the operating parameters, we consider their influence on the shaking frequencies and inertial forces generated by the shaken liquid. Those mechanical quantities have a direct impact on the size and power of the shaker motor and on the strength of the supporting structure, especially at large sizes. Assuming an arbitrary culture volume of a water-like fluid, we may compute the shaking frequency necessary to attain breaking inception for every couple of  $\tilde{d}_s$  and  $\tilde{H}_0$  values, using the relations given in Sec. 5.3.1. Moreover, the moment of inertia  $I_m$  of a body around an arbitrary axis of rotation is defined as:

$$I_m = \int_V \rho(d) d^2 dV \quad (5.16)$$

where  $d$  is the distance of each point of the body from the axis of rotation and  $\rho(d)$  is the density of the volume at each location  $d$ . In the case of liquid under orbital shaking, the distance between the axis of the motor of the shaker and each location within the liquid is:

$$d(r, \theta) = \sqrt{\left(\frac{d_s^2}{4} + d_s r \cos \theta + r^2\right)} \quad (5.17)$$

and, since  $\rho(d) = \rho_w \cdot (\xi(d) + H_0)$ , where  $\rho_w$  is the constant water density, the moment of inertia is calculated as:

$$I_m = \rho_w \int_{r=0}^{D/2} \int_{\theta=0}^{2\pi} (\xi(r, \theta) + H_0) d^2 r dr d\theta. \quad (5.18)$$

The wave shape is approximated using the linear solution of the model, with the breaking inception amplitude. This crude approximation underestimates the actual moment of inertia of a wave near the breaking, but approximates with sufficient precision the trends when an operating parameter is changed. Together, shaking frequency and moment of inertia are proportional to the power required to the motor, and are therefore to be minimized.

In Fig. 5.12a are shown the shaking frequencies necessary to break the wave generated by a 1000 litres culture of a water-like liquid, for  $\tilde{H}_0$  ranging from 0.2 to 1 and  $\tilde{d}_s$  from 0.01 and 0.2, while the corresponding moments of inertia are shown in Fig. 5.12b. We observe, as expected,

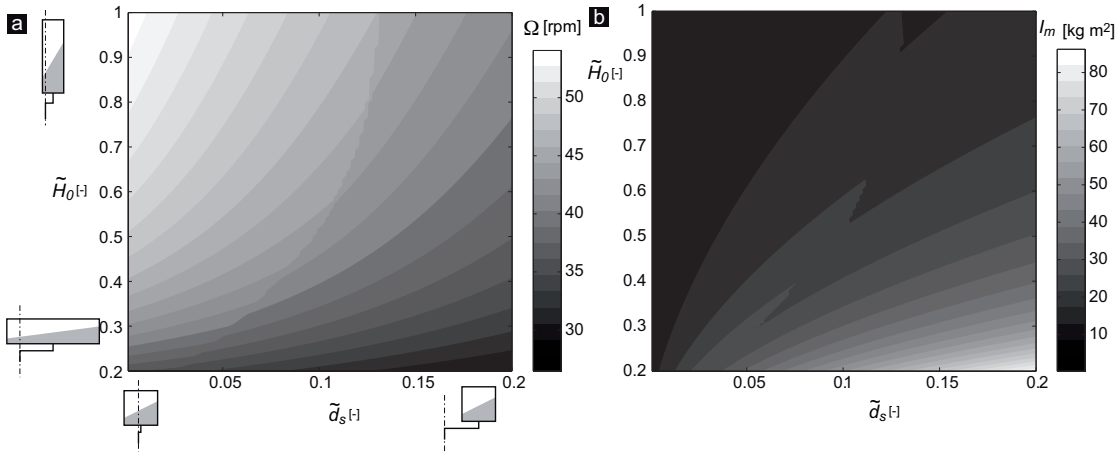


**Figure 5.12 | a:** shaking frequency necessary to attain incipient breaking of a 1000 litres culture of water-like liquid, as a function of the dimensionless unperturbed liquid height  $\tilde{H}_0$  and shaking diameter  $\tilde{d}_s$ . On the axis are schematic illustrations of the culture proportions according to the varying of the dimensionless parameters. **b:** Moment of inertia of the same culture.

that high shaking frequencies are required at very small shaking diameters and large liquid height. This is due to the fact that the first natural frequency  $\omega_{11}$  has high values (due to large  $\tilde{H}_0$ ) and that similar amplitude are obtained with larger shaking frequencies when the shaking diameter is smaller. Conversely, the smaller values are observed at low  $\tilde{H}_0$  and large  $\tilde{d}_s$ . The moment of inertia generally increases with the reduction of  $\tilde{H}_0$ .

Another important structural parameter, affecting the mechanical dimensioning of the shaker, is the centripetal force necessary to maintain the container on its trajectory, given by

$$F_c = M \cdot d \cdot \Omega^2 \quad (5.19)$$

where  $M$  is the total mass of the body and  $d$  the distance between the axis of rotation and the centre of mass. Using the same hypothesis than in the case of moment of inertia, the

centre of mass of the liquid is numerically determined. In Fig. 5.13 is depicted the centripetal force of a 1000 litres culture, at the same ranges of dimensionless parameters used in Fig. 5.12. As reported before, the present computation underestimates the forces, but preserves the trends. We notice that the minimum values are observed at small  $\tilde{H}_0$ , regardless of the shaking diameter  $\tilde{d}_s$ . Thus we suggest to use values of small  $\tilde{H}_0$ , e.g. below 0.4.

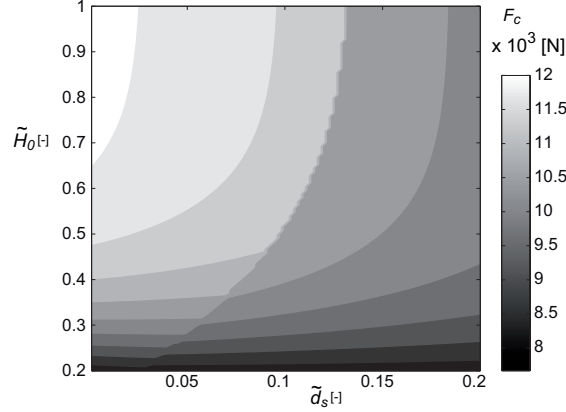


**Figure 5.13** | Estimated centripetal force of a 1000 litres culture at the breaking inception, as a function of the shaking diameter  $\tilde{d}_s$  and the filling ratio  $\tilde{H}_0$ .

#### 5.3.3 The best shaking configuration

Summarizing the previous results, we expect to obtain the best mixing and oxygenation in the entire container, with minimal inertial forces in the shaker structure and average power requirement for single crested waves at the incipient breaking, with  $\tilde{H}_0$  between 0.2 and 0.4,  $\tilde{d}_s = 0.1349 \cdot \tanh^2(2.5\tilde{H}_0)$  (to obtain non-synchronous breaking) or slightly lower (to obtain synchronous single crested breaking). The shaking frequency is to be adjusted to achieve waves with breaker localized at the upper part of the crest (values estimated using the relations in Sec. 5.3.1).

However, we have to consider that mixing is proportional to the velocity gradients in the liquid phase, as it is the shear stress. The optimal shaking configuration proposed here may thus generate stresses not acceptable by the cells. In this case, we suggest to adopt breaking double crested waves, which are obtained for  $\tilde{d}_s > 0.1349 \cdot \tanh^2(2.5\tilde{H}_0)$ . Using a shaker with fixed shaking diameter  $\tilde{d}_s$  the different configurations may be obtained changing the unperturbed liquid height  $\tilde{H}_0$ , and the shaking frequency. Lower mixing efficiency is obtained by non breaking multiple crested, and lower still by non-breaking single crested. It has to be kept in mind that sometimes enhanced mixing may be obtained increasing the working volume, or changing the shaking diameter rather than increasing the shaking frequency.





## 6 Conclusions

The cultivation of cells in orbital shaken containers is a promising and expanding technology. However, it presents several unknowns from the hydrodynamics point of view. In this work we investigated the physics of free surface liquids within circular cylinder subject to orbital shaking, with the help of wave height, velocity field and mixing measurements. Summarizing our results, we have:

- charted the richness and complexity of the wave patterns and their evolution in a large amount of shaking configurations;
- provided a clear physical explanation of the mixing phenomena;
- established a potential model, predicting linear and weakly non-linear phenomena for non-breaking, single and double crested waves;
- assessed the validity and limitations of the theoretical model using the flow measurements, highlighting the importance of the modal response of the shaken liquids;
- identified the dimensionless parameters ensuring hydrodynamic similarity between different scales;
- found the most promising wave shapes in terms of mixing and gas exchange, and proposed ranges of operations for optimal bioreactors performances.



## 7 Perspectives

The motion of liquid under orbital shaking was investigated focusing both on the physics of the flow and on the application to cellular cultures. The interesting results and finding that we have obtained, in the field of wave motion, mixing and optimization, open the way to further investigations, summarized as follows:

### **Hydrodynamics issues**

- Using the potential model, we have shown that the free surface height and the velocity fields are predicted for non-breaking. However, the model may be used to investigate other aspects of the flow, e.g. the stability limits of the potential regime, in a manner similar to the one presented by Hutton [33]. Moreover, since our analyses focused on large scale containers, the analytical solution does not take into account the influence of viscosity or surface tension. In small vessel both properties are expected to play a dominant role, and the model would need to be adapted. Viscous dumping in sloshing motion is presented in [50], chapter 3.
- We still lack a characterization of the liquid motion after the breaking of the waves. At very strong agitation, the flow is expected to be in solid rotation, with the free surface defined by a paraboloid, but it is not clear how this regime is reached from the incipient breaking behaviour, and what are the intermediate steps.
- Non-synchronous waves are very interesting phenomena, that we have discovered in particular shaking configurations. They offer promising performances in terms of mixing. Although their occurrence and main characteristics were identified, we still lack a rigorous physical explanation, and their effect on the mixing needs to be further assessed. We suggest the use of time resolved PIV or of volumetric velocity measurements (e.g. light fields PIV), coupled with instantaneous measurements of the wave height at the entire surface (or at least at the entire wall). The use of POD or other modal filtering techniques is also recommended.

### Bioengineering issues

- We have suggested ranges of shaking parameters ensuring, according to our analyses, optimal conditions in terms of mixing and (we expect) aeration. Those operating ranges have to be confirmed by actual cells cultivations, since, as we have discussed, excessive mixing may also be harmful to cells, especially at large scale. Furthermore, the fine optimization of the shaking parameters must be performed with living cells cultures.
- We suppose that the dispersion of the gas within the container is mainly due to the mixing, and that the gas exchange is maximum at the wave breaking. Although several measurements of the gas transfer have been performed [21, 79, 74, 107], they do not clearly relate the measured values to the regimes and patterns of the waves. This investigation has to be performed to further improve the optimization of the operating parameters.
- The dispersion of the cells, the nutrient and the diluted gasses within the container obviously depends on the flow and is so far unknown. Substituting the cells by seeding particles, it would be possible to determinate the segregation of the cells under each wave regime, and therefore helps establishing numerical or analytical models to predict the inhomogeneities within the container.

# Appendices

## A Surface from diffraction reconstruction

It is possible to use the surface by diffraction paradigm [53] to reconstruct the entire free surface three-dimensionally and instantaneously. This is achieved by measuring the apparent displacement (due to the free surface deformation) of a series of points at the container bottom, due to the deformation of the free surface. A camera above the container follows the displacements of the crossing of a grid, using appropriate image processing routines. The Snell law [114] determines the diffraction angles of the light path caused by the gas-liquid interface:

$$\frac{\sin \theta_1}{\sin \theta_2} = \frac{n_2}{n_1} \quad (\text{A.1})$$

where  $\theta_1$  is the angle between the incident light-path and the free surface,  $\theta_2$  between the diffracted light-path and the free surface,  $n_1$  and  $n_2$  are the refractive index of the gaseous and liquid phase, (Fig. A.1a). The geometric relation between the observed displacement  $\Delta$ , the local liquid elevation  $H$  and the angle of the free surface  $\alpha$  take the form:

$$\Delta = H \cdot \tan \left( \arcsin \left( \frac{n_1}{n_2} \sin(\alpha) \right) - \alpha \right) \quad (\text{A.2})$$

The previous equation has two unknowns:  $H$  and  $\alpha$ . Since in each measurements location is solved in two directions, we have three unknowns for a three dimensional shape reconstruction, namely  $H$ ,  $\alpha_x$  and  $\alpha_y$ . This system of equation was solved iteratively, with the closure condition that the total volume of water is conserved. Moreover, the equation actually used in the calculation took into account also the angle between the observation direction and the free surface, both at the resting and during operation, adding some further trigonometric calculation.

Figure A.1b shows the example of the grid from the top of the container, at  $D=287\text{mm}$ ,  $d_s=50\text{mm}$ ,  $H_0=200\text{mm}$ ,  $\Omega=60\text{rpm}$ . The reconstruction in this case was accurate to some millimetres compare to the potential mode, but with a very poor resolution near the wall. Moreover, the reconstruction of the free surface give acceptable results as long as the interface was not excessively perturbed, by bubbles or by capillary waves. Figure A.1c depicts an image

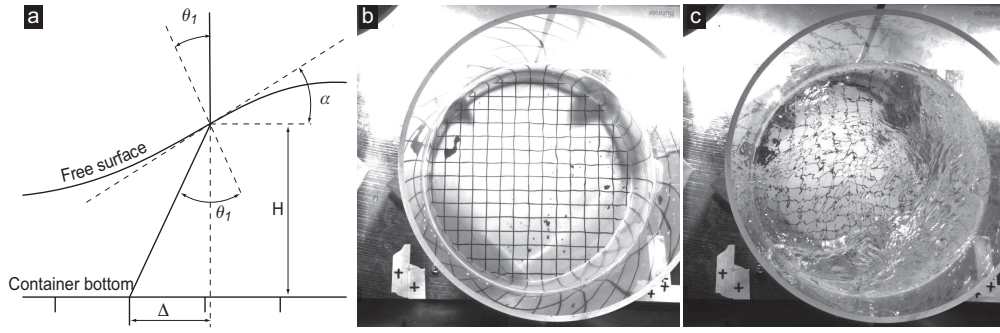


**Figure A.1** | **a:** schematic illustration of the dimensions involved with the reconstruction of the free surface from diffraction. **b:** Example of image of the grid displacement, for  $D=287\text{mm}$ ,  $H_0=200\text{mm}$ ,  $d_s=50\text{mm}$ ,  $\Omega=60\text{rpm}$ . **c:** Example of image of the grid displacement, for  $D=287\text{mm}$ ,  $H_0=200\text{mm}$ ,  $d_s=50\text{mm}$ ,  $\Omega=100\text{rpm}$ .

from the high speed camera when the shaking frequency is increased to 100tpm. Due to the high number of superficial capillary waves, bubbles and other perturbations, it is impossible to reconstruct the crossings of the reference grid and to measure the apparent displacements, hence precluding the reconstruction of the free surface. As the light paths from the grid to the camera became more and more reflected and refracted the reconstruction of the free surface increases in complexity, and became in some cases impossible [62].

Several possibilities to improve the present method have been contemplated. For example, Zhang uses a similar approach [120, 118], where a combination of large lens and coloured screen is used to determine the slope at each surface location. The use of PIV software to reconstruct the apparent displacement of an image at the vessel bottom was also considerate. However, none of the contemplated options improved the precision of the present method near the container walls, nor was reliable and robust enough to be used in automated measurements. Further development was therefore dropped in favour of the measurement at the container wall, described in Sec. 3.2.1.

## B Bessel's functions

The Bessel functions of the first ( $J_{\pm\nu}(x)$ ), of the second ( $Y_\nu(x)$  or sometimes  $I_\nu(x)$ ) and of the third kind ( $H_\nu^{(1)}(x) = J_\nu(x) + Y_\nu(x)$  or  $H_\nu^{(2)}(x) = J_\nu(x) - Y_\nu(x)$ ) are canonical solutions of the form  $y(x)$  of the Bessel's differential equation [2, 111]:

$$x^2 \frac{d^2 y}{dx^2} + x \frac{dy}{dx} + (x^2 - \nu^2)y = 0, \quad (\text{B.1})$$

and their values as a function of  $\nu$  and  $x$  are shown in Fig. B.1. They may be expressed in several integral forms, depending on the value of  $\nu$  (see [2]). Alternatively the first kind may be found expanded in a Taylor series around  $x = 0$ :

$$J_\nu(x) = \left(\frac{1}{2}x\right)^\nu \sum_{k=0}^{\infty} \frac{(-1/4 \cdot x^2)^k}{k! \Gamma(\nu + k + 1)}, \quad (\text{B.2})$$

where  $\Gamma$  is the Gamma function, while the second kind is usually found according to:

$$Y_\nu(x) = \frac{J_\nu(x) \cos(\nu\pi) - J_{-\nu}(x)}{\sin(\nu\pi)}. \quad (\text{B.3})$$

In the case of resolution of Laplace's equation in cylindrical coordinates, it is usual to obtain

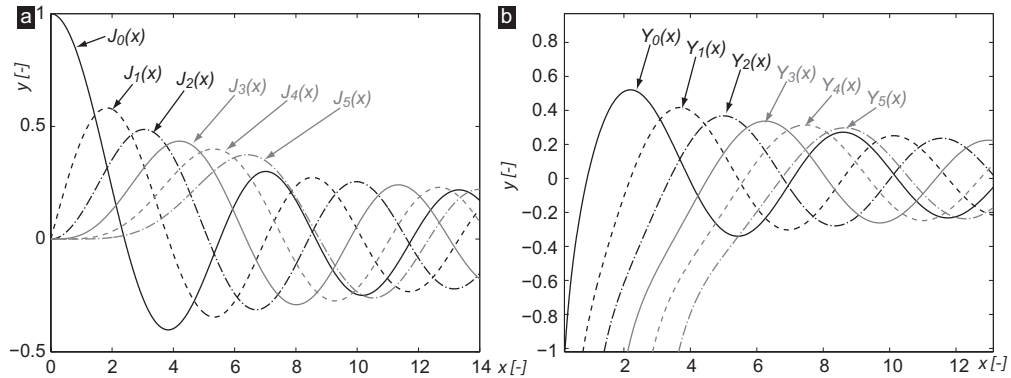


**Figure B.1** | **a:** Bessel's function of the first kind  $J_{\pm\nu}(x)$  and **b:** of the second kind  $Y_\nu(x)$  for  $\nu=0, 1, 2, 3, 4$  and  $5$ , computed by the build-in Matlab function which uses Eqs. B.2 and B.3.

separate solution for each variables  $r$ ,  $\theta$  and  $z$ . The solution in the  $r$  direction is a sum of Bessel's functions of the first and of the second kind [51]. Since the potential must remain bounded within the container, the contribution of the second kind must be zero. Some useful

identities of the Bessel's function of the first kind used in the present work are:

$$J_{-v}(z) = (-1)^v J_v(z) \quad (\text{B.4})$$

$$J'_v(z) = \frac{1}{2} (J_{v-1}(z) - J_{v+1}(z)) \quad v \neq 0 \quad (\text{B.5})$$

$$J'_0(x) = -J_1(x), \quad (\text{B.6})$$

$$\frac{d}{dx} [x^v J_v(x)] = x^v J_{v-1}(x) \quad (\text{B.7})$$

$$\frac{d}{dx} [x^{-v} J_v(x)] = -x^{-v} J_{v-1}(x) \quad (\text{B.8})$$

$$\int_0^b x^{v+1} J_v(\lambda_{vn} x) dx = \frac{b^{v+1}}{\lambda_{vn}} J_{v+1}(\lambda_{vn} b) \quad (\text{B.9})$$

$$v J_v(x) - x J'_v(x) = x J_{v+1}(x) \quad (\text{B.10})$$

while the roots  $\varepsilon_{vn}$  of the derivative of the Bessel function of the first kind are the listed in Table B.1. calculated according [2] or using Matlab approximation.

	n=1	n=2	n=3	n=4	n=5
$v=0$	3.8317059702	7.0155866698	10.173468135	13.323691936	16.470630051
$v=1$	1.8411837813	5.3314427735	8.5363163663	11.706004903	14.863588634
$v=2$	3.0542369282	6.7061331941	9.9694678230	13.170370856	16.347522318
$v=3$	4.2011889412	8.0152365983	11.345924310	14.585848286	17.788747866
$v=4$	5.3175531260	9.2823962852	12.681908442	15.964107038	19.196028800
$v=5$	6.4156163757	10.519860873	13.987188630	17.312842488	20.575514521
$v=6$	7.5012661446	11.734935953	15.268181461	18.637443009	21.931715018
$v=7$	8.5778364897	12.932386237	16.529365884	19.941853367	23.268052926
$v=8$	9.6474216519	14.115518907	17.774012367	21.229062623	24.587197486
$v=9$	10.711433970	15.286737667	19.004593538	22.501398727	25.891277277
$v=10$	11.770876674	16.447852748	20.223031413	23.760715860	27.182021527

**Table B.1** | Roots of the derivative of the Bessel's function of the first kind

## B.1 The Fourier-Bessel Series

Let  $f(x)$  be a function defined within a domain  $[0, b]$ , the Fourier-Bessel series is the linear combination of many orthogonal versions of the same Bessel function of the first kind:

$$f(x) \approx \sum_{n=1}^{\infty} c_n J_m\left(\frac{\gamma_{mn}}{b} x\right) \quad (\text{B.11})$$



where  $\gamma_{mn}$  is a root associated with the Bessel function  $J_m(x)$ . The coefficients are determined projecting the function  $f(x)$  into the respective Bessel functions:

$$c_n = \frac{\langle f(x), J_m(\gamma_{mn}x/b) \rangle}{\langle J_m(\gamma_{mn}x/b), J_m(\gamma_{mn}x/b) \rangle} \quad (\text{B.12})$$

where the inner product is defined as:

$$\langle f(x), g(x) \rangle = \int_0^b x f(x) g(x) dx. \quad (\text{B.13})$$

A particular case of the Fourier Bessel series, called Dini series, is used throughout the present document. When the condition at the limit  $b$  is defined as  $b f'(b) + c f(b) = 0$  where  $c$  is any constant, the series is defined as [111, 83]:

$$f(x) \approx C_0 + \sum_{n=1}^{\infty} c_n J_m\left(\frac{\varepsilon_{mn}}{b} x\right) = C_0 + \sum_{n=1}^{\infty} c_n J_m(\lambda_{mn} x) \quad (\text{B.14})$$

where  $\varepsilon_{mn}$  is the  $n^{th}$  roots of  $x J'_m(x) + c J_m(x) = 0$  and  $\lambda_{mn} = \varepsilon_{mn}/b$ . The coefficients are:

$$c_n = \frac{2\varepsilon_{mn}^2}{b^2(c^2 + \varepsilon_{mn}^2 - m^2) J_m^2(\varepsilon_{mn})} \int_0^b J_m(\lambda_{mn} x) x f(x) dx. \quad (\text{B.15})$$

and

$$C_0(t) = \begin{cases} 0 & \text{if } c + m > 0 \\ \frac{2(m+1)x^m}{b^2} \int_0^b x^{m+1} f(x) dx & \text{if } c + m = 0 \\ \frac{\lambda_{m0}^2 I_m(\lambda_{m0} x)}{b^2(\lambda_{m0}^2 + m^2) I_m^2(\lambda_{m0} x) - \lambda_{m0}^2 I_m^2(\lambda_{m0})} \int_0^b x f(x) I_m(\lambda_{m0} x) dx & \text{if } c + m < 0 \end{cases} \quad (\text{B.16})$$

where  $I_m$  is the modified Bessel's function of the first kind. In the particular case of Eq.2.49, where  $c=0$ ,  $b=D/2$ ,  $m=1$ ,  $x=r$  and  $f(x)=r$ ,  $C_0 = 0$  the coefficients become:

$$c_n = \frac{8\varepsilon_{1n}^2}{D^2(\varepsilon_{1n}^2 - 1) J_1^2(\varepsilon_{1n})} \int_0^{D/2} J_1(\lambda_{1n} r) r^2 dr \quad (\text{B.17})$$

Using Eqs. B.9 and B.10, and since  $J'_1(\varepsilon_{1n}) = 0$  we obtain:

$$c_n = \frac{\varepsilon_{1n} D}{(\varepsilon_{1n}^2 - 1) J_1^2(\varepsilon_{1n})} J_2(\varepsilon_{1n}) = \frac{D}{(\varepsilon_{1n}^2 - 1) J_1(\varepsilon_{1n})} \quad (\text{B.18})$$

## C Three-dimensional drift calculations

The second term of Eq. 2.29 became (omitting the specification  $(\mathbf{x}_0, t')$  for each component of the velocity):

$$\nabla q_r(\mathbf{x}_0, t) \cdot \left( \int_0^t \mathbf{q}(\mathbf{x}_0, t') dt' \right) = \frac{\partial q_r}{\partial r} \int_0^t q_r dt' + \frac{\partial q_r}{r \partial \theta} \int_0^t q_\theta dt' + \frac{\partial q_r}{\partial z} \int_0^t q_z dt' \quad (\text{C.1a})$$

$$\nabla q_\theta(\mathbf{x}_0, t) \cdot \left( \int_0^t \mathbf{q}(\mathbf{x}_0, t') dt' \right) = \frac{\partial q_\theta}{\partial r} \int_0^t q_r dt' + \frac{\partial q_\theta}{r \partial \theta} \int_0^t q_\theta dt' + \frac{\partial q_\theta}{\partial z} \int_0^t q_z dt' \quad (\text{C.1b})$$

$$\nabla q_z(\mathbf{x}_0, t) \cdot \left( \int_0^t \mathbf{q}(\mathbf{x}_0, t') dt' \right) = \frac{\partial q_z}{\partial r} \int_0^t q_r dt' + \frac{\partial q_z}{r \partial \theta} \int_0^t q_\theta dt' + \frac{\partial q_z}{\partial z} \int_0^t q_z dt' \quad (\text{C.1c})$$

We have the following relation for the integrals of the velocities:

$$\int_0^t q_r(\mathbf{x}_0, t') dt' = \frac{d_s}{2} \cos(\Omega t - \theta_0) \cdot A \quad (\text{C.2a})$$

$$\text{where } A = \sum_{n=1}^{\infty} \frac{2\varepsilon_{1n}}{(\varepsilon_{1n}^2 - 1)} \frac{\Omega^2}{(\omega_{1n}^2 - \Omega^2)} \frac{J_1'(2\varepsilon_{1n}r_0/D)}{J_1(\varepsilon_{1n})} \frac{\cosh(2\varepsilon_{1n}(z_0 + H_0)/D)}{\cosh(2\varepsilon_{1n}H_0/D)},$$

$$\int_0^t q_\theta(\mathbf{x}_0, t') dt' = \frac{d_s D}{2r} \sin(\Omega t - \theta_0) \cdot B \quad (\text{C.2b})$$

$$\text{where } B = \sum_{n=1}^{\infty} \frac{1}{(\varepsilon_{1n}^2 - 1)} \frac{\Omega^2}{(\omega_{1n}^2 - \Omega^2)} \frac{J_1(2\varepsilon_{1n}r_0/D)}{J_1(\varepsilon_{1n})} \frac{\cosh(2\varepsilon_{1n}(z_0 + H_0)/D)}{\cosh(2\varepsilon_{1n}H_0/D)},$$

$$\int_0^t q_z(\mathbf{x}_0, t') dt' = \frac{d_s}{2} \cos(\Omega t - \theta_0) \cdot C \quad (\text{C.2c})$$

$$\text{where } C = \sum_{n=1}^{\infty} \frac{2\varepsilon_{1n}}{(\varepsilon_{1n}^2 - 1)} \frac{\Omega^2}{(\omega_{1n}^2 - \Omega^2)} \frac{J_1(2\varepsilon_{1n}r_0/D)}{J_1(\varepsilon_{1n})} \frac{\sinh(2\varepsilon_{1n}(z_0 + H_0)/D)}{\cosh(2\varepsilon_{1n}H_0/D)}.$$

We have the various derivatives derived from equations 2.3. First component:

$$\frac{\partial q_r}{\partial r} = -\frac{d_s \Omega}{2D} \sin(\Omega t - \theta_0) \cdot E \quad (\text{C.3a})$$

$$\text{where } E = \sum_{n=1}^{\infty} \frac{4\varepsilon_{1n}^2}{(\varepsilon_{1n}^2 - 1)} \frac{\Omega^2}{(\omega_{1n}^2 - \Omega^2)} \frac{J_1''(2\varepsilon_{1n}r_0/D)}{J_1(\varepsilon_{1n})} \frac{\cosh(2\varepsilon_{1n}(z_0 + H_0)/D)}{\cosh(2\varepsilon_{1n}H_0/D)};$$

$$\frac{\partial q_r}{r \partial \theta} = \frac{d_s \Omega}{2r} \cos(\Omega t - \theta_0) \cdot A \quad (\text{C.3b})$$

$$\frac{\partial q_r}{\partial z} = -\frac{d_s \Omega}{2D} \sin(\Omega t - \theta_0) \cdot F \quad (\text{C.3c})$$

$$\text{where } F = \sum_{n=1}^{\infty} \frac{4\varepsilon_{1n}^2}{(\varepsilon_{1n}^2 - 1)} \frac{\Omega^2}{(\omega_{1n}^2 - \Omega^2)} \frac{J_1'(2\varepsilon_{1n}r_0/D)}{J_1(\varepsilon_{1n})} \frac{\sinh(2\varepsilon_{1n}(z_0 + H_0)/D)}{\cosh(2\varepsilon_{1n}H_0/D)}.$$

Second component:

$$\frac{\partial q_\theta}{\partial r} = \left( -\frac{d_s \Omega D}{2r_0^2} \cdot B + \frac{d_s \Omega}{2r} \cdot A \right) \cos(\Omega t - \theta_0) \quad (\text{C.4a})$$

$$\frac{\partial q_\theta}{r \partial \theta} = \frac{d_s D \Omega}{2r_0^2} \sin(\Omega t - \theta_0) \cdot B \quad (\text{C.4b})$$

$$\frac{\partial q_\theta}{\partial z} = \frac{d_s \Omega}{2r_0} \cos(\Omega t - \theta_0) \cdot C \quad (\text{C.4c})$$

The definitions of  $A$ ,  $B$  and  $C$  are given in the previous page. The gradient of the third component gives:

$$\frac{\partial q_z}{\partial r} = -\frac{d_s \Omega}{2D} \sin(\Omega t - \theta_0) \cdot F \quad (\text{C.5a})$$

$$\frac{\partial q_z}{r \partial \theta} = \frac{d_s \Omega}{2r_0} \cos(\Omega t - \theta_0) \cdot C \quad (\text{C.5b})$$

$$\frac{\partial q_z}{\partial z} = -\frac{d_s \Omega}{2D} \sin(\Omega t - \theta_0) \cdot G \quad (\text{C.5c})$$

$$\text{where } G = \sum_{n=1}^{\infty} \frac{4\varepsilon_{1n}^2}{(\varepsilon_{1n}^2 - 1)} \frac{\Omega^2}{(\omega_{1n}^2 - \Omega^2)} \frac{J_1(2\varepsilon_{1n}r_0/D)}{J_1(\varepsilon_{1n})} \frac{\cosh(2\varepsilon_{1n}(z_0 + H_0)/D)}{\cosh(2\varepsilon_{1n}H_0/D)}.$$

so for the first component of the speed:

$$\begin{aligned} \nabla q_r(\mathbf{x}_0, t) \cdot \left( \int_0^t \mathbf{q}(\mathbf{x}_0, t') dt' \right) &= \left( -\frac{d_s \Omega}{2D} \sin(\Omega t - \theta_0) E \right) \left( \frac{d_s}{2} \cos(\Omega t - \theta_0) A \right) \\ &+ \left( \frac{d_s \Omega}{2r_0} \cos(\Omega t - \theta_0) A \right) \left( \frac{d_s D}{2r_0} \sin(\Omega t - \theta_0) B \right) \\ &+ \left( -\frac{d_s \Omega}{2D} \sin(\Omega t - \theta_0) F \right) \left( \frac{d_s}{2} \cos(\Omega t - \theta_0) C \right) = \\ &= - \left( \frac{d_s^2 \Omega}{4D} AE - \frac{d_s^2 \Omega D}{4r_0^2} AB + \frac{d_s^2 \Omega}{4D} CF \right) \cos(\Omega t - \theta_0) \sin(\Omega t - \theta_0) \end{aligned} \quad (\text{C.6})$$

second component:

$$\begin{aligned}
 \nabla q_\theta(\mathbf{x}_0, t) \cdot \left( \int_0^t \mathbf{q}(\mathbf{x}_0, t') dt' \right) &= \\
 &= \left[ - \left( \frac{d_s \Omega D}{2r_0^2} \cdot B + \frac{d_s \Omega}{2r_0} \cdot A \right) \cos(\Omega t - \theta_0) \right] \left( \frac{d_s}{2} \cos(\Omega t - \theta_0) A \right) + \dots \\
 &\quad + \left( \frac{d_s D \Omega}{2r_0^2} \sin(\Omega t - \theta_0) B \right) \left( \frac{d_s D}{2r_0} \sin(\Omega t - \theta_0) B \right) + \dots \\
 &\quad + \left( \frac{d_s \Omega}{2r_0} \cos(\Omega t - \theta_0) C \right) \left( \frac{d_s}{2} \cos(\Omega t - \theta_0) C \right) = \\
 &= \left[ - \frac{d_s^2 \Omega D}{4r_0^2} AB + \frac{d_s^2 \Omega}{4r_0} (A^2 + C^2) \right] \cos^2(\Omega t - \theta_0) + \frac{d_s^2 D^2 \Omega}{4r_0^3} \sin^2(\Omega t - \theta_0) B^2 \quad (C.7)
 \end{aligned}$$

and for the third component:

$$\begin{aligned}
 \nabla q_z(\mathbf{x}_0, t) \cdot \left( \int_0^t \mathbf{q}(\mathbf{x}_0, t') dt' \right) &= \left( \frac{d_s \Omega}{2D} \sin(\Omega t - \theta_0) F \right) \left( \frac{d_s}{2} \cos(\Omega t - \theta_0) A \right) \\
 &\quad + \left( \frac{d_s \Omega}{2r_0} \cos(\Omega t - \theta_0) C \right) \left( \frac{d_s}{2r_0^2} \sin(\Omega t - \theta_0) B \right) \\
 &\quad + \left( \frac{d_s \Omega}{2D} \sin(\Omega t - \theta_0) G \right) \left( \frac{d_s}{2} \cos(\Omega t - \theta_0) C \right) = \\
 &= \left( \frac{d_s^2 \Omega}{4D} AF + \frac{d_s^2 \Omega D}{4r_0^2} BC + \frac{d_s^2 \Omega}{4D} CG \right) \cos(\Omega t - \theta_0) \sin(\Omega t - \theta_0) \quad (C.8)
 \end{aligned}$$

where the division by  $r_0$  is introduced to obtain the value in radians instead of meters. Averaging the found second approximation of the velocity at  $t$  we have vanishing first and third component of the velocity, and only the second remains:

$$\begin{aligned}
 \bar{\mathbf{q}}_L &= \frac{1}{2} \left[ \frac{d_s^2 \Omega}{4r_0} (A^2 + C^2) - \frac{d_s^2 \Omega D}{4r_0^2} AB + \frac{d_s^2 D^2 \Omega}{4r_0^3} B^2 \right] \mathbf{e}_\theta = \\
 &= \frac{1}{2} \frac{d_s^2 \Omega}{4r_0} \left[ (A^2 + C^2) - \frac{D}{r_0} AB + \frac{D^2}{r_0^2} B^2 \right] \mathbf{e}_\theta \quad (C.9)
 \end{aligned}$$

## D Combination of time coefficients of first order solution

The of the time coefficients of the expansion at the first order are (Eqs.2.71a, 2.71b, 2.72a and 2.72b):

$$\alpha_{11}(t) = -\frac{d_s \Omega^3 c_1}{2(\omega_{11}^2 - \Omega^2)} \sin \Omega t \quad (\text{D.1a})$$

$$\beta_{11}(t) = +\frac{d_s \Omega^3 c_1}{2(\omega_{11}^2 - \Omega^2)} \cos \Omega t \quad (\text{D.1b})$$

$$a_{11}(t) = \frac{d_s \Omega^2 c_1 \omega_{11}^2}{2g(\omega_{11}^2 - \Omega^2)} \cos \Omega t \quad (\text{D.1c})$$

$$b_{11}(t) = \frac{d_s \Omega^2 c_1 \omega_{11}^2}{2g(\omega_{11}^2 - \Omega^2)} \sin \Omega t. \quad (\text{D.1d})$$

We have then the following relations for  $\alpha_{11}$  and  $a_{11}$ :

$$\alpha_{11}^2 = \frac{d_s^2 \Omega^6 c_1^2}{4(\omega_{11}^2 - \Omega^2)^2} \sin^2 \Omega t = \frac{d_s^2 \Omega^6 c_1^2}{8(\omega_{11}^2 - \Omega^2)^2} (1 - \cos 2\Omega t) \quad (\text{D.2a})$$

$$\alpha_{11} \cdot a_{11} = -\frac{d_s^2 \Omega^5 c_1^2 \omega_{11}^2}{4g(\omega_{11}^2 - \Omega^2)^2} \sin \Omega t \cos \Omega t = -\frac{d_s^2 \Omega^5 c_1^2 \omega_{11}^2}{8g(\omega_{11}^2 - \Omega^2)^2} \sin 2\Omega t \quad (\text{D.2b})$$

$$\dot{\alpha}_{11} \cdot a_{11} = -\frac{d_s^2 \Omega^6 c_1^2 \omega_{11}^2}{4g(\omega_{11}^2 - \Omega^2)^2} \cos^2 \Omega t = -\frac{d_s^2 \Omega^6 c_1^2 \omega_{11}^2}{8g(\omega_{11}^2 - \Omega^2)^2} (1 + \cos 2\Omega t) \quad (\text{D.2c})$$

and for  $\beta_{11}$  and  $b_{11}$  we have consequently:

$$\beta_{11}^2 = \frac{d_s^2 \Omega^6 c_1^2}{8(\omega_{11}^2 - \Omega^2)^2} (1 + \cos 2\Omega t) \quad (\text{D.3a})$$

$$\beta_{11} \cdot b_{11} = \frac{d_s^2 \Omega^5 c_1^2 \omega_{11}^2}{8g(\omega_{11}^2 - \Omega^2)^2} \sin 2\Omega t \quad (\text{D.3b})$$

$$\dot{\beta}_{11} \cdot b_{11} = -\frac{d_s^2 \Omega^6 c_1^2 \omega_{11}^2}{8g(\omega_{11}^2 - \Omega^2)^2} (1 - \cos 2\Omega t) \quad (\text{D.3c})$$

## Appendices

---

The expression with mixed  $\alpha_{11}$ ,  $a_{11}$ ,  $\beta_{11}$  and  $b_{11}$  are:

$$\alpha_{11} \cdot \beta_{11} = -\frac{d_s^2 \Omega^6 c_1^2}{8(\omega_{11}^2 - \Omega^2)^2} \sin 2\Omega t \quad (\text{D.4a})$$

$$\alpha_{11} \cdot b_{11} = -\frac{d_s^2 \Omega^5 c_1^2 \omega_{11}^2}{8g(\omega_{11}^2 - \Omega^2)^2} (1 - \cos 2\Omega t) \quad (\text{D.4b})$$

$$\beta_{11} \cdot a_{11} = \frac{d_s^2 \Omega^5 c_1^2 \omega_{11}^2}{8g(\omega_{11}^2 - \Omega^2)^2} (1 + \cos 2\Omega t) \quad (\text{D.4c})$$

$$\dot{\alpha}_{11} \cdot a_{11} = -\frac{d_s^2 \Omega^6 c_1^2 \omega_{11}^2}{8g(\omega_{11}^2 - \Omega^2)^2} (1 + \cos 2\Omega t) \quad (\text{D.4d})$$

$$\dot{\beta}_{11} \cdot b_{11} = -\frac{d_s^2 \Omega^6 c_1^2 \omega_{11}^2}{8g(\omega_{11}^2 - \Omega^2)^2} (1 - \cos 2\Omega t) \quad (\text{D.4e})$$

$$\dot{\alpha}_{11} \cdot b_{11} = -\frac{d_s^2 \Omega^6 c_1^2 \omega_{11}^2}{8g(\omega_{11}^2 - \Omega^2)^2} \sin 2\Omega t \quad (\text{D.4f})$$

$$\dot{\beta}_{11} \cdot a_{11} = -\frac{d_s^2 \Omega^6 c_1^2 \omega_{11}^2}{8g(\omega_{11}^2 - \Omega^2)^2} \sin 2\Omega t \quad (\text{D.4g})$$

Thus the sums of the previous results are:

$$\alpha_{11}^2 + \beta_{11}^2 = \frac{d_s^2 \Omega^6 c_1^2}{4(\omega_{11}^2 - \Omega^2)^2} \quad (\text{D.5a})$$

$$\alpha_{11}^2 - \beta_{11}^2 = -\frac{d_s^2 \Omega^6 c_1^2}{4(\omega_{11}^2 - \Omega^2)^2} \cos 2\Omega t \quad (\text{D.5b})$$

$$\alpha_{11} a_{11} + \beta_{11} b_{11} = 0 \quad (\text{D.5c})$$

$$\alpha_{11} a_{11} - \beta_{11} b_{11} = -\frac{d_s^2 \Omega^5 c_1^2 \omega_{11}^2}{4g(\omega_{11}^2 - \Omega^2)^2} \sin 2\Omega t \quad (\text{D.5d})$$

$$\alpha_{11} b_{11} + \beta_{11} a_{11} = \frac{d_s^2 \Omega^5 c_1^2 \omega_{11}^2}{4g(\omega_{11}^2 - \Omega^2)^2} \cos 2\Omega t \quad (\text{D.5e})$$

$$\dot{\alpha}_{11} a_{11} + \dot{\beta}_{11} b_{11} = -\frac{d_s^2 \Omega^6 c_1^2 \omega_{11}^2}{4g(\omega_{11}^2 - \Omega^2)^2} \quad (\text{D.5f})$$

$$\dot{\alpha}_{11} a_{11} - \dot{\beta}_{11} b_{11} = -\frac{d_s^2 \Omega^6 c_1^2 \omega_{11}^2}{4g(\omega_{11}^2 - \Omega^2)^2} \cos 2\Omega t \quad (\text{D.5g})$$

$$\dot{\alpha}_{11} b_{11} + \dot{\beta}_{11} a_{11} = -\frac{d_s^2 \Omega^6 c_1^2 \omega_{11}^2}{4g(\omega_{11}^2 - \Omega^2)^2} \sin 2\Omega t \quad (\text{D.5h})$$

---

#### D. Combination of time coefficients of first order solution

---

Several relations, used throughout the present document, are:

$$\dot{\alpha}_{11}a_{11} + \dot{\beta}_{11}b_{11} = -(\alpha_{11}^2 + \beta_{11}^2)\frac{\omega_{11}^2}{g} \quad (\text{D.6a})$$

$$\dot{\alpha}_{11}a_{11} - \dot{\beta}_{11}b_{11} = (\alpha_{11}^2 - \beta_{11}^2)\frac{\omega_{11}^2}{g} \quad (\text{D.6b})$$

$$\dot{\alpha}_{11}b_{11} + \dot{\beta}_{11}a_{11} = \alpha_{11} \cdot \beta_{11} \frac{2\omega_{11}^2}{g} \quad (\text{D.6c})$$

$$\frac{\partial(\alpha_{11}^2 - \beta_{11}^2)}{\partial t} = -(\alpha_{11}a_{11} - \beta_{11}b_{11})\frac{2\Omega^2 g}{\omega_{11}^2} \quad (\text{D.6d})$$

$$\frac{\partial(\alpha_{11}\beta_{11})}{\partial t} = -(\alpha_{11}b_{11} + \beta_{11}a_{11})\frac{\Omega^2 g}{\omega_{11}^2} \quad (\text{D.6e})$$





# Bibliography

- [1] *Le grand Larousse du vin*. Larousse, 2010.
- [2] M. Abramowitz and I. A. Stegun. *Handbook of Mathematical Functions with Formulas, Graphs, and Mathematical Tables*, chapter 9, pages 355–378. Dover, 1965. Available online at [http://people.math.sfu.ca/~cbm/aands/page\\_355.htm](http://people.math.sfu.ca/~cbm/aands/page_355.htm).
- [3] H. N. Abramson. Dynamics of contained liquids: A personal odyssey. *Applied Mechanics Reviews*, 56(1), 2003.
- [4] H. N. Abramson, W. H. Chu, and D. D. Kana. Some studies of nonlinear lateral sloshing in rigid containers. *Journal of Applied Mechanics*, 33(4):777–784, 1966.
- [5] R. Adrian. Particle-imaging techniques for experimental fluid mechanics. *Annual Review of Fluid Mechanics*, 23(1):261–304, 1991.
- [6] R. J. Adrian, K. T. Christensen, and Z.-C. Liu. Analysis and interpretation of instantaneous turbulent velocity fields. *Experiments in Fluids*, 29:275–290, 2000.
- [7] H. E. Albrecht, N. Damaschke, M. Borys, and C. Tropea. *Laser Doppler and phase Doppler measurement techniques*. Springer, 2003.
- [8] M. P. Arroyo and C. A. Greated. Stereoscopic particle image velocimetry. *Measurement Science and Technology*, 2(12):1181, 1991.
- [9] N. Aubry, R. Guyonnet, and R. Lima. Spatiotemporal analysis of complex signals: Theory and applications. *Journal of Statistical Physics*, 64:683–739, 1991.
- [10] M. Banner and D. Peregrine. Wave breaking in deep water. *Annual review of fluid mechanics*, 25(1):373–397, 1993.
- [11] J. a. Battjes. Surf-Zone Dynamics. *Annual Review of Fluid Mechanics*, 20(1):257–291, Jan. 1988.
- [12] J. A. Battjes and T. Sakai. Velocity field in a steady breaker. *Journal of Fluid Mechanics*, 111:421–437, 1981.
- [13] H. Bauer and W. Eidel. Non-linear liquid motion in conical containers. *Acta Mechanica*, 73:11–31, 1988.

## Bibliography

---

- [14] H. Bauer and W. Eidel. Frictionless liquid sloshing in circular cylindrical container configurations. *Aerospace Science and Technology*, 3(5):301 – 311, 1999.
- [15] H. Bauer and K. Komatsu. Coupled frequencies of a frictionless liquid in a circular cylindrical tank with an elastic partial surface cover. *Journal of Sound and Vibration*, 230(5):1147 – 1163, 2000.
- [16] H. F. Bauer. Fluid oscillations in the containers of a space vehicle and their influence upon stability. Technical Report TR-R-187, NASA, 1964.
- [17] H. F. Bauer. Theory of liquid sloshing in compartmented cylindrical tanks due to bending excitation. Technical Report TM-X-51944, MTP-AERO-62-61, NASA, 1964.
- [18] H. F. Bauer. Hydroelastic vibrations in a rectangular container. *International Journal of Solids and Structures*, 17(7):639 – 652, 1981.
- [19] J. C. Bird, R. de Ruiter, L. Courbin, and H. A. Stone. Daughter bubble cascades produced by folding of ruptured thin films. *Nature*, 465(7299):759–62, June 2010.
- [20] P. Bonmarin. Geometric properties of deep-water breaking waves. *Journal of fluid mechanics*, 209(1):405–433, 1989.
- [21] J. Büchs. Introduction to advantages and problems of shaken cultures. *Biochemical Engineering Journal*, 7(2):91–98, Mar. 2001.
- [22] J. Büchs, U. Maier, C. Milbradt, and B. Zoels. Power consumption in shaking flasks on rotary shaking machines: I. Power consumption measurement in unbaffled flasks at low liquid viscosity. *Biotechnology and Bioengineering*, 68(6):589–93, June 2000.
- [23] J. Buechs, U. Maier, S. Lotter, and C. P. Peter. Calculating liquid distribution in shake flasks on rotary shakers at waterlike viscosities. *Biochemical Engineering Journal*, 34(3):200–208, 2007.
- [24] F. Cabaret, S. Bonnot, L. Fradette, and P. A. Tanguy. Mixing time analysis using colorimetric methods and image processing. *Industrial & Engineering Chemistry Research*, 46(14):5032–5042, 2007.
- [25] A. Cariou and G. Casella. Liquid sloshing in ship tanks: a comparative study of numerical simulation. *Marine Structures*, 12(3):183 – 198, 1999.
- [26] J. E. Chappellear. Shallow-water waves. *Journal of Geophysical Research*, 67(12):4693–4704, 1962.
- [27] R. J. Clarke. *Wine Flavour Chemistry*. Blackwell Publishing Ltd, Oxford, UK, Aug. 2004.
- [28] S. N. Cohen, A. C. Y. Chang, H. W. Boyer, and R. B. Helling. Construction of biologically functional bacterial plasmids in vitro. *Proceedings of the National Academy of Sciences*, 70(11):3240–3244, 1973.

- 
- [29] A. Craik. The origins of water wave theory. *Annual Review of Liquid Mechanics*, 36:1–28, 2004.
- [30] M. J. De Jesus, P. Girard, M. Bourgeois, G. Baumgartner, B. Jacko, H. Amstutz, and F. M. Wurm. TubeSpin satellites: a fast track approach for process development with animal cells using shaking technology. *Biochemical Engineering Journal*, 17(3):217–223, Mar. 2004.
- [31] W. A. Duetz. Microtiter plates as mini-bioreactors: miniaturization of fermentation methods. *Trends in Microbiology*, 15(10):469 – 475, 2007.
- [32] W. a. Duetz and B. Witholt. Effectiveness of orbital shaking for the aeration of suspended bacterial cultures in square-deepwell microtiter plates. *Biochemical Engineering Journal*, 7(2):113–115, Mar. 2001.
- [33] H. R. E. An investigation of resonant, non-linear, non-planar free surface oscillation of a fluid. Technical Report TN D-1870, NASA, 1963.
- [34] A. Einstein. Die ursache der mäanderbildung der flussläufe und des sogenannten baerschen gesetzes. *Naturwissenschaften*, 14(11):223–224, 1926. Available online in English at <http://people.ucalgary.ca/~kmuldrew/river.html>.
- [35] J. Fenton. A fifth-order Stokes theory for steady waves. *Journal of Waterway, Port, Coastal, and Ocean Engineering*, 111(2):216–234, 1985.
- [36] J. Fenton. The numerical solution of steady water wave problems. *Computers & Geosciences*, 14(3):357 – 368, 1988.
- [37] J. Fournier and A. M. Cazab. Tears of wine. *Europhysics Letters*, 20(6):517–522, 1992.
- [38] D. Freedman. The shaker in biotechnology. In *Methods in Microbiology*, chapter VI, pages 175–185. Elsevier Science, 1970.
- [39] F. Garcia-Ochoa and E. Gomez. Prediction of gas-liquid mass transfer coefficient in sparged stirred tank bioreactors. *Biotechnology and bioengineering*, 92(6):761–72, Dec. 2005.
- [40] L. Graftieaux, M. Michard, and N. Grosjean. Combining PIV, POD and vortex identification algorithms for the study of unsteady turbulent swirling flows. *Measurement Science and Technology*, 12(9):1422, 2001.
- [41] M. A. Grant. The singularity at the crest of a finite amplitude progressive stokes wave. *Journal of Fluid Mechanics*, 59:257–262, 1973.
- [42] D. L. Hacker, M. De Jesus, and F. M. Wurm. 25 Years of Recombinant Proteins From Reactor-Grown Cells - Where Do We Go From Here? *Biotechnology advances*, 27(6):1023–7, 2009.

## Bibliography

---

- [43] G. M. Hale and M. R. Query. Optical constants of water in the 200-nm to 200- $\mu$ m wavelength region. *Applied Optics*, 12:555–563, 1973.
- [44] A. Handa-Corrigan, A. Emery, and R. Spier. Effect of gas—liquid interfaces on the growth of suspended mammalian cells: mechanisms of cell damage by bubbles. *Enzyme and Microbial Technology*, 11(4):230 – 235, 1989.
- [45] R. G. Harrison, M. J. Greenman, F. P. Mall, and C. M. Jackson. Observations of the living developing nerve fiber. *The Anatomical Record*, 1(5):116–128, 1907.
- [46] P. Hasal, J.-L. Montes, H.-C. Boisson, and I. Fořt. Macro-instabilities of velocity field in stirred vessel: : detection and analysis. *Chemical Engineering Science*, 55(2):391 – 401, 2000.
- [47] P. Holmes, J. Lumley, and G. Berkooz. *Turbulence, Coherent Structures, Dynamical Systems and Symmetry*. Cambridge Monographs on Mechanics. Cambridge University Press, 1996.
- [48] P. J. Holmes, J. L. Lumley, G. Berkooz, J. C. Mattingly, and R. W. Wittenberg. Low-dimensional models of coherent structures in turbulence. *Physics Reports*, 287(4):337 – 384, 1997.
- [49] T. Hummel. Effects of the form of glasses on the perception of wine flavors: a study in untrained subjects. *Appetite*, 41(2):197–202, Oct. 2003.
- [50] R. A. Ibrahim. *Liquid Sloshing Dynamics*. 2005.
- [51] J. Jackson. *Classical electrodynamics*, chapter 3.6-3.7, pages 60–77. Wiley, 1962.
- [52] R. S. Jackson. *Wine tasting: a professional handbook*. Academic Press, 2002.
- [53] B. Jähne, J. Klinker, and S. Waas. Imaging of short ocean wind waves: a critical theoretical review. *Journal of the Optical Society of America A*, 11(8):2197, Aug. 1994.
- [54] B. Jähne and H. Haußecker. Air-water gas exchange. *Annual Review of Fluid Mechanics*, 30(1):443–468, 1998.
- [55] L.-K. Ju and G. Chase. Improved scale-up strategies of bioreactors. *Bioprocess Engineering*, 8:49–53, 1992.
- [56] T. Karstens and K. Kobs. Rhodamine B and rhodamine 101 as reference substances for fluorescence quantum yield measurements. *The Journal of Physical Chemistry*, 84(14):1871–1872, 1980.
- [57] M. Koochesfahani and P. E. Dimotakis. Laser-Induced Fluorescence Measurements of Mixed Fluid Concentration in a Liquid Plane Shear Layer. *AIAA journal*, 23(11):1700–1707, 1985.

- 
- [58] G. Kretzmer. Industrial processes with animal cells. *Applied Microbiology and Biotechnology*, 59(2-3):135–42, July 2002.
- [59] G. Kretzmer and K. Schügerl. Response of mammalian cells to shear stress. *Applied Microbiology and Biotechnology*, 34:613–616, 1991.
- [60] R. Kubin and A. Fletcher. Fluorescence quantum yields of some rhodamine dyes. *Journal of Luminescence*, 27(4):455 – 462, 1983.
- [61] S. Kumar, C. Wittmann, and E. Heinzle. Minibioreactors. *Biotechnology Letters*, 26(1):1–10, 2004.
- [62] K. N. Kutulakos and E. Steger. A Theory of Refractive and Specular 3D Shape by Light-Path Triangulation. *International Journal of Computer Vision*, 76(1):13–29, July 2007.
- [63] E. Lamarre and W. Melville. Air entrainment and dissipation in breaking waves. *Nature*, 351(6326):469–472, 1991.
- [64] H. Lamb. *Hydrodynamics*. Cambridge Mathematical Library. The University Press, 1932.
- [65] A. Lara, E. Galindo, O. Ramírez, and L. Palomares. Living with heterogeneities in bioreactors. *Molecular Biotechnology*, 34:355–381, 2006.
- [66] S. Lee, M. Kim, D. Lee, J. Kim, and Y. Kim. The effects of lng-tank sloshing on the global motions of lng carriers. *Ocean Engineering*, 34(1):10 – 20, 2007.
- [67] T. Levi-Civita. Détermination rigoureuse des ondes permanentes d’amplitude finie. *Mathematische Annalen*, 93:264–314, 1925.
- [68] C. M. Liu and L. N. Hong. Development of a shaking bioreactor system for animal cell cultures. *Biochemical Engineering Journal*, 7(2):121–125, Mar. 2001.
- [69] D. O. Lomen. Digital analysis of liquid propellant sloshing in mobile tanks with rotational symmetry. Technical Report CR-230, NASA, 1965.
- [70] D. O. Lomen. Liquid propellant sloshing in mobile tanks of arbitrary shape. Technical Report CR-222, NASA, April 1965.
- [71] M. S. Longuet-Higgins. The instabilities of gravity waves of finite amplitude in deep water. I. superharmonics. *Proceedings of the Royal Society A: Mathematical, Physical and Engineering Sciences*, 360(1703):471–488, Apr. 1978.
- [72] M. S. Longuet-Higgins and M. Tanaka. On the crest instabilities of steep surface waves. *Journal of Fluid Mechanics*, 336:51–68, Apr. 1997.
- [73] S. Lotter and J. Büchs. Utilization of specific power input measurements for optimization of culture conditions in shaking flasks. *Biochemical Engineering Journal*, 17(3):195 – 203, 2004.

## Bibliography

---

- [74] U. Maier, M. Losen, and J. Buchs. Advances in understanding and modeling the gas-liquid mass transfer in shake flasks. *Biochemical Engineering Journal*, 17(3):155–167, Mar. 2004.
- [75] L. E. McDaniel and E. G. Bailey. Effect of shaking speed and type of closure on shake flask cultures. *Applied Microbiology*, 17(2):286–90, Feb. 1969.
- [76] W. K. Melville. The Role of Surface-Wave Breaking in Air-Sea Interaction. *Annual Review of Fluid Mechanics*, 28(1):279–321, Jan. 1996.
- [77] M. Micheletti, T. Barrett, S. D. Doig, F. Baganz, M. S. Levy, J. M. Woodley, and G. J. Lye. Fluid mixing in shaken bioreactors: Implications for scale-up predictions from microlitre-scale microbial and mammalian cell cultures. *Chemical Engineering Science*, 61(9, Sp. Iss. SI):2939–2949, 2006.
- [78] N. Muller, M. Derouazi, F. Van Tilborgh, S. Wulhfard, D. L. Hacker, M. Jordan, and F. M. Wurm. Scalable transient gene expression in Chinese hamster ovary cells in instrumented and non-instrumented cultivation systems. *Biotechnology Letters*, 29(5):703–711, 2007.
- [79] N. Muller, P. Girard, D. L. Hacker, M. Jordan, and F. M. Wurm. Orbital shaker technology for the cultivation of mammalian cells in suspension. *Biotechnology and bioengineering*, 89(4):400–406, 2005.
- [80] K. Nadaoka, M. Hino, and Y. Koyano. Structure of the turbulent flow field under breaking waves in the surf zone. *Journal of Fluid Mechanics*, 204:359–387, 1987.
- [81] A. W. Nienow. *Stirred Tank Reactors*. Wiley-VCH Verlag GmbH & Co. KGaA, 2000.
- [82] E. T. Papoutsakis. Fluid-mechanical damage of animal cells in bioreactors. *Trends in Biotechnology*, 9(1):427 – 437, 1991.
- [83] R. Pathak and O. Singh. Finite hankel transforms of distributions. *Pacific Journal of Mathematics*, 99(2):439–458, 1982.
- [84] W. Penney and A. Price. Part ii. finite periodic stationary gravity waves in a perfect liquid. *Philosophical Transactions of the Royal Society of London. Series A, Mathematical and Physical Sciences*, 244(882):254–284, 1952.
- [85] D. H. Peregrine. Breaking Waves on Beaches. *Annual Review of Fluid Mechanics*, 15(1):149–178, Jan. 1983.
- [86] O. M. Phillips. *The dynamics of the upper ocean*. Cambridge University Press, first edition, 1966.
- [87] M. Polyanskiy. RefractiveIndex.Info. 2013. <http://refractiveindex.info/?group=PLASTICS&material=PMMA>.

- [88] A. Prasad and R. Adrian. Stereoscopic particle image velocimetry applied to liquid flows. *Experiments in Fluids*, 15:49–60, 1993.
- [89] S. Quinodoz. *Numerical Simulation of Orbitally Shaken Reactors*. PhD thesis, Ecole Polytechnique Fédérale de Lausanne, 2012.
- [90] S. E. Ramberg and O. M. Griffin. Laboratory study of steep and breaking deep water waves. *Journal of Waterway, Port, Coastal and Ocean Engineering*, 113(5):493, 1987.
- [91] M. M. Rienecker and J. D. Fenton. A fourier approximation method for steady water waves. *Journal of Fluid Mechanics*, 104:119–137, 1981.
- [92] A. Royon-Lebeaud, E. J. Hopfinger, and A. Cartellier. Liquid sloshing and wave breaking in circular and square-base cylindrical containers. *Journal of Fluid Mechanics*, 577:467, Apr. 2007.
- [93] I. L. Ryhming. *Dynamique des fluides*. Presse Polytechniques et Universitaires Romandes, ii edition, 2004.
- [94] L. Schwartz and J. Fenton. Strongly Non-Linear Waves. *Annual Review of Fluid Mechanics*, 14:39–60, 1982.
- [95] L. W. Schwartz. Computer extension and analytic continuation of stokes’ expansion for gravity waves. *Journal of Fluid Mechanics*, 62:553–578, 1974.
- [96] G. Sicheri. *Il libro completo del vino*. DeAgostini, 13 edition, 2008.
- [97] L. Sirovich. Turbulence and the dynamics of coherent structures. part i: Coherent structures. *Quart. Applied Mathematics*, 45(3):561 – 571, 1987.
- [98] L. Sirovich. Chaotic dynamics of coherent structures. *Physica D: Nonlinear Phenomena*, 37(1–3):126 – 145, 1989.
- [99] M. Stettler, N. Jaccard, D. Hacker, M. De Jesus, F. M. Wurm, and M. Jordan. New disposable tubes for rapid and precise biomass assessment for suspension cultures of mammalian cells. *Biotech. and Bioeng.*, 95(6):1228–1233, 2006.
- [100] G. G. Stokes. On the theory of oscillatory waves. *Trans Cambridge Philos Soc*, 8:441–473, 1847.
- [101] G. G. Stokes. Considerations relative to the greatest height of oscillatory irrotational waves which can be propagated without change of form. *Mathematical and Physical Papers*, 1:225, 1880.
- [102] D. Struik. Détermination rigoureuse des ondes irrotationnelles périodiques dans un canal à profondeur finie. *Mathematische Annalen*, 95:595–634, 1926.

## Bibliography

---

- [103] J. Svoboda, I. Hložánek, O. Mach, A. Michlová, J. Říman, and M. Urbánková. Transfection of chicken fibroblasts with single exposure to dna from virogenic mammalian cells. *Journal of General Virology*, 21(1):47–55, 1973.
- [104] R.-K. Tan, W. Eberhard, and J. Buechs. Measurement and characterization of mixing time in shake flasks. *Chemical Engingeering Science*, 66(3):440–447, Feb. 2011.
- [105] M. Tanaka. The stability of steep gravity waves. *Journal of the Physical Society of Japan*, 52(9):3047–3055, 1983.
- [106] E. A. Terray, M. A. Donelan, Y. C. Agrawal, W. M. Drennan, K. K. Kahma, A. J. Williams, P. A. Hwang, and S. A. Kitaigorodskii. Estimates of kinetic energy dissipation under breaking waves. *Journal of Physical Oceanography*, 26(5):792–807, 1996.
- [107] S. Tissot. *OrbShake Bioreactors for Mammalian Cell Cultures: Engineering and Scale-up*. PhD thesis, Ecole Polytechnique Fédérale de Lausanne, 2011.
- [108] S. Tissot, M. Farhat, D. L. Hacker, T. Anderlei, M. Kühner, C. Comninellis, and F. M. Wurm. Determination of a scale-up factor from mixing time studies in orbitally shaken bioreactors. *Biochemical Engineering Journal*, 52(2-3):181–186, Nov. 2010.
- [109] S. Tissot, A. Oberbek, M. Reclari, M. Dreyer, D. L. Hacker, L. Baldi, M. Farhat, and F. M. Wurm. Efficient and reproducible mammalian cell bioprocesses without probes and controllers ? *New biotechnology*, Feb. 2011.
- [110] S. M. Walker. Particle image velocimetry: study of the flow field within an erlenmeyer flask on an orbital shaker table. *Proceedings of SPIE*, 5058:34–50, 2003.
- [111] G. N. Watson. *A treatise on the theory of Bessel functions*. Cambridge University Press, 1995.
- [112] W. Weheliye, M. Yianneskis, and A. Ducci. On the fluid dynamics of shaken bioreactors—flow characterization and transition. *AIChE Journal*, 59(1):334–344, 2013.
- [113] G. Whitham. *Linear and nonlinear waves*. Pure and applied mathematics. Wiley, 1974.
- [114] K. B. Wolf and G. Krotzsch. Geometry and dynamics in refracting systems. *European Journal of Physics*, 16(1):14–20, Jan. 1995.
- [115] F. M. Wurm. Production of recombinant protein therapeutics in cultivated mammalian cells. *Nature Biotechnology*, 22(11):1393–1398, Nov. 2004.
- [116] Z. Xing, B. M. Kenty, Z. J. Li, and S. S. Lee. Scale-up analysis for a cho cell culture process in large-scale bioreactors. *Biotechnology and Bioengineering*, 103(4):733–746, 2009.
- [117] A. Zhang and K. Suzuki. A comparative study of numerical simulations for fluid–structure interaction of liquid-filled tank during ship collision. *Ocean Engineering*, 34(5–6):645 – 652, 2007.



- [118] X. Zhang. An algorithm for calculating water surface elevations from surface gradient image data. *Experiments in Fluids*, 21:43–48, 1996.
- [119] X. Zhang, C.-A. Bürki, M. Stettler, D. De Sanctis, M. Perrone, M. Discacciati, N. Parolini, M. DeJesus, D. L. Hacker, A. Quarteroni, and F. M. Wurm. Efficient oxygen transfer by surface aeration in shaken cylindrical containers for mammalian cell cultivation at volumetric scales up to 1000L. *Biochemical Engineering Journal*, 45(1):41–47, June 2009.
- [120] X. Zhang and C. Cox. Measuring the two-dimensional structure of a wavy water surface optically: a surface gradient detector. *Experiments in Fluids*, 17:225–237, 1994.
- [121] A. Zobeiri, P. Ausoni, F. Avellan, and M. Farhat. How oblique trailing edge of a hydrofoil reduces the vortex-induced vibration. *Journal of Fluids and Structures*, 32(0):78 – 89, 2012.



## Reclari Martino, Ing. Mec. dipl. EPF

Via Tosello  
CH - 6946 Ponte Capriasca  
+41 79 395 98 44  
martino.reclari@gmail.com

11.04.1984  
Single  
Swiss / Italian

## EDUCATION

<b>Doctoral School in Mechanical Engineering</b> Thesis: Hydrodynamics of Orbital Shaken Bioreactors Laboratory for Hydraulic Machines (EPFL)	<b>2010 – March 2013</b>
<b>Master in Mechanical Engineering</b> Specialization in Aero-Hydrodynamics, secondary specialization in Energy. Master thesis on wing tip vortex cavitation, awarded Ryhming Prize (EPFL), for distinguishing work in fluid mechanics. EPFL Lausanne	<b>2007 – 2009</b>
<b>Swiss Army Officer School</b> Panzer /Artillerie Offizier Schule and active duty as army officer, Frauenfeld, Bern, Thun	<b>2006 – 2007</b>
<b>Bachelor in Mechanical Engineering</b> EPFL Lausanne	<b>2003 – 2006</b>
<b>High School and Swiss Federal Scientific Maturity</b> Liceo Cantonale Lugano 1	<b>1999 – 2003</b>

## WORK EXPERIENCE

<b>Scientific Advisor</b> Researches on energy production for Team Rivage (Vendee Globe solo round the world sailing race), Laboratory for Hydraulic Machines (EPFL).	<b>2010 –2013</b>
<b>Lecturer</b> Participation to the teaching of the aerodynamic courses (Master) with lectures on the boundary layer.	<b>2011 –2012</b>
<b>Scientific Advisor</b> Researches on skin drag reduction for Alinghi Team (at the time America's Cup defender). Laboratory for Hydraulic Machines (EPFL).	<b>2009 –2010</b>
<b>Active duty as Army Officer</b> Experience in team leading, taking responsibility and initiative, and practice in management of manpower and resources.	<b>since 2007</b> (1 month yearly)

## LANGUAGES

Italian	: native language	
French	: fluent	(C2 of the European standards of languages)
English	: good	(B2-C1)
German	: basic knowledge	(B1-B2)

## TECHNICAL KNOWLEDGE

**Computer:** Windows and Unix OS, DS Catia, Ansys CFX, Icem, Fluent, Matlab, C++, MS Basic, MS Office  
**Experimental:** Particle Image Velocimetry, Laser Doppler Velocimetry, High Speed Imaging

## OTHERS CERTIFICATES

<b>Leadership 1 Certificate</b> , Swiss Association for Leader Training (SVF-ASFC)	<b>2007</b>
<b>Snowboard Instructor license</b> (Second Level and Freeride J+S Switzerland)	<b>2002</b>

## SPORTS

Fencing, snowboarding, telemarking, kite surfing